

APPLICATION AND INTEGRATION OF RUTHENIUM CATALYSTS FOR WATER
TREATMENT AND RESOURCE RECOVERY

by

Xiangchen Huo

A thesis submitted to the Faculty and the Board of Trustees of the Colorado School of Mines in partial fulfillment of the requirements for the degree of Doctor of Philosophy (Civil and Environmental Engineering).

Golden, Colorado

Date: _____

Signed: _____

Xiangchen Huo

Signed: _____

Dr. Timothy J. Strathmann
Thesis Advisor

Golden, Colorado

Date: _____

Signed: _____

Dr. Terri S. Hogue
Professor and Head
Department of Civil and Environmental Engineering

ABSTRACT

Water contaminants in oxidized form can be preferably removed or transformed to less harmful species by chemical or biological reduction. Hydrogenation metal-catalyzed reduction has emerged as a promising treatment technology for oxidized pollutants (e.g., oxyanions, halo- and nitro-organics). To date, Pd-based catalysts have received significant attention and demonstrate good activity and stability in reducing a number of contaminants relevant to drinking water or groundwater, but the deployment of catalytic reduction systems remains limited, in large part, by the high cost and volatile market price of this metal. The narrow focus on Pd-based materials also hinders the advancement of catalytic reduction technology because other hydrogenation metals are being overlooked which may have exhibited higher activity for specific contaminants. In addition, demonstrating catalytic activity with multiple metals can reduce uncertainty in the cost of the technology by allowing for metal substitution during market price spikes. Thus, it is necessary to expand catalyst “toolbox” for the water treatment applications and to integrate catalysts with other technologies (e.g., separations processes) to advance the development of practical water catalysis technologies.

To develop alternative hydrogenation metal catalysts for water purification, several supported platinum group metals catalysts were assessed with a suite of representative oxyanion pollutants. Rh, Ru, Pt and Ir were found to exhibit higher activity, wider substrate selectivity or variable pH dependence in comparison to Pd. A detailed investigation, coupling experiments with computational work, was then conducted to identify mechanisms controlling nitrate and nitrite reduction by supported Ru catalysts. Pseudo-first-order rate constants and turnover frequencies were determined for carbon- and alumina-supported Ru, and this work demonstrated

Ru's high activity for hydrogenation of nitrate at ambient temperature and H₂ pressure. Pretreatment of the catalysts was found to enhance nitrate reduction activity by removing catalyst surface contaminants and exposing highly reducible surface Ru oxides. Ru reduces nitrate selectively to ammonia and nitrite to a mixture of ammonia and N₂, with the product distribution determined by the initial aqueous nitrite concentrations. Experimental observation and Density Functional Theory calculations together support a reaction mechanism wherein sequential hydrogenation of nitrate to nitrite and NO is followed by parallel pathways involving the adsorbed NO that lead to ammonia and N₂.

The activity of supported Ru catalysts was further evaluated for reducing *N*-nitrosamines, including the toxic disinfection byproduct *N*-nitrosodimethylamine (NDMA) and other organic water contaminants. Using NDMA as a representative contaminant, commercial Ru/Al₂O₃ catalyst showed high activity with an initial turnover frequency (TOF₀) of 58.0 ± 7.0 h⁻¹. A second Ru/Al₂O₃ catalyst was synthesized using an incipient wetness impregnation technique, and this catalyst exhibited higher initial pseudo-first-order rate constant than the commercial catalyst due to higher dispersion of Ru nanoparticles on the catalyst support. NDMA was reduced to dimethylamine (DMA) and ammonia end-products, and a small amount of 1,1-dimethylhydrazine (UDMH) was detected as a transient intermediate. Experiments with a mixture of five *N*-nitrosamines spiked into tap water (1 μg L⁻¹ each) demonstrated that Ru catalysts are very effective in reducing a range of *N*-nitrosamine structures at environmentally relevant concentrations. These results encourage the further development of Ru catalysts as part of the water purification and remediation toolbox.

Supported Ru catalyst was then integrated into a hybrid catalytic hydrogenation/membrane distillation process to improve nitrate-contaminated ion exchange

waste brine management and recover valuable nitrogen resources. The ability of a commercial Ru/C catalyst to reduce concentrated nitrate was demonstrated in a semi-batch reactor under typical waste brine conditions. Nitrate hydrogenation exhibited zero-order kinetics, attributed to saturation of available surface reaction sites, and the apparent rate constant was influenced by both solution chemistry and reaction temperature. The resulting ammonia product was efficiently recovered using membrane distillation. At low temperatures (<35 °C), solution pH showed significant impact on ammonia mass transfer coefficient by controlling the free ammonia species fraction. Ammonia recovery efficiency was not affected by salt levels in the brine, indicating the feasibility of membrane distillation for recovering ammonia from waste ion exchange brine. The hybrid catalytic hydrogenation/membrane distillation process was also applied to a real ion exchange waste brine and demonstrated high nitrate hydrogenation and ammonia recovery efficiency. These findings provide alternative catalyst for catalytic treatment of ion exchange waste brine and design option of efficient, low footprint system for nitrogen resource recovery from waste ion exchange brines.

In addition, the efforts of catalyst and process development were extended to the field of bio-renewable energy. Leveraging fuel property predictive models, a non-cyclic branched C₁₄ hydrocarbon (5-ethyl-4-propylnonane) was identified to be a potential target molecule for renewable diesel applications. This target molecule is accessible from butyric acid through sequential catalytic reactions of acid ketonization, ketone condensation, and hydrodeoxygenation. Catalytic activity, product selectivity, and catalyst stability for individual conversion step were first evaluated, followed by demonstration of hydrocarbon blendstock production from butyric acid through integrated conversion process scheme. Experimental fuel property testing of the conversion product validated its suitability for use as diesel blendstock.

TABLE OF CONTENTS

ABSTRACT.....	iii
LIST OF FIGURES	xiii
LIST OF TABLES.....	xxii
ACKNOWLEDGEMENTS.....	xxiv
CHAPTER 1 INTRODUCTION AND MAIN OBJECTIVES	1
1.1 Background	1
1.1.1 Catalytic treatment of oxyanion water contaminants	1
1.1.2 <i>N</i> -nitrosamines as emerging water contaminants and treatment options	5
1.1.3 Supported Ruthenium catalysts and their applications.....	7
1.1.4 Strategies for regenerating nitrate-contaminated ion exchange waste brine.....	10
1.2 Main Objectives	13
1.3 Intellectual Merits and Broader Impacts	15
1.4 References	16
CHAPTER 2 EXPLORING BEYOND PALLADIUM: CATALYTIC REDUCTION OF AQUEOUS OXYANION POLLUTANTS WITH ALTERNATIVE PLATINUM GROUP METALS AND NEW MECHANISTIC IMPLICATIONS	25
2.1 Abstract	25
2.2 Introduction	26
2.3 Experimental	27

2.3.1	Chemicals and materials	27
2.3.2	Catalytic reduction of oxyanion contaminants	28
2.3.2.1	Bromate (BrO_3^-)	28
2.3.2.2	Chlorate (ClO_3^-)	29
2.3.2.3	Nitrate (NO_3^-)	29
2.3.2.4	Preparation of Re-M/C and reduction of perchlorate (ClO_4^-)	29
2.3.3	Water sample analysis	30
2.3.4	Catalyst characterization	30
2.3.5	Kinetic data analysis	31
2.4	Results and Discussion	31
2.4.1	Catalytic reduction of bromate	31
2.4.2	Catalytic reduction of chlorate	33
2.4.3	Catalytic reduction of nitrate	36
2.4.4	Effect of metal catalyst support materials	37
2.4.5	Catalytic reduction of perchlorate	37
2.4.6	Mechanistic insights from metal and AO_3^- reactivity cross comparisons....	40
2.4.7	Outlook in catalyst development and application	44
2.5	Conclusions	45
2.6	References	45
CHAPTER 3 HYDROGENATION OF AQUEOUS NITRATE AND NITRITE WITH RUTHENIUM CATALYSTS		51

3.1	Abstract	51
3.2	Introduction	52
3.3	Materials and methods	55
3.3.1	Catalysts	55
3.3.2	Nitrate and nitrite reduction kinetics	56
3.3.3	Isotope labeling experiments	57
3.3.4	Computational methods	58
3.4	Results and Discussion	59
3.4.1	Catalytic nitrate reduction	59
3.4.2	Effect of pretreatment on nitrate reduction activity	65
3.4.3	Catalytic nitrite reduction	70
3.4.4	Site-limited reduction kinetics	72
3.4.5	Proposed reaction pathway	74
3.4.6	Implications for technology development	77
3.5	Conclusions	79
3.6	References	79
CHAPTER 4 RUTHENIUM CATALYSTS FOR REDUCTION OF <i>N</i> -NITROSAMINE WATER CONTAMINANTS		88
4.1	Abstract	88
4.2	Introduction	89
4.3	Experimental Section	92

4.3.1	Chemicals	92
4.3.2	Catalyst preparation and characterization	92
4.3.3	Catalytic reduction of NDMA	93
4.3.4	Catalytic reduction of <i>N</i> -nitrosamines under environmentally relevant conditions	95
4.3.5	Analytical methods	96
4.4	Results and Discussion	97
4.4.1	Catalytic NDMA reduction activity	97
4.4.2	NDMA reduction products	102
4.4.3	Mechanistic considerations	104
4.4.4	Catalytic reduction of <i>N</i> -nitrosamines under environmentally relevant conditions	106
4.4.5	Role of Ru catalysts in water purification and remediation toolbox	108
4.5	References	110

CHAPTER 5 A HYBRID CATALYTIC HYDROGENATION/MEMBRANE DISTILLATION PROCESS FOR NITROGEN RESOURCE RECOVERY FROM NITRATE-CONTAMINATED WASTE ION EXCHANGE BRINES		115
--	--	-----

5.1	Abstract	115
5.2	Introduction	116
5.3	Materials and Methods	119
5.3.1	Materials	119
5.3.2	Catalytic hydrogenation experiments	119

5.3.3	Membrane distillation experiments	121
5.3.4	Aqueous analysis	123
5.4	Results and Discussion	123
5.4.1	Catalytic hydrogenation of nitrate	123
5.4.2	Ammonia recovery by membrane distillation	129
5.4.3	Ion exchange waste brine nitrate removal and nitrogen recovery	134
5.4.4	Application considerations of the hybrid process	138
5.5	Conclusions	142
5.6	References	143
CHAPTER 6 TAILORING DIESEL BIOBLENDSTOCK FROM INTEGRATED CATALYTIC UPGRADING OF CARBOXYLIC ACIDS: A “FUEL PROPERTY FIRST” APPROACH.....		149
6.1	Abstract	149
6.2	Introduction	150
6.3	Results	153
6.3.1	Fuel property prediction	153
6.3.1.1	Mapping hydrocarbons derived from C2/C4 acids.....	153
6.3.1.2	Down-selection of targets for diesel blendstock.....	157
6.3.2	Catalytic upgrading of butyric acid	158
6.3.2.1	Single step conversion of model compounds.....	158
6.3.2.2	Integrated conversion of model and bio-butyric acid	163

6.3.3	Blendstock and blend fuel properties verification.....	167
6.4	Discussion	171
6.5	Conclusions	175
6.6	Materials and Methods	175
6.6.1	Predictive models	175
6.6.2	Catalytic upgrading	177
6.6.3	Fuel property testing.....	178
6.7	References	179
CHAPTER 7 SUMMARY, CONCLUSIONS, AND FUTURE WORK		188
7.7	Conclusions	188
7.7	Future Work	190
APPENDIX A SUPPLEMENTARY DATA FOR CHAPTER 2.....		194
APPENDIX B SUPPLEMENTARY DATA FOR CHAPTER 3.....		198
B.1	Experimental Methods	198
B.1.1	Chemical reagents	198
B.1.2	Catalyst characterization	198
B.1.3	Calculation of kinetic parameters.....	200
B.1.4	Analytical methods.....	201
B.2	Experimental Results.....	203
B.2.1	Evaluation of mass transfer limitation.....	203

B.2.2	Experimental results	205
B.2.2	DFT calculation notes and results	207
B.2.3	References	209
APPENDIX C	SUPPLEMENTARY DATA FOR CHAPTER 4.....	211
C.1	Evaluation of Internal Mass Transfer Limitation	211
C.2	Experimental Results.....	212
C.3	References	217
APPENDIX D	SUPPLEMENTARY DATA FOR CHAPTER 5.....	219
APPENDIX E	SUPPLEMENTARY DATA FOR CHAPTER 6.....	220
E.1	Experimental Methods	220
E.1.1	Catalyst synthesis and characterization	220
E.1.2	Catalytic testing.....	222
E.1.3	Chemical analysis.....	224
E.1.4	Lignocellulosic sugars fermentation and acids separation	226
E.2	Experimental Results.....	228
E.3	References	238
APPENDIX F	PERMISSIONS	240

LIST OF FIGURES

Figure 1.1 Nitrate hydrogenation pathway on Pd-based bimetallic catalysts.....	3
Figure 1.2 Representative approaches for transforming <i>N</i> -nitrosamines by breaking N-NO bond.	7
Figure 1.3 Flow diagram of the hybrid ion exchange-catalyst treatment system. Reproduced from Bergquist <i>et al.</i> ¹⁰¹	13
Figure 2.1 Timecourse profiles with for reduction of (a) 1 mM BrO ₃ ⁻ by 0.1 g L ⁻¹ M/C catalysts and (b) 1 mM ClO ₃ ⁻ by 0.5 g L ⁻¹ M/C catalysts with 1 atm H ₂ at pH 7.2 and 22 °C (nominal 5 wt% metal for Pd, Rh, Ru, and Pt; 1 wt% metal for Ir). ..	32
Figure 2.2 Timecourse profiles with for reduction of (a) 1 mM BrO ₃ ⁻ by 0.1 g L ⁻¹ M/Al ₂ O ₃ catalysts and (b) 1 mM ClO ₃ ⁻ by 0.5 g L ⁻¹ M/Al ₂ O ₃ catalysts with 1 atm H ₂ at pH 7.2 and 22 °C (nominal 5 wt% metal for all catalysts).....	38
Figure 2.3 (a) Mechanisms for Re–M/C catalyst reactions with ClO ₄ ⁻ and ClO _x ⁻ intermediates (x = 3, 2, or 1); adapted from Refs ^{50, 51} . (b) Reduction of 5 mM ClO ₄ ⁻ with 2 g L ⁻¹ Re–M/C (5 wt% Re, 5 wt% M) bimetallic catalysts.	39
Figure 2.4 Mechanism illustrations of (a) the reduction of oxyanion substrates (AO _x ⁻) requiring direct interaction with the hydrogenation metal nanoparticles; (b) the reaction between AO _x ⁻ and spilled over atomic hydrogen at the catalyst support surface away from the hydrogenation metal nanoparticles.	41
Figure 2.5 Catalyst loading normalized rate constants at different pH for the reduction of 1 mM (a) BrO ₃ ⁻ , (b) ClO ₃ ⁻ and (c) NO ₃ ⁻ with Rh/C and Ru/C catalysts. Error bars represent replicate-averaged 95% confidence intervals. “NR” indicates no reaction observed within the reaction period monitored.	42
Figure 2.6 Influence of pH on the zeta potential of 0.5 g L ⁻¹ Rh/C and Ru/C catalysts in H ₂ -saturated aqueous suspension at 22 °C.	43
Figure 3.1 Nitrate hydrogenation pathway on Pd-based bimetallic catalysts.....	54
Figure 3.2 Measured reaction timecourses for nitrate reduction and first-order model fits on 5 wt% Ru/C, 5 wt% Pd/C, and 5 wt% Pd-1 wt% Cu/C in the semi-batch reactor system (0.2 g L ⁻¹ catalyst, [NO ₃ ⁻] ₀ = 1.6 mM, 1 atm H ₂ continuous sparging except in control experiments where 1 atm N ₂ continuous sparging was used, pH 5.0 maintained by pH stat, 25 ± 0.5 °C). Error bars represent standard deviations of triplicate reactions.	60

Figure 3.3 HAADF-STEM images of (a) <i>ex situ</i> H ₂ pretreated Ru/C, (b) Ru/C after re-use experiment, (c) as-received Ru/C and (d) <i>ex situ</i> H ₂ pretreated Ru/Al ₂ O ₃ . The insets show Ru particle size distributions.	63
Figure 3.4 Timecourses showing aqueous and gaseous intermediates and products during Ru/C-catalyzed reduction of ¹⁵ N-labeled (a) nitrate and (b) nitrite monitored in closed-bottle batch systems (0.2 g L ⁻¹ catalyst, [¹⁵ NO ₃ ⁻] ₀ or [¹⁵ NO ₂ ⁻] ₀ = 1.6 mM, initially 1 atm H ₂ , pH 5.5 buffered by 40 mM MES, 21 ± 1 °C). Error bars represent standard deviations of triplicate reactions (smaller than symbol if not visible).	64
Figure 3.5 Influence of catalyst pretreatments (as-received catalyst or <i>ex situ</i> pretreated in flowing H ₂ or N ₂ at 350 °C for 2 h) on reactivity with aqueous nitrate (0.2 g L ⁻¹ catalyst with nominal 5 wt% Ru or Pd, [NO ₃ ⁻] ₀ = 1.6 mM, 1 atm H ₂ continuous sparging, pH 5.0 maintained by automatic pH stat, 25 ± 0.5 °C). Error bars represent standard deviations of triplicate measurements (smaller than symbol if not visible). NR = no reaction observed.	66
Figure 3.6 XRD patterns of (a) Ru/C and (b) Ru/Al ₂ O ₃ collected after different <i>ex situ</i> pretreatments. Peaks assigned to Ru metal (○) and RuO ₂ (*) are indicated.	67
Figure 3.7 TPR profiles of (a) as-received Ru/C, (b) <i>ex situ</i> N ₂ pretreated Ru/C, (c) <i>ex situ</i> H ₂ pretreated Ru/C, (d) as-received Ru/Al ₂ O ₃ , (e) <i>ex situ</i> N ₂ pretreated Ru/Al ₂ O ₃ , and (f) <i>ex situ</i> H ₂ pretreated Ru/Al ₂ O ₃ . TCD signals are normalized with sample mass.	69
Figure 3.8 (a) Comparison of Ru/C-catalyzed nitrite reaction kinetics with nitrate reaction at standard conditions (0.2 g L ⁻¹ Ru/C, [NO ₃ ⁻] ₀ or [NO ₂ ⁻] ₀ = 1.6 mM). (b) TOF ₀ of Ru/C-catalyzed nitrate and nitrite reduction as a function of initial concentration of the target oxyanion (0.2 g L ⁻¹ Ru/C). (c) Measured timecourses for the simultaneous reduction of nitrate and nitrite added to a suspension containing Ru/C (0.2 g L ⁻¹ catalyst, [NO ₃ ⁻] ₀ = [NO ₂ ⁻] ₀ = 1.6 mM). Other conditions include 1 atm H ₂ continuous sparging, pH 5.0 maintained by automatic pH stat, and 25 ± 0.5 °C. Error bars in panels a-b represent standard deviations of triplicate measurements.	71
Figure 3.9 Effect of initial (a) nitrate and (b) nitrite concentration on NH ₄ ⁺ /N ₂ product selectivity (yellow: NH ₄ ⁺ ; blue: N ₂). Product selectivity is based on percent molar N concentration. Error bars represent standard deviations of triplicate measurements (smaller than symbol if not visible).	72
Figure 3.10 Energy profile of the most thermodynamically favorable reaction pathways for aqueous nitrate and nitrite reduction on Ru ₁₈ clusters as calculated using PBE0 functional and LANL2DZ (Ru)/6-31+G(d,p)(N, H, O) basis sets.	76

Figure 4.1 Timecourse of NDMA reduction with different catalysts in the semi-batch reactor system ($[\text{NDMA}]_0 = 100 \mu\text{M}$, 0.1 g L^{-1} catalyst, pH 6.0 buffered by 10 mM MES buffer, continuous sparging of 1 atm H_2 , $22 \pm 0.5 \text{ }^\circ\text{C}$). Error bars represent standard deviations of triplicate reactions. Catalyst formulation details provided in Table 4.1.	98
Figure 4.2 HAADF-STEM images of (a) commercial $\text{Ru}/\text{Al}_2\text{O}_3$ and (b) in-house prepared $\text{Ru}/\text{Al}_2\text{O}_3$. The insets show Ru particle size distributions.	101
Figure 4.3 (a) Carbon and (b) nitrogen balance of NDMA reduction on commercial $\text{Ru}/\text{Al}_2\text{O}_3$ in the batch system ($[\text{NDMA}]_0 = 100 \mu\text{M}$, 0.1 g L^{-1} catalyst, pH 6.0 buffered by 10 mM MES buffer, 1 atm H_2 , $22 \pm 0.5 \text{ }^\circ\text{C}$). Error bars represent range of results from duplicate reactions (smaller than symbol if not visible).	103
Figure 4.4 Proposed mechanism of NDMA reduction on Ru catalyst surfaces.	106
Figure 4.5 Catalytic reduction of a mixture of <i>N</i> -nitrosamines added to tap water ($1 \mu\text{g L}^{-1}$ of each <i>N</i> -nitrosamine, 0.1 g L^{-1} commercial $\text{Ru}/\text{Al}_2\text{O}_3$ catalyst, initial solution pH 9.0, continuous sparging of 1 atm H_2 , $22 \pm 0.5 \text{ }^\circ\text{C}$). Lines show pseudo-first-order model fits for disappearance of each <i>N</i> -nitrosamine. Error bars represent the range of measured values in duplicate reactions (smaller than symbol if not visible).	107
Figure 5.1 Flow diagram of the hybrid catalytic hydrogenation/membrane distillation process to enable ion exchange regenerant brine reuse and nitrogen resource recovery.	119
Figure 5.2 Schematic diagram of the bench scale membrane distillation system.	123
Figure 5.3 Catalytic nitrate hydrogenation under baseline testing condition and evolution of solution pH. Conditions: 5 g L^{-1} Ru/C , initial $[\text{NO}_3^-] = 100 \text{ mM}$, brine matrix (5 wt% NaCl , 100 mM NaHCO_3 , 100 mM Na_2SO_4), 30°C , no solution pH control, 1 atm H_2 headspace maintained by flowing H_2 at ca. 300 mL min^{-1} . Error bars indicate standard deviation from duplicate measurements (smaller than symbol if not visible). Solid line indicates zero-order rate law fit. Dashed line indicates change in measured pH during the reaction.	126
Figure 5.4 (A) Ammonia removal from brine by membrane distillation under baseline testing conditions. (B) Ammonia mass balance in feed and H_2SO_4 adsorbent solution. Solid line in (A) refers to the first-order rate law fit.	131
Figure 5.5 Catalytic nitrate hydrogenation in real waste brine and synthetic waste brine prepared with similar anionic composition. Conditions: 6 g L^{-1} Ru/C , $30 \text{ }^\circ\text{C}$, no	

<p>solution pH control, 1 atm H₂ headspace maintained by flowing H₂ at ca. 300 mL min⁻¹. The effect of pH control by flowing CO₂ (at ca. 65 mL min⁻¹) was also examined. Error bars indicate standard deviation from duplicate measurements (smaller than symbol if not visible). Solid line refers to the zero-order rate law fit.....</p>	135
<p>Figure 5.6 (A) Ammonia removal from real waste brine and synthetic solution by membrane distillation. Conditions: 4 L feed at 1.5 L min⁻¹, 1.15 L 0.25 M H₂SO₄ adsorbent solution at 1.5 L min⁻¹, 30 °C. (B) Ammonia mass balance in real waste brine feed and H₂SO₄ adsorbent solution. Solid line in (A) refers to the first-order rate law fit.</p>	137
<p>Figure 5.7 Ru/C reused for three reaction cycles in real waste brine: (a) nitrate hydrogenation time courses, and (b) apparent zero-order rate constants. Conditions: 6 g L⁻¹ Ru/C, 30 °C, no solution pH control, 1 atm H₂ headspace maintained by flowing H₂ at ca. 300 mL min⁻¹, catalyst dried at 70°C in between reuse cycles.....</p>	140
<p>Figure 5.8 Aqueous concentration of nitrate and total ammonia during real waste brine catalytic hydrogenation: (a) no pH control (b) pH maintained by flowing CO₂. Conditions: 6 g L⁻¹ Ru/C, 30 °C, 1 atm H₂ headspace maintained by flowing H₂ at ca. 300 mL min⁻¹, in (b) CO₂ flow at ca. 65 mL min⁻¹. Error bars indicate standard deviation from duplicate measurements (smaller than symbol if not visible).</p>	142
<p>Figure 6.1 “Fuel property first” design approach to leverage fuel property predictive models for the design of performance-advantaged diesel bioblendstock.</p>	153
<p>Figure 6.2 Upgrading scheme for converting C₂/C₄ carboxylic acids to hydrocarbon molecules via ketonization (KET), condensation (COND), and hydrodeoxygenation (HDO).</p>	154
<p>Figure 6.3 On-stream performance and product distribution of commercial butyric acid ketonization over 3 g ZrO₂ in flowing Ar [1 atm, 100 mL (STP) min⁻¹] at 435 °C and WHSV = 3.8 h⁻¹. WHSV was calculated using the mass flow rate of butyric acid and the mass of the catalyst.....</p>	159
<p>Figure 6.4 Nb₂O₅ reused for 4-heptanone condensation four times in a batch reactor by regeneration at 350 °C in between cycles. Reaction conditions: 15 g feed, 20 wt% 4-heptanone in toluene, 0.75 g catalyst, catalyst-to-ketone mass ratio = 1:4, initial He headspace at atmospheric pressure, 180 °C, 10 h.....</p>	160
<p>Figure 6.5 On-stream performance and product distribution of dimer HDO over 1 g Pt/Al₂O₃</p>	

in flowing H ₂ [500 psi, 165 mL (STP) min ⁻¹] at 334 °C and WHSV = 4.4 h ⁻¹ . The dimer feed (81% dimer purity) was derived from commercial 4-heptanone. WHSV was calculated using the mass flow rate of the dimer feed and the mass of the catalyst.	163
Figure 6.6 Integrated process scheme for upgrading butyric acid to hydrocarbon diesel blendstock.	165
Figure 6.7 Carbon yield analysis of ketonization, condensation, and HDO when upgrading commercial butyric acid to hydrocarbon diesel blendstock through the integrated process scheme as shown in Figure 6.6. Conditions: ketonization same as in Figure 6.3; condensation same as in Figure E.2a in Appendix E, 24 h reaction, C distribution not accounting for solvent; HDO same as in Figure 6.5, 2 hours of time-on-stream. Analysis assumed ideal mass recovery.	165
Figure 6.8 GC-Polyarc/FID chromatograms of organic phase products from (A) ketonization, (B) condensation, and (C) HDO (solvent was removed from biologically derived product by distillation) when upgrading butyric acid through the integrated process scheme.	168
Figure A.1 Timecourse profiles with Br mass balance for reduction of 1 mM BrO ₃ ⁻ and Br ⁻ product formation using 0.1 g L ⁻¹ M/C (nominal 5 wt% metal for Pd, Rh, Ru, and Pt; 1 wt% metal for Ir) and 1 atm H ₂ (100 mL min ⁻¹ sparging rate) at pH 7.2, 22 °C.	194
Figure A.2 Timecourse profiles observed at acidic pH conditions (pH 3.0) for reduction of (a) 1 mM BrO ₃ ⁻ by 0.1 g L ⁻¹ M/C catalysts and (b) 1 mM ClO ₃ ⁻ by 0.5 g L ⁻¹ M/C catalysts. All experiments were carried out in continuously mixed aqueous suspensions and sparged with 1 atm H ₂ at 22 °C.	195
Figure A.3 Timecourse profiles with Cl mass balance for reduction of 1 mM ClO ₃ ⁻ and Cl ⁻ product formation using 0.5 g L ⁻¹ M/C (nominal 5 wt% metal for Pd, Rh, Ru, and Pt; 1 wt% metal for Ir) and 1 atm H ₂ (20 mL min ⁻¹ sparging rate) at pH 7.2, 22 °C.	196
Figure A.4 Reduction profiles for 1 mM NO ₃ ⁻ by 0.5 g L ⁻¹ Ru/C catalyst at different pH.	196
Figure B.1 Example calibration curve of total N- ¹⁵ N ₂ in the reactor.	202
Figure B.2 Influence of 5 wt% Ru/C catalyst loading in the aqueous suspension on the initial rate of nitrate reduction (1 atm H ₂ continuous sparging, pH 5.0 maintained by automatic pH stat, 25 ± 0.5 °C, [NO ₃ ⁻] ₀ = 1.6 mM). Error bars represent standard deviations of triplicate reactions.	204

Figure B.3 Re-use of Ru/C in semi-batch system. Error bar for fresh catalyst represents standard deviations of triplicate reactions. For reuse experiments, error bars represent the min/max values measured in duplicate reactions.....	205
Figure B.4 Influence of pH on the Ru-mass-normalized pseudo-first-order rate constants for nitrate reduction on Ru/C (1 atm H ₂ continuous sparging, 25 ± 0.5 °C, 0.2 g L ⁻¹ Ru/C, [NO ₃ ⁻] ₀ = 1.6 mM). Error bars represent standard deviations of triplicate reactions.....	205
Figure B.5 (a) HAADF-STEM image of <i>ex situ</i> H ₂ pretreated Pd/C and (b) TEM image of <i>ex situ</i> H ₂ pretreated Pd/Al ₂ O ₃ . The insets show Pd particle size distributions.	206
Figure B.6 Temperature-programmed desorption profile of Ru/C.....	207
Figure C.1 Control experiments for NDMA reaction in H ₂ -sparged solution (no catalyst) and suspensions of commercial Ru/Al ₂ O ₃ catalyst sparged with Ar (inert gas) in place of H ₂ . Error bars representing the range of values measured in duplicate reactions are all smaller than symbols shown.....	212
Figure C.2 Initial reaction rate as a function of initial NDMA concentration. Lines represent least-squares fit of Langmuir-Hinshelwood model to the data shown. Error bars represent standard deviations of triplicate experiments.....	214
Figure C.3 NDMA reduction activity of commercial Ru/Al ₂ O ₃ in repetitive NDMA spiking experiments (0.1 g L ⁻¹ catalyst, pH 6.0 buffered by 10 mM MES buffer, continuous sparging of 1 atm H ₂ , 22 ± 0.5 °C). Error bars represent range of results from duplicate reactions (smaller than symbol if not visible).....	214
Figure C.4 NDMA reduction product selectivity to ammonia as a function of solution pH. Error bars represent the range of observed values in duplicate experiments.	215
Figure C.5 (A) Comparison of metal weight-normalized pseudo-first-order rate constants for reduction of NDMA and UDMH, and (B) UDMH reduction product selectivity as a function of initial UDMH concentration in the semi-batch reactor system (0.1 g L ⁻¹ catalyst, pH 6.0 buffered by 10 mM MES buffer, continuous sparging of 1 atm H ₂ , 22 ± 0.5 °C). Error bars represent standard deviations obtained from triplicate experiments.....	215
Figure C.6 Structures of <i>N</i> -nitrosamines examined in treatment experiments conducted in tap water.....	216
Figure C.7 Catalytic reduction of a mixture of <i>N</i> -nitrosamines added to deionized water (1 ug L ⁻¹ of each <i>N</i> -nitrosamine, 0.1 g L ⁻¹ commercial Ru/Al ₂ O ₃ catalyst, initial	

<p>solution pH 9.0, continuous sparging of 1 atm H₂, 22 ± 0.5 °C). Error bars represent the range of measured values in duplicate reactions (smaller than symbol if not visible).</p>	216
<p>Figure C.8 Comparison between Ru/Al₂O₃ and Pd/Al₂O₃ catalyst activities for reduction of different N-containing contaminants and halogenated aromatic contaminants. Error bars represent standard deviations of triplicate reactions. Data for NO₃⁻ from previous study.⁹</p>	217
<p>Figure D.1 Initial nitrate hydrogenation rate as a function of Ru/C loading. Conditions: Initial [NO₃⁻] = 100 mM, brine matrix (5 wt% NaCl, 100 mM NaHCO₃, 100 mM Na₂SO₄), 30 °C, no solution pH control, 1 atm H₂ headspace maintained by flowing H₂ at ca. 300 mL min⁻¹. Error bars indicate standard deviation from duplicate measurements (smaller than symbol if not visible).</p>	219
<p>Figure D.2 Plot of initial rate versus the inverse of initial nitrate concentrations. Error bars indicate standard deviation from duplicate measurements (smaller than symbol if not visible).</p>	219
<p>Figure E.1 Plot of model predictions of (A) melting point, (B) boiling point, (C) flash point, (D) lower heating value, (E) cetane number, and (F) yield sooting index. Error bars represent standard deviations of multiple model predictions summarized in Table E.1. Grey dash lines and arrows represent screening criteria.</p>	230
<p>Figure E.2 (A) Conversion of commercial 4-heptanone and selectivity to dimer with reaction time (15 g feed, 20 wt.% 4-heptanone in toluene, 0.75 g fresh Nb₂O₅, catalyst-to-ketone mass ratio = 1:4, 180 °C). (B) Decreasing average rate for 4-heptanone condensation with reaction time (same reaction as figure A). (C) Performance of recycled catalyst (15 g feed, 20 wt% 4-heptanone in toluene, 0.75 g spent catalyst after washing with solvent and drying at room temperature, catalyst-to-ketone mass ratio = 1:4, 180 °C, 10 h or 24 h). All experiments were conducted in an initial He headspace at atmospheric pressure.</p>	231
<p>Figure E.3 (A) 4-Heptanone condensation at varying ketone loadings (15 g feed, 0.75 g fresh Nb₂O₅, 20–100 wt% 4-heptanone in toluene, corresponding catalyst-to-ketone mass ratio from 1:4 to 1:20, 180 °C, 10h). (B) Average rate for 4-heptanone condensation (same reaction as figure A). (C) 4-Heptanone and dimer concentrations in the organic phase product at varying fresh Nb₂O₅ loadings (15 g feed, neat 4-heptanone, catalyst-to-ketone mass ratio from 1:20 to 1:5, 180 °C, 24 h). All experiments were conducted in an initial He headspace at atmospheric pressure.</p>	231
<p>Figure E.4 (A) Conversion of 4-heptanone at varying temperatures (15 g feed, 20 wt% 4-heptanone in toluene, 0.75 g fresh Nb₂O₅, catalyst-to-ketone mass ratio = 1:4, 10</p>	

h). (B) Arrhenius plot for 4-heptanone condensation. All experiments were conducted in an initial He headspace at atmospheric pressure.	232
Figure E.5 Simulated distillation curves of purified dimer and heavier compounds (heavies were obtained from removing dimer by distillation).	232
Figure E.6 High resolution mass spectra of the C ₁₄ hydrocarbon.	233
Figure E.7 ¹³ C NMR spectrum of purified C ₁₄ hydrocarbon.	233
Figure E.8 Mass recovery and dimer purity in three distillation fractions when distilling condensation product.	234
Figure E.9 GC-Polyarc/FID chromatogram of crude hydrocarbon blendstock from upgrading commercial butyric acid. The major component is the target non-cyclic branched C ₁₄ hydrocarbon. Scale was adjusted to highlight minor components. Peak at 4.6 min was from solvent impurity.	234
Figure E.10 GC×GC-TOFMS chromatogram of crude hydrocarbon blendstock from upgrading commercial butyric acid: (a) dilution 20:1 and (b) dilution 400:1. The major component is the target non-cyclic C ₁₄ hydrocarbon. The most abundant classes present in the mixture are non-cyclic alkanes and cyclic alkanes, although there is potential overlap between these classes and ambiguous identification of linear alkanes and alkenes in these regions. Other structures identified in the plot include aromatics. Note that results are not quantitative.	235
Figure E.11 ¹³ C NMR analysis of crude hydrocarbon blendstock from upgrading commercial butyric acid. The crude blendstock exhibited approximately 2% carbon in double bond or aromatic bond. Compared with pure C ₁₄ hydrocarbon, the crude blendstock displayed 3% decrease in the ratio of primary carbon. The ratio of carbon having two hydrogen attached (mostly secondary carbon) also decreased 3%. Accordingly, the ratio of carbon having one or no hydrogen attached (e.g., tertiary carbon, quaternary carbon, aromatic carbon) slightly increased.	236
Figure E.12 Batch conversion of lignocellulosic sugars by <i>Clostridium butyricum</i> (ATCC 19398). (A) Sugar utilization and bacterial growth measured as optical density at 600 nm (OD). (B) Butyric acid and byproducts formation. Data show the average of two biological replicates. Error bars represent the absolute difference between those replicates.	237
Figure E.13 Simulated distillation curves of commercial butyric acid derived crude C ₁₄ blendstock, base diesel, and diesel blend with 20 vol% bioblendstock (D86	

correlation was applied to all three curves). 238

Figure E.14 Pot of (A) CN and (B) normalized soot concentration over blend ratio of commercial butyric acid derived crude C₁₄ blendstock (and biblendstock as indicated in figure). Dotted lines are to guide the eye. 238

LIST OF TABLES

Table 1.1 Current regulatory status of selected oxyanions in drinking water.	2
Table 2.1 Catalyst information and characterization data	34
Table 2.2 Initial turnover frequencies for the reaction of 1 mM oxyanions with M/C, M/Al ₂ O ₃	35
Table 3.1 Properties of catalysts used for nitrate activity test	62
Table 4.1 Properties of catalysts used for NDMA reduction activity test.	100
Table 5.1 Ion exchange waste brine composition.	121
Table 5.2 Summary of nitrate hydrogenation zero-order rate constants under different reaction conditions (1 atm H ₂ , Ru/C dose 5 g L ⁻¹)	127
Table 5.3 Summary of ammonia mass transfer coefficient (K) and initial mass flux (J _{NH3}) with different feed characteristics and operating conditions	132
Table 5.4 Water quality comparison of initial real waste brine, brine solution after treatment with Ru/C, and solution after membrane distillation.	136
Table 6.1 Model predictions of melting point, boiling point, flash point, lower heating value (LHV), cetane number (CN), and yield sooting index (YSI, normalized to carbon number in parentheses) for down-selected hydrocarbon molecules. Average values reported when multiple predictions are available. Full list of molecule candidates and model predictions provided in Table E.1 in Appendix E.	157
Table 6.2 Conversion of target reactants (butyric acid, 4-heptanone, and dimer) and carbon yield to the desired products (4-heptanone, dimer, and C ₁₄ hydrocarbon, respectively) from upgrading biologically-derived and commercial butyric acid through the integrated process scheme.	167
Table 6.3 Measured fuel properties of C ₁₄ blendstocks, base diesel, and a 20 vol% blend.	170
Table A.1 Market price range of the five hydrogenation metals. ^a	197
Table A.2 Perchlorate reduction results by M/C catalysts (without Re). ^a	197

Table B.1 Nitrate reduction activity of Pd-Cu and Ru catalysts in batch reactor and using H ₂ as a reductant.	206
Table B.2 Surface and bulk properties of Ru catalysts from chemisorption analyses.....	206
Table B.3 TOF ₀ of nitrate reduction and nitrite reduction measured in mixture of nitrate and nitrite added to Ru/C reactors with varying initial concentration ratio.	207
Table B.4 Adsorption energies (eV) of nitrogen species (major reactants, hypothesized intermediates, and products) on Ru ₁₈ clusters. ^a	208
Table B.5 Energetics of the most thermodynamically favorable reaction pathways for aqueous nitrate reduction on Ru ₁₈ clusters.	209
Table C.1 Composition of dechlorinated tap water.	212
Table C.2 NDMA reduction activity and products over different catalysts.	213
Table E.1 Model predictions of melting point, boiling point, flash point, lower heating value, cetane number, and yield sooting index (normalized to carbon number in parentheses) for mapped hydrocarbons.	229
Table E.2 Surface area, acidity and metal dispersion of fresh ZrO ₂ , Nb ₂ O ₅ , and Pt/Al ₂ O ₃	230
Table E.3 Carbon content, surface area and total acidity of fresh Nb ₂ O ₅ and regenerated Nb ₂ O ₅ in Figure 6.4.	231
Table E.4 Physicochemical properties of fresh and regenerated Pt/Al ₂ O ₃	233
Table E.5 Concentrations of monomeric and total sugars in concentrated deacetylated dilute acid enzyme hydrolysate. Total sugars account for soluble oligomeric sugars.....	236
Table E.6 Impurities in the acid feed and organic phase products from upgrading of biologically derived butyric acid	237

ACKNOWLEDGEMENTS

I extend my immense gratitude to my advisor, Professor Timothy Strathmann, who provided me with guidance and support, and granted me great freedom and trust to pursue my graduate research. Those fun conversations, whether technical, professional, or philosophical, will be very missed. I give my special gratitude to Dr. Derek Vardon, who provided me with the opportunity to work with interdisciplinary teams to tackle great challenges in renewable energy. Derek has always given me critical feedback and candid advice, which I am sure will aid me through my professional development in the long run. I thank my thesis committee: Professor Tzahi Cath, Professor Svitlana Pylypenko, Professor Brian Trewyn, Professor Christopher Higgins, and Professor Cristian Ciobanu, for providing feedback and influencing the direction of my research.

I acknowledge colleagues, collaborators, and friends who aided my research throughout different stages of my PhD study. I thank the collective team of the Strathmann group for ensuring the continuity of our group's knowledge, especially when we moved from Illinois to Colorado in 2015. I thank Professor Charles Werth, Professor Shubham Vyas, Professor Ryan Richards, Professor Svitlana Pylypenko, Professor Brian Trewyn, Professor Tzahi Cath, Professor Christopher Higgins and their groups for granting me access to their lab resources and expertise. I thank Professor Jinyong Liu, Professor Danmeng Shuai, Daniel Van Hoomissen, Dr. Martin Menart, Dr. Mengze Xu, and Dr. Johan Vanneste for their assistance with experiments and helpful discussion. I thank the many individuals at the National Renewable Energy Laboratory for their insights and contribution to all manners of biological conversion, catalysis and fuel testing for the last chapter of my graduate research.

Finally, I appreciate the support of my family and friends. It has been a long journey, and I would not have been able to make it this far without their love and support. Particularly, I thank my husband, Dr. Kyle Michelson, for his patience, advice, and thought-provoking conversations on both research and life.

CHAPTER 1

INTRODUCTION AND MAIN OBJECTIVES

1.1 Background

1.1.1 Catalytic treatment of oxyanion water contaminants

Toxic oxyanions, such as nitrate (NO_3^-), nitrite (NO_2^-), bromate (BrO_3^-), chlorate (ClO_3^-), and perchlorate (ClO_4^-), are common drinking water contaminants. Nitrate contamination of surface and groundwater has gradually increased due to excess fertilizer applications, poor disposal of animal waste, and release of incompletely treated industrial and domestic wastewater.¹⁻³ The presence of bromate is mainly due to the ozonation of bromide-containing source waters, and bromide has various natural and anthropogenic sources, such as seawater intrusion, pesticide run-off, industrial wastes and impurities from road de-icing salts.⁴ Perchlorate contamination is attributed to the manufacturing of rocket fuel and explosives, Chilean nitrate fertilizer, and other naturally occurring sources.⁵

These contaminants target multiple organs, exhibiting carcinogenic, mutagenic, or endocrine disrupting properties. For example, nitrate can be converted to nitrite in the human body and can cause methemoglobinemia (i.e., blue baby syndrome), and nitrite can be transformed in vivo to potentially carcinogenic nitrosamines via nitrosation.^{6, 7} Bromate was classified by the International Agency for Research on Cancer in Group 2B (possibly carcinogenic for humans).⁸ The main risks are associated with the kidneys. Perchlorate is an endocrine disrupting compound (EDC) that interferes with iodine uptake by the thyroid gland and synthesis of thyroid hormones.⁹ Current regulatory status of these oxyanions is listed in Table 1.1.

Table 1.1 Current regulatory status of selected oxyanions in drinking water.

Oxyanion	Regulation
Nitrate	MCL of 10 mg/L NO ₃ -N
Nitrite	MCL of 1 mg/L NO ₂ -N
Bromate	MCL of 10 µg/L as BrO ₃ ⁻
Perchlorate	NPDWR initiated in 2011
Chlorate	Listed on the CCL4

MCL: Maximum Contaminant Level
 NPDWR: National Primary Drinking Water Regulations
 CCL4: Contaminant Candidate List 4

In addition to conventional treatment technologies for oxyanions, including ion exchange and reverse osmosis which only serve to transfer the contaminant between phases, hydrogenation metal-based catalyst materials have emerged as a promising alternative. These materials enable reduction of oxyanion using H_{2(g)}, which can be generated from a variety of renewable sources. In the 1990s, Pd and Pd-Cu were identified in screening studies as the optimum catalysts for reduction of nitrite and nitrate, respectively.^{10, 11} In a more recent screening study, a total of ten activated carbon-supported metal catalysts were prepared in house and tested for nitrate and nitrite reduction.¹² Pd, Ir, Pt, and Rh presented significant activities for nitrite reduction, and the activity was correlated with the hydrogen chemisorption energy per atom of metal. The study concluded that none of these metals is practically active for nitrate reduction by itself. Subsequently, 15 bimetallic catalysts were prepared and tested, with Rh-Cu showing the highest activity and producing a large amount of ammonium. Pd-Cu catalyst was considered most promising catalyst if selectivity to N₂ is desired.^{12, 13} A large body of literature exists on nitrate reduction with Pd-based bimetallic catalysts.¹⁴⁻²¹ Our current understanding of metal-catalyzed nitrate hydrogenation mechanisms has been limited mostly to reactions occurring with these materials. The prevailing reaction pathway follows a two-step process (Figure 1.1): (1) hydrogenation of nitrate to nitrite on bimetallic clusters followed by (2) further hydrogenation of

nitrite on Pd sites to a mixture of N₂ and NH₄⁺ stable endproducts.^{11, 18, 22-24} The proposed sequential reduction pathway is supported by the observation of nitrite as a transient reaction intermediate,^{14, 25} increasing with pH as the rate of Pd-catalyzed nitrite reduction decreases,^{22, 26} and isotope labeling experiments showing Pd-catalyzed reduction of NO to the same mixture of endproducts, but selective conversion of N₂O to N₂.²³ The distribution of endproducts, presumed to be controlled by the Pd-catalyzed reactions of nitrite or its daughter products (e.g., adsorbed NO), has been reported to vary with catalyst composition,¹⁵ metal nanoparticle size,²⁷ support,²⁸ and solution pH.²⁹

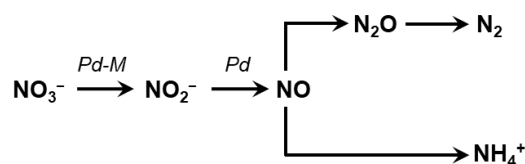


Figure 1.1 Nitrate hydrogenation pathway on Pd-based bimetallic catalysts.

Catalytic reduction of bromate was first studied with Ru oxide catalyst that couples bromate reduction with water oxidation, and adding an alcohol (e.g., methanol) as electron donor increases the reaction rate by promoting reduction of RuO₃ to catalytically active RuO₂.^{30, 31} Chen and co-workers for the first time reported catalytic hydrogenation of bromate using H₂ as electron donor. Pd/Al₂O₃ exhibited higher activity than Pt/Al₂O₃, and the activity of Pd was found to be sensitive to Pd particle size.³² The Pereira and Neves team assessed several monometallic catalysts supported on activated carbon for the catalytic reduction of bromate under hydrogen.³³ The Pd catalyst was found to be the most active when normalized by active metal mass, whereas other metals such as Pt surpass Pd if the activity is normalized to the available metal surface area. Among zeolite-supported catalysts comprising one or two of four metals, Pd, Cu, Th, and Rh, Pd-Cu bimetallic catalysts was concluded to be the most promising

catalyst.^{34, 35} While Th also exhibits high activity, it is not suitable for use in water treatment processes due to its pyrophoricity and radioactivity. Pd catalyst with Cu as a secondary metal was also found to be the most active catalyst for bromate reduction among 10 combinations of a noble metal and a secondary non-noble metal screened, and the activity of Pd-Cu bimetallic catalyst was shown to depend on the atomic ratio between Pd and Cu.³⁶ Support also affects catalyst activity. Pd supported on Al₂O₃ showed higher activity than that on SiO₂ or activated carbon, which was attributed to its higher isoelectric point that enhances adsorption of the bromate anion under pH conditions tested.³² The bromate reduction activity of different supported monometallic catalysts followed the trend TiO₂ > multiwall carbon nanotube (MWCNT) > activated carbon, with TiO₂ and MWCNT exhibiting catalytic activity by themselves.³⁷ In all studies of catalytic bromate reduction, stoichiometric reduction to bromide is observed with no detectable reaction intermediates.

In comparison to the other oxyanions, perchlorate is kinetically inert and few catalysts have been found to be active under ambient temperature and pressure conditions. In 2007, Pd-Re catalysts were first proposed to reduce perchlorate to chloride in water by H₂ under mild conditions.³⁸ The catalyst was prepared by adsorption of inorganic Re(VII) precursors onto Pd/C. Chloride is the only observed product with no detectable intermediates, and mechanistic investigations linked reduction to an oxygen atom transfer (OAT) mechanism catalyzed by the immobilized Re ions. Liu and co-workers promoted the development of this innovative technology by improving the design of catalyst to achieve significantly enhanced activity. The change of Re precursor from inorganic perrhenate (ReO₄⁻) to organometallic oxorhenium complexes (e.g., *hoz*, or 2-(2'-hydroxyphenyl)-2-oxazoline) increased perchlorate reduction activity by approximately 100 fold.³⁹ By replacing Pd with Rh, the immobilized Re is also

stabilized, presumably by reducing proposed intermediates (chlorate, chlorite, and hypochlorite) at a faster rate, thereby limiting reactions of these intermediates with Re that can lead to leaching of the Re complex from the support material.⁴⁰ The noble metal particles (i.e., Pd or Rh) serve to activate H₂ to reduce the oxidized Re(VII) complexes back to active Re(V) complex to complete the catalytic OAT cycle.⁴⁰ It has been reported that activity of carbon-supported monometallic catalysts follow the trend Rh/C > Pd/C > Ru/C.⁴⁰

1.1.2 *N*-nitrosamines as emerging water contaminants and treatment options

In addition to inorganics, multiple organic compounds have also received attention due to their occurrence in water sources and health concern. Particularly, *N*-nitrosamines are a group of disinfection byproducts (DBPs)⁴¹ that exhibit carcinogenicity and genotoxicity.⁴² These compounds are widely detected in surface water, ground water, and treated water.⁴³⁻⁴⁵ Although they are not currently regulated by NPDWR, U.S. EPA has included five *N*-nitrosamines on the CCL4,⁴⁶ and the World Health Organization (WHO) has established a guideline value of 0.1 µg L⁻¹ for *N*-nitrosodimethylamine (NDMA) in drinking water.⁴⁷

Physical treatment technologies are ineffective at removing *N*-nitrosamines. Adsorption of these compounds to activated carbon or soil is relatively insignificant, especially for lower molecular weight molecules like NDMA.^{48, 49} They are also able to pass through membranes used for drinking water treatment including reverse osmosis membrane,^{45, 50, 51} causing significant concern for potable reuse of municipal wastewater. Chemical destruction may be achieved by strongly oxidizing hydroxyl radicals generated in the advanced oxidation processes (AOPs).⁵² However, *N*-nitrosamines are usually present at µg L⁻¹ level, which is comparable to or much lower than the concentrations of non-target radical scavengers (e.g., natural organic

matter and bicarbonate) commonly found in water matrices, resulting in inefficient utilization of hydroxyl radical oxidants.

As *N*-nitrosamines are identified by a characteristic *N*-nitroso group, processes targeting to break the N-NO bond are promising for treating these recalcitrant contaminants. Several approaches have been reported effective for such purpose, including UV photolysis, metal reduction, and catalytic reduction (Figure 1.2). Among these approaches, UV photolysis is a common water treatment technology and has been applied at scale.^{45, 53} Although it is relatively established, this technology has a major downside of high energy demand and cost associated with the required UV fluences, which are order-of-magnitude higher than those applied in disinfection processes.^{45, 54} The *N*-nitrosamine removal efficiency by UV processes can be improved by hydrated electrons,⁵⁵ which requires adding elevated concentrations of photosensitizer such as KI. In contrast, both metal reduction and catalytic reduction rely on surface hydrogen atom as a reductant to break the N-NO bond. For example, zerovalent metals (e.g., Fe) form surface adsorbed atomic hydrogen upon water corrosion. This process is slow, and hazardous intermediates from *N*-nitrosamine reduction were observed to accumulate in the treated water.^{56, 57} Earth-abundant metal Ni in the form of porous Raney Ni was found to be highly active at catalyzing *N*-nitrosamine reduction.⁵⁸ However, development of Ni materials for water treatment is limited by health concerns of Ni leached into treated water.⁵⁹ Pd-based catalysts have demonstrated fast kinetics and high stability for *N*-nitrosamine reduction.⁶⁰⁻⁶² As mentioned earlier, a major barrier for developing and adopting these catalysts for water treatment is the use of expensive Pd. Therefore, development of active, stable, and lower cost catalysts will be critical to advancing the treatment technology for *N*-nitrosamines.



Figure 1.2 Representative approaches for transforming *N*-nitrosamines by breaking N-NO bond.

1.1.3 Supported Ruthenium catalysts and their applications

Pt group metals (Os, Ru, Ir, Rh, Pt, and Pd) are transition metals with high resistance to corrosion and widely used as catalysts.⁶³ Ru has historically had a lower price compared to other metals in Pt group⁶⁴ and found applications both as organometallic catalysts and supported metal catalysts.⁶⁵ Supported Ru catalysts have shown excellent performance in dehydrogenation,⁶⁶ oxidation,^{67, 68} glycerol steam reforming,⁶⁹ and hydrogenolysis.⁷⁰ Particularly, recent studies applied supported Ru catalysts to a variety of hydrogenation reactions, including C₅ and C₆ sugars,^{71, 72} organic acids (e.g., levulinic acid and lactic acid),^{73, 74} benzene,⁷⁵ substituted arenes,^{75, 76} and heteroaromatics (e.g., substituted furans).⁷⁷ The interest in Ru catalysts may be attributed to the growing research field of biomass conversion, where Ru catalysts have shown outstanding activity for the aqueous-phase hydrogenation of biosourced carbonyl compounds.⁷⁸

Supported Ru catalysts have a distribution of surface sites that varies with particle size and shape. Understanding site-specific activity and developing controlled synthesis strategies are critical to the design of high-performance catalysts for reactions that are sensitive to catalyst structure. Ammonia synthesis and decomposition on Ru have been known to be structure-sensitive reactions, and B₅-type step sites have been identified to be the most active sites.⁷⁹ By controlling the pretreatment conditions of Ru/ γ -Al₂O₃, Karim *et al.* obtained a suit of catalysts

differing in Ru particle size and shape.⁸⁰ Combining microscopy, chemisorption, and extended X-ray absorption fine structure (EXAFS) techniques, the Ru particle shape was reconstructed and shown to change from round for smaller particles to elongated or flat for larger particles. The number of B₅ sites highly depended on particle shape and increased with particle size up to 7 nm for flat nanoparticles, leading to the highest ammonia decomposition turnover frequency (TOF). The size-dependence of catalytic activity has also been observed for sugar hydrogenation using supported Ru catalysts.⁷¹ Carbon-supported Ru particles of size ranging from 1 to 8 nm were prepared by incipient wetness impregnation and colloidal method, and the highest TOF was observed with a catalyst that has an average Ru particle size of ca. 3 nm. To differentiate the CO dissociation activity of step sites and terrace site of 2D-like Ru islands supported on rutile TiO₂, Liuzzi *et al.* blocked the step-edge sites of Ru by addition of boron.⁸¹ Their results showed that initial reaction rate for B-doped Ru/TiO₂ was lower than that of non-doped Ru/TiO₂. Interestingly, the steady-state rates were identical for these two catalysts, indicating that the more active step-edge sites were modified under realistic Fischer–Tropsch synthesis conditions.

The major role of catalyst support is facilitating active metal phase dispersion to reduce metal loading and cost. Due to the close proximity with metal particles, catalyst support can also have an impact on metal activity and stability. Xiao *et al.* reported the synthesis of few-layer graphene (FLG)-supported Ru nanoparticle catalysts using a polyol approach and their high activity for levulinic acid hydrogenation.⁷³ The selectivity to γ -valerolactone was complete, and the catalysts demonstrated much higher stability compared with traditional activated carbon-supported Ru catalysts. The superior catalytic properties of FLG-supported Ru catalysts were attributed to greater metallic Ru content and large number of defects, where the sp² dangling bonds strongly interact with the dsp states of the Ru nanoparticles to mitigate nanoparticle

migration or aggregation. The ability of graphene to modulate electronic and geometric structures of Ru nanoparticles was also reported in other studies. For example, thermally exfoliated graphite oxide (TEGO)-supported Ru catalysts synthesized by incipient wetness impregnation imparted thermal stability to Ru nanoparticles heated at 700 °C in N₂ flow.⁷⁵ Ru nanoparticles on TEGO were observed to be more flat at high temperature reduction due to the strong interaction between Ru and TEGO. In addition, TEGO is a stronger electron-withdrawing support than carbon nanotubes, leading to relatively electron-deficient Ru nanoparticles and subsequently higher activities for benzene and *p*-chloronitrobenzene hydrogenation. Leng *et al.* observed chemoselective hydrogenation of nitrobenzene to aniline with C₆₀-supported Ru nanoparticles.⁷⁶ Density functional theory calculations suggested that the Ru nanoparticles supported on C₆₀ are electron-deficient, consistent with experimental observations.

In addition to designing catalyst support, the controlled incorporation of other metals to Ru can also be utilized to tune catalytic properties. During levulinic acid hydrogenation in a 2-sec-butyl-phenol solvent, the catalytic properties of Ru/C were significantly modified by the addition of Sn.⁸² Specifically, a catalyst containing equal amounts of Ru and Sn showed complete selectivity for levulinic acid hydrogenation versus the solvent and displayed stable time-on-stream activity. The ratio between Ru and Sn was found to be critical. While bimetallic Ru-Sn alloys had lower activity but improved stability, high loading of Sn led to β-Sn phase formation, which was not active for hydrogenation reactions and leached under reaction conditions. The bimetallic Ru-Fe catalysts were shown to achieve catalytic properties that differ from individual metals alone.⁷⁷ When hydrogenating multifunctional aromatic and heteroaromatic substrates, pure Ru nanoparticles exhibited selectivity following C=C > arene > C=O, while pure Fe nanoparticles were not active for hydrogenation reactions. At Fe contents in

the range of ca. 20–30%, the bimetallic nanoparticles exhibited selectivity following $C=C > C=O \gg$ arene. Bimetallic catalysts provide ample opportunities to new catalyst formulations and novel catalytic properties. Major challenges in the field include controlled synthesis of bimetallic nanoparticles and structure-activity relationship elucidation.⁸³

Although Ru catalysts have received increasing attention in chemical synthesis and biomass conversion applications, the use of Ru catalysts for catalytic reduction water treatment remains very limited. The current focus of research is largely on Pd-based materials. The fact that Pd exhibits poor activity for reduction of selected contaminants, together with the scarcity and the high cost of this metal, necessitates an expansion of available catalyst formulations. Given the promising catalytic properties of supported Ru catalysts in hydrogenation reactions, their potential to be lower-cost alternative to Pd-based materials for water treatment applications should be explored.

1.1.4 Strategies for regenerating nitrate-contaminated ion exchange waste brine

Ion exchange is an established method for removing nitrate from drinking water. It has advantages including fast start-up, insensitivity to low temperature, stable operation, and ease of intermittent operation.^{1, 84} However, this process requires large quantities of concentrated NaCl solution for resin regeneration, resulting in waste brine high in nitrate, chloride, and sulfate concentrations that requires further management. As a result, there is considerable interest in treating waste ion exchange brines to allow for brine re-use.

Efforts to biologically denitrify ion exchange waste brine have been pursued for over three decades. In the 1980s, Van der Hoek and co-workers proposed a combined ion exchange/biological denitrification process in which nitrate in ground water is removed by an ion exchange column and the resins are regenerated in a closed circuit through a biological

denitrification reactor.⁸⁵⁻⁸⁷ The process demonstrated a reduction of 95% in waste brine volume and a reduction of 80% in regeneration salt requirement.⁸⁷ Clifford and co-workers studied biological denitrification of spent regenerate brine in a sequencing batch reactor (SBR).⁸⁸⁻⁹⁰ They examined higher sodium chloride concentration (0.5 N) and nitrate concentration (up to 835 mg NO₃⁻-N L⁻¹) than previous research effort and reported more than 95% denitrification within 8 h using an optimal methanol-to-nitrate-nitrogen ratio of 2.7. The salt consumption was lowered 50%, and the salt discharge can be reduced about 90%.⁸⁹ The authors further developed a mixed culture capable of rapidly reducing nitrate in 60 g L⁻¹ NaCl, although the stability of the culture requires added sulfide, trace metals and phosphate.⁹¹

The main drawback of biological treatment of waste brine is public perception of the risk associated with microbes contaminating the drinking water supply. Additionally, biological treatment may also not be ideal for intermittent treatment applications, such as periodic treatment of ion exchange waste brines, due to slow start-up. Compared with biological treatment methods, chemical treatment options have the advantages of higher operational flexibility and minimal risk of microbial contamination in treated water. Among potential reducing agents, zero valent iron (ZVI) has relatively high efficiency and low cost. The majority of the studies with ZVI concluded nitrate is predominantly reduced to ammonia.⁹²⁻⁹⁴ Studies of applying ZVI to nitrate reduction in brine matrix are limited. Although chloride is considered to induce corrosion of Fe⁰ surface and thereby enhance reactivity or surface area,⁹⁵ elevated concentrations of NaCl (3-12 g L⁻¹) significantly slowed nitrate reduction with nanoscale ZVI.^{96, 97} In a most recent study, however, high level of chloride (1.37 M) showed insignificant effect on nitrate reduction rate⁹². Despite fast kinetics and easy operation, the attractiveness of chemical reduction is compromised

by the requirement of highly excessive amount of ZVI (e.g., Fe to nitrate molar ratio >10)⁹⁸ and production of metal oxides waste sludge.

Compared with chemical reduction, catalytic reduction treatment leverages metal catalysts, which enhance reaction rate and enable the utilization of H₂ as a low cost and more sustainable electron donor than the carbon-based donors typically employed in biological denitrification schemes.⁹⁹ Fast kinetics also decreases the volume and footprint of the reactor. Pintar and co-workers first proposed a closed loop ion exchange-catalyst system for brine reuse, in which a 0.25-1 wt% NaCl solution was continuously circulated through the catalyst column and resin column until all nitrate was removed.¹⁰⁰ Alternatively, our group proposed a two-stage hybrid treatment system in which ion exchange process is used for treating nitrate contaminated water source and the exhausted resins are regenerated by using fresh brine or waste brine that is catalytically treated with Pd-In/C in a separate reactor (Figure 1.3).^{99, 101} The catalytic reduction treatment was investigated in batch reactor, fixed bed reactor (FBR) or trickle bed reactor (TBR).^{99, 101, 102} A separate catalytic reactor is more readily incorporated into current ion exchange process without the need to resizing of the ion exchange column. Elevated levels of non-target ions such as chloride and sulfate were found to inhibit catalyst activity.^{99, 100} A major limitation of catalytic treatment process is the high capital cost of Pd-based catalysts. Efforts have also typically focused on converting nitrate to N₂ over the NH₄⁺ endproduct. However, conversion to NH₄⁺ may, in fact, be advantageous if a suitable process for recovering the endproduct as a fertilizer product (e.g., (NH₄)₂SO₄) is available.

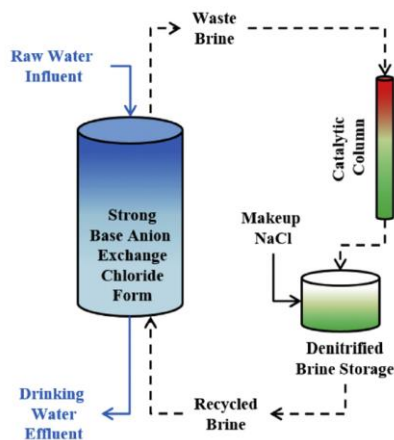


Figure 1.3 Flow diagram of the hybrid ion exchange-catalyst treatment system. Reproduced from Bergquist *et al.*¹⁰¹

1.2 Main Objectives

This dissertation was designed to address challenges raised in the development of catalytic reduction technologies, namely identifying alternatives to Pd-based catalysts and integration of catalytic treatment into existing treatment processes like ion exchange. The main goals of the dissertation were to develop catalysts and processes to advance the application of catalytic reduction water treatment technologies. The specific objectives and hypotheses of this research are as follows:

1. *Assess selected Pt group metals for their activity, solution pH dependence, scope of substrate reactivity, and economic benefit with a suite of oxyanions (chapter 2).* Pd-based catalysts have been studied for their activity in catalyzing the hydrogenation of oxyanions. I hypothesize that other Pt group metals, such as Ru, Rh, Ir, and Pt, will show activity in reducing one or multiple oxyanion contaminants of concern, including nitrate, bromate and chlorate. I also anticipate that some of these metals can be combined with Re (an oxygen atom transfer catalyst) to achieve reduction of perchlorate, a kinetically inert oxyanion. I also hypothesize that catalyst activity and

its dependence on solution pH will be determined by the identity of metal and less affected by the support.

2. *Evaluate the kinetics and investigate the mechanism of nitrate and nitrite reactions with supported Ru catalysts (chapter 3).* Catalyst screening experiments revealed that Ru/C has unexpectedly higher activity of nitrate reduction than other Pt group metals. The reactivity and mechanistic features of reactions on Ru catalyst surfaces is unknown. I hypothesize that the high activity observed here results from high dispersion of Ru nanoparticles in commercial catalysts and catalyst pretreatment protocols that restore Ru surfaces to their active form. I also hypothesize that nitrate reacts by a similar mechanism observed for Pd-based bimetallic catalysts.
3. *Extend the evaluation of Ru catalyst activity to N-nitrosamines and other trace organic water contaminants (chapter 4).* Previously, bimetallic Pd catalysts that react with nitrate have been shown to also reduce NDMA to less toxic products. Thus, I hypothesize that Ru catalysts that are reactive with nitrate and nitrite will also exhibit high reactivity with NDMA and related N-nitrosamines. Likewise, I expect reactivity will extend, to varying degrees, other classes of organic pollutants where Pd catalyst activity has been previously documented (e.g., halo- and nitro-organics).
4. *Develop integrated process coupling ion exchange, catalytic nitrate reduction, and membrane distillation to treat nitrate-contaminated water sources while reducing brine consumption and producing a value-added fertilizer product (chapter 5).* Reuse of waste brine from regenerating ion exchange resin has been studied with bimetallic Pd catalysts, which reduces concentrated nitrate in the brine to a mixture of nitrogen gas and ammonia. The production of ammonia has typically been deemed as

undesirable but appears to be unavoidable due to the nature of catalyst and limitation of hydrogen transfer. I hypothesize that substitution of Pd-based catalysts with Ru catalysts will be technically feasible to remove nitrate from waste brine and be economic competitive due to the much lower cost of Ru. I further hypothesize that integrating a third process, membrane distillation, will enable recovery of the ammonia byproduct as ammonium sulfate, $(\text{NH}_4)_2\text{SO}_4$, a commercial fertilizer product.

In addition to the dissertation's major topic, I extended my research scope to include renewable energy and leveraged catalysis and process integration to produce a performance-advantaged renewable hydrocarbon diesel blendstock from low-cost, biologically-derived butyric acid. Renewable diesel fuel is critical to reducing the carbon footprint of the transportation sector, and lignocellulosic biomass is a particularly promising non-food feedstock for such applications. Short-chain carboxylic acids are among the most abundant bio-intermediates from anaerobic fermentation of lignocellulosic sugars. In chapter 6, a C_{14} hydrocarbon molecule is predicted to exhibit desired fuel characteristics, and its synthesis is demonstrated from upgrading butyric acid through sequential catalytic reaction pathways.

1.3 Intellectual Merits and Broader Impacts

This research work will contribute to a better understanding of catalytic reduction treatment technology from both fundamental science and process design perspectives. It will improve fundamental understanding of multiple Pt group hydrogenation metals for reducing aqueous oxyanion contaminants with different reactivity. Particularly, for the first time, it will reveal the activities of Ru catalysts for a range of inorganic and organic molecules in aqueous phase under ambient temperature and hydrogen at atmospheric pressure and the relationship

between catalyst physical and chemical properties with catalyst activity. This research will also demonstrate an engineering strategy for simultaneous water purification and resource recovery by combining catalysts with physical separations technologies.

This research work will have several broader impacts. It will facilitate the future rational selection of metal catalyst for oxyanion contaminants, providing a suite of options that can be modified based on prevailing market prices. The results will also provide useful guidance for the development of lower cost Ru-based catalysts for various water treatment applications, as both stand-alone or hybrid systems. Outcomes from this work will provide a path forward for the further development and deployment of practical catalytic water processing technologies.

1.4 References

1. Kapoor, A.; Viraraghavan, T. Nitrate removal from drinking water - Review. *J. Environ. Eng.-ASCE* **1997**, *123* (4), 371-380.
2. Puckett, L. J. Identifying the major sources of nutrient water pollution. *Environ. Sci. Technol.* **1995**, *29* (9), 408A-414A.
3. Pintar, A. Catalytic processes for the purification of drinking water and industrial effluents. *Catal. Today* **2003**, *77* (4), 451-465.
4. Kirisits, M. J.; Snoeyink, V. L.; Kruithof, J. C. The reduction of bromate by granular activated carbon. *Water Res.* **2000**, *34* (17), 4250-4260.
5. Dasgupta, P. K.; Dyke, J. V.; Kirk, A. B.; Jackson, W. A. Perchlorate in the United States. Analysis of Relative Source Contributions to the Food Chain. *Environ. Sci. Technol.* **2006**, *40* (21), 6608-6614.
6. Weyer, P. J.; Cerhan, J. R.; Kross, B. C.; Hallberg, G. R.; Kantamneni, J.; Breuer, G.; Jones, M. P.; Zheng, W.; Lynch, C. F. Municipal drinking water nitrate level and cancer risk in older women: the Iowa Women's Health Study. *Epidemiology* **2001**, *12* (3), 327-38.
7. Gulis, G.; Czompolyova, M.; Cerhan, J. R. An ecologic study of nitrate in municipal drinking water and cancer incidence in Trnava District, Slovakia. *Environ. Res.* **2002**, *88* (3), 182-187.
8. Climent, M. J.; Corma, A.; Iborra, S. Conversion of biomass platform molecules into fuel additives and liquid hydrocarbon fuels. *Green Chemistry* **2014**, *16* (2), 516-547.

9. Greer, M. A.; Goodman, G.; Pleus, R. C.; Greer, S. E. Health effects assessment for environmental perchlorate contamination: the dose response for inhibition of thyroidal radioiodine uptake in humans. *Environ. Health Perspect.* **2002**, *110* (9), 927-937.
10. Hörold, S.; Tacke, T.; Vorlop, K. D. Catalytical removal of nitrate and nitrite from drinking water: 1. Screening for hydrogenation catalysts and influence of reaction conditions on activity and selectivity. *Environ. Technol.* **1993**, *14* (10), 931-939.
11. Hörold, S.; Vorlop, K. D.; Tacke, T.; Sell, M. Development of catalysts for a selective nitrate and nitrite removal from drinking water. *Catal. Today* **1993**, *17* (1-2), 21-30.
12. Soares, O.; Orfao, J. J. M.; Pereira, M. F. R. Activated carbon supported metal catalysts for nitrate and nitrite reduction in water. *Catal. Lett.* **2008**, *126* (3-4), 253-260.
13. Soares, O. S. G. P.; Orfao, J. J. M.; Pereira, M. F. R. Bimetallic catalysts supported on activated carbon for the nitrate reduction in water: Optimization of catalysts composition. *Appl. Catal. B-Environ.* **2009**, *91* (1-2), 441-448.
14. Pintar, A.; Batista, J.; Levec, J.; Kajiuchi, T. Kinetics of the catalytic liquid-phase hydrogenation of aqueous nitrate solutions. *Appl. Catal., B* **1996**, *11* (1), 81-98.
15. Yoshinaga, Y.; Akita, T.; Mikami, I.; Okuhara, T. Hydrogenation of Nitrate in Water to Nitrogen over Pd-Cu Supported on Active Carbon. *J. Catal.* **2002**, *207* (1), 37-45.
16. Pintar, A.; Batista, J.; Arčon, I.; Kodre, A. Characterization of γ -Al₂O₃ supported Pd-Cu bimetallic catalysts by EXAFS, AES and kinetic measurements. In *Stud. Surf. Sci. Catal.*; B. Delmon; P.A. Jacobs; R. Maggi; J.A. Martens; Grange, P.; Poncelet, G., Eds. Elsevier: Louvain-la-Neuve, Belgium, 1998; Vol. 118, pp 127-136.
17. Ilinitch, O. M.; Nosova, L. V.; Gorodetskii, V. V.; Ivanov, V. P.; Trukhan, S. N.; Gribov, E. N.; Bogdanov, S. V.; Cuperus, F. P. Catalytic reduction of nitrate and nitrite ions by hydrogen: investigation of the reaction mechanism over Pd and Pd-Cu catalysts. *J. Mol. Catal. A: Chem.* **2000**, *158* (1), 237-249.
18. Marchesini, F. A.; Irusta, S.; Querini, C.; Miró, E. Spectroscopic and catalytic characterization of Pd-In and Pt-In supported on Al₂O₃ and SiO₂, active catalysts for nitrate hydrogenation. *Appl. Catal., A* **2008**, *348* (1), 60-70.
19. Miyazaki, A.; Matsuda, K.; Papa, F.; Scurtu, M.; Negrila, C.; Dobrescu, G.; Balint, I. Impact of particle size and metal-support interaction on denitration behavior of well-defined Pt-Cu nanoparticles. *Catal. Sci. Technol.* **2015**, *5* (1), 492-503.
20. Bae, S.; Jung, J.; Lee, W. The effect of pH and zwitterionic buffers on catalytic nitrate reduction by TiO₂-supported bimetallic catalyst. *Chem. Eng. J.* **2013**, *232*, 327-337.

21. Chaplin, B. P.; Roundy, E.; Guy, K. A.; Shapley, J. R.; Werth, C. J. Effects of natural water ions and humic acid on catalytic nitrate reduction kinetics using an alumina supported Pd–Cu catalyst. *Environ. Sci. Technol.* **2006**, *40* (9), 3075-3081.
22. Guy, K. A.; Xu, H.; Yang, J. C.; Werth, C. J.; Shapley, J. R. Catalytic nitrate and nitrite reduction with Pd-Cu/PVP colloids in water: Composition, structure, and reactivity correlations. *J. Phys. Chem. C* **2009**, *113* (19), 8177-8185.
23. Zhang, R.; Shuai, D. M.; Guy, K. A.; Shapley, J. R.; Strathmann, T. J.; Werth, C. J. Elucidation of nitrate reduction mechanisms on a Pd-In bimetallic catalyst using isotope labeled nitrogen species. *ChemCatChem* **2013**, *5* (1), 313-321.
24. Fan, X.; Franch, C.; Palomares, E.; Lapkin, A. A. Simulation of catalytic reduction of nitrates based on a mechanistic model. *Chem. Eng. J.* **2011**, *175* (0), 458-467.
25. Jung, S.; Bae, S.; Lee, W. Development of Pd–Cu/hematite catalyst for selective nitrate reduction. *Environ. Sci. Technol.* **2014**, *48* (16), 9651-9658.
26. Centi, G.; Perathoner, S. Remediation of water contamination using catalytic technologies. *Appl. Catal., B* **2003**, *41* (1–2), 15-29.
27. Zhang, F. X.; Miao, S.; Yang, Y. L.; Zhang, X.; Chen, J. X.; Guan, N. J. Size-dependent hydrogenation selectivity of nitrate on Pd-Cu/TiO₂ catalysts. *J. Phys. Chem. C* **2008**, *112* (20), 7665-7671.
28. Xu, Z.; Chen, L.; Shao, Y.; Yin, D.; Zheng, S. Catalytic hydrogenation of aqueous nitrate over Pd–Cu/ZrO₂ catalysts. *Ind. Eng. Chem. Res.* **2009**, *48* (18), 8356-8363.
29. D'Arino, M.; Pinna, F.; Strukul, G. Nitrate and nitrite hydrogenation with Pd and Pt/SnO₂ catalysts: the effect of the support porosity and the role of carbon dioxide in the control of selectivity. *Appl. Catal., B* **2004**, *53* (3), 161-168.
30. Zhu, Q.; Wang, Y. Y.; Zhang, H. N.; Duan, R.; Chen, C. C.; Song, W. J.; Zhao, J. C. Localized Ti-III mediated dissociative electron transfer for carbon halogen bond activation on TiO₂. *Appl. Catal. B-Environ.* **2017**, *219*, 322-328.
31. Thakur, D. B.; Tiggelaar, R. M.; Weber, Y.; Gardeniers, J. G. E.; Lefferts, L.; Seshan, K. Ruthenium catalyst on carbon nanofiber support layers for use in silicon-based structured microreactors. Part II: Catalytic reduction of bromate contaminants in aqueous phase. *Applied Catalysis B: Environmental* **2011**, *102* (1–2), 243-250.
32. Chen, H.; Xu, Z.; Wan, H.; Zheng, J.; Yin, D.; Zheng, S. Aqueous bromate reduction by catalytic hydrogenation over Pd/Al₂O₃ catalysts. *Appl. Catal., B* **2010**, *96* (3–4), 307-313.
33. Restivo, J.; Soares, O. S. G. P.; Órfão, J. J. M.; Pereira, M. F. R. Metal assessment for the catalytic reduction of bromate in water under hydrogen. *Chem. Eng. J.* **2015**, *263*, 119-126.

34. Freitas, C. M. A. S.; Soares, O. S. G. P.; Orfao, J. J. M.; Fonseca, A. M.; Pereira, M. F. R.; Neves, I. C. Highly efficient reduction of bromate to bromide over mono and bimetallic ZSM5 catalysts. *Green Chemistry* **2015**, *17* (8), 4247-4254.
35. Soares, O. S. G. P.; Freitas, C. M. A. S.; Fonseca, A. M.; Órfão, J. J. M.; Pereira, M. F. R.; Neves, I. C. Bromate reduction in water promoted by metal catalysts prepared over faujasite zeolite. *Chemical Engineering Journal* **2016**, *291*, 199-205.
36. Restivo, J.; Soares, O. S. G. P.; Órfão, J. J. M.; Pereira, M. F. R. Bimetallic activated carbon supported catalysts for the hydrogen reduction of bromate in water. *Catal. Today* **2015**, *249*, 213-219.
37. Restivo, J.; Soares, O. S. G. P.; Órfão, J. J. M.; Pereira, M. F. R. Catalytic reduction of bromate over monometallic catalysts on different powder and structured supports. *Chem. Eng. J.* **2017**, *309*, 197-205.
38. Hurley, K. D.; Shapley, J. R. Efficient heterogeneous catalytic reduction of perchlorate in water. *Environ. Sci. Technol.* **2007**, *41* (6), 2044-2049.
39. Liu, J.; Choe, J. K.; Wang, Y.; Shapley, J. R.; Werth, C. J.; Strathmann, T. J. Bioinspired complex-nanoparticle hybrid catalyst system for aqueous perchlorate reduction: Rhenium speciation and its influence on catalyst activity. *ACS Catal.* **2014**, 511-522.
40. Liu, J.; Chen, X.; Wang, Y.; Strathmann, T. J.; Werth, C. J. Mechanism and mitigation of the decomposition of an oxorhenium complex-based heterogeneous catalyst for perchlorate reduction in water. *Environ. Sci. Technol.* **2015**.
41. Krasner, S. W.; Mitch, W. A.; McCurry, D. L.; Hanigan, D.; Westerhoff, P. Formation, precursors, control, and occurrence of nitrosamines in drinking water: A review. *Water Res.* **2013**, *47* (13), 4433-4450.
42. Richardson, S. D.; Plewa, M. J.; Wagner, E. D.; Schoeny, R.; DeMarini, D. M. Occurrence, genotoxicity, and carcinogenicity of regulated and emerging disinfection by-products in drinking water: A review and roadmap for research. *Mutat. Res.-Rev. Mut. Res.* **2007**, *636* (1-3), 178-242.
43. Han, Y.; Chen, Z.; Shen, J.; Wang, J.; Li, W.; Li, J.; Wang, B.; Tong, L. The role of Cu(II) in the reduction of *N*-nitrosodimethylamine with iron and zinc. *Chemosphere* **2017**, *167*, 171-177.
44. Sen, N. P.; Baddoo, P. A.; Weber, D.; Boyle, M. A sensitive and specific method for the determination of *N*-nitrosodimethylamine in drinking water and fruit drinks. *Int. J. Environ. Anal. Chem.* **1994**, *56* (2), 149-163.
45. Mitch, W. A.; Sharp, J. O.; Trussell, R. R.; Valentine, R. L.; Alvarez-Cohen, L.; Sedlak, D. L. *N*-nitrosodimethylamine (NDMA) as a drinking water contaminant: A review. *Environ. Eng. Sci.* **2003**, *20* (5), 389-404.

46. Fernandez, Y.; Arenillas, A.; Diez, M. A.; Pis, J. J.; Menendez, J. A. Pyrolysis of glycerol over activated carbons for syngas production. *Journal of Analytical and Applied Pyrolysis* **2009**, *84* (2), 145-150.
47. World Health Organization. *Guidelines for Drinking-Water Quality*; WHO: Geneva, Switzerland, 2011; Vol. 216, pp 303-4.
48. Beita-Sandí, W.; Ersan, M. S.; Uzun, H.; Karanfil, T. Removal of *N*-nitrosodimethylamine precursors with powdered activated carbon adsorption. *Water Res.* **2016**, *88*, 711-718.
49. Gunnison, D.; Zappi, M. E.; Teeter, C.; Pennington, J. C.; Bajpai, R. Attenuation mechanisms of *N*-nitrosodimethylamine at an operating intercept and treat groundwater remediation system. *J. Hazard. Mater.* **2000**, *73* (2), 179-197.
50. Li, Y.; Kemper, J. M.; Datuin, G.; Akey, A.; Mitch, W. A.; Luthy, R. G. Reductive dehalogenation of disinfection byproducts by an activated carbon-based electrode system. *Water Res.* **2016**, *98*, 354-362.
51. Miyashita, Y.; Park, S.-H.; Hyung, H.; Huang, C.-H.; Kim, J.-H. Removal of *N*-nitrosamines and their precursors by nanofiltration and reverse osmosis membranes. *J. Environ. Eng.* **2009**, *135* (9), 788-795.
52. Lee, C.; Yoon, J.; Von Gunten, U. Oxidative degradation of *N*-nitrosodimethylamine by conventional ozonation and the advanced oxidation process ozone/hydrogen peroxide. *Water Res.* **2007**, *41* (3), 581-590.
53. Plumlee, M. H.; López-Mesas, M.; Heidlberger, A.; Ishida, K. P.; Reinhard, M. *N*-nitrosodimethylamine (NDMA) removal by reverse osmosis and UV treatment and analysis via LC-MS/MS. *Water Res.* **2008**, *42* (1), 347-355.
54. Sedlak, D. L.; Deeb, R. A.; Hawley, E. L.; Mitch, W. A.; Durbin, T. D.; Mowbray, S.; Carr, S. Sources and fate of nitrosodimethylamine and its precursors in municipal wastewater treatment plants. *Water Environ. Res.* **2005**, *77* (1), 32-39.
55. Sun, Z.; Zhang, C.; Zhao, X.; Chen, J.; Zhou, Q. Efficient photoreductive decomposition of *N*-nitrosodimethylamine by UV/iodide process. *J. Hazard. Mater.* **2017**, *329*, 185-192.
56. Han, Y.; Chen, Z.; Tong, L.; Yang, L.; Shen, J.; Wang, B.; Liu, Y.; Liu, Y.; Chen, Q. Reduction of *N*-nitrosodimethylamine with zero-valent zinc. *Water Res.* **2013**, *47* (1), 216-224.
57. Gui, L.; Gillham, R. W.; Odziemkowski, M. S. Reduction of *N*-nitrosodimethylamine with granular iron and nickel-enhanced iron. 1. Pathways and kinetics. *Environ. Sci. Technol.* **2000**, *34* (16), 3489-3494.
58. Friedrich, A. J.; Shapley, J. R.; Strathmann, T. J. Rapid reduction of *N*-nitrosamine disinfection byproducts in water with hydrogen and porous nickel catalysts. *Environ. Sci. Technol.* **2008**, *42* (1), 262-269.

59. Cempel, M.; Nikel, G. Nickel: A review of its sources and environmental toxicology. *Polish Journal of Environmental Studies* **2006**, *15* (3).
60. Davie, M. G.; Reinhard, M.; Shapley, J. R. Metal-catalyzed reduction of *N*-nitrosodimethylamine with hydrogen in water. *Environ. Sci. Technol.* **2006**, *40* (23), 7329-7335.
61. Davie, M. G.; Shih, K.; Pacheco, F. A.; Leckie, J. O.; Reinhard, M. Palladium-indium catalyzed reduction of *N*-nitrosodimethylamine: Indium as a promoter metal. *Environ. Sci. Technol.* **2008**, *42* (8), 3040-3046.
62. Shuai, D.; McCalman, D. C.; Choe, J. K.; Shapley, J. R.; Schneider, W. F.; Werth, C. J. Structure sensitivity study of waterborne contaminant hydrogenation using shape- and size-controlled Pd nanoparticles. *ACS Catal.* **2013**, *3* (3), 453-463.
63. Garcia-Segura, S.; Lanzarini-Lopes, M.; Hristovski, K.; Westerhoff, P. Electrocatalytic reduction of nitrate: Fundamentals to full-scale water treatment applications. *Applied Catalysis B: Environmental* **2018**, *236*, 546-568.
64. <http://www.platinum.matthey.com/prices/price-charts>. (Accessed January 1, 2019)
65. Kettler, P. B. Platinum group metals in catalysis: Fabrication of catalysts and catalyst precursors. *Organic Process Research & Development* **2003**, *7* (3), 342-354.
66. Yao, Q.; Lu, Z.-H.; Yang, K.; Chen, X.; Zhu, M. Ruthenium nanoparticles confined in SBA-15 as highly efficient catalyst for hydrolytic dehydrogenation of ammonia borane and hydrazine borane. *Scientific Reports* **2015**, *5*, 15186.
67. Yamaguchi, K.; Mizuno, N. Supported Ruthenium Catalyst for the Heterogeneous Oxidation of Alcohols with Molecular Oxygen. *Angewandte Chemie* **2002**, *114* (23), 4720-4724.
68. Muthusamy, S.; Kumarswamyreddy, N.; Kesavan, V.; Chandrasekaran, S. Recent advances in aerobic oxidation with ruthenium catalysts. *Tetrahedron Lett.* **2016**, *57* (50), 5551-5559.
69. Gallegos-Suárez, E.; Guerrero-Ruiz, A.; Rodríguez-Ramos, I. Efficient hydrogen production from glycerol by steam reforming with carbon supported ruthenium catalysts. *Carbon* **2016**, *96*, 578-587.
70. Kobayashi, H.; Komanoya, T.; Hara, K.; Fukuoka, A. Water-tolerant mesoporous-carbon-supported ruthenium catalysts for the hydrolysis of cellulose to glucose. *ChemSusChem* **2010**, *3* (4), 440-443.
71. Simakova, I. L.; Demidova, Y. S.; Murzina, E. V.; Aho, A.; Murzin, D. Y. Structure sensitivity in catalytic hydrogenation of galactose and arabinose over Ru/C catalysts. *Catalysis Letters* **2016**, *146* (7), 1291-1299.
72. Aho, A.; Roggan, S.; Simakova, O. A.; Salmi, T.; Murzin, D. Y. Structure sensitivity in catalytic hydrogenation of glucose over ruthenium. *Catalysis Today* **2015**, *241*, 195-199.

73. Xiao, C.; Goh, T.-W.; Qi, Z.; Goes, S.; Brashler, K.; Perez, C.; Huang, W. Conversion of levulinic acid to γ -valerolactone over few-layer graphene-supported ruthenium catalysts. *ACS Catal.* **2016**, *6* (2), 593-599.
74. Jones, D. R.; Iqbal, S.; Kondrat, S. A.; Lari, G. M.; Miedziak, P. J.; Morgan, D. J.; Parker, S. F.; Hutchings, G. J. An investigation of the effect of carbon support on ruthenium/carbon catalysts for lactic acid and butanone hydrogenation. *Phys. Chem. Chem. Phys.* **2016**, *18* (26), 17259-17264.
75. Wang, Y.; Rong, Z.; Wang, Y.; Qu, J. Ruthenium nanoparticles loaded on functionalized graphene for liquid-phase hydrogenation of fine chemicals: Comparison with carbon nanotube. *Journal of Catalysis* **2016**, *333*, 8-16.
76. Leng, F.; Gerber, I. C.; Lecante, P.; Moldovan, S.; Girleanu, M.; Axet, M. R.; Serp, P. Controlled and Chemoselective Hydrogenation of Nitrobenzene over Ru@C₆₀ Catalysts. *ACS Catal.* **2016**, *6* (9), 6018-6024.
77. Luska, K. L.; Bordet, A.; Tricard, S.; Sinev, I.; Grünert, W.; Chaudret, B.; Leitner, W. Enhancing the Catalytic Properties of Ruthenium Nanoparticle-SILP Catalysts by Dilution with Iron. *ACS Catal.* **2016**, *6* (6), 3719-3726.
78. Michel, C.; Gallezot, P. Why Is ruthenium an efficient catalyst for the aqueous-phase hydrogenation of biosourced carbonyl compounds? *ACS Catal.* **2015**, *5* (7), 4130-4132.
79. Gavnholt, J.; Schiøtz, J. Structure and reactivity of ruthenium nanoparticles. *Physical Review B* **2008**, *77* (3), 035404.
80. Karim, A. M.; Prasad, V.; Mpourmpakis, G.; Lonergan, W. W.; Frenkel, A. I.; Chen, J. G.; Vlachos, D. G. Correlating particle size and shape of supported Ru/ γ -Al₂O₃ catalysts with NH₃ decomposition activity. *J. Am. Chem. Soc.* **2009**, *131* (34), 12230-12239.
81. Liuzzi, D.; Perez-Alonso, F. J.; Garcia-Garcia, F. J.; Calle-Vallejo, F.; Fierro, J. L. G.; Rojas, S. Identifying the time-dependent predominance regimes of step and terrace sites for the Fischer-Tropsch synthesis on ruthenium based catalysts. *Catalysis Science & Technology* **2016**, *6* (17), 6495-6503.
82. Wettstein, S. G.; Bond, J. Q.; Alonso, D. M.; Pham, H. N.; Datye, A. K.; Dumesic, J. A. RuSn bimetallic catalysts for selective hydrogenation of levulinic acid to γ -valerolactone. *Applied Catalysis B: Environmental* **2012**, *117-118*, 321-329.
83. Sankar, M.; Dimitratos, N.; Miedziak, P. J.; Wells, P. P.; Kiely, C. J.; Hutchings, G. J. Designing bimetallic catalysts for a green and sustainable future. *Chemical Society Reviews* **2012**, *41* (24), 8099-8139.
84. Peyton, B. M.; Mormile, M. R.; Petersen, J. N. Nitrate reduction with *halomonas campisalis*: Kinetics of denitrification at pH 9 and 12.5% NaCl. *Water Research* **2001**, *35* (17), 4237-4242.

85. van der Hoek, J. P.; Klapwijk, A. Nitrate removal from ground water. *Water Research* **1987**, *21* (8), 989-997.
86. van der Hoek, J. P.; van der Ven, P. J. M.; Klapwijk, A. Combined ion exchange/biological denitrification for nitrate removal from ground water under different process conditions. *Water Research* **1988**, *22* (6), 679-684.
87. van der Hoek, J. P.; Klapwijk, A. Reduction of regeneration salt requirement and waste disposal in an ion exchange process for nitrate removal from ground water. *Waste Management* **1989**, *9* (4), 203-210.
88. Clifford, D.; Liu, X. Biological denitrification of spent regenerant brine using a sequencing batch reactor. *Water Research* **1993**, *27* (9), 1477-1484.
89. Liu, X.; Clifford, D. A. Ion exchange with denitrified brine reuse. *American Water Works Association. Journal* **1996**, *88* (11), 88.
90. Lehman, S. G.; Badruzzaman, M.; Adham, S.; Roberts, D. J.; Clifford, D. A. Perchlorate and nitrate treatment by ion exchange integrated with biological brine treatment. *Water Research* **2008**, *42* (4-5), 969-976.
91. Cang, Y.; Roberts, D. J.; Clifford, D. A. Development of cultures capable of reducing perchlorate and nitrate in high salt solutions. *Water Research* **2004**, *38* (14), 3322-3330.
92. Fux, I.; Birnhack, L.; Tang, S. C.; Lahav, O. Removal of nitrate from rinking water by ion-exchange followed by nZVI-based reduction and electrooxidation of the ammonia product to N_{2(g)}. *ChemEngineering* **2017**, *1* (1), 2.
93. Hwang, Y. H.; Kim, D. G.; Shin, H. S. Mechanism study of nitrate reduction by nano zero valent iron. *J. Hazard. Mater.* **2011**, *185* (2-3), 1513-1521.
94. Ryu, A.; Jeong, S.-W.; Jang, A.; Choi, H. Reduction of highly concentrated nitrate using nanoscale zero-valent iron: Effects of aggregation and catalyst on reactivity. *Appl. Catal., B* **2011**, *105* (1), 128-135.
95. Choe, S.; Liljestrand, H. M.; Khim, J. Nitrate reduction by zero-valent iron under different pH regimes. *Appl. Geochem.* **2004**, *19* (3), 335-342.
96. Hwang, Y.; Kim, D.; Shin, H.-S. Inhibition of nitrate reduction by NaCl adsorption on a nano-zero-valent iron surface during a concentrate treatment for water reuse. *Environ. Technol.* **2015**, *36* (9), 1178-1187.
97. Xiong, Z.; Zhao, D.; Pan, G. Rapid and controlled transformation of nitrate in water and brine by stabilized iron nanoparticles. *J. Nanopart. Res.* **2009**, *11* (4), 807-819.
98. Yang, G. C. C.; Lee, H.-L. Chemical reduction of nitrate by nanosized iron: kinetics and pathways. *Water Res.* **2005**, *39* (5), 884-894.

99. Choe, J. K.; Bergquist, A. M.; Jeong, S.; Guest, J. S.; Werth, C. J.; Strathmann, T. J. Performance and life cycle environmental benefits of recycling spent ion exchange brines by catalytic treatment of nitrate. *Water Res.* **2015**, *80* (0), 267-280.
100. Pintar, A.; Batista, J.; Levec, J. Integrated ion exchange/catalytic process for efficient removal of nitrates from drinking water. *Chem. Eng. Sci.* **2001**, *56* (4), 1551-1559.
101. Bergquist, A. M.; Choe, J. K.; Strathmann, T. J.; Werth, C. J. Evaluation of a hybrid ion exchange-catalyst treatment technology for nitrate removal from drinking water. *Water Res.* **2016**, *96*, 177-187.
102. Bergquist, A. M.; Bertoch, M.; Gildert, G.; Strathmann, T. J.; Werth, C. J. Catalytic denitrification in a trickle bed reactor: Ion exchange waste brine treatment. *Journal - American Water Works Association* **2017**, *109* (5), E129-E151.

CHAPTER 2

EXPLORING BEYOND PALLADIUM: CATALYTIC REDUCTION OF AQUEOUS OXYANION POLLUTANTS WITH ALTERNATIVE PLATINUM GROUP METALS AND NEW MECHANISTIC IMPLICATIONS

A modified version of this chapter was published in *Chemical Engineering Journal*

Xi Chen,¹ Xiangchen Huo,¹ Jinyong Liu,^{*1} Yin Wang, Charles J. Werth,

and Timothy J. Strathmann

2.1 Abstract

For over two decades, Pd has been the primary hydrogenation metal studied for reductive catalytic water treatment applications. Herein, we report that alternative platinum group metals (Rh, Ru, Pt and Ir) can exhibit substantially higher activity, wider substrate selectivity and variable pH dependence in comparison to Pd. Cross comparison of multiple metals and oxyanion substrates provides new mechanistic insights into the heterogeneous reactions. Activity differences and pH effects mainly originate from the chemical nature of individual metals. Considering the advantages in performance and cost, results support renewed investigation of alternative hydrogenation metals to advance catalytic technologies for water purification and other environmental applications.

*Reprinted with permission from Chen, X.; Huo, X.; Liu, J.; Wang, Y.; Werth, C. J.; Strathmann, T. J. Exploring beyond palladium: Catalytic reduction of aqueous oxyanion pollutants with alternative platinum group metals and new mechanistic implications. *Chem. Eng. J.* **2017**, *313*, 745–752. Copyright 2016 Elsevier. ¹These authors contributed equally. X.C. performed most of the kinetic experiments; X.H. performed most of the material characterization; J.L. wrote the paper with input from all authors; Y.W. provided technical support and helpful advice; C.J.W. and T.J.S. provided supervision. X.C. is affiliated with Columbia University; X.H. and T.J.S. are affiliated with Colorado School of Mines; J.L. is affiliated with University of California, Riverside; Y.W. is affiliated with University of Wisconsin-Milwaukee, Milwaukee; C.J.W. is affiliated with University of Texas at Austin.

2.2 Introduction

Toxic oxyanions, such as BrO_3^- , ClO_3^- , NO_3^- and ClO_4^- , are ubiquitous drinking water contaminants originating from both anthropogenic and natural sources,¹⁻⁴ or are generated during water treatment processes (e.g., chlorination, ozonation, desalination, and electrochemical treatment).⁵⁻⁹ These ions target multiple organs, and can have carcinogenic, mutagenic, and/or endocrine disrupting properties.¹⁰⁻¹² Ion exchange is the primary technology used to treat oxyanion-contaminated water; reverse osmosis is also used when salt removal is required. These technologies effectively serve to either trap the contaminants in a resin matrix, or to concentrate the contaminants in a waste brine. Thus, it would be preferable to apply destructive treatment technologies to convert oxyanions into less toxic or innocuous end products (e.g., Br^- , Cl^- and N_2), contributing to more sustainable drinking water treatment processes.¹³⁻¹⁶

Pd-based heterogeneous catalysis has garnered significant attention as a potential strategy for reduction of oxyanions and other highly oxidized contaminants (e.g., halogenated and nitro organics).¹⁷ Ever since 1993 when Pd was identified as the “optimum” hydrogenation metal for water treatment applications (based on the screening of hydrogenation metals for nitrite reduction¹⁸), research efforts have reported on many aspects of Pd-based catalysis, including the effects of Pd nanoparticle size and morphology,¹⁹ catalyst supports,²⁰⁻²³ bimetallic formulations for treating recalcitrant substrates,^{14, 24, 25} water matrix effects,^{26, 27} and pilot-scale field testing.²⁸⁻
³⁰ We argue here that the narrow focus on Pd has limited advancement of reductive water treatment catalyst technologies. Little effort has been devoted to investigating water treatment applications with periodically related hydrogenation metals, e.g., Rh, Ru, Pt and Ir, which have seen many advances in other areas of catalytic science, including organic synthesis,³¹ biomass valorization,³² and vehicle exhaust gas conversion.³³

In recent screening studies by the Pereira and Neves team,³⁴⁻³⁸ several hydrogenation metals were evaluated for BrO_3^- and NO_3^- reduction, and Pd-based catalysts were still reported as having the highest activity. However, our group recently found that a Rh/C catalyst exhibited substantially higher activity than Pd/C for ClO_3^- reduction in acidic solution.³⁹ In literature, Rh/ Al_2O_3 ⁴⁰⁻⁴² and Pt/C⁴³ also exhibit unique activities, such as hydrodefluorination, that the corresponding Pd-based catalysts do not. These findings suggest that other hydrogenation metals besides Pd may have unique catalyst attributes that could benefit individual water treatment applications and therefore deserve renewed attention.

Herein we report results of a series of catalytic water treatment experiments comparing the activities of alternative platinum group metals (supported on activated carbon or alumina) for reduction of four oxyanion contaminants with a broad range of chemical reactivity ($\text{BrO}_3^- \gg \text{ClO}_3^- > \text{NO}_3^- \gg \text{ClO}_4^-$). Rh exhibits substantially higher activity than Pd during reduction of BrO_3^- , ClO_3^- and NO_3^- . Ru, with a substantially lower cost compared to the other four metals (Pd, Rh, Pt and Ir), shows unique pH insensitivity and the highest activity for ClO_3^- and NO_3^- reduction at circumneutral pH conditions. All five metals are also able to reduce ClO_4^- when combined with Re species as bimetallic Re–M/C catalysts. Cross comparison of multiple oxyanion substrates and metals reveals new mechanistic insights and suggest new directions to develop novel catalysts for challenging water contaminants.

2.3 Experimental

2.3.1 Chemicals and materials

Unless otherwise specified, all chemicals and metal catalysts (nominal 5 wt% or 1 wt% hydrogenation metal nanoparticles dispersed on activated carbon and alumina supports) were purchased from Sigma–Aldrich or Alfa–Aesar. Detailed catalyst information and

characterization data are shown in Table 2.1. The Ru/Al₂O₃ catalyst required a pretreatment (1 atm H₂ flow in a tube furnace under 350 °C for 2 h) for metal reduction and activation of oxyanion reduction activity.⁴⁴ Aqueous solutions were prepared using deionized (DI) water (resistivity 18.2 MΩ cm). H₂ gas (99.9999% UHP, Matheson) was used for catalytic reactions.

2.3.2 Catalytic reduction of oxyanion contaminants

2.3.2.1 Bromate (BrO₃⁻)

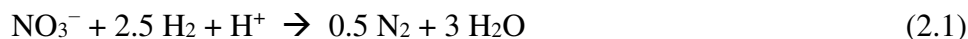
In a 50-mL pear-shaped flask (round bottom, 24/40 joint), a magnetic stir bar, 5 mg of catalyst (dry weight basis), and 50 mL of DI water were added and sonicated for 1 min to make a 0.1 g L⁻¹ catalyst suspension. A rubber stopper loaded with two 16 gauge stainless needles capped the flask. H₂ was sparged through one needle below the liquid surface, and the head space was open to the atmosphere through another needle above the liquid surface. All batch reactions were conducted under 1 atm H₂ at room temperature (20-22 °C). The solution pH was adjusted by 1 mM HCl (pH 3.0), 0.5 mM Na₂HPO₄ plus 0.5 mM NaH₂PO₄ (pH 7.2), or 0.5 mM NaHCO₃ plus 0.5 mM Na₂CO₃ (pH 10.3). The possible competitive adsorption of buffer anions with oxyanions on catalyst surface was not considered and may require further evaluation. Tests showed that these buffers were sufficient to maintain the pH for BrO₃⁻ and ClO₃⁻ reductions. After the suspension was pre-sparged for 1 h to pre-reduce any surface oxides present on the immobilized metal nanoparticles, the reaction was initiated by adding 1 mL of the 50 mM NaBrO₃ stock solution (C₀ = 1 mM). For the rapid BrO₃⁻ reduction reactions, a high H₂ flow rate (~100 mL min⁻¹) was necessary to observe pseudo-first-order kinetics in the batch experiments. Samples were collected at periodic time intervals using a 3-mL syringe introduced through the H₂ outlet needle, and the collected aliquot was immediately filtered (0.45-μm nylon membrane) to quench the reaction before subsequent analysis of the filtrate sample.

2.3.2.2 Chlorate (ClO₃⁻)

The reaction setup was the same as for BrO₃⁻ reduction, except that the catalyst loading in the suspension was increased to 0.5 g L⁻¹ because initial tests showed this oxyanion to generally exhibit lower reactivity with the catalysts. H₂ gas flow rates higher than ~20 mL min⁻¹ did not increase reaction rates. An aliquot of KClO₃ stock solution (50 mM, 1 mL) was added to the reactor to initiate individual batch reactions with C₀ = 1 mM.

2.3.2.3 Nitrate (NO₃⁻)

The reaction setup was the same as for ClO₃⁻ reduction, and a NaNO₃ stock solution (50 mM) was added to initiate batch reactions with C₀ = 1 mM. The pH was stabilized using higher buffer concentrations [1 mM HCl plus 10 mM H₃PO₄ (pH pre-adjusted with NaOH to 3.0), 5 mM Na₂HPO₄ plus 5 mM NaH₂PO₄ (pH 7.2), or 5 mM NaHCO₃ plus 5 mM Na₂CO₃ (pH 10.3)] because NO₃⁻ reduction consumes one (N₂ product, Eq. 2.1) or up to two equivalents of H⁺ (NH₄⁺ product, Eq. 2.2).¹⁴



2.3.2.4 Preparation of Re-M/C and reduction of perchlorate (ClO₄⁻)

In a 50-mL pear shape flask, a magnetic stir bar, 50 mg of M/C catalyst and 25 mL of DI water (pH pre-adjusted to 3.0 using 1 mM HCl) were added and sonicated for 1 min to yield a 2.0 g L⁻¹ catalyst suspension. A NH₄ReO₄ stock solution (5000 ppm as Re, 0.5 mL) was added to the M/C catalyst suspension to reductively immobilize Re (C_T = 100 ppm) into the porous carbon support matrix under H₂ sparging (flow rate ~10 mL min⁻¹). The immobilization process was monitored by measuring dissolved ReO₄⁻ in filtered water samples with ion chromatography until concentrations were below detection.¹⁴ Overnight sparging with H₂ led to complete

immobilization of Re and yielded bimetallic catalysts containing 5 wt% Re. Reactions with ClO_4^- were then initiated by adding an aliquot of NaClO_4 stock solution (200 mM, 0.625 mL) to the suspension ($C_0 = 5$ mM). Samples were collected and filtered using the same procedures described above.

2.3.3 Water sample analysis

The concentrations of BrO_3^- , Br^- , ClO_3^- , Cl^- , and NO_3^- were determined by a Dionex ICS-3000 ion chromatography system (25- μL injection loop and a suppressed conductivity detector). An IonPac AS19 column maintained at 30 °C was used as the stationary phase and 10 mM KOH at 1.0 mL min^{-1} was the eluent. The concentrations of ClO_4^- and ReO_4^- were analyzed by a Dionex ICS-2000 ion chromatography system (25- μL injection loop and a suppressed conductivity detector). An IonPac AS16 column maintained at 30 °C was used as the stationary phase and 65 mM KOH at 1.2 mL min^{-1} was the eluent.

2.3.4 Catalyst characterization

Specific surface area (BET method) and average pore size (BJH method) of the catalyst support materials were measured by N_2 physisorption with a Micromeritics ASAP 2020 analyzer. Dispersion of the hydrogenation metals was determined by chemisorption based on literature methods⁴⁵⁻⁴⁷ with a Micromeritics AutoChem II analyzer equipped with a thermal conductivity detector. Results of physisorption and chemisorption measurements are summarized in **Table 2.1**. To determine surface zeta potentials of selected catalysts under varied pH and the H_2 atmosphere, catalyst suspensions (0.5 g L^{-1}) containing different pH buffers (as described in 2.2.1) were sparged with 1 atm H_2 for 30 min, and immediately transferred into an anaerobic glovebox (97% N_2 , 3% H_2 ; Coy Laboratories). An aliquot of suspension was then transferred into a cuvette and sealed with the plastic cap before analyzing for zeta potential (Malvern Zetasizer Nano ZS).

2.3.5 Kinetic data analysis

Under the reaction conditions described above, reduction of all oxyanion contaminants generally followed a pseudo-first-order rate law for at least two half-lives (i.e., 75% decay). The initial turnover frequency (TOF_0 , min^{-1}), which represents the number of oxyanion molecules reduced per surface metal site per minute, was calculated by Eq. 2.3:¹⁹

$$\text{TOF}_0 = \frac{kC_0}{C_{\text{surface metal}}} = \frac{kC_0M_{\text{metal}}}{C_{\text{total metal}}D_{\text{metal}}} \quad (2.3)$$

where k is the measured pseudo-first-order rate constant (min^{-1}) for oxyanion reduction in the batch reaction, C_0 is the initial oxyanion concentration (mol L^{-1}), $C_{\text{surface metal}}$ is the concentration of surface metal in the catalyst suspension (mol L^{-1}), M_{metal} is the molar mass of metal element (g mol^{-1}), $C_{\text{total metal}}$ is the total concentration of metal loaded in the catalyst suspension (g L^{-1}), and D_{metal} is the metal dispersion on the catalyst support material (Table 2.1), representing the fraction of metal atoms exposed on the surface of the dispersed metal nanoparticles.

2.4 Results and Discussion

2.4.1 Catalytic reduction of bromate

Figure 2.1a shows catalytic reduction of bromate (BrO_3^-) at pH 7.2 by the five activated carbon supported metal catalysts [M/C, 0.1 g L^{-1} catalyst loading with nominal 5 wt% (Pd, Pt, Rh, Ru) or 1 wt% (Ir) of each metal]. A good mass balance between BrO_3^- and Br^- is obtained for each catalyst (Figure A.1 in Appendix A), demonstrating complete BrO_3^- reduction with negligible accumulation of BrO_x^- ($x < 3$) intermediates Eq. 2.4.



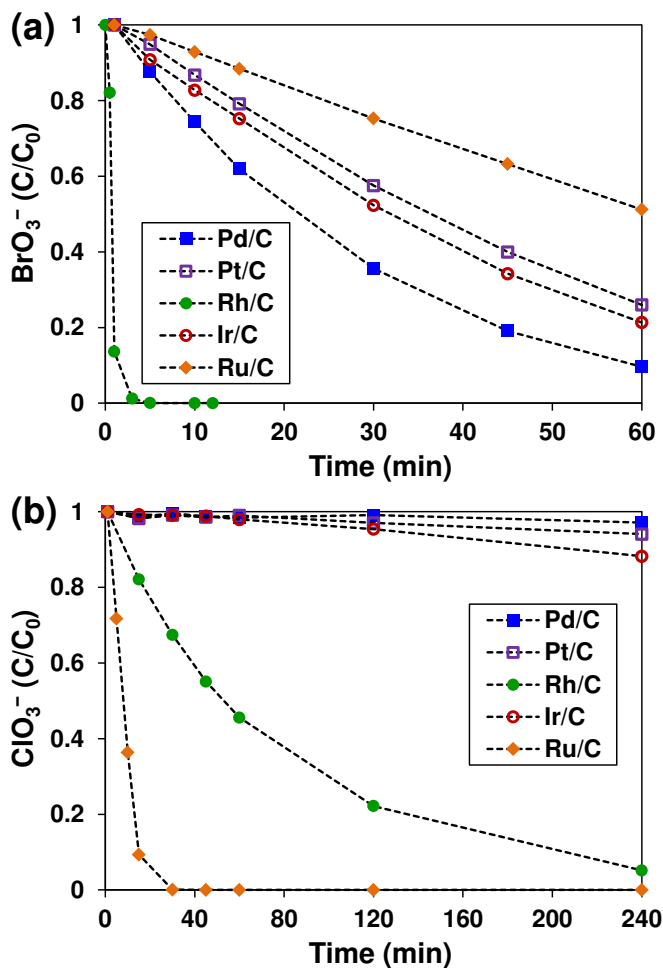


Figure 2.1 Timecourse profiles with for reduction of (a) 1 mM BrO₃⁻ by 0.1 g L⁻¹ M/C catalysts and (b) 1 mM ClO₃⁻ by 0.5 g L⁻¹ M/C catalysts with 1 atm H₂ at pH 7.2 and 22 °C (nominal 5 wt% metal for Pd, Rh, Ru, and Pt; 1 wt% metal for Ir).

Comparing the observed BrO₃⁻ reduction profiles shows that Rh/C is substantially more active than the other four M/C catalysts. At the catalyst loading of 0.1 g L⁻¹, the reduction of 1 mM BrO₃⁻ is complete within 5 min. The activity of Rh/C is much higher than most supported hydrogenation metal catalysts reported to date when compared on a metal mass-normalized basis.^{34, 36-38, 48, 49} Since the metal dispersion of individual catalysts differ (Table 2.1), the activities of hydrogenation metals are further compared using initial turnover frequency values (TOF₀, Eq. 2.3). As shown in Table 2.2, Rh/C exhibited significantly higher TOF₀ than other

catalysts at pH 7.2. Although the apparent reactivity of Ir/C with BrO_3^- is slightly lower than that of Pd/C (Figure 2.1a), Ir/C exhibited the second highest TOF_0 . Thus, the catalysts incorporating the two Group 9 metals, Rh and Ir, show the highest activity for BrO_3^- reduction at neutral pH conditions that are highly relevant for water treatment systems.

Acidic pH conditions have been previously reported to accelerate BrO_3^- reduction by Pd catalysts.^{20, 48} To examine if this trend extends to other hydrogenation metals, BrO_3^- reduction by all five M/C catalysts was also measured at pH 3.0. Results from these experiments (Table 2.2 and Figure A.2a in Appendix A) show that catalysts incorporating the two Group 10 metals, Pd and Pt, exhibit significant pH dependence, with TOF_0 increasing by more than an order of magnitude when pH is lowered from 7.2 to 3.0. In comparison, the catalysts incorporating Group 9 (Rh and Ir) and Group 8 (Ru) metals show less activity change when pH is lowered. TOF_0 for Rh/C and Ru/C decrease by 35-40%, and Ir/C increases 3-fold when the pH is lowered from 7.2 to 3.0.

2.4.2 Catalytic reduction of chlorate

Results for catalytic reduction of chlorate (ClO_3^-) by M/C at pH 7.2 are shown in Figure 2.1b. In comparison to BrO_3^- , ClO_3^- is much more inert to reduction (note that the suspension catalyst loading used in the experiments was increased to 0.5 g L^{-1}). Like BrO_3^- , a good mass balance with ClO_3^- and Cl^- (Figure A.3 in Appendix A) is observed during reactions, consistent with the following reaction Eq. 2.5 and confirming negligible accumulation of ClO_x^- ($x < 3$) intermediates.



The highest apparent reactivity with ClO_3^- is observed with Ru/C, a Group 8 metal, and the resulting TOF_0 (6.0 min^{-1}) is substantially higher than catalysts incorporating the other four

Table 2.1 Catalyst information and characterization data

Entry	Metal	Supplier and catalog number	Surface area (m ² g ⁻¹)	Average pore size (nm)	Metal dispersion	Metal particle diameter (nm)
<i>Activated Carbon Support</i>						
1	5 wt% Pd	Sigma-Aldrich #205680	958	3.1	30.3%	3.7
2	5 wt% Rh	Sigma-Aldrich #206164	870	3.6	31.3%	3.5
3	5 wt% Ru	Alfa-Aesar #44338	704	3.4	11.2%	11.8
4	5 wt% Pt	Sigma-Aldrich #205931	1370	3.4	23.9%	4.7
5	1 wt% Ir	Alfa-Aesar #38330	839	3.3	31.8%	3.7
<i>Alumina Support</i>						
6	5 wt% Pd	Sigma-Aldrich #205710	106	8.9	66.3%	1.7
7	5 wt% Rh	Sigma-Aldrich #212857	168	10.0	64.1%	1.7
8	5 wt% Ru	Sigma-Aldrich #381152	93	15.3	9.8%	13.5
9	5 wt% Pt	Sigma-Aldrich #205974	94	9.2	23.4%	4.8

Table 2.2 Initial turnover frequencies for the reaction of 1 mM oxyanions with M/C, M/Al₂O₃

Entry	Catalyst	Catalytic oxyanion reduction turnover frequency (TOF ₀ , min ⁻¹) ^a					
		BrO ₃ ⁻		ClO ₃ ⁻		NO ₃ ⁻	
		pH 7.2	pH 3.0	pH 7.2	pH 3.0	pH 7.2	pH 3.0
1	Pd/C (10) ^b	2.7 ± 0.1 ^c	33.4 ± 2.7	0.0012 ± 0.0005	0.070 ± 0.002	ND ^d	ND
2	Rh/C (9)	54.4 ± 5.5	32.3 ± 0.6	0.17 ± 0.01	6.7 ± 0.5	0.0019 ± 0.0001	0.046 ± 0.004
3	Ru/C (8)	2.0 ± 0.1	1.3 ± 0.5	6.0 ± 1.1	0.11 ± 0.01	0.33 ± 0.01	0.71 ± 0.01
4	Pt/C (10)	3.7 ± 0.1	42.9 ± 0.4	0.0076 ± 0.0010	0.090 ± 0.006	ND	ND
5	Ir/C (9)	15.5 ± 0.5	47.0 ± 1.9	0.061 ± 0.003	1.2 ± 0.1	ND	ND
6	Pd/Al ₂ O ₃	0.83 ± 0.01		ND		ND	
7	Rh/Al ₂ O ₃	5.9 ± 0.6		0.014 ± 0.001		0.0025 ± 0.0001	
8	Ru/Al ₂ O ₃	7.0 ± 0.4		1.1 ± 0.1		0.30 ± 0.02	
9	Pt/Al ₂ O ₃	6.5 ± 0.3		0.0058 ± 0.0001		ND	

^aDetermined for catalyst reactions with 1 mM oxyanions, 22°C, continuous mixing and sparging with 1 atm H₂. 0.1 g L⁻¹ catalyst suspensions used for reactions with BrO₃⁻, 0.5 g L⁻¹ used for ClO₃⁻ and NO₃⁻.

^bNumber in parenthesis indicate the Periodic Table group number of the hydrogenation metal.

^cErrors represent 95% confidence intervals.

^dMeaningful catalytic activity not detected within the 4 h of reaction at the 0.5 g L⁻¹ catalyst loading.

Group 9 and 10 metals (Table 2.2), due, in part, to the low dispersion of Ru nanoparticles on the carbon support. TOF₀ values measured for the two Group 9 metals (0.17 min⁻¹ for Rh and 0.061 min⁻¹ for Ir) are higher than those observed for the two Group 10 metals (< 0.01 min⁻¹ for Pd and Pt). Thus, for neutral pH conditions, periodic trends suggest that ClO₃⁻ reactivity follows Group 8 >> Group 9 >> Group 10 metals.

Comparing pH dependences for ClO₃⁻ reactions with the different M/C reveals some other interesting trends. Catalysts incorporating the Group 9 and 10 metals show significantly enhanced reactivity with ClO₃⁻ under acidic pH conditions compared to pH 7.2 (Figure A.2b in Appendix A and Table 2), whereas reactions are inhibited under these conditions for Ru, the Group 8 metal. At pH 3.0, Rh/C is the most active catalyst for ClO₃⁻ reduction (TOF₀ increases from 0.17 min⁻¹ at pH 7.2 to 6.7 min⁻¹). A mirror trend is observed for Ru/C, where TOF₀ decreases from 6.0 min⁻¹ at pH 7.2 to 0.11 min⁻¹ at pH 3.0. The unique pH dependence observed for Ru/C suggests different rate-controlling surface reaction mechanisms for this catalyst compared to those incorporating Group 9 and 10 metals.

2.4.3 Catalytic reduction of nitrate

Of the catalysts examined, only Rh/C and Ru/C show meaningful reactivity with the more recalcitrant nitrate ion (NO₃⁻) in 0.5 g L⁻¹ catalyst suspensions monitored for 4 h. As shown in Table 2.2 and Figure A.4 in Appendix A, Ru shows much higher activity than Rh, and both metals exhibit enhanced activities when pH is reduced from 7.2 to 3.0. The observed product of NO₃⁻ reduction by these two metals under the test conditions is mostly NH₃/NH₄⁺ (Eq. 2.2) rather than the desired N₂ (Eq. 2.1). Nevertheless, results show that monometallic Rh and Ru catalysts are capable of reducing NO₃⁻ without the need for secondary promoter metals (e.g., In, Cu, Sn, and Re) used to activate Pd catalysts towards NO₃⁻ reduction^{14, 18, 25}. Motivated by the

low market price of Ru ($\$1.4 \text{ g}^{-1}$) in comparison to the other metals ($\$17$ to $\$38 \text{ g}^{-1}$) (Table A.1), an in-depth study of Ru-catalyzed NO_3^- and NO_2^- reduction by our team was undertaken and reported separately.⁴⁴

2.4.4 Effect of metal catalyst support materials

We also examined reactions of the three tri-oxy anions with Pd, Pt, Rh, and Ru supported on porous alumina ($\text{M}/\text{Al}_2\text{O}_3$), another common catalyst support material, and found generally the same reactivity trends observed for the M/C catalysts. Alumina is unstable under acidic pH conditions, so reactivity was only compared with M/C at pH 7.2. Compared to activated carbon support materials, the alumina supports generally have an order of magnitude lower specific surface areas and two times larger pore average size (Table 2.1). As shown in Figure 2.2 and Table 2.2, $\text{M}/\text{Al}_2\text{O}_3$ catalysts generally exhibit similar activity compared to the corresponding M/C.

Still, the highest activity for BrO_3^- reduction at pH 7.2 is observed with both Rh/C and Rh/ Al_2O_3 , and the highest activity for ClO_3^- and NO_3^- reduction is observed with both Ru/C and Ru/ Al_2O_3 . These similar trends suggest that activity differences among the catalysts primarily originate from the chemical nature of the immobilized metal nanoparticles, and the effects of the support materials may be minor.

2.4.5 Catalytic reduction of perchlorate

For the tetra-oxyanion perchlorate (ClO_4^-), the most inert of the target oxyanions examined, no reaction is observed using any of the monometallic catalysts (Table A.2 in Appendix A). We previously reported on preparation of bimetallic Re–Pd/C catalysts that are able to reduce aqueous ClO_4^- because the immobilized surface oxorhenium(V) species [from the catalytic reduction of oxorhenium(VII) with Pd/C, Eq. 2.6] are able to abstract the most

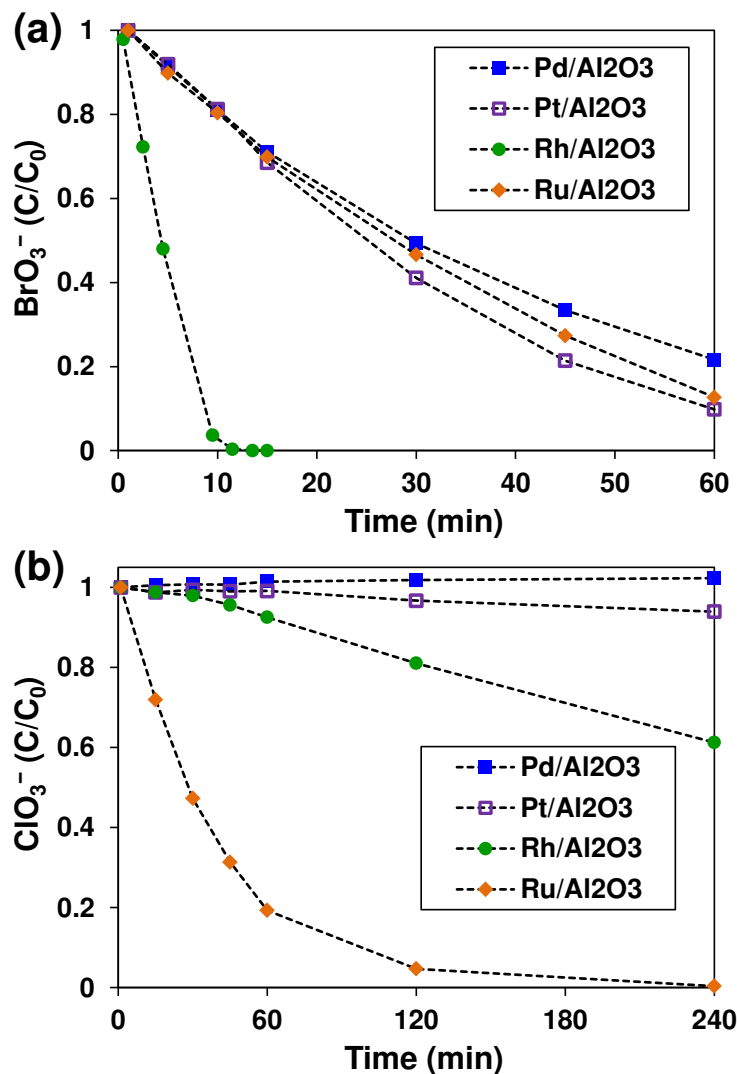
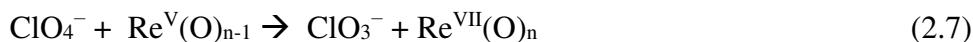


Figure 2.2 Timecourse profiles with for reduction of (a) 1 mM BrO₃⁻ by 0.1 g L⁻¹ M/Al₂O₃ catalysts and (b) 1 mM ClO₃⁻ by 0.5 g L⁻¹ M/Al₂O₃ catalysts with 1 atm H₂ at pH 7.2 and 22 °C (nominal 5 wt% metal for all catalysts).

challenging oxygen atom, via oxygen atom transfer (OAT) reaction, converting ClO₄⁻ to ClO₃⁻ (Eq. 2.7), which is further reduced to Cl⁻ (Eq. 2.8) by OAT with Re^V or directly by reaction with hydrogenation nanoparticles (Figure 2.3a).^{39, 50, 51}





And thus the overall reaction is



In order to assess the dependence of ClO_4^- reduction on the other four hydrogenation metals, we followed the same approach for bimetallic catalyst synthesis^{14, 52} to prepare Re–M/C catalysts using each of the M/C catalysts discussed already. Figure 2.3b shows the reactivity of 5 mM ClO_4^- with 2 g L⁻¹ of each Re–M/C catalyst. The apparent reactivity of the bimetallic catalysts follows Re–Pd/C > Re–Ru/C > Re–Rh/C > Re–Ir/C > Re–Pt/C. Mechanistic

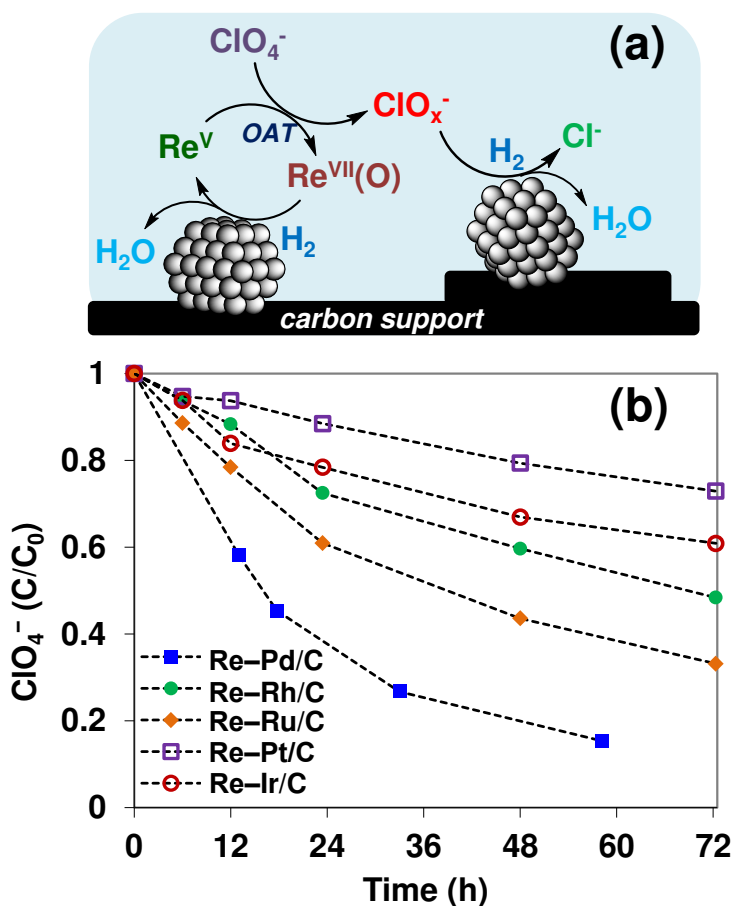


Figure 2.3 (a) Mechanisms for Re–M/C catalyst reactions with ClO_4^- and ClO_x^- intermediates ($x = 3, 2, \text{ or } 1$); adapted from Refs^{50, 51}. (b) Reduction of 5 mM ClO_4^- with 2 g L⁻¹ Re–M/C (5 wt% Re, 5 wt% M) bimetallic catalysts.

interpretation of this trend is unclear at this time. This is complicated by the fact that previous work shows that the rate of ClO_4^- reduction by OAT reactions is more heavily influenced by the speciation of the immobilized Re species than the identity of the hydrogenation metal.^{53, 54} Nevertheless, these results demonstrate that all five hydrogenation metals are capable of sustaining the redox turnover of surface Re species (Eqs. 2.6 and 2.7) required to catalyze the OAT reaction with ClO_4^- (turn over number, TON = 38 for each Re atom to fully reduce 5 mM ClO_4^- to Cl^- with the catalyst loadings used in the experiment).

2.4.6 Mechanistic insights from metal and AO_3^- reactivity cross comparisons

Comparison of observed reactivity trends among the platinum group metals and trioxyanion substrates (AO_3^-) reveals new insights on the controlling reaction mechanisms. First, since the optimum metals for the reduction of BrO_3^- (Rh at pH 7.2) and ClO_3^- (Ru at pH 7.2) differ, the oxyanion substrates should have direct interactions with metal nanoparticle surfaces to undergo reduction (Figure 2.4a). If the oxyanions mainly react with dissociated atomic hydrogen that is “spilled” away from the metal nanoparticles (Figure 2.4b),^{55, 56} the order of catalytic activity for the five metals toward the three oxyanions may be expected to be more

similar. However, the measured activity order is $\text{Rh} > \text{Ir} > \text{Pt} \sim \text{Pd} \sim \text{Ru}$ for BrO_3^- reduction at pH 7.2, and $\text{Ru} \gg \text{Rh} > \text{Ir} > \text{Pt} > \text{Pd}$ for ClO_3^- reduction at pH 7.2 (Table 2.2). In addition, we note that the observed activity trends are different from those previously report by Restivo *et al.*,³⁴ where the M/C catalysts were prepared in the researchers’ own laboratory and exhibited much lower BrO_3^- reduction activity (e.g., > 15 min was required to completely reduce 0.078 mM BrO_3^- by 2 g L⁻¹ of 1 wt% M/C catalysts) than our experimental results (e.g., 5 min to completely reduce 1.0 mM BrO_3^- by 0.1 g L⁻¹ 5 wt% Rh/C). We note that the differences of BrO_3^- concentration and catalyst loading have outweighed the effect of metal loading.

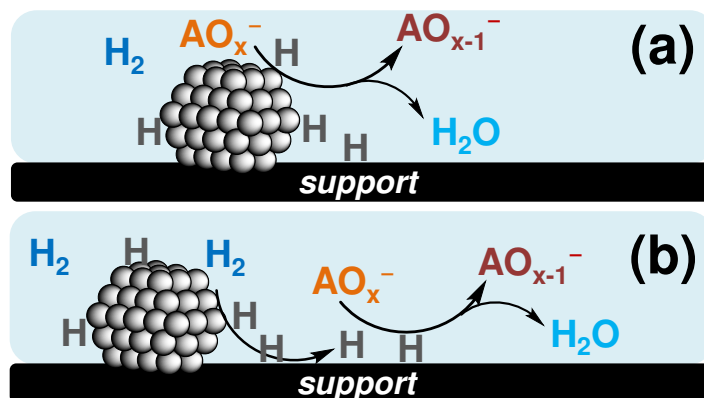


Figure 2.4 Mechanism illustrations of (a) the reduction of oxyanion substrates (AO_x^-) requiring direct interaction with the hydrogenation metal nanoparticles; (b) the reaction between AO_x^- and spilled over atomic hydrogen at the catalyst support surface away from the hydrogenation metal nanoparticles.

Explanation of the discrepancies of catalyst activity in different reports, if necessary, would require substantial amount of catalyst characterization and comparison. It is probable that critical catalytic properties of individual metals might have not be revealed when using a uniform catalyst preparation recipe for all metals (i.e., the recipes were not optimized for individual metal) by the Pereira and Neves team.

Nevertheless, results suggest that the mechanistic interpretation, which might be used as design rationale for future catalyst development work, should be considered with caution. Restivo *et al.* observed Pt and Ru to be the most active metals for BrO_3^- reduction, and this observation was correlated with the hydrogen chemisorption energy on each metal using the Sabatier principle.³⁴ However, based on the activity of Rh and Ir in the current study, we propose that hydrogen chemisorption energy might not necessarily be the key parameter controlling reactivity of different metals with BrO_3^- , and that the interaction between oxyanion substrates and different metal surfaces should also be considered.

Second, the pH responses of the five metals are also different. For BrO_3^- reduction, the pH responses of Rh and Ru contrast those of Pd, Pt and Ir (Table 2.2). Also, the same Rh/C catalyst exhibits differing pH dependence for BrO_3^- reduction compared to ClO_3^- and NO_3^- reduction (Figure 2.5, activity presented in apparent rate constants normalized by the mass of M/C catalysts), even though the three oxyanions carry the same -1 charge in solutions between

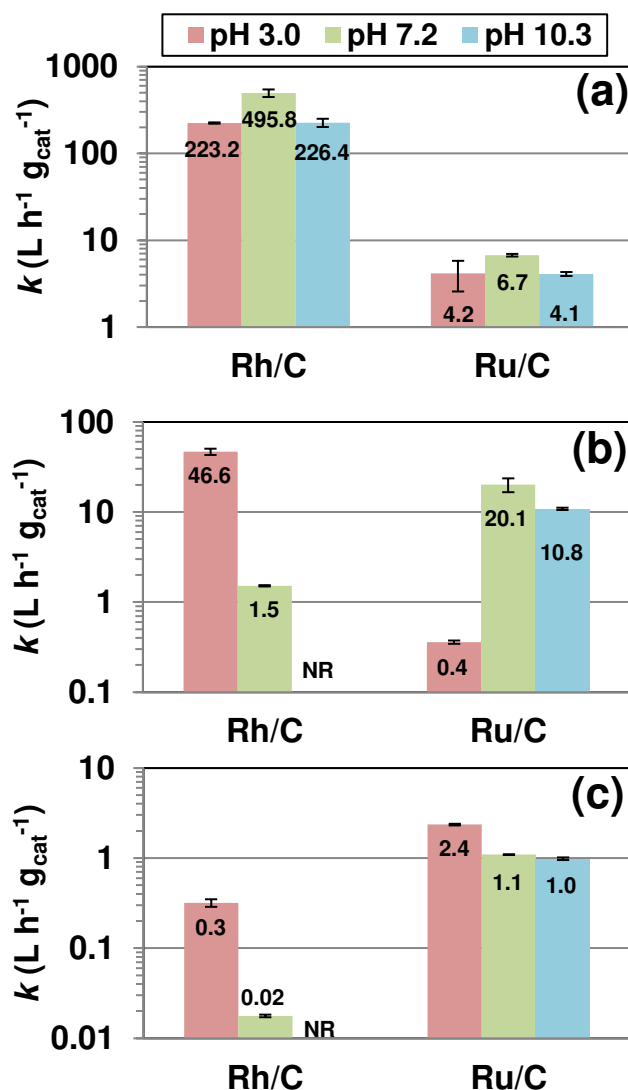


Figure 2.5 Catalyst loading normalized rate constants at different pH for the reduction of 1 mM (a) BrO_3^- , (b) ClO_3^- and (c) NO_3^- with Rh/C and Ru/C catalysts. Error bars represent replicate-averaged 95% confidence intervals. "NR" indicates no reaction observed within the reaction period monitored.

pH 3.0 and 10.3. In comparison, Ru/C catalyst did not show a simple trend of pH dependence. Zeta potentials of Rh/C and Ru/C under variable pH (with a H₂ atmosphere^{20, 52}) were measured and results are shown in Figure 2.6. Although the zeta potentials of both catalysts are significantly increased when the pH decreases from 7.2 to 3.0, the BrO₃⁻ reduction by Rh/C and Ru/C (Figure 2.6a) as well as the ClO₃⁻ reduction by Ru/C (Figure 2.6b) are not accelerated. Previous reports attribute slower rates of BrO₃⁻ reduction by Pd catalysts at higher pH to increased negative surface charge and the resulting unfavorable electrostatic interactions between the surface and the negatively charged oxyanions.^{20, 57} Here, results demonstrate that a more positively charged support at lower pH does not necessarily increase rates of oxyanion reduction for all M/C. Hence, the intrinsic reactivity of metals may outweigh the effects of catalyst surface charge. Therefore, the priority of designing an oxyanion reduction catalyst should consider the selection of active metal according to the characteristics of oxyanion substrates and reaction conditions (e.g., solution pH).

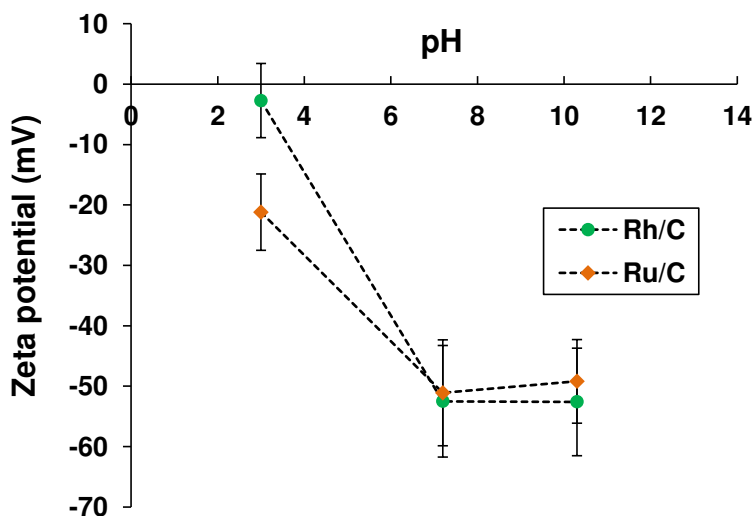


Figure 2.6 Influence of pH on the zeta potential of 0.5 g L⁻¹ Rh/C and Ru/C catalysts in H₂-saturated aqueous suspension at 22 °C.

2.4.7 Outlook in catalyst development and application

In this study, four platinum group metals, which have been largely overlooked during the development of Pd-based water treatment catalysts, exhibit much higher or at least similar performance in comparison to Pd, in terms of catalytic turnover frequency, pH dependence, and oxyanion substrate scope. Specifically, Ru shows outstanding activity for ClO_3^- and NO_3^- reduction over a wide pH range, and the price of Ru is more than an order of magnitude lower than the other four metals (Table A.1 in Appendix A). Thus, lower cost and more sustainable reductive catalytic technologies^{15, 16} may be achieved by developing Ru-based multi-functional materials. Moreover, our research group has developed highly stable ClO_4^- reduction catalysts based on Rh rather than Pd, because the former could rapidly scavenge ClO_x^- intermediates that can deactivate Re complex reaction sites.^{39, 54} Results from this study are expected to initiate the development of new catalysts for a variety of water treatment scenarios.

Various factors such as size and morphology of both the metal nanoparticles and the support materials can also influence the reactivity of platinum group metals,^{19, 57} but the effects are generally less pronounced compared to the effects of metal identity (e.g., Pd versus Rh in ClO_3^- reduction, or Pd versus Ru in NO_3^- reduction) as demonstrated in this study. Computational studies^{19, 58} are also needed to provide detailed theoretical insights into these metal-specific effects and metal-substrate interactions. We emphasize that research priority should be given to further examining novel activity of these previously overlooked metals in water treatment applications, such as (1) exploring multi-functional activities in treating various emerging and challenging contaminants (e.g., nitro,⁵⁹ fluoro,⁴⁰⁻⁴³ and polychloro^{60, 61} compounds), and (2) rational development of catalyst formulation and engineering processes to apply these metals for practical water treatment.

2.5 Conclusions

Four platinum group metals (Ru, Rh, Ir, and Pt), largely overlooked in the development of water treatment catalysts compared to Pd, are shown here to exhibit favorable reactivity with aqueous bromate, chlorate, nitrate and perchlorate at ambient conditions. Specifically, Rh and Ru show significant advantages over Pd in terms of catalytic turnover frequency, pH dependence, oxyanion substrate scope, or cost. Cross comparison of multiple metals and tri-oxyanion substrates suggest that some previous interpretations of the pH influence on catalyst reactivity should be revisited. The chemical nature of each metal element is a key factor determining the catalyst activity and adaptability to different water treatment conditions. We recommend that rational selection of metals could be one of the current priorities in the development of water treatment catalysts.

2.6 References

1. Snyder, S. A.; Vanderford, B. J.; Rexing, D. J. Trace analysis of bromate, chlorate, iodate, and perchlorate in natural and bottled waters. *Environmental science & technology* **2005**, *39* (12), 4586-4593.
2. Spalding, R. F.; Exner, M. E. Occurrence of nitrate in groundwater—a review. *Journal of environmental quality* **1993**, *22* (3), 392-402.
3. Urbansky, E. T. Perchlorate as an environmental contaminant. *Environmental Science and Pollution Research* **2002**, *9* (3), 187-192.
4. Kosaka, K.; Asami, M.; Matsuoka, Y.; Kamoshita, M.; Kunikane, S. Occurrence of perchlorate in drinking water sources of metropolitan area in Japan. *Water research* **2007**, *41* (15), 3474-3482.
5. Weinberg, H. S.; Delcomyn, C. A.; Unnam, V. Bromate in chlorinated drinking waters: occurrence and implications for future regulation. *Environmental science & technology* **2003**, *37* (14), 3104-3110.
6. Butler, R.; Godley, A.; Lytton, L.; Cartmell, E. Bromate environmental contamination: review of impact and possible treatment. *Critical reviews in environmental science and technology* **2005**, *35* (3), 193-217.

7. Bolyard, M.; Fair, P. S.; Hautman, D. P. Occurrence of chlorate in hypochlorite solutions used for drinking water disinfection. *Environmental science & technology* **1992**, *26* (8), 1663-1665.
8. Oh, B. S.; Oh, S. G.; Hwang, Y. Y.; Yu, H.-W.; Kang, J.-W.; Kim, I. S. Formation of hazardous inorganic by-products during electrolysis of seawater as a disinfection process for desalination. *Science of the total environment* **2010**, *408* (23), 5958-5965.
9. Azizi, O.; Hubler, D.; Schrader, G.; Farrell, J.; Chaplin, B. P. Mechanism of perchlorate formation on boron-doped diamond film anodes. *Environmental science & technology* **2011**, *45* (24), 10582-10590.
10. Boorman, G. A. Drinking water disinfection byproducts: review and approach to toxicity evaluation. *Environmental Health Perspectives* **1999**, *107* (Suppl 1), 207.
11. Bruning-Fann, C. S.; Kaneene, J. The effects of nitrate, nitrite and N-nitroso compounds on human health: a review. *Veterinary and human toxicology* **1993**, *35* (6), 521-538.
12. Greer, M. A.; Goodman, G.; Pleus, R. C.; Greer, S. E. Health effects assessment for environmental perchlorate contamination: the dose response for inhibition of thyroidal radioiodine uptake in humans. *Environmental Health Perspectives* **2002**, *110* (9), 927.
13. McAdam, E.; Judd, S. Biological treatment of ion-exchange brine regenerant for re-use: A review. *Separation and Purification Technology* **2008**, *62* (2), 264-272.
14. Liu, J.; Choe, J. K.; Sasnow, Z.; Werth, C. J.; Strathmann, T. J. Application of a Re–Pd bimetallic catalyst for treatment of perchlorate in waste ion-exchange regenerant brine. *Water Res.* **2013**, *47* (1), 91-101.
15. Choe, J. K.; Mehnert, M. H.; Guest, J. S.; Strathmann, T. J.; Werth, C. J. Comparative assessment of the environmental sustainability of existing and emerging perchlorate treatment technologies for drinking water. *Environmental science & technology* **2013**, *47* (9), 4644-4652.
16. Choe, J. K.; Bergquist, A. M.; Jeong, S.; Guest, J. S.; Werth, C. J.; Strathmann, T. J. Performance and life cycle environmental benefits of recycling spent ion exchange brines by catalytic treatment of nitrate. *Water research* **2015**, *80*, 267-280.
17. Chaplin, B. P.; Reinhard, M.; Schneider, W. F.; Schüth, C.; Shapley, J. R.; Strathmann, T. J.; Werth, C. J. Critical review of Pd-based catalytic treatment of priority contaminants in water. *Environ. Sci. Technol.* **2012**, *46* (7), 3655-3670.
18. Hörold, S.; Vorlop, K.-D.; Tacke, T.; Sell, M. Development of catalysts for a selective nitrate and nitrite removal from drinking water. *Catalysis Today* **1993**, *17* (1), 21-30.
19. Shuai, D.; McCalman, D. C.; Choe, J. K.; Shapley, J. R.; Schneider, W. F.; Werth, C. J. Structure sensitivity study of waterborne contaminant hydrogenation using shape-and size-controlled Pd nanoparticles. *ACS Catal.* **2013**, *3* (3), 453-463.

20. Wang, Y.; Liu, J.; Wang, P.; Werth, C. J.; Strathmann, T. J. Palladium nanoparticles encapsulated in core-shell silica: A structured hydrogenation catalyst with enhanced activity for reduction of oxyanion water pollutants. *ACS Catal.* **2014**, *4* (10), 3551-3559.
21. Marco, Y.; García-Bordejé, E.; Franch, C.; Palomares, A. E.; Yuranova, T.; Kiwi-Minsker, L. Bromate catalytic reduction in continuous mode using metal catalysts supported on monoliths coated with carbon nanofibers. *Chem. Eng. J.* **2013**, *230*, 605-611.
22. Shuai, D.; Choe, J. K.; Shapley, J. R.; Werth, C. J. Enhanced activity and selectivity of carbon nanofiber supported Pd catalysts for nitrite reduction. *Environmental science & technology* **2012**, *46* (5), 2847-2855.
23. Strukul, G.; Gavagnin, R.; Pinna, F.; Modafferri, E.; Perathoner, S.; Centi, G.; Marella, M.; Tomaselli, M. Use of palladium based catalysts in the hydrogenation of nitrates in drinking water: from powders to membranes. *Catal. Today* **2000**, *55* (1-2), 139-149.
24. Liu, J.; Choe, J. K.; Wang, Y.; Shapley, J. R.; Werth, C. J.; Strathmann, T. J. Bio-inspired Complex-Nanoparticle Hybrid Catalyst System for Aqueous Perchlorate Reduction: Rhenium Speciation and Its Influence on Catalyst Activity *ACS Catalysis* **2015**, *5*, 511-522.
25. Prüsse, U.; Vorlop, K.-D. Supported bimetallic palladium catalysts for water-phase nitrate reduction. *J. Mol. Catal. A: Chem.* **2001**, *173* (1-2), 313-328.
26. Ambonguilat, S.; Gallard, H.; Garron, A.; Epron, F.; Croué, J. P. Evaluation of the catalytic reduction of nitrate for the determination of dissolved organic nitrogen in natural waters. *Water research* **2006**, *40* (4), 675-682.
27. Chaplin, B. P.; Roundy, E.; Guy, K. A.; Shapley, J. R.; Werth, C. J. Effects of natural water ions and humic acid on catalytic nitrate reduction kinetics using an alumina supported Pd-Cu catalyst. *Environmental science & technology* **2006**, *40* (9), 3075-3081.
28. McNab, W. W.; Ruiz, R.; Reinhard, M. In-situ destruction of chlorinated hydrocarbons in groundwater using catalytic reductive dehalogenation in a reactive well: Testing and operational experiences. *Environmental Science & Technology* **2000**, *34* (1), 149-153.
29. Davie, M. G.; Cheng, H.; Hopkins, G. D.; LeBron, C. A.; Reinhard, M. Implementing heterogeneous catalytic dechlorination technology for remediating TCE-contaminated groundwater. *Environmental science & technology* **2008**, *42* (23), 8908-8915.
30. Schüth, C.; Kummer, N.-A.; Weidenthaler, C.; Schad, H. Field application of a tailored catalyst for hydrodechlorinating chlorinated hydrocarbon contaminants in groundwater. *Appl. Catal., B* **2004**, *52* (3), 197-203.
31. Nishimura, S. *Handbook of heterogeneous catalytic hydrogenation for organic synthesis*; Wiley New York etc: 2001.

32. Lin, Y.-C.; Huber, G. W. The critical role of heterogeneous catalysis in lignocellulosic biomass conversion. *Energy & Environmental Science* **2009**, *2* (1), 68-80.
33. Gandhi, H.; Graham, G.; McCabe, R. W. Automotive exhaust catalysis. *Journal of Catalysis* **2003**, *216* (1), 433-442.
34. Restivo, J.; Soares, O.; Órfão, J.; Pereira, M. Metal assessment for the catalytic reduction of bromate in water under hydrogen. *Chem. Eng. J.* **2015**, *263*, 119-126.
35. Soares, O. S. G.; Órfão, J. J.; Pereira, M. F. R. Activated carbon supported metal catalysts for nitrate and nitrite reduction in water. *Catalysis letters* **2008**, *126* (3-4), 253-260.
36. Soares, O. S.; Freitas, C. M.; Fonseca, A. M.; Órfão, J. J.; Pereira, M. F.; Neves, I. C. Bromate reduction in water promoted by metal catalysts prepared over faujasite zeolite. *Chem. Eng. J.* **2016**, *291*, 199-205.
37. Freitas, C.; Soares, O.; Órfão, J.; Fonseca, A.; Pereira, M.; Neves, I. Highly efficient reduction of bromate to bromide over mono and bimetallic ZSM5 catalysts. *Green Chemistry* **2015**, *17* (8), 4247-4254.
38. Restivo, J.; Soares, O.; Órfão, J.; Pereira, M. Bimetallic activated carbon supported catalysts for the hydrogen reduction of bromate in water. *Catal. Today* **2015**, *249*, 213-219.
39. Liu, J.; Chen, X.; Wang, Y.; Strathmann, T. J.; Werth, C. J. Mechanism and mitigation of the decomposition of an oxorhenium complex-based heterogeneous catalyst for perchlorate reduction in water. *Environ. Sci. Technol.* **2015**, *49* (21), 12932-12940.
40. Baumgartner, R.; McNeill, K. Hydrodefluorination and hydrogenation of fluorobenzene under mild aqueous conditions. *Environmental science & technology* **2012**, *46* (18), 10199-10205.
41. Baumgartner, R.; Stieger, G. K.; McNeill, K. Complete hydrodehalogenation of polyfluorinated and other polyhalogenated benzenes under mild catalytic conditions. *Environmental science & technology* **2013**, *47* (12), 6545-6553.
42. Yu, Y.-H.; Chiu, P. C. Kinetics and Pathway of Vinyl Fluoride Reduction over Rhodium. *Environmental Science & Technology Letters* **2014**, *1* (11), 448-452.
43. Sawama, Y.; Yabe, Y.; Shigetsura, M.; Yamada, T.; Nagata, S.; Fujiwara, Y.; Maegawa, T.; Monguchi, Y.; Sajiki, H. Platinum on Carbon-Catalyzed Hydrodefluorination of Fluoroarenes using Isopropyl Alcohol-Water-Sodium Carbonate Combination. *Advanced Synthesis & Catalysis* **2012**, *354* (5), 777-782.
44. Huo, X.; Van Hoomissen, D. J.; Liu, J.; Vyas, S.; Strathmann, T. J. Hydrogenation of aqueous nitrate and nitrite with ruthenium catalysts. *Appl. Catal., B* **2017**, *211*, 188-198.

45. Vardon, D. R.; Franden, M. A.; Johnson, C. W.; Karp, E. M.; Guarneri, M. T.; Linger, J. G.; Salm, M. J.; Strathmann, T. J.; Beckham, G. T. Adipic acid production from lignin. *Energy & Environmental Science* **2015**, *8* (2), 617-628.
46. Vardon, D. R.; Sharma, B. K.; Jaramillo, H.; Kim, D.; Choe, J. K.; Ciesielski, P. N.; Strathmann, T. J. Hydrothermal catalytic processing of saturated and unsaturated fatty acids to hydrocarbons with glycerol for in situ hydrogen production. *Green Chemistry* **2014**, *16* (3), 1507-1520.
47. Maris, E. P.; Davis, R. J. Hydrogenolysis of glycerol over carbon-supported Ru and Pt catalysts. *J. Catal.* **2007**, *249* (2), 328-337.
48. Chen, H.; Xu, Z.; Wan, H.; Zheng, J.; Yin, D.; Zheng, S. Aqueous bromate reduction by catalytic hydrogenation over Pd/Al₂O₃ catalysts. *Appl. Catal., B* **2010**, *96* (3-4), 307-313.
49. Sun, W.; Li, Q.; Gao, S.; Shang, J. K. Highly efficient catalytic reduction of bromate in water over a quasi-monodisperse, superparamagnetic Pd/Fe₃O₄ catalyst. *Journal of Materials Chemistry A* **2013**, *1* (32), 9215-9224.
50. Hurley, K. D.; Shapley, J. R. Efficient heterogeneous catalytic reduction of perchlorate in water. *Environ. Sci. Technol.* **2007**, *41* (6), 2044-2049.
51. Choe, J. K.; Shapley, J. R.; Strathmann, T. J.; Werth, C. J. Influence of rhenium speciation on the stability and activity of Re/Pd bimetal catalysts used for perchlorate reduction. *Environ. Sci. Technol.* **2010**, *44* (12), 4716-4721.
52. Hurley, K. D.; Zhang, Y.; Shapley, J. R. Ligand-Enhanced Reduction of Perchlorate in Water with Heterogeneous Re-Pd/C Catalysts. *J. Am. Chem. Soc.* **2009**, *131* (40), 14172-14173.
53. Liu, J.; Han, M.; Wu, D.; Chen, X.; Choe, J. K.; Werth, C. J.; Strathmann, T. J. A new bioinspired perchlorate reduction catalyst with significantly enhanced stability via rational tuning of rhenium coordination chemistry and heterogeneous reaction pathway. *Environ. Sci. Technol.* **2016**, *50*, 5874-5881.
54. Contescu, C. I.; Brown, C. M.; Liu, Y.; Bhat, V. V.; Gallego, N. C. Detection of hydrogen spillover in palladium-modified activated carbon fibers during hydrogen adsorption. *J. Phys. Chem. C* **2009**, *113* (14), 5886-5890.
55. Chen, L.; Cooper, A. C.; Pez, G. P.; Cheng, H. Mechanistic study on hydrogen spillover onto graphitic carbon materials. *J. Phys. Chem. C* **2007**, *111* (51), 18995-19000.
56. Zhang, P.; Jiang, F.; Chen, H. Enhanced catalytic hydrogenation of aqueous bromate over Pd/mesoporous carbon nitride. *Chem. Eng. J.* **2013**, *234*, 195-202.
57. Shin, H.; Jung, S.; Bae, S.; Lee, W.; Kim, H. Nitrite Reduction Mechanism on a Pd Surface. *Environmental science & technology* **2014**, *48* (21), 12768-12774.

58. Phillips, D. L. *Palladium-Catalyzed Destruction of Nitro Aromatic-Contaminated Groundwater*; DTIC Document: 2003.
59. Bovkun, T. T.; Sasson, Y.; Blum, J. Conversion of chlorophenols into cyclohexane by a recyclable Pd-Rh catalyst. *Journal of Molecular Catalysis A: Chemical* **2005**, *242* (1), 68-73.
60. Ghattas, A.; Abu-Reziq, R.; Avnir, D.; Blum, J. Exhaustive hydrodechlorination of chlorinated aromatic environmental pollutants to alicyclic compounds. *Green Chemistry* **2003**, *5* (1), 40-43.

CHAPTER 3

HYDROGENATION OF AQUEOUS NITRATE AND NITRITE WITH RUTHENIUM CATALYSTS

A modified version of this chapter was published in *Applied Catalysis B: Environmental*

Xiangchen Huo, Daniel J. Van Hooymissen, Jinyong Liu, Shubham Vyas,

and Timothy J. Strathmann*

3.1 Abstract

Historically, development of catalysts for treatment of nitrate-contaminated water has focused on supported Pd-based catalysts, but high costs of the Pd present a barrier to commercialization. As part of an effort to develop lower cost hydrogenation catalysts for water treatment applications, we investigated catalysts incorporating Ru with lower cost. Pseudo-first-order rate constants and turnover frequencies were determined for carbon- and alumina-supported Ru and demonstrated Ru's high activity for hydrogenation of nitrate at ambient temperature and H₂ pressure. *Ex situ* gas pretreatment of the catalysts was found to enhance nitrate reduction activity by removing catalyst surface contaminants and exposing highly reducible surface Ru oxides. Ru reduces nitrate selectively to ammonium, and no aqueous nitrite intermediate is observed during reactions. In contrast, reactions initiated with nitrite yield a mixture of two endproducts, with selectivity shifting from ammonium towards N₂ at increasing

*Reprinted with permission from Huo, X.; Van Hooymissen, D. J.; Liu, J.; Vyas, S.; Strathmann, T. J. Hydrogenation of aqueous nitrate and nitrite with ruthenium catalysts. *Appl. Catal. B: Environ.* **2017**, *211*, 188-198. Copyright 2017 Elsevier. X.H. performed most of the experiments and analyzed data; D. J. V. H. and S.V. performed the Density Functional Theory calculations; J.L. provided technical support and helpful advice; X.H. and T.J.S. wrote the paper with input from all authors. All authors are affiliated with Colorado School of Mines.

initial aqueous nitrite concentrations. Experimental observation and Density Functional Theory calculations together support a reaction mechanism wherein sequential hydrogenation of nitrate to nitrite and NO is followed by parallel pathways involving the adsorbed NO: (1) sequential hydrogenation to ammonium, and (2) N-N coupling with aqueous nitrite followed by hydrogenation to the detected N₂O intermediate and N₂ endproduct. These findings open the door to development of alternative catalysts for purifying and recovering nutrients from nitrate-contaminated water sources, and insights into the controlling surface reaction mechanisms can guide rational design efforts aimed at increasing activity and tuning endproduct selectivity.

3.2 Introduction

Nitrate contamination of drinking water sources is among the greatest public health threats around the world.¹ Nitrate concentrations exceeding health-based standards are routinely detected in drinking water sources due to excess fertilizer applications and release of incompletely treated industrial and domestic wastewater.²⁻⁴ The growing contamination of drinking water sources raises health concerns because nitrate can be transformed into hazardous chemicals, including nitrite, which causes methemoglobinemia (i.e., blue baby syndrome), and potentially carcinogenic nitrosamines.^{5,6} As a result, there is great interest in the development of efficient, robust and low-cost technologies for treating nitrate-contaminated water.

Several technologies are available to separate nitrate from water, including ion exchange,^{7,8} high pressure membrane filtration,⁹ and electrodialysis,¹⁰ and have demonstrated their effectiveness in full-scale practice.^{2,11} The principal drawback of these systems is the production of a nitrate concentrate stream that requires further treatment before disposal.^{12,13} Biological denitrification is widely used for the treatment of municipal and industrial wastewater, but concerns about pathogen introduction, the need for costly organic carbon amendments and

potential residuals, and biological sludge production have limited application for drinking water treatment.^{14, 15} More recently, chemical reduction of nitrate has been increasingly explored. Zerovalent metals, including iron,¹⁶ aluminum,¹⁷ and magnesium,¹⁸ stoichiometrically couple nitrate reduction with metal corrosion, but reactions are hindered by the formation of oxide surface coatings, and the need to constantly replenish the metals as reducing equivalents are consumed creates operational challenges.

As an alternative to stoichiometric metal reductants, our team and others have been investigating the application of metal hydrogenation catalysts that couple nitrate reduction with H₂ oxidation.^{7, 19-23} Nitrate can be transformed into two endproducts with different H₂ and acidity requirements:



Because the metals are acting as catalysts rather than stoichiometric reactants, they are not consumed in the process or generate a secondary solid waste stream that requires disposal. H₂ is an inexpensive electron donor that has lower life cycle environmental impacts than organic electron donors applied in most biological denitrification processes.²⁴ To date, most work has focused on the development of nitrate and nitrite treatment processes employing supported Pd-based catalysts.^{13, 25, 26} Pd catalysts are highly effective in converting nitrite, the first daughter product of nitrate reduction, to harmless N₂ gas at an incomparable rate,²⁷⁻²⁹ but monometallic Pd catalysts show little reactivity with nitrate.^{30, 31} Deposition of a second “promoter” metal (e.g., Cu, In, Sn) together with Pd is typically required to facilitate reduction of nitrate to nitrite.^{23, 31, 32} A large body of literature has reported on aqueous nitrate reduction with Pd-based bimetallic catalysts,^{20, 30, 31, 33-37} and our current understanding of metal-catalyzed nitrate hydrogenation

mechanisms has been limited to reactions occurring with these materials. The prevailing reaction pathway follows a two-step process depicted in Figure 3.1: (1) hydrogenation of nitrate to nitrite on bimetallic clusters followed by (2) further hydrogenation of nitrite on Pd sites to a mixture of N_2 and ammonium stable endproducts, the net processes being reflected by Eqs. (3.1-3.2).^{22, 35, 38-}

40

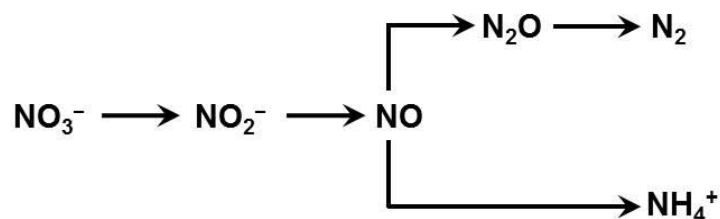


Figure 3.1 Nitrate hydrogenation pathway on Pd-based bimetallic catalysts.

The proposed sequential reduction pathway is supported by the observation of nitrite as a transient reaction intermediate,^{23, 33} increasing with pH as the rate of Pd-catalyzed nitrite reduction decreases,^{39, 41} and isotope labeling experiments showing Pd-catalyzed reduction of NO to the same mixture of endproducts and selective conversion of N_2O to N_2 .²² The distribution of endproducts, presumed to be controlled by the Pd-catalyzed reactions of nitrite or its daughter products (e.g., adsorbed NO), has been reported to vary with catalyst composition,³¹ metal nanoparticle size,⁴² support,⁴³ and solution pH.⁴⁴

Although years of effort have been invested in improving the activity, endproduct selectivity, and long-term stability of Pd-based bimetallic catalysts^{31, 45} (and to a lesser extent Pt-based catalysts,^{36, 46}) deployment of practical catalytic treatment systems remains limited, in large part, due to high costs of Pd.⁴⁷ Precious metal-free catalysts based on Ni have been explored,^{15, 48, 49} but instability in aqueous matrices,⁵⁰ and serious concerns about the associated

leaching of dissolved Ni²⁺⁵¹ and the pyrophoric nature of highly active Raney Ni⁵² have limited further development efforts.

As a result of the low nitrate and nitrite reduction activity reported in early catalyst screening studies,^{27, 28} Ru hydrogenation catalysts have been largely overlooked for such applications. However, a renewed examination of the application of Ru-based catalysts is warranted because of the historically much lower price of Ru in comparison to Pd and Pt⁴⁷ as well as the metal's documented catalytic activity for a diverse range of reactions, including hydrogenation, hydrodeoxygenation and hydrodechlorination reactions.^{53, 54} In addition, work on electrochemical reduction of nitrate (in acidic media) has shown that Ru electrodes exhibit higher activity than Pt, Pd and Ir electrodes.⁵⁵ After recently screening a range of metal catalysts as alternatives to Pd for reduction of oxyanion pollutants,⁵⁶ this contribution focuses on a renewed evaluation of the kinetics and mechanisms of nitrate and nitrite reduction by supported Ru catalysts. Reaction kinetics, product distribution analysis, and catalyst characterization studies are combined with Density Functional Theory (DFT) calculations to improve our understanding of interaction between nitrate (and nitrite) and Ru metal surfaces and elucidate the origin of endproduct selectivity.

3.3 Materials and methods

3.3.1 Catalysts

A full listing of chemical reagents is provided in Section B.1.1 in Appendix B. Ru and Pd catalysts immobilized on carbon and alumina supports (nominal 5 wt% metal) were purchased from Sigma-Aldrich. Unless otherwise noted, the as-received Ru and Pd catalysts were pretreated *ex situ* in flowing H₂ at 350 °C for 2 h prior to use in aqueous oxyanion reduction experiments. The only exception to this was for experiments specifically examining the effects of

different *ex situ* pretreatments (see Section 3.4.2), wherein the as-received catalysts (no pretreatment), catalysts pretreated *ex situ* in flowing N₂ at 350 °C for 2 h, and catalysts pretreated *ex situ* in flowing H₂ as mentioned above were compared. No precautions were taken following pretreatment to avoid surface passivation upon exposure to air. Bimetallic Pd-Cu/C, Ru-Cu/C, and Ru-In/C catalysts were prepared by incipient wetness impregnation⁵⁷ of 1 wt% of Cu (as Cu(NO₃)₂·3H₂O) or In (as In(NO₃)₃·3H₂O) on as-received commercial Pd/C and Ru/C, respectively, followed by air drying at 110 °C for 12 h and H₂ at 350 °C for 2 h.

Catalysts were extensively characterized, including metal content (inductively coupled plasma-optical emission spectrometry, ICP-OES), specific surface area and average pore diameter of the support materials (N₂ physisorption), metal dispersion (the percentage of Ru or Pd atoms present on the clean surface of the immobilized metal nanoparticles, CO chemisorption), active surface (the percentage of Ru or Pd atoms accessible to reactants under simulated *in situ* conditions, CO chemisorption), morphology and size of the metal nanoparticles (transmission electron microscopy and high-angle annular dark-field-scanning transmission electron microscopy, TEM and HAADF-STEM), Ru reducibility (H₂ temperature-programmed reduction, H₂ TPR), and long-range structural order (X-ray diffraction, XRD). Details of each methodology are provided in Section B.1.2 in Appendix B.

3.3.2 Nitrate and nitrite reduction kinetics

Aqueous nitrate and nitrite reduction kinetics were measured in an open semi-batch system under continuous H₂ sparging (1 atm, 40 mL min⁻¹) at constant temperature (25 ± 0.5 °C). A 250 mL three-neck reactor was filled with 150 mL deionized water and predetermined mass of catalyst. The suspension was sonicated for 5 min and sparged with H₂ gas for 30 min before introducing a small volume of NaNO₃ or NaNO₂ stock solution to initiate the reaction. Reaction

progress was monitored by periodic collection of suspension aliquots (1.5 mL) that were immediately filtered (0.22 μm cellulose acetate) to remove catalyst particles and quench reactions prior to analysis by ion chromatography (NO_3^- and NO_2^-) and colorimetric assay (NH_4^+). The suspension was mixed by a Teflon-coated magnetic stir bar at 700 rpm. Solution pH was maintained by HCl addition from an automatic pH-stat (Radiometer TitraLab 854). Catalyst activity was assessed by quantifying initial mass-normalized pseudo-first-order rate constants (k_0 , $\text{L g}_{\text{Ru/Pd}}^{-1} \text{min}^{-1}$) and turnover frequencies (TOF_0 , min^{-1}), defined as the number of nitrate or nitrite ions reduced per active surface site per minute. The active surface was estimated from CO chemisorption measurement using an assumed 1:1 CO: Metal adsorption stoichiometry.^{58, 59} Additional details of the procedures for kinetics parameter calculations and aqueous analytical measurements are provided in Sections B.1.3 and B.1.4 in Appendix B. A catalyst re-use experiment was carried out to evaluate the stability of Ru/C. After a semi-batch reaction was complete, the catalyst solid was collected on a filter (glass fiber filter; EMD Millipore), washed with deionized water several times, and vacuum dried at 65 °C overnight before re-suspending in water for the subsequent semi-batch reaction. The catalyst was also re-characterized after completion of the re-use experiment.

3.3.3 Isotope labeling experiments

Nitrogen mass balances and endproduct distributions were quantified using closed-bottle batch experiments with the aid of ^{15}N -labeled nitrate and nitrite salts to avoid the interference from atmospheric $^{14}\text{N}_2$ during mass spectrometry measurement of the N_2 endproduct.²² A 160 mL serum bottle with 75 mL of an organic buffer, 4-morpholineethanesulfonic acid (MES) (pH 5.5, 40 mM), a predetermined mass of catalyst, and a Teflon-coated magnetic stir bar was sealed by a 1.0 cm-thick rubber stopper held in place by an Al crimp cap. Experiments were conducted

at ambient temperature (21 ± 1 °C) and suspensions were mixed in the same manner as the semi-batch experiments. The reactor was sparged with H₂ for 30 min to saturate the headspace and solution before introducing the target oxyanion pollutant. A H₂-sparged stock solution of Na¹⁵NO₃ or Na¹⁵NO₂ was then added to the reactor to initiate the reaction, and 1.5 mL aqueous aliquots were withdrawn by syringe through the gas-tight septa to monitor disappearance of the parent reactant and the evolution of aqueous intermediates and products. Headspace samples (0.1 mL) were collected separately and immediately analyzed for labeled gaseous intermediates and products (¹⁵NO, ¹⁵N₂O, and ¹⁵N₂) by gas chromatography-mass spectrometry (GC-MS, details in Section B.1.4 in Appendix B). Headspace gases were assumed to be maintained in equilibrium with the aqueous phase at all times,⁶⁰ which was supported by good nitrogen mass balance closure. Analyte values in these experiments are reported in moles of nitrogen because products include both liquid and gas species as well as both mono- and diatomic nitrogen species. The total mass of H₂ initially added to the sealed batch reactor (~3.4 mmol) was in significant excess of the stoichiometric requirement for the complete reduction of the added NO₃⁻ to NH₄⁺ (~0.5 mmol).

3.3.4 Computational methods

DFT calculations of N-containing species associated with Ru metal surfaces were performed with the Gaussian 09 suite of programs.⁶¹ A Ru₁₈ metal cluster structure was used to model Ru catalysts based on the work of Aguilera-Granja *et al.*⁶² and Zhang *et al.*⁶³ It was shown that Ru and Rh clusters with fewer than 20 atoms adopt simple cubic or distorted cubic structure. Geometry optimizations of Ru clusters were completed at the PBE0⁶⁴ level of theory with the Lanl2DZ basis set.^{65, 66} The core electrons of Ru atoms were modeled using the SDD effective core pseudo-potential.^{65, 67} The PBE0 functional was shown to be a reliable method in predicting

both the properties and reactions involved with transition metals and metal clusters⁶⁸, including Ru, with accuracies approaching or exceeding other functionals commonly utilized in solid state systems.⁶⁹

Small molecule (i.e., nitrate, nitrite, and other reacting species) adsorption to the metal clusters were optimized at the PBE0/Lanl2DZ(Ru)/6-31+G(d,p)(H, N, O) level of theory. The geometry optimization of small molecules was performed with the Ru cluster fixed. Thermodynamic barriers were calculated from the bottom of the well energies, as thermodynamic corrections would be an unnecessary addition of error due to the frozen bond constraints given to the metal atom centers. The integral equation formalism polarizable continuum model (IEF-PCM)⁷⁰ was used to implicitly model the aqueous environment and was present in all optimizations and single point energy calculations. To correct for spin contamination for unpaired electron intermediates, single point energies utilizing a restricted open shell (RO) wavefunction were calculated at the ROPBE0/Lanl2DZ(Ru)/6-31+G(d,p)(H, N, O) level of theory. When multiple conformations of adsorbed N-containing species were possible, the complexes with the lowest energy were chosen for the calculation of reaction energies.

3.4 Results and Discussion

3.4.1 Catalytic nitrate reduction

Figure 3.2 shows the catalytic reduction of aqueous nitrate on Ru/C in comparison to monometallic Pd/C and bimetallic Pd-Cu/C. In contrast to an earlier report of limited nitrate reactivity with Ru catalysts,²⁸ these experiments demonstrate that Ru is an effective catalyst, exhibiting much greater activity than monometallic Pd/C of the same mass loading and similar activity to Pd/C after immobilization of 1 wt% Cu as secondary promoter metal. For all three catalysts shown in Figure 3.2, nitrate reduction kinetics follow a pseudo-first-order rate law over

at least the first reaction half-life, and model fits of the data shown yield Ru- and Pd-mass-normalized pseudo-first-order rate constants of $4.13 \pm 0.30 \text{ L g}_{\text{Ru}}^{-1} \text{ min}^{-1}$, $0.46 \pm 0.08 \text{ L g}_{\text{Pd}}^{-1} \text{ min}^{-1}$, and $4.18 \pm 0.01 \text{ L g}_{\text{Pd}}^{-1} \text{ min}^{-1}$ for Ru/C, Pd/C, and Pd-Cu/C catalysts, respectively.

The rate constants are calculated using the metal loading reported in Table 3.1. Control experiments conducted under continuous N_2 sparging (catalyst suspensions sparged with H_2 for 30 min followed by N_2 for another 60 min to displace H_2 before introducing nitrate to the reactor) show negligible loss of nitrate, demonstrating minimal adsorption onto the catalyst supports. Since the catalysts were subjected to the same *in situ* H_2 pre-reduction step before switching to N_2 sparging, this observation also indicates negligible direct reduction of nitrate by the metallic Ru or Pd phases. Initial rates of nitrate reduction vary linearly with catalyst loading between 0 and 0.5 g L^{-1} Ru/C (Figure B.2 in Appendix B), indicating that catalyst suspensions were well mixed and under the studied conditions. The estimated Weisz-Prater parameter (C_{wp})

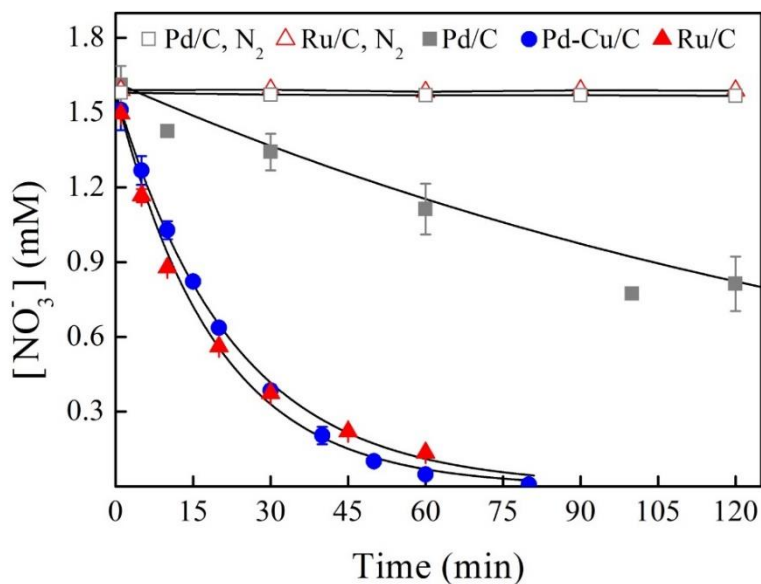


Figure 3.2 Measured reaction timecourses for nitrate reduction and first-order model fits on 5 wt% Ru/C, 5 wt% Pd/C, and 5 wt% Pd-1 wt% Cu/C in the semi-batch reactor system (0.2 g L^{-1} catalyst, $[\text{NO}_3^-]_0 = 1.6 \text{ mM}$, 1 atm H_2 continuous sparging except in control experiments where 1 atm N_2 continuous sparging was used, pH 5.0 maintained by pH stat, $25 \pm 0.5 \text{ }^\circ\text{C}$). Error bars represent standard deviations of triplicate reactions.

(Section B.2.1 in Appendix B) is $\ll 1$, indicating that the internal mass transfer within the porous catalyst support particles is also not rate limiting. Ru/C exhibited good stability in batch re-use experiments, with activity decreasing $<5\%$ after each run (Figure B.3 in Appendix B). Dissolved Ru measured in the supernatant of catalyst suspensions was below 1 ppb, demonstrating negligible leaching of the active metal. Electron microscopy of the catalyst collected following repeated re-use shows no agglomeration or growth of Ru nanoparticles (Figure 3.3a and b). The small drop in activity observed between runs is speculated to be caused by material loss during the filtration recovery protocol used between runs. Immobilization of secondary promoter metals (1 wt% Cu and In) that have been reported to enhance nitrate reduction activity for Pd catalysts did not enhance Ru/C reactions with nitrate (data not shown).

Reductive transformation of nitrate, rather than adsorption or other transformation process, is also confirmed by the good nitrogen mass balance closure (Figure 3.4a) observed using closed-bottle batch experiments with the aid of a ^{15}N -labeled nitrate salt that eliminated potential artifacts from atmospheric contamination during analysis of N_2 . For Ru/C, nitrate is converted selectively to ammonium without producing any detectable $^{15}\text{N}_2$ by GC-MS analysis, and none of the transient aqueous or gaseous intermediates typically observed for Pd-based catalysts (nitrite and N_2O)^{39, 71} are detected.

The effect of solution pH on nitrate reactions with Ru/C was evaluated in the open semi-batch systems using HCl/NaOH to maintain pH (Figure B.4 in Appendix B). Ru-mass-normalized pseudo-first-order rate constants are relatively constant between pH 5-8, but decrease significantly at lower and higher pH conditions. Since gaseous nitrogen species cannot be measured in the open semi-batch reactors sparged continuously with H_2 , a stringent mass balance analysis of endproducts was not feasible. However, ammonium product yields reached $\geq 90\%$ of

Table 3.1 Properties of catalysts used for nitrate activity test.

Catalyst	BET surface area (m ² g ⁻¹)	Total pore volume ^a (cm ³ g ⁻¹)	Average pore diameter ^b (nm)	Metal loading (wt%)	Metal dispersion (%)	Active surface (%)	Chemisorption particle size (nm)	TEM particle size (nm)	TOF ₀ (min ⁻¹) ^c
Ru/C	859.7	0.74	3.46	5.38 ^d	38	32	3.5	2.2 ± 0.8	2.1 ± 0.2
Ru/Al ₂ O ₃	93.1	0.36	15.34	5 ^e	15	9	8.8	8.1 ± 3.0	2.4 ± 0.5
Pd/C	856.9	0.72	3.35	6.24 ^d	17	19	6.5	4.1 ± 2.2	0.42 ± 0.07
Pd/Al ₂ O ₃	98.4	0.24	9.69	5.85 ^d	16	15	6.9	4.2 ± 1.1	NR ^f

^aAdsorption total pore volume at P/P₀ = 0.97. ^bCalculated from total pore volume and BET surface area. ^cCalculated based on active surface. ^dMeasured by ICP-OES analysis. ^eNominal value provided by supplier. ^fNo reaction observed.

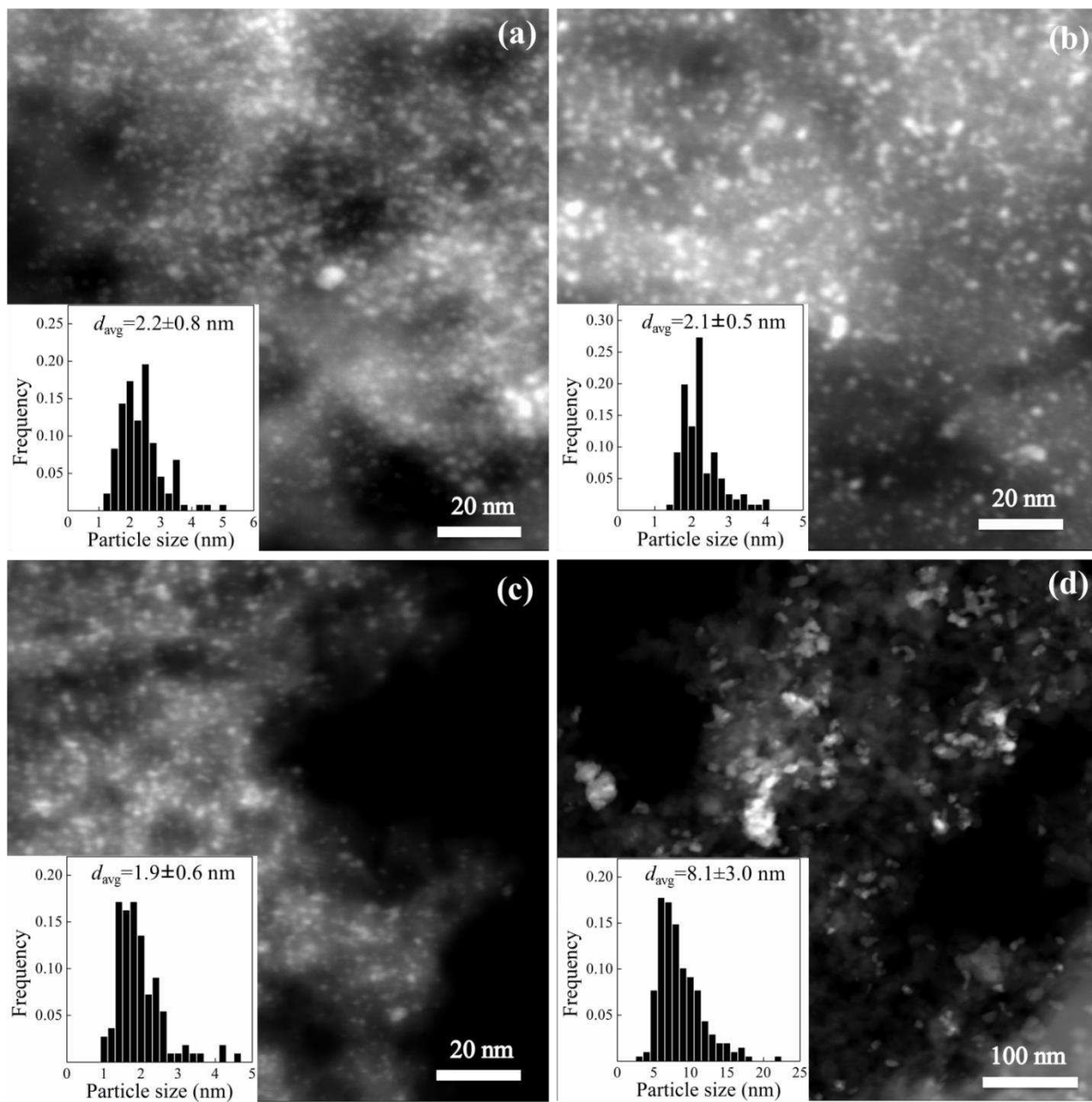


Figure 3.3 HAADF-STEM images of (a) *ex situ* H₂ pretreated Ru/C, (b) Ru/C after re-use experiment, (c) as-received Ru/C and (d) *ex situ* H₂ pretreated Ru/Al₂O₃. The insets show Ru particle size distributions.

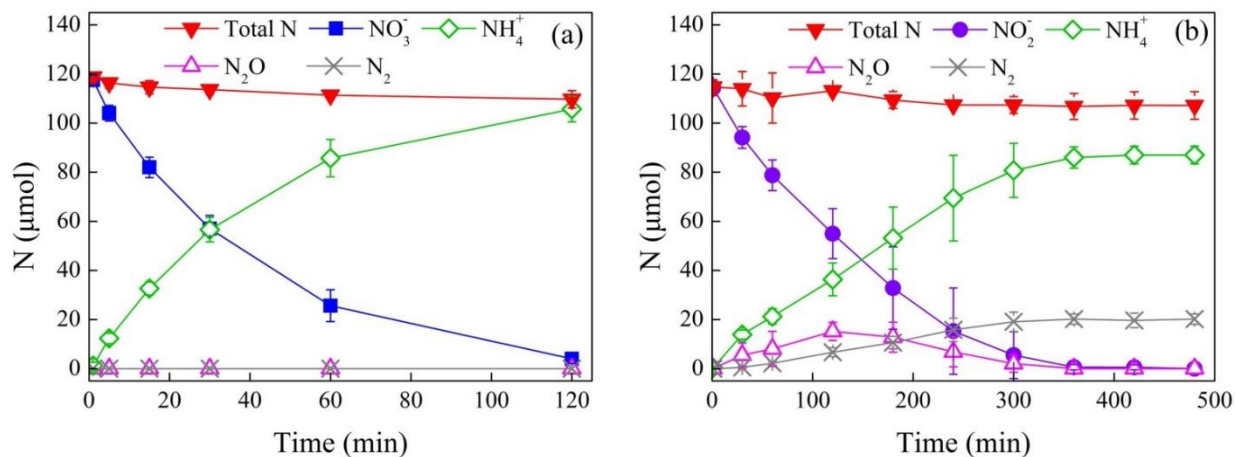


Figure 3.4 Timecourses showing aqueous and gaseous intermediates and products during Ru/C-catalyzed reduction of ^{15}N -labeled (a) nitrate and (b) nitrite monitored in closed-bottle batch systems (0.2 g L^{-1} catalyst, $[^{15}\text{NO}_3^-]_0$ or $[^{15}\text{NO}_2^-]_0 = 1.6 \text{ mM}$, initially 1 atm H_2 , pH 5.5 buffered by 40 mM MES, $21 \pm 1 \text{ }^\circ\text{C}$). Error bars represent standard deviations of triplicate reactions (smaller than symbol if not visible).

the initial nitrate concentrations for all pH conditions, consistent with the high selectivity measured in the closed reactor experiment conducted at pH 5.5 using ^{15}N -labeled species (Figure 3.4a).

Comparison between metal dispersion and active surface in Table 3.1 suggests that 30 min of H_2 treatment at $25 \text{ }^\circ\text{C}$ is sufficient to re-reduce a large fraction of any surface oxides that might form upon air passivation of *ex situ* H_2 pretreated catalysts. Despite the heterogeneity in particle morphology (Figure 3.3 and Figure B.5 in Appendix B) and an assumed 1:1 CO:Metal adsorption stoichiometry for all catalysts irrespective of metal particle size and support, metal dispersion values derived from CO chemisorption analysis⁷² are reasonably consistent with particle sizes observed by electron microscopy (Table 3.1). The rate constants for monometallic catalysts correspond to initial turnover frequencies (TOF_0) of $2.1 \pm 0.2 \text{ min}^{-1}$ for Ru/C and $0.42 \pm 0.07 \text{ min}^{-1}$ for Pd/C based on active metal surface. TOF_0 of nitrate reduction on Ru/C is five times greater than that of Pd/C. The higher reactivity of monometallic Ru/C than Pd/C is especially noteworthy because the Pd/C reactivity observed in Figure 3.2 is actually much

greater than that reported in earlier studies that found either no reaction with nitrate or a very low extent of reaction.^{30, 31, 56, 73-75} Trawczyński *et al.*⁷¹ calculated TOF₀ of nitrate reduction on an in-house prepared Pd/C catalyst to be $\sim 0.03 \text{ min}^{-1}$, which is one order-of-magnitude lower than the TOF₀ calculated from data for Pd/C in Figure 3.2. Considering that deionized water ($\geq 18 \text{ M}\Omega\cdot\text{cm}^{-1}$) was used for all experiments and known promoter metals for Pd catalyst including Cu, In, and Sn were not detected by Energy Dispersive X-ray spectroscopy analysis of Pd/C, we believe that the higher activity of Pd/C observed here is not due to promoter metal contamination from solution or surface residues present following synthesis of catalyst support.

The nature of active sites in Pd-Cu bimetallic catalysts is not well understood or characterized. Although it is technically possible to estimate surface atoms by H₂ chemisorption,^{23, 76} we believe the measurement does not represent bimetallic sites and chose not to calculate the TOF₀ for nitrate reduction on Pd-Cu/C or compare the intrinsic activity between Ru and Pd-Cu bimetallic surface. However, it can be seen from Table B.1 in Appendix B that the Pd-Cu/C catalyst prepared for comparison in this study exhibits activity on a Pd mass-normalized basis that is comparable with other studies that focused in greater depth on the activity and mechanism of such bimetallic catalysts.

3.4.2 Effect of pretreatment on nitrate reduction activity

The high activity of Ru/C with nitrate observed here in comparison with earlier reports warrants further examination. Several studies have documented that the reactivity of supported metal nanoparticles is influenced by nanoparticle size and shape, chemical state, support properties and metal-support interaction, which are subject to the starting materials (support material and metal precursor), synthesis methods and activation steps.^{36, 77} The present study used commercially produced catalysts to take advantage of materials with optimized industrial

production and adapted for large scale applications. However, the high reactivity with aqueous nitrate of Ru catalysts was demonstrated with the catalyst pretreated *ex situ* in flowing H₂ at 350 °C for 2 h prior to use, and the as-received Ru/C and Ru/Al₂O₃ show low or no activity. To further characterize the effects of *ex situ* pretreatment on catalyst activity, we had commercial Ru/C, Ru/Al₂O₃, Pd/C and Pd/Al₂O₃ subjected to *ex situ* heat treatment (350 °C, 2 h) in both inert gas (N₂) and reducing gas (H₂) and tested of their nitrate reduction activity. The metal mass-normalized pseudo-first-order rate constants for nitrate reduction with these materials are calculated and presented in Figure 3.5. *Ex situ* pretreatment of Ru/C, either with flowing H₂ or N₂, leads to more than a threefold increase in catalyst activity compared to the as-received catalyst. The effect of pretreatment is most pronounced for Ru/Al₂O₃, in that the catalyst is only active after pretreatment in flowing H₂. In comparison, pretreatment has no effect on the activity of Pd/C. Pd/Al₂O₃ exhibited no activity for nitrate reduction irrespective of catalyst pretreatment.

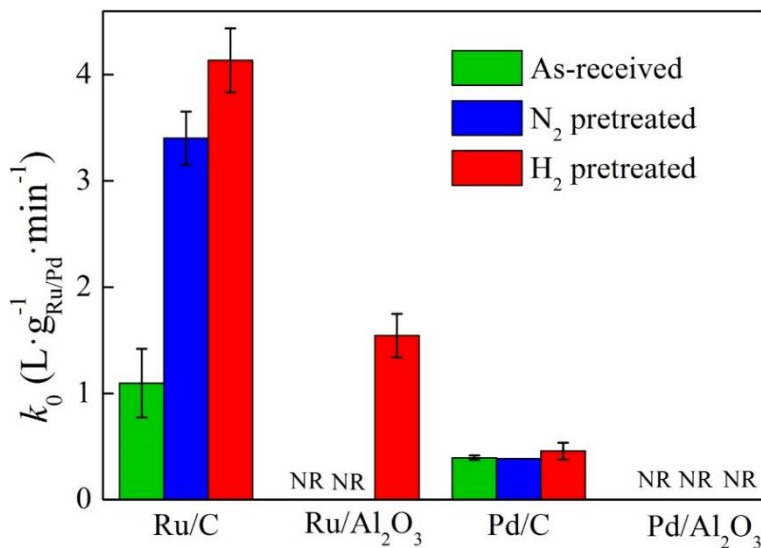


Figure 3.5 Influence of catalyst pretreatments (as-received catalyst or *ex situ* pretreated in flowing H₂ or N₂ at 350 °C for 2 h) on reactivity with aqueous nitrate (0.2 g L⁻¹ catalyst with nominal 5 wt% Ru or Pd, [NO₃⁻]₀ = 1.6 mM, 1 atm H₂ continuous sparging, pH 5.0 maintained by automatic pH stat, 25 ± 0.5 °C). Error bars represent standard deviations of triplicate measurements (smaller than symbol if not visible). NR = no reaction observed.

A battery of characterization analyses was conducted to rationalize the dramatic influence of *ex situ* pretreatment on Ru catalysts. XRD scan of Ru/C (Figure 3.6a) shows mainly peaks associated with crystalline carbon phases, but no significant peaks for Ru metal (ca. 44° and 38°, JCPDS card No. 06-0663) or RuO₂ (ca. 28°, 35° and 54°, JCPDS card No. 43-1027), indicating small crystal size below XRD detection limit. The XRD pattern for Ru/Al₂O₃ (Figure 3.6b) shows crystalline RuO₂ in both the as-received and *ex situ* N₂ pretreated materials, but these features disappear and new features characteristic of crystalline Ru metal appear in the H₂ pretreated Ru/Al₂O₃. For both Ru/C and Ru/Al₂O₃ catalysts, the catalyst activity (Figure 3.5) roughly correlates with the active Ru surface of catalysts (Table B.2 in Appendix B), suggesting that catalyst pretreatment increased the Ru surface area active for catalytic reaction.

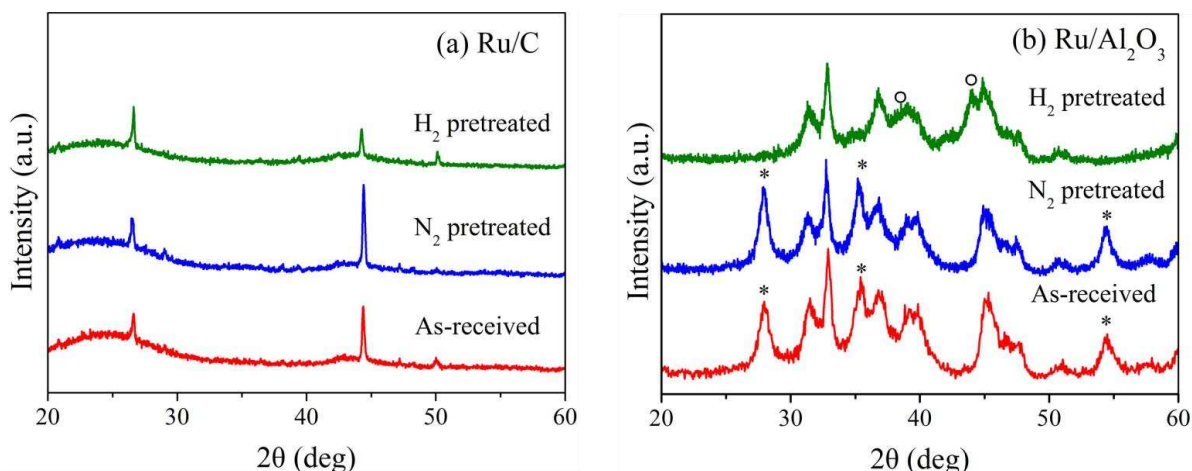


Figure 3.6 XRD patterns of (a) Ru/C and (b) Ru/Al₂O₃ collected after different *ex situ* pretreatments. Peaks assigned to Ru metal (○) and RuO₂ (*) are indicated.

Increasing surface area often results from decreased particle size, which is not the case for Ru/C in this study. The size distribution of Ru particles in the as-received Ru/C (1.9 ± 0.6 nm, Figure 3.3c) is not statistically different from that measured following the *ex situ* H₂ pretreatment process (2.2 ± 0.8 nm, Figure 3.3a). Another possibility is that the Ru catalyst surface in the as-received Ru/C is blocked by residues from synthesis, which may be partially or fully removed by

the high temperature pretreatment processes. H₂ TPR analysis provides evidence to support this hypothesis. The TPR profiles (Figure 3.7) of *ex situ* H₂- and N₂-pretreated Ru/C are similar, with a first reduction peak located between 50 and 55 °C and a second broad reduction peak above 400 °C. The reduction peak temperature of supported Ru oxides formed during catalyst calcination has been reported to vary between 65 °C and 185 °C.^{78, 79} Though the temperature of the first reduction peak observed here falls below this range, the H₂ consumption quantified from the peak area (Table B.2 in Appendix B) is consistent with the theoretical stoichiometry for H₂ consumption during RuO₂ reduction⁷⁸:



The Ru oxides formed upon re-oxidation of pretreated Ru upon exposure to ambient air are redox-labile, enabling re-reduction by H₂ at 25 °C. The second reduction peak is assigned to the direct reduction of aldehyde, quinone and phenol groups on the carbon support.⁸⁰ The TPR profile for as-received Ru/C is markedly different from those of *ex situ* pretreated Ru/C. A much larger H₂ consumption and a dip in the TCD signal match the features of surface species decomposition and desorption, supporting the hypothesis that the as-received catalyst surface is blocked by residues that desorb upon heat pretreatment. Temperature-programmed desorption study of as-received Ru/C and *ex situ* H₂ pretreated Ru/C in Ar provides further confirmation of surface species desorption at 47 °C for as-received Ru/C (Figure B.6 in Appendix B). Therefore, as-received Ru/C consists of highly reducible Ru oxides that are covered by surface contaminants. The *ex situ* pretreatment of Ru/C increased catalyst activity mainly by removing these surface contaminants while causing minimal effect on Ru oxides particles.

The as-received Ru/Al₂O₃ and *ex situ* N₂ pretreated Ru/Al₂O₃ exhibit a TPR pattern consistent with RuO₂ reduction reported in the literature, which is also in agreement with the

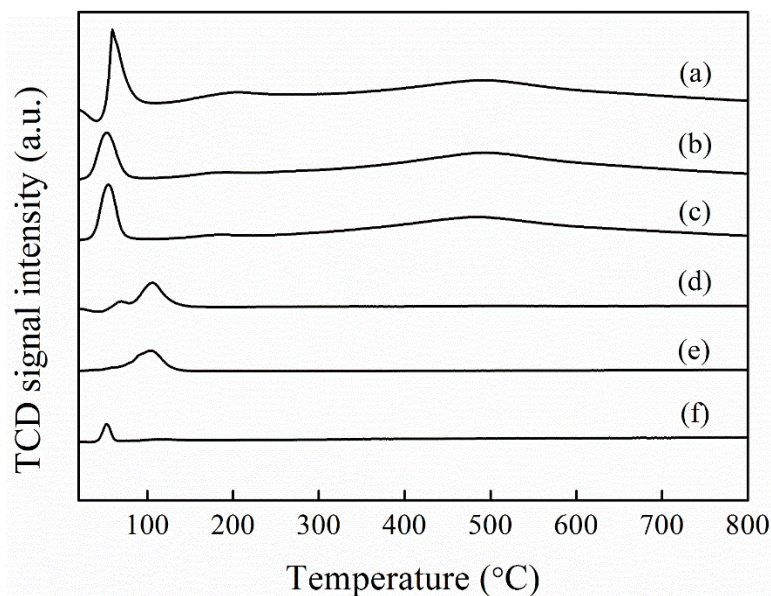


Figure 3.7 TPR profiles of (a) as-received Ru/C, (b) *ex situ* N₂ pretreated Ru/C, (c) *ex situ* H₂ pretreated Ru/C, (d) as-received Ru/Al₂O₃, (e) *ex situ* N₂ pretreated Ru/Al₂O₃, and (f) *ex situ* H₂ pretreated Ru/Al₂O₃. TCD signals are normalized with sample mass.

crystalline RuO₂ identified by XRD analysis. Although the stoichiometry for H₂ consumption of RuO₂ in these two Ru/Al₂O₃ catalysts is similar to that of RuO₂ in *ex situ* H₂- and N₂-pretreated Ru/C (Table B.2 in Appendix B), the Ru oxides on the two supports show significant differences in reducibility as evidenced by the much lower reduction peak temperature of Ru/C catalysts. Besides, the surface of RuO₂ in *ex situ* H₂- and N₂-pretreated Ru/C is easily reduced by H₂ at 25 °C, while the surface of RuO₂ in as-received Ru/Al₂O₃ and *ex situ* N₂ pretreated Ru/Al₂O₃ is not reducible with H₂ at 25 °C (Table B.2 in Appendix B). In contrast, *ex situ* H₂ pretreated Ru/Al₂O₃ shows a small H₂ consumption peak at 45 °C, similar to the highly reducible RuO₂ in *ex situ* H₂- and N₂-pretreated Ru/C and consistent with crystalline metallic Ru in *ex situ* H₂ pretreated Ru/Al₂O₃ identified by XRD analysis. Based on these observations, it can be concluded that *ex situ* H₂ pretreatment activates Ru/Al₂O₃ by reducing the crystalline RuO₂ to a metallic Ru phase, whose surface is re-oxidized upon exposure to ambient temperature air to a more redox-labile form of RuO₂ (e.g., less crystalline) that can be re-reduced by H₂ at 25 °C. A

complete re-oxidation of pretreated Ru/C compared with partial re-oxidation of H₂ pretreated Ru/Al₂O₃ is attributed to a much smaller size of Ru nanoparticles in Ru/C than in Ru/Al₂O₃. The *ex situ* N₂ pretreatment fails to activate Ru/Al₂O₃ due to the inability of N₂ to transform crystalline RuO₂ to redox-labile species. Therefore, it is further confirmed that redox-labile surface Ru oxides are essential to achieve good performance in catalytic nitrate reduction applications.

3.4.3 Catalytic nitrite reduction

Based on the prevailing mechanism for nitrate reduction with Pd-based catalysts, the first reduction intermediate is anticipated to be nitrite,^{32, 81, 82} and the fact that no nitrite intermediate is observed when monitoring nitrate reactions (Figure 3.4a) would suggest nitrite reduction is much faster than nitrate reduction at comparable conditions (similar to observations reported for Pd catalysts under most conditions^{31, 73, 83}). Compared to nitrate, reduction of nitrite is less well described by a pseudo-first-order rate law, with the reaction appearing to accelerate as nitrite concentration continues to drop after the first two half-lives (Figure 3.8a). Nevertheless, the pseudo-first-order rate constants for nitrite reduction over the first two half-lives was calculated to provide a rough measure of catalyst activity to compare with that measured for nitrate reduction under similar conditions. Surprisingly, the observed reaction kinetics for nitrite are markedly slower than for nitrate under the same conditions. The mass-normalized pseudo-first-order rate constant for nitrite reduction derived from the model fit of data in Figure 3.8a is $1.44 \pm 0.15 \text{ L g}_{\text{Ru}}^{-1} \text{ min}^{-1}$, corresponding to an TOF₀ of $0.73 \pm 0.06 \text{ min}^{-1}$. This value is about one third of the TOF₀ for nitrate measured under the same conditions ($2.1 \pm 0.2 \text{ min}^{-1}$). The lower activity of nitrite in comparison to nitrate contrasts with typical results reported for Pd-based bimetallic

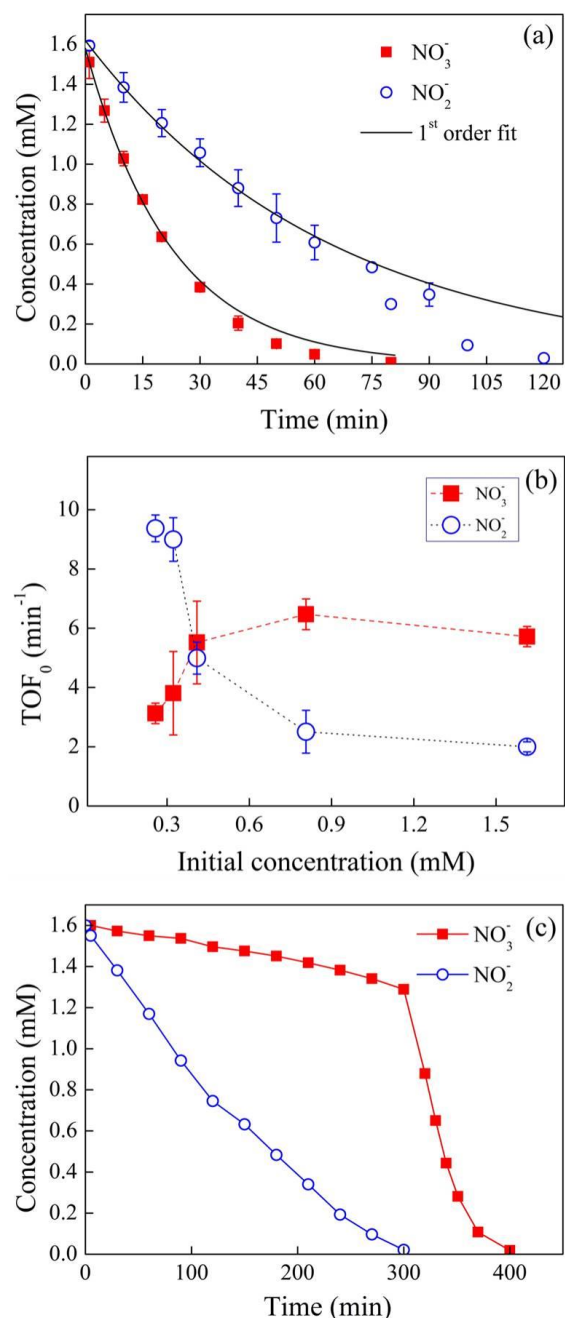


Figure 3.8 (a) Comparison of Ru/C-catalyzed nitrite reaction kinetics with nitrate reaction at standard conditions (0.2 g L^{-1} Ru/C, $[\text{NO}_3^-]_0$ or $[\text{NO}_2^-]_0 = 1.6 \text{ mM}$). (b) TOF₀ of Ru/C-catalyzed nitrate and nitrite reduction as a function of initial concentration of the target oxyanion (0.2 g L^{-1} Ru/C). (c) Measured timecourses for the simultaneous reduction of nitrate and nitrite added to a suspension containing Ru/C (0.2 g L^{-1} catalyst, $[\text{NO}_3^-]_0 = [\text{NO}_2^-]_0 = 1.6 \text{ mM}$). Other conditions include 1 atm H_2 continuous sparging, pH 5.0 maintained by automatic pH stat, and $25 \pm 0.5 \text{ }^\circ\text{C}$. Error bars in panels a-b represent standard deviations of triplicate measurements.

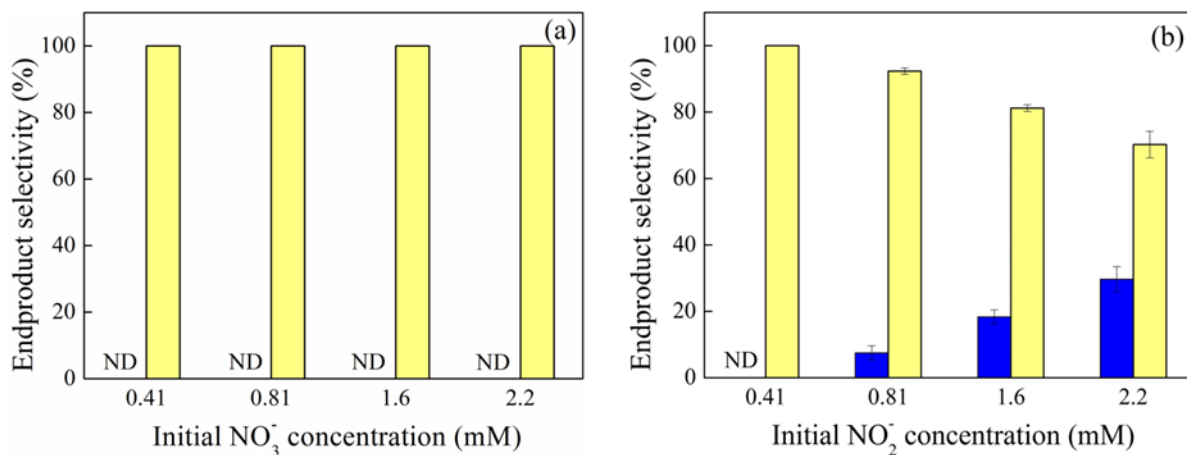


Figure 3.9 Effect of initial (a) nitrate and (b) nitrite concentration on NH_4^+/N_2 product selectivity (yellow: NH_4^+ ; blue: N_2). Product selectivity is based on percent molar N concentration. Error bars represent standard deviations of triplicate measurements (smaller than symbol if not visible).

catalysts, where nitrite is much more reactive than the parent nitrate ion.^{39, 73} Nitrite reaction with Pd/C at the same conditions shown in Figure 3.8a yields a TOF_0 of $57.7 \pm 9.2 \text{ min}^{-1}$.

The isotope labeling mass balance closure experiment conducted with nitrite as a starting reactant (Figure 3.4b) further reveals a distinct behavior of Ru-catalyzed nitrite reduction. In contrast to the experiment initiated with nitrate, nitrite reduction yields a mixture of N_2 and ammonium endproducts, and N_2O is observed as a reaction intermediate. Whereas the sole product of nitrate reduction detected is ammonium irrespective of initial nitrate concentration (Figure 3.9a), the distribution of N_2 :ammonium observed in nitrite reduction experiments shifts increasingly towards N_2 with increasing initial nitrite concentration (Figure 3.9b).

3.4.4 Site-limited reduction kinetics

As mentioned earlier, measured nitrite concentrations drop below pseudo-first-order kinetic model predictions as the reaction progresses and nitrite concentration decreases (Figure 3.8a). To examine this further, TOF_0 of nitrate and nitrite reduction were determined at varying initial concentration of each oxyanion. Results of these measurements (Figure 3.8b) reveal

contrasting behavior for nitrate and nitrite. For nitrate, the observed trend is consistent with the classical Langmuir-Hinshelwood model for heterogeneous reactions, where TOF_0 increases with increasing initial nitrate concentration until it approaches a maximum value due to saturation of available surface reaction sites.⁸⁴ Similar behavior has been documented for many heterogeneous catalytic reactions, including nitrate, nitrite, and bromate reactions with Pd-based catalyst.^{33, 85, 86} The small drop in TOF_0 observed at the highest initial nitrate concentration tested may result from competitive adsorption between nitrate and H_2 on the same reaction sites.⁸⁷ A contrasting and atypical behavior is observed for nitrite, where TOF_0 values are greatest at the lowest initial nitrite concentration and decrease to minimum value with increasing nitrite concentration. To rationalize this trend within the framework of a Langmuir-Hinshelwood model requires an assumption that nitrite competes directly with H_2 for the same reaction sites and the former has a much higher affinity for the sites than the latter, thereby inhibiting uptake and dissociation of the required H_2 reductant at higher nitrite concentrations. An important implication of this finding is that the relative reactivities observed for nitrate versus nitrite (e.g., Figure 3.8a) are heavily dependent upon the initial oxyanion concentrations used in the reactions. The heightened reactivity of nitrite at low nitrite concentrations can also potentially explain why the species is not observed as a reaction intermediate during Ru catalyst reactions initiated with nitrate; when nitrite is formed at low concentrations on the catalyst surface, its rapid turnover under these conditions prevents detection in the overlying aqueous solution. The competition between nitrite and H_2 adsorption may also contribute to the observed shift in endproduct selectivity towards ammonium at lower initial nitrite concentration (Figure 3.9b); conversion of nitrite to ammonium has a relatively higher stoichiometric requirement for H_2 than reduction to N_2 , so an increase in H_2 :nitrite ratio could favor the pathway for ammonium production by increasing surface

coverage of hydrogen and decreasing surface coverage of nitrogen species. The decreasing nitrite concentration is also expected to reduce the rate of N-N pairing reactions necessary to N₂O and N₂. Detailed pathways will be discussed in the following section.

Since separate reactions conducted with nitrate and nitrite suggest that the oxyanions both compete with H₂ for chemisorption at Ru active sites, competitive reactions between the two oxyanions were further examined by reaction initiated with mixtures of nitrate and nitrite. Figure 3.8c shows the reaction of an equimolar mixture of nitrate and nitrite at the same conditions as the individual oxyanion reactions shown in Figure 3.8a. Interestingly, despite the fact that nitrite reacts slower than nitrate when the two oxyanions are reacted with Ru/C separately, the presence of nitrite severely inhibits nitrate reduction. Nitrate reduction kinetics proceeds in two phases. A severely inhibited reduction phase is observed while nitrite is present, but the reaction accelerates once the nitrite is fully depleted. Variation of the ratio of initial nitrate and nitrite confirmed competition between the two oxyanions for available catalysts reaction sites, since the initial rate of nitrate reduction in the first phase increases with increasing nitrate/nitrite ratio, which is the same case for nitrite reduction measured in the presence of nitrate (Table B.3 in Appendix B).

3.4.5 Proposed reaction pathway

Ru catalysts behave differently from Pd-based catalysts in nitrate reduction product selectivity. For example, Ru catalysts favor complete selectivity for ammonium (Figure 3.4a), in contrast with a mixture of ammonium and N₂ endproducts reported for Pd-based bimetallic catalysts.^{23, 31} Consistently high (and possibly complete) selectivity for ammonium was observed for Ru catalysts under various solution pH, whereas the ratio between ammonium and N₂ varies with shifting pH conditions for Pd-based bimetallic catalysts.^{31, 41, 88} On the other hand, Ru

catalysts and Pd-based catalysts share similarity in nitrite reduction product selectivity. For Ru/C, the distribution of N_2 :ammonium shifts increasingly towards N_2 with increasing initial nitrite concentration (Figure 3.9b), similar to trends reported for Pd-based catalysts.⁸⁹ Figure 3.1 depicts the generally accepted mechanism of nitrate reduction on Pd-based catalysts. The experimental observations of nitrite reduction with Ru catalysts appear to be consistent with the reaction pathways proposed for Pd-based catalysts. Reactions initiated with nitrite yield transient intermediates and endproducts consistent with the two parallel pathways for NO reduction (Figure 3.4b). It may not be straightforward to apply the scheme to nitrate reduction with Ru catalysts considering the differences mentioned above and that reactions initiated with nitrate show no detectable nitrite intermediate (Figure 3.4a). However, the lack of observed nitrite intermediate is consistent with the elevated turnover rate of this species observed at low initial concentrations (Figure 3.8b) and selective reactivity of nitrite in the presence of nitrate (Figure 3.8c). Along this line, the complete selectivity for ammonium is possibly a result of high selectivity to ammonium at low nitrite concentration (Figure 3.9b).

It should be pointed out that Figure 3.1 only provides a macroscopic picture for the reaction. When considering the reaction from the microscopic viewpoint, the mechanism involves much more diverse intermediates that are adsorbed on the surface or in the aqueous phase. To obtain molecular insights into the mechanism of the reaction over Ru, DFT calculations were conducted to evaluate the thermodynamics of adsorption and transformation steps. Adsorption energies and conformations of major reactants, hypothesized intermediates and products are provided in Table B.4 in Appendix B. The elementary steps underlying the reaction pathways in Figure 3.1 are illustrated in Figure 3.10, and the energetics of each step are listed in Table B5 in Appendix B. The strong adsorption of NO_2^- (-1.3 eV) and NO (-2.0 eV) from water

to the Ru cluster surface may be contributing to the fact that desorbed aqueous species of the latter two were never observed during reactions initiated with nitrate. The further sequential reduction of NO_{ads} to $\text{NH}_{3,ads}$ occurs through a series of exothermic reaction steps. Previous observations of the complete selectivity for ammonium in reactions initiated with nitrate (Figure 3.9a) and the shift in endproduct selectivity towards N_2 for nitrite reactions conducted with higher initial aqueous concentrations (Figure 3.9b) indicate that buildup of aqueous nitrite concentrations is a prerequisite for the reaction pathway leading to diatomic nitrogen species. We found that initiating N-N coupling by reaction of the NO_{ads} intermediate with aqueous nitrite is exothermic, and subsequent reduction of the resulting intermediate to form both the detectable N_2O intermediate and stable N_2 endproduct are also favorable. Some have proposed that NO_{ads}

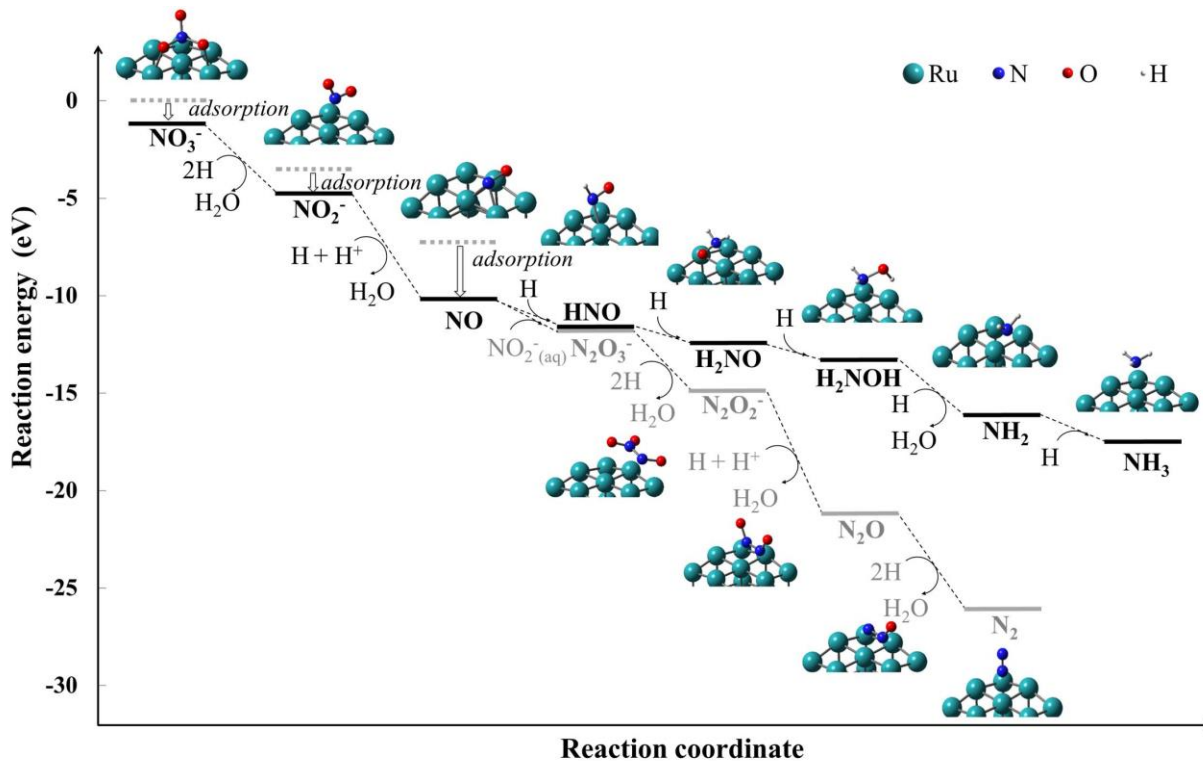


Figure 3.10 Energy profile of the most thermodynamically favorable reaction pathways for aqueous nitrate and nitrite reduction on Ru18 clusters as calculated using PBE0 functional and LANL2DZ (Ru)/6-31+G(d,p)(N, H, O) basis sets.

dissociates first to N_{ads} and O_{ads} on catalyst metal surfaces before reacting further to form the observed products.^{30, 89} DFT calculations indicate that this route cannot be ruled out based on energetics, but coupling between N_{ads} and NO_{ads} is unfavorable. The findings from DFT calculations that both reaction pathways are thermodynamically favorable implies that the kinetic factors, rather than thermodynamic constraints, are likely responsible for controlling the reaction product selectivity. Computing activation barriers and establishing microkinetic models will be needed to provide further insights into the reaction rates and endproduct selectivities observed in experiments.

3.4.6 Implications for technology development

The results of this study demonstrate that Ru catalysts effectively reduce nitrate at ambient temperature and H_2 pressure. Ru possesses many of the benefits of other Pt group metal catalysts (e.g., high stability) but is less expensive than Pd and Pt, showing potential to reduce barriers to catalyst technology adoption for treatment of recalcitrant water contaminants. The reductant (H_2) is low cost, can be generated on-site electrochemically, and has lower life-cycle environmental impacts than organic electron donors typically used in biological denitrification processes.²⁴ The catalysts used in the study are a commercially available material from a vendor capable to high volume production, making the process accessible to near-term commercial applications. The sole endproduct from nitrate reduction by the supported Ru catalysts investigated was ammonium, indicating that Ru catalysts are not suitable for treating drinking water with dilute nitrate in a single process. On the other hand, highly selective conversion of nitrate to ammonium, especially in concentrate matrices like waste ion exchange regenerant brines,⁹⁰ if followed by separation unit processes (e.g., membrane electrolysis⁹¹), may be a promising strategy for sustainably recovering an economically valuable product (e.g.,

(NH₄)₂SO₄), which is in line with a growing interest in resource recovery from waste streams.⁹² A number of technology development challenges remain to demonstrate viability, safety, and to de-risk the technology, but findings in this study suggest a path forward for development of an economical and sustainable technology for treatment and resource recovery from nitrate-contaminated water sources.

Rational design that emphasizes “design-for-purpose” is important to advance next-generation water treatment technologies.⁹³ Pt group metals are known to activate H₂. In order to couple H₂ oxidation with nitrate reduction, the activity of nitrate activation on Ru and the steps controlling selectivity need to be understood and is the objective of this study. Examination of the reaction mechanism revealed that selectivity for N₂ endproduct is limited during nitrate reduction with the Ru catalyst formulations examined here because N-N coupling requires significant aqueous nitrite concentrations to buildup and pairing between adsorbed N species is negligible. This suggests a target for future Ru catalyst design: tailor active sites for selective adsorption with nitrate over nitrite and/or reducing barriers to mobility and pairing of adsorbed N species. Surface alloying may be used to alter small molecule binding strength and rates of surface species diffusion.^{94,95} Alternatively, bio-inspired catalyst structures that attempt to mimic the multi-component features and activated metalloenzyme centers of biological systems may offer a promising strategy for enhancing catalyst activity. For example, Liu and co-workers recently demonstrated >100-fold improvement in catalytic reduction of the recalcitrant oxyanion perchlorate by modifying the Re component within Pd-Re/C bimetallic catalysts by complexing with oxazoline ligands that enhance the metal’s oxygen atom transfer (OAT) reactivity,⁹⁶ mimicking the design of Mo-centered OAT metal complexes in the perchlorate reductase enzyme. Inspired by the heme-containing active sites of nitrate and (per)chlorate reductase, Ford

and co-workers constructed a non-heme iron complex for catalytic nitrate and perchlorate reduction, and the homogeneous catalyst is regenerated by electrons and protons provided by 1,2-diphenylhydrazine.⁹⁷ Biomimetic catalysts incorporating Ru as the active metal center for nitrate or nitrite reduction have not been reported to date.

3.5 Conclusions

Supported Ru nanoparticles showed promising catalytic performance in reducing nitrate in water at ambient temperature and H₂ pressure. It is demonstrated that Ru has a high intrinsic activity in nitrate activation, which is five times higher than that of Pd under standard testing conditions. The key features for supported Ru catalysts that need to be controlled to achieve high activity are that reduced Ru surface can be obtained by H₂ reduction at reaction temperature and that the surface is not blocked by synthesis residues. Ru reduces nitrate selectively to ammonium, while nitrite is reduced to yield a mixture of N₂ and ammonium, with selectivity shifting towards N₂ at increasing nitrite:hydrogen ratio. The reaction mechanism is proposed that sequential hydrogenation of nitrate to nitrite and NO is followed by parallel pathways involving the adsorbed NO: (1) sequential hydrogenation to ammonium, and (2) N-N coupling with aqueous nitrite followed by hydrogenation to the detected N₂O intermediate and N₂ endproduct. Future work is needed to strategically design catalyst to control selectivity and develop integrated processes for nitrogen recovery.

3.6 References

1. Spalding, R. F.; Exner, M. E. Occurrence of nitrate in groundwater - A review. *J. Environ. Qual.* **1993**, 22 (3), 392-402.
2. Kapoor, A.; Viraraghavan, T. Nitrate removal from drinking water - Review. *J. Environ. Eng.-ASCE* **1997**, 123 (4), 371-380.

3. Puckett, L. J. Identifying the major sources of nutrient water pollution. *Environ. Sci. Technol.* **1995**, 29 (9), 408A-414A.
4. Pintar, A. Catalytic processes for the purification of drinking water and industrial effluents. *Catal. Today* **2003**, 77 (4), 451-465.
5. Weyer, P. J.; Cerhan, J. R.; Kross, B. C.; Hallberg, G. R.; Kantamneni, J.; Breuer, G.; Jones, M. P.; Zheng, W.; Lynch, C. F. Municipal drinking water nitrate level and cancer risk in older women: the Iowa Women's Health Study. *Epidemiology* **2001**, 12 (3), 327-38.
6. Gulis, G.; Czompolyova, M.; Cerhan, J. R. An ecologic study of nitrate in municipal drinking water and cancer incidence in Trnava District, Slovakia. *Environ. Res.* **2002**, 88 (3), 182-187.
7. Choe, J. K.; Bergquist, A. M.; Jeong, S.; Guest, J. S.; Werth, C. J.; Strathmann, T. J. Performance and life cycle environmental benefits of recycling spent ion exchange brines by catalytic treatment of nitrate. *Water Res.* **2015**, 80 (0), 267-280.
8. Samatya, S.; Kabay, N.; Yuksel, U.; Arda, M.; Yuksel, M. Removal of nitrate from aqueous solution by nitrate selective ion exchange resins. *React. Funct. Polym.* **2006**, 66 (11), 1206-1214.
9. Bohdziewicz, J.; Bodzek, M.; Wasik, E. The application of reverse osmosis and nanofiltration to the removal of nitrates from groundwater. *Desalination* **1999**, 121 (2), 139-147.
10. El Midaoui, A.; Elhannouni, F.; Taky, M.; Chay, L.; Sahli, M. A. M.; Echihabi, L.; Hafsi, M. Optimization of nitrate removal operation from ground water by electrodialysis. *Sep. Purif. Technol.* **2002**, 29 (3), 235-244.
11. Hell, F.; Lahnsteiner, J.; Frischherz, H.; Baumgartner, G. Experience with full-scale electrodialysis for nitrate and hardness removal. *Desalination* **1998**, 117 (1-3), 173-180.
12. Bae, B.-U.; Jung, Y.-H.; Han, W.-W.; Shin, H.-S. Improved brine recycling during nitrate removal using ion exchange. *Water Res.* **2002**, 36 (13), 3330-3340.
13. Barrabés, N.; Sá, J. Catalytic nitrate removal from water, past, present and future perspectives. *Appl. Catal., B* **2011**, 104 (1-2), 1-5.
14. Shrimali, M.; Singh, K. P. New methods of nitrate removal from water. *Environ. Pollut.* **2001**, 112 (3), 351-359.
15. Mikami, I.; Yoshinaga, Y.; Okuhara, T. Rapid removal of nitrate in water by hydrogenation to ammonia with Zr-modified porous Ni catalysts. *Applied Catalysis B: Environmental* **2004**, 49 (3), 173-179.
16. Huang, C.-P.; Wang, H.-W.; Chiu, P.-C. Nitrate reduction by metallic iron. *Water Res.* **1998**, 32 (8), 2257-2264.
17. Murphy, A. P. Chemical removal of nitrate from water. *Nature* **1991**, 350 (6315), 223-225.

18. Kumar, M.; Chakraborty, S. Chemical denitrification of water by zero-valent magnesium powder. *J. Hazard. Mater.* **2006**, *135* (1–3), 112-121.
19. Gauthard, F.; Epron, F.; Barbier, J. Palladium and platinum-based catalysts in the catalytic reduction of nitrate in water: effect of copper, silver, or gold addition. *J. Catal.* **2003**, *220* (1), 182-191.
20. Chaplin, B. P.; Roundy, E.; Guy, K. A.; Shapley, J. R.; Werth, C. J. Effects of natural water ions and humic acid on catalytic nitrate reduction kinetics using an alumina supported Pd–Cu catalyst. *Environ. Sci. Technol.* **2006**, *40* (9), 3075-3081.
21. Dodouche, I.; Barbosa, D. P.; Rangel, M. d. C.; Epron, F. Palladium–tin catalysts on conducting polymers for nitrate removal. *Appl. Catal., B* **2009**, *93* (1–2), 50-55.
22. Zhang, R.; Shuai, D. M.; Guy, K. A.; Shapley, J. R.; Strathmann, T. J.; Werth, C. J. Elucidation of nitrate reduction mechanisms on a Pd-In bimetallic catalyst using isotope labeled nitrogen species. *ChemCatChem* **2013**, *5* (1), 313-321.
23. Jung, S.; Bae, S.; Lee, W. Development of Pd–Cu/hematite catalyst for selective nitrate reduction. *Environ. Sci. Technol.* **2014**, *48* (16), 9651-9658.
24. Choe, J. K.; Mehnert, M. H.; Guest, J. S.; Strathmann, T. J.; Werth, C. J. Comparative assessment of the environmental sustainability of existing and emerging perchlorate treatment technologies for drinking water. *Environ. Sci. Technol.* **2013**, *47* (9), 4644-4652.
25. Prüsse, U.; Vorlop, K.-D. Supported bimetallic palladium catalysts for water-phase nitrate reduction. *J. Mol. Catal. A: Chem.* **2001**, *173* (1–2), 313-328.
26. Jung, J.; Bae, S.; Lee, W. Nitrate reduction by maghemite supported Cu-Pd bimetallic catalyst. *Appl. Catal., B* **2012**, *127*, 148-158.
27. Hörold, S.; Tacke, T.; Vorlop, K. D. Catalytical removal of nitrate and nitrite from drinking water: 1. Screening for hydrogenation catalysts and influence of reaction conditions on activity and selectivity. *Environ. Technol.* **1993**, *14* (10), 931-939.
28. Soares, O.; Orfao, J. J. M.; Pereira, M. F. R. Activated Carbon Supported Metal Catalysts for Nitrate and Nitrite Reduction in Water. *Catal. Lett.* **2008**, *126* (3-4), 253-260.
29. Shuai, D.; Choe, J. K.; Shapley, J. R.; Werth, C. J. Enhanced Activity and Selectivity of Carbon Nanofiber Supported Pd Catalysts for Nitrite Reduction. *Environ. Sci. Technol.* **2012**, *46* (5), 2847-2855.
30. Ilinitch, O. M.; Nosova, L. V.; Gorodetskii, V. V.; Ivanov, V. P.; Trukhan, S. N.; Gribov, E. N.; Bogdanov, S. V.; Cuperus, F. P. Catalytic reduction of nitrate and nitrite ions by hydrogen: investigation of the reaction mechanism over Pd and Pd–Cu catalysts. *J. Mol. Catal. A: Chem.* **2000**, *158* (1), 237-249.

31. Yoshinaga, Y.; Akita, T.; Mikami, I.; Okuhara, T. Hydrogenation of Nitrate in Water to Nitrogen over Pd–Cu Supported on Active Carbon. *J. Catal.* **2002**, *207* (1), 37-45.
32. Prüsse, U.; Hähnlein, M.; Daum, J.; Vorlop, K.-D. Improving the catalytic nitrate reduction. *Catal. Today* **2000**, *55* (1–2), 79-90.
33. Pintar, A.; Batista, J.; Levec, J.; Kajiuchi, T. Kinetics of the catalytic liquid-phase hydrogenation of aqueous nitrate solutions. *Appl. Catal., B* **1996**, *11* (1), 81-98.
34. Pintar, A.; Batista, J.; Arčon, I.; Kodre, A. Characterization of γ -Al₂O₃ supported Pd-Cu bimetallic catalysts by EXAFS, AES and kinetic measurements. In *Stud. Surf. Sci. Catal.*; B. Delmon; P.A. Jacobs; R. Maggi; J.A. Martens; Grange, P.; Poncelet, G., Eds. Elsevier: Louvain-la-Neuve, Belgium, 1998; Vol. 118, pp 127-136.
35. Marchesini, F. A.; Irusta, S.; Querini, C.; Miró, E. Spectroscopic and catalytic characterization of Pd–In and Pt–In supported on Al₂O₃ and SiO₂, active catalysts for nitrate hydrogenation. *Appl. Catal., A* **2008**, *348* (1), 60-70.
36. Miyazaki, A.; Matsuda, K.; Papa, F.; Scurtu, M.; Negrila, C.; Dobrescu, G.; Balint, I. Impact of particle size and metal-support interaction on denitration behavior of well-defined Pt-Cu nanoparticles. *Catal. Sci. Technol.* **2015**, *5* (1), 492-503.
37. Bae, S.; Jung, J.; Lee, W. The effect of pH and zwitterionic buffers on catalytic nitrate reduction by TiO₂-supported bimetallic catalyst. *Chem. Eng. J.* **2013**, *232*, 327-337.
38. Hörold, S.; Vorlop, K. D.; Tacke, T.; Sell, M. Development of catalysts for a selective nitrate and nitrite removal from drinking water. *Catal. Today* **1993**, *17* (1–2), 21-30.
39. Guy, K. A.; Xu, H.; Yang, J. C.; Werth, C. J.; Shapley, J. R. Catalytic Nitrate and Nitrite Reduction with Pd-Cu/PVP Colloids in Water: Composition, Structure, and Reactivity Correlations. *J. Phys. Chem. C* **2009**, *113* (19), 8177-8185.
40. Fan, X.; Franch, C.; Palomares, E.; Lapkin, A. A. Simulation of catalytic reduction of nitrates based on a mechanistic model. *Chem. Eng. J.* **2011**, *175* (0), 458-467.
41. Centi, G.; Perathoner, S. Remediation of water contamination using catalytic technologies. *Appl. Catal., B* **2003**, *41* (1–2), 15-29.
42. Zhang, F. X.; Miao, S.; Yang, Y. L.; Zhang, X.; Chen, J. X.; Guan, N. J. Size-dependent hydrogenation selectivity of nitrate on Pd-Cu/TiO₂ catalysts. *J. Phys. Chem. C* **2008**, *112* (20), 7665-7671.
43. Xu, Z.; Chen, L.; Shao, Y.; Yin, D.; Zheng, S. Catalytic Hydrogenation of Aqueous Nitrate over Pd–Cu/ZrO₂ Catalysts. *Ind. Eng. Chem. Res.* **2009**, *48* (18), 8356-8363.

44. D'Arino, M.; Pinna, F.; Strukul, G. Nitrate and nitrite hydrogenation with Pd and Pt/SnO₂ catalysts: the effect of the support porosity and the role of carbon dioxide in the control of selectivity. *Appl. Catal., B* **2004**, *53* (3), 161-168.
45. Chen, H. Y.; Lo, S. L.; Ou, H. H. Catalytic hydrogenation of nitrate on Cu-Pd supported on titanate nanotube and the experiment after aging, sulfide fouling and regeneration procedures. *Appl. Catal., B* **2013**, *142*, 65-71.
46. Epron, F.; Gauthard, F.; Pinéda, C.; Barbier, J. Catalytic Reduction of Nitrate and Nitrite on Pt-Cu/Al₂O₃ Catalysts in Aqueous Solution: Role of the Interaction between Copper and Platinum in the Reaction. *J. Catal.* **2001**, *198* (2), 309-318.
47. <http://www.platinum.matthey.com/prices/price-charts>. (Accessed January 7, 2017).
48. Brunet Espinosa, R.; Lefferts, L. Ni in CNFs: Highly Active for Nitrite Hydrogenation. *ACS Catal.* **2016**, *6* (8), 5432-5440.
49. <http://www.infomine.com/investment/metal-prices/nickel/>. (Accessed January 7, 2017).
50. Calvo, L.; Gilarranz, M. A.; Casas, J. A.; Mohedano, A. F.; Rodriguez, J. J. Denitrification of Water with Activated Carbon-Supported Metallic Catalysts. *Ind. Eng. Chem. Res.* **2010**, *49* (12), 5603-5609.
51. Chaplin, B. P.; Reinhard, M.; Schneider, W. F.; Schuth, C.; Shapley, J. R.; Strathmann, T. J.; Werth, C. J. Critical review of Pd-based catalytic treatment of priority contaminants in water. *Environ. Sci. Technol.* **2012**, *46* (7), 3655-3670.
52. Petró, J.; Bóta, A.; László, K.; Beyer, H.; Kálmán, E.; Dódon, I. A new alumina-supported, not pyrophoric Raney-type Ni-catalyst. *Appl. Catal., A* **2000**, *190* (1-2), 73-86.
53. Chen, L.; Zhu, Y.; Zheng, H.; Zhang, C.; Zhang, B.; Li, Y. Aqueous-phase hydrodeoxygenation of carboxylic acids to alcohols or alkanes over supported Ru catalysts. *J. Mol. Catal. A: Chem.* **2011**, *351*, 217-227.
54. Yoneda, T.; Takido, T.; Konuma, K. Hydrodechlorination of para-substituted chlorobenzenes over a ruthenium/carbon catalyst. *Appl. Catal., B* **2008**, *84* (3-4), 667-677.
55. Dima, G. E.; de Vooy, A. C. A.; Koper, M. T. M. Electrocatalytic reduction of nitrate at low concentration on coinage and transition-metal electrodes in acid solutions. *J. Electroanal. Chem.* **2003**, *554-555* (0), 15-23.
56. Chen, X.; Huo, X.; Liu, J.; Wang, Y.; Werth, C. J.; Strathmann, T. J. Exploring beyond palladium: Catalytic reduction of aqueous oxyanion pollutants with alternative platinum group metals and new mechanistic implications. *Chem. Eng. J.* **2017**, *313*, 745-752.

57. Lemaigen, L.; Tong, C.; Begon, V.; Burch, R.; Chadwick, D. Catalytic denitrification of water with palladium-based catalysts supported on activated carbons. *Catal. Today* **2002**, *75* (1–4), 43-48.
58. Yin, S.-F.; Zhang, Q.-H.; Xu, B.-Q.; Zhu, W.-X.; Ng, C.-F.; Au, C.-T. Investigation on the catalysis of CO_x-free hydrogen generation from ammonia. *J. Catal.* **2004**, *224* (2), 384-396.
59. García-García, F. R.; Guerrero-Ruiz, A.; Rodríguez-Ramos, I. Role of B5-type sites in Ru catalysts used for the NH₃ decomposition reaction. *Top. Catal.* **2009**, *52* (6), 758-764.
60. R. Sander, Compilation of Henry's Law Constants for Inorganic and Organic Species of Potential Importance in Environmental Chemistry (Accessed July 2016) <http://www.henry-law.org>.
61. Frisch, M. J.; Trucks, G. W.; Schlegel, H. B.; Scuseria, G. E.; Robb, M. A.; Cheeseman, J. R.; Scalmani, G.; Barone, V.; Mennucci, B.; Petersson, G. A.; Nakatsuji, H.; Caricato, M.; Li, X.; Hratchian, H. P.; Izmaylov, A. F.; Bloino, J.; Zheng, G.; Sonnenberg, J. L.; Hada, M.; Ehara, M.; Toyota, K.; Fukuda, R.; Hasegawa, J.; Ishida, M.; Nakajima, T.; Honda, Y.; Kitao, O.; Nakai, H.; Vreven, T.; Montgomery Jr, J. A.; Peralta, J. E.; Ogliaro, F.; Bearpark, M. J.; Heyd, J.; Brothers, E. N.; Kudin, K. N.; Staroverov, V. N.; Kobayashi, R.; Normand, J.; Raghavachari, K.; Rendell, A. P.; Burant, J. C.; Iyengar, S. S.; Tomasi, J.; Cossi, M.; Rega, N.; Millam, N. J.; Klene, M.; Knox, J. E.; Cross, J. B.; Bakken, V.; Adamo, C.; Jaramillo, J.; Gomperts, R.; Stratmann, R. E.; Yazyev, O.; Austin, A. J.; Cammi, R.; Pomelli, C.; Ochterski, J. W.; Martin, R. L.; Morokuma, K.; Zakrzewski, V. G.; Voth, G. A.; Salvador, P.; Dannenberg, J. J.; Dapprich, S.; Daniels, A. D.; Farkas, Ö.; Foresman, J. B.; Ortiz, J. V.; Cioslowski, J.; Fox, D. J. Gaussian 09, Gaussian, Inc.: Wallingford, CT, USA, 2009.
62. Aguilera-Granja, F.; Balbás, L. C.; Vega, A. Study of the Structural and Electronic Properties of RhN and RuN Clusters (N < 20) within the Density Functional Theory. *J. Phys. Chem. A* **2009**, *113* (48), 13483-13491.
63. Zhang, W.; Zhao, H.; Wang, L. The Simple Cubic Structure of Ruthenium Clusters. *J. Phys. Chem. B* **2004**, *108* (7), 2140-2147.
64. Adamo, C.; Barone, V. Toward reliable density functional methods without adjustable parameters: The PBE0 model. *J. Chem. Phys.* **1999**, *110* (13), 6158-6170.
65. Dunning, H. T., Jr.; Hay, P. J. Gaussian Basis Sets for Molecular Calculations. In *Methods of Electronic Structure Theory*; Iii, H. F. S., Ed. Springer US: New York, 1977; pp 1-27.
66. Hay, P. J.; Wadt, W. R. Ab initio effective core potentials for molecular calculations. Potentials for K to Au including the outermost core orbitals. *J. Chem. Phys.* **1985**, *82* (1), 299-310.
67. Andrae, D.; Häußermann, U.; Dolg, M.; Stoll, H.; Preuß, H. Energy-adjusted ab initio pseudopotentials for the second and third row transition elements. *Theor. Chim. Acta* **1990**, *77* (2), 123-141.

68. Quintal, M. M.; Karton, A.; Iron, M. A.; Boese, A. D.; Martin, J. M. L. Benchmark Study of DFT Functionals for Late-Transition-Metal Reactions. *J. Phys. Chem. A* **2006**, *110* (2), 709-716.
69. Janthon, P.; Luo, S.; Kozlov, S. M.; Viñes, F.; Limtrakul, J.; Truhlar, D. G.; Illas, F. Bulk Properties of Transition Metals: A Challenge for the Design of Universal Density Functionals. *J. Chem. Theory. Comput.* **2014**, *10* (9), 3832-3839.
70. Tomasi, J.; Mennucci, B.; Cancès, E. The IEF version of the PCM solvation method: an overview of a new method addressed to study molecular solutes at the QM ab initio level. *J. Mol. Struct.-THEOCHEM* **1999**, *464* (1-3), 211-226.
71. Trawczyński, J.; Gheek, P.; Okal, J.; Zawadzki, M.; Gomez, M. J. I. Reduction of nitrate on active carbon supported Pd-Cu catalysts. *Appl. Catal., A* **2011**, *409-410* (0), 39-47.
72. Chaplin, B.; Shapley, J.; Werth, C. The selectivity and sustainability of a Pd-In/ γ -Al₂O₃ catalyst in a packed-bed reactor: The effect of solution composition. *Catal. Lett.* **2009**, *130* (1-2), 56-62.
73. AutoChem 2920 Automated Catalyst Characterization System Operator's Manual V4.00, Micromeritics, 2009. Retrieved from http://www.micromeritics.com/repository/files/autochem_ii_2920_operator_manual_v4.00.pdf.
74. Deganello, F.; Liotta, L. F.; Macaluso, A.; Venezia, A. M.; Deganello, G. Catalytic reduction of nitrates and nitrites in water solution on pumice-supported Pd-Cu catalysts. *Appl. Catal., B* **2000**, *24* (3-4), 265-273.
75. Garron, A.; Epron, F. Use of formic acid as reducing agent for application in catalytic reduction of nitrate in water. *Water Res.* **2005**, *39* (13), 3073-3081.
76. Sá, J.; Vinek, H. Catalytic hydrogenation of nitrates in water over a bimetallic catalyst. *Appl. Catal., B* **2005**, *57* (4), 247-256.
77. Maia, M. P.; Rodrigues, M. A.; Passos, F. B. Nitrate catalytic reduction in water using niobia supported palladium-copper catalysts. *Catal. Today* **2007**, *123* (1-4), 171-176.
78. Shuai, D.; McCalman, D. C.; Choe, J. K.; Shapley, J. R.; Schneider, W. F.; Werth, C. J. Structure sensitivity study of waterborne contaminant hydrogenation using shape- and size-controlled Pd nanoparticles. *ACS Catal.* **2013**, *3* (3), 453-463.
79. Hosokawa, S.; Kanai, H.; Utani, K.; Taniguchi, Y.-i.; Saito, Y.; Imamura, S. State of Ru on CeO₂ and its catalytic activity in the wet oxidation of acetic acid. *Appl. Catal., B* **2003**, *45* (3), 181-187.
80. Deng, W.; Tan, X.; Fang, W.; Zhang, Q.; Wang, Y. Conversion of Cellulose into Sorbitol over Carbon Nanotube-Supported Ruthenium Catalyst. *Catal. Lett.* **2009**, *133* (1-2), 167-174.

81. Kundu, S.; Wang, Y.; Xia, W.; Muhler, M. Thermal Stability and Reducibility of Oxygen-Containing Functional Groups on Multiwalled Carbon Nanotube Surfaces: A Quantitative High-Resolution XPS and TPD/TPR Study. *J. Phys. Chem. C* **2008**, *112* (43), 16869-16878.
82. Epron, F.; Gauthard, F.; Barbier, J. Catalytic Reduction of Nitrate in Water on a Monometallic Pd/CeO₂ Catalyst. *J. Catal.* **2002**, *206* (2), 363-367.
83. Costa, A. O.; Ferreira, L. S.; Passos, F. B.; Maia, M. P.; Peixoto, F. C. Microkinetic modeling of the hydrogenation of nitrate in water on Pd–Sn/Al₂O₃ catalyst. *Appl. Catal., A* **2012**, *445–446* (0), 26-34.
84. Hamid, S.; Kumar, M. A.; Lee, W. Highly reactive and selective Sn-Pd bimetallic catalyst supported by nanocrystalline ZSM-5 for aqueous nitrate reduction. *Appl. Catal., B* **2016**, *187*, 37-46.
85. Shin, H.; Jung, S.; Bae, S.; Lee, W.; Kim, H. Nitrite Reduction Mechanism on a Pd Surface. *Environ. Sci. Technol.* **2014**, *48* (21), 12768-12774.
86. Vannice, M. A. *Kinetics of Catalytic Reactions*; Springer: New York, 2005; p p. 240.
87. Chinthaginjala, J. K.; Lefferts, L. Support effect on selectivity of nitrite reduction in water. *Appl. Catal., B* **2010**, *101* (1–2), 144-149.
88. Chen, H.; Xu, Z.; Wan, H.; Zheng, J.; Yin, D.; Zheng, S. Aqueous bromate reduction by catalytic hydrogenation over Pd/Al₂O₃ catalysts. *Appl. Catal., B* **2010**, *96* (3–4), 307-313.
89. Knitt, L. E.; Shapley, J. R.; Strathmann, T. J. Rapid metal-catalyzed hydrodehalogenation of iodinated X-ray contrast media. *Environ. Sci. Technol.* **2008**, *42* (2), 577-583.
90. Bergquist, A. M.; Choe, J. K.; Strathmann, T. J.; Werth, C. J. Evaluation of a hybrid ion exchange-catalyst treatment technology for nitrate removal from drinking water. *Water Res.* **2016**, *96*, 177-187.
91. Desloover, J.; Abate Woldeyohannis, A.; Verstraete, W.; Boon, N.; Rabaey, K. Electrochemical Resource Recovery from Digestate to Prevent Ammonia Toxicity during Anaerobic Digestion. *Environ. Sci. Technol.* **2012**, *46* (21), 12209-12216.
92. Kuntke, P.; Śmiech, K. M.; Bruning, H.; Zeeman, G.; Saakes, M.; Sleutels, T. H. J. A.; Hamelers, H. V. M.; Buisman, C. J. N. Ammonium recovery and energy production from urine by a microbial fuel cell. *Water Res.* **2012**, *46* (8), 2627-2636.
93. Li, R.; Zhang, L.; Wang, P. Rational design of nanomaterials for water treatment. *Nanoscale* **2015**, *7* (41), 17167-17194.
94. St. John, S.; Atkinson, R. W.; Unocic, R. R.; Zawodzinski, T. A.; Papandrew, A. B. Ruthenium-Alloy Electrocatalysts with Tunable Hydrogen Oxidation Kinetics in Alkaline Electrolyte. *J. Phys. Chem. C* **2015**, *119* (24), 13481-13487.

95. Nilekar, A. U.; Greeley, J.; Mavrikakis, M. A Simple Rule of Thumb for Diffusion on Transition-Metal Surfaces. *Angew. Chem. Int. Ed.* **2006**, *45* (42), 7046-7049.
96. Liu, J.; Choe, J. K.; Wang, Y.; Shapley, J. R.; Werth, C. J.; Strathmann, T. J. Bioinspired complex-nanoparticle hybrid catalyst system for aqueous perchlorate reduction: Rhenium speciation and its Influence on catalyst activity. *ACS Catal.* **2014**, 511-522.
97. Ford, C. L.; Park, Y. J.; Matson, E. M.; Gordon, Z.; Fout, A. R. A bioinspired iron catalyst for nitrate and perchlorate reduction. *Science* **2016**, *354* (6313), 741-743.

CHAPTER 4

RUTHENIUM CATALYSTS FOR REDUCTION OF *N*-NITROSAMINE WATER CONTAMINANTS

A modified version of this chapter was published in *Environmental Science & Technology*

Xiangchen Huo, Jinyong Liu, and Timothy J. Strathmann*

4.1 Abstract

N-nitrosamines have raised extensive concern due to their high toxicity and detection in treated wastewater and drinking water. Catalytic reduction is a promising alternative technology to treat *N*-nitrosamines, but to advance this technology pathway, there is a need to develop more efficient and cost-effective catalysts. We have previously discovered that commercial catalysts containing ruthenium (Ru) are unexpectedly active in reducing nitrate. This study evaluated supported Ru activity for catalyzing reduction of *N*-nitrosamines. Experiments with *N*-nitrosodimethylamine (NDMA) show that contaminant is rapidly reduced on both commercial and in-house prepared Ru/Al₂O₃ catalysts, with the commercial material yielding an initial metal weight-normalized pseudo-first-order rate constant (k_0) of $1103 \pm 133 \text{ L g}_{\text{Ru}}^{-1} \text{ h}^{-1}$ and an initial turnover frequency (TOF₀) of $58.0 \pm 7.0 \text{ h}^{-1}$. NDMA is reduced to dimethylamine (DMA) and ammonia end-products, and a small amount of 1,1-dimethylhydrazine (UDMH) was detected as a transient intermediate. Experiment with a mixture of five *N*-nitrosamines spiked into tap water

*Reprinted with permission from Huo, X.; Liu, J.; Strathmann, T. J. Ruthenium Catalysts for the Reduction of *N*-Nitrosamine Water Contaminants. *Environ. Sci. Technol.* **2018**, *52* (7), 4235-4243. Copyright 2018 American Chemical Society. X.H. performed most of the experiments and analyzed data; J.L. provided technical support and helpful advice; X.H. and T.J.S. wrote the paper with input from all authors. X.H. and T.J.S. are affiliated with Colorado School of Mines; J.L. is affiliated with University of California, Riverside.

(1 $\mu\text{g L}^{-1}$ each) demonstrates that Ru catalysts are very effective in reducing a range of *N*-nitrosamine structures at environmentally relevant concentrations. Cost competitiveness and high catalytic activities with a range of contaminants provide strong argument for developing Ru catalysts as part of the water purification and remediation toolbox.

4.2 Introduction

N-nitrosamines are a class of compounds with a nitroso group bonded to a secondary amine ($\text{R}_1\text{R}_2\text{N-NO}$). These compounds are of great health concern due to their elevated carcinogenicity and genotoxicity.¹ Much of the current focus on *N*-nitrosamines, especially *N*-nitrosodimethylamine (NDMA), is related to their occurrence in water sources and formation as disinfection byproducts (DBPs) during drinking water and wastewater treatment.² NDMA contamination events that have received considerable spotlights include the detection of up to 40 $\mu\text{g L}^{-1}$ NDMA in municipal wells and surface water in Ontario, Canada,³ and the detection of high levels (up to 400 $\mu\text{g L}^{-1}$) in groundwater at a rocket engine testing facility in California, USA.⁴ The World Health Organization (WHO) has established a guideline value of 0.1 $\mu\text{g L}^{-1}$ for NDMA in drinking water.⁵ Although there is currently no federal maximum contaminant level (MCL) for *N*-nitrosamines in drinking water, the U.S. EPA included NDMA and four other *N*-nitrosamines on the fourth Contaminant Candidate List (CCL4).⁶ The awareness of *N*-nitrosamine formation as a byproduct from drinking water disinfection processes and the advancement in analytical methods have resulted in widespread detection of NDMA in sourcewater and treated water samples.⁷ The growing interest in potable reuse of municipal wastewater, particularly in water-limited regions, further increases concerns about exposure to *N*-nitrosamines because of their chemical recalcitrance and ability to pass through the final reverse osmosis membranes barrier typically used in such facilities.^{4, 8}

It follows that there has been extensive research conducted on NDMA treatment technologies. Currently, UV photolysis is the major treatment technology applied specifically to treat NDMA,^{4, 9} producing dimethylamine (DMA) and methylamine (MA) as terminal endproducts.¹⁰ While effective, the high UV fluences required an order-of-magnitude higher than fluences typically applied for disinfection purposes,^{4, 11} leading to high costs and energy use. Powdered activated carbon,¹² nanofiltration, and reverse osmosis,¹³ have been reported to effectively remove NDMA precursors. However, these physical removal processes are ineffective for *N*-nitrosamines themselves, especially for lower molecular weight *N*-nitrosamines like NDMA.^{13, 14} Chemical destruction can be achieved by advanced oxidation process such as ozone/hydrogen peroxide,¹⁵ but these processes are inefficient due to the non-selective nature of the hydroxyl radical oxidants and the presence of elevated concentrations of non-target radical scavengers in most water sources (e.g., HCO_3^- and natural organic matter).

The reducibility of N-NO group has inspired research on reductive processes as an alternative treatment strategy for *N*-nitrosamines. Mezyk and co-workers reported a bimolecular rate constant for the reaction of hydrated electron (e_{aq}^- , $E_{\text{H}} = -2.9 \text{ V}$)¹⁶ with NDMA ($1.41 \times 10^{10} \text{ M}^{-1} \text{ s}^{-1}$) that is two orders-of-magnitude higher than that reported for reaction with hydroxyl radical ($4.30 \times 10^8 \text{ M}^{-1} \text{ s}^{-1}$).¹⁷ Practical generation of hydrated electrons requires application of UV light together with elevated concentrations of a photo-sensitizer, often KI or K_2SO_3 , and alkaline pH conditions (e.g., $\text{pH} > 9$).¹⁸ Corrosion of zerovalent metals, such as iron, in water can generate adsorbed atomic hydrogen atom, but the slow kinetics reported for these processes¹⁹ and buildup of a hazardous intermediate²⁰ prompted a search for more efficient catalysts for generating adsorbed atomic hydrogen. To date, the majority of studies have focused on Pd-based catalysts²¹⁻²⁴ due to their high activity and stability in aquatic matrices. However, the high and

variable cost of Pd²⁵ has limited the further development and adoption of reductive catalytic water treatment technologies. Initial evaluation of alternative low-cost Ni-based catalysts (e.g., Raney Ni) reported high activities for *N*-nitrosamine reduction,²⁶ but further development was limited by safety concerns associated with the pyrophoric properties of porous Ni catalysts, poor catalyst stability in aqueous matrices, and health concerns related to leaching of Ni into product water. Thus, there continues to be strong interest in the development of alternative catalysts for *N*-nitrosamine reduction that are effective, stable, and less costly than Pd-based materials.

As part of a larger effort aimed at expanding the range of metals that can be applied for reductive treatment processes, we recently found supported Ru materials to be very active for catalyzing aqueous nitrate and nitrite reduction with H₂ under room temperature and atmospheric pressure.²⁷ No intermediate was detected during nitrate reduction, suggesting that proposed intermediates such as nitrite and nitrous oxide at low concentrations are rapidly converted. This represents a potential breakthrough because the cost of Ru is historically much lower than Pd. The high activity of Ru observed with nitrate and its NO_x intermediates is suggestive of potential for catalyzing reduction of the N-NO group within *N*-nitrosamine structures. The overall goal of this contribution is to test this hypothesis and to examine reactivities of NDMA and related *N*-nitrosamine contaminants with supported Ru catalysts under relevant water quality conditions. Reaction kinetics and products for NDMA with Ru catalysts are examined and compared to Pd-based catalysts, and reaction of mixture of *N*-nitrosamine structures spiked at trace levels (1 μg L⁻¹ each) into tap water is evaluated to validate the applicability of the technology to relevant treatment conditions. Finally, the activity of Ru and Pd catalysts with a suite of aquatic contaminants is compared to assess the broad applicability of Ru-based catalysts as substitutes for Pd catalysts.

4.3 Experimental Section

4.3.1 Chemicals

Neat *N*-nitrosodiethylamine (NDEA), *N*-nitrosopiperidine (NPIP), and *N*-nitrosomorpholine (NMOR) were purchased from Ultra Scientific. Neat NDMA and *N*-nitrosodi-*n*-propylamine (NDPA), dimethylamine (DMA) solution (40 wt% in water), 1-fluoro-2,4-dinitrobenzene, 4-nitrobenzaldehyde, 4-chlorophenol, 4-nitrophenol, sodium diatrizoate hydrate, triethylamine, NH₄Cl, MES hydrate pH buffer, H₃PO₄ (85 wt% in water), and NaH₂PO₄ were obtained from Sigma-Aldrich. Isotopically labeled standards [6-²H] NDMA (NDMA-*d*₆, 98%) and [14-²H] NDPA (NDPA-*d*₁₄, 98%) (1000 mg L⁻¹ in dichloromethane) were acquired from Cambridge isotope laboratories. 1,1-dimethylhydrazine (unsymmetrical dimethylhydrazine, UDMH) hydrochloride was purchased from TCI America. Methanol, acetonitrile, dichloromethane, acetic acid, Na₂SO₄, NaOH, and HCl were obtained from Fisher. Ultra-high purity H₂, Ar, and N₂ were supplied by General Air.

4.3.2 Catalyst preparation and characterization

The majority of experiments used a commercial Ru/Al₂O₃ (nominal 5 wt% Ru) catalyst from Sigma-Aldrich. A separate Ru/Al₂O₃ material was also prepared from Ru(NO)(NO₃)₃ (Alfa Aesar) aqueous solution and Al₂O₃ (Sigma-Aldrich) using an incipient wetness impregnation technique.²⁸ Commercial Pd/Al₂O₃ (nominal 5 wt% Pd) was also obtained from Sigma-Aldrich and used to prepare a bimetallic Pd-In/Al₂O₃ catalyst with In(NO₃)₃·3H₂O (Alfa Aesar) aqueous solution following a reported method.²² Prior to use, dry catalysts were *ex situ* reduced in flowing H₂ at 120 °C for 1 h before cooling to room temperature in flowing Ar.

Actual metal contents of the catalysts were determined by inductively coupled plasma-atomic emission spectrometry (ICP-AES) (PerkinElmer 5300DV) after digestion in HF-HCl-

HNO₃ (for Pd catalysts) or by alkaline fusion (for Ru catalysts). Surface area and pore structure analyses were determined by N₂ BET adsorption-desorption isotherms measured at 77 K using a Micromeritics ASAP 2020 analyzer. Dispersion of Ru or Pd was determined by CO chemisorption using an assumed 1:1 CO:Metal adsorption stoichiometry.^{29, 30} For Pd-In/Al₂O₃ catalysts, CO was assumed to be chemisorbed only on Pd surfaces. Morphology of the Ru nanoparticles was characterized by high angle annular dark field (HAADF) imaging with scanning transmission electron microscopy (FEI Titan S/TEM operated at 200 kV). To obtain the particle size distribution, at least 150 particles were counted for each image.

4.3.3 Catalytic reduction of NDMA

Catalyst activity was evaluated in a semi-batch system under continuous H₂ sparging (1 atm, 200 mL min⁻¹) at room temperature (22 ± 0.5 °C). The relatively high H₂ flow rate was used to ensure solution saturation of H_{2(aq)} and minimize potential H₂ gas-to-aqueous mass transfer limitations during experiments. A 250 mL round-bottom flask was filled with desired mass of catalyst and 120 mL 10 mM 4-morpholineethanesulfonic acid (MES) pH buffer at pH 6.0. The catalyst suspension was mixed by magnetic stirring and sparged with H₂ for 3 h before introducing a small volume of concentrated aqueous NDMA stock solution to initiate the reaction. The effect of stirring speed on reaction rate was evaluated in preliminary tests, and a stirring speed of 900 rpm was chosen to eliminate external mass transfer limitations. Aliquots were then collected at predetermined times to monitor the disappearance of NDMA. H_{2(aq)}-free control tests were conducted by sparging catalyst suspension with H₂ for 3 h followed by Ar for 1 h before adding the NDMA stock solution. In one set of experiments, the reduction of repeated spikes of NDMA was monitored in the semi-batch reactor to evaluate catalyst stability and potential deactivation. The volume of NDMA stock solution used for each spike was carefully

calculated to achieve an initial concentration of 100 μM in the resulting solution. Mass-normalized rate constants were calculated for each spike. The overall repeated-spike test was run in duplicate.

Catalyst activity was assessed by quantifying initial metal weight-normalized pseudo-first-order rate constants (k_0 , $\text{L g}_{\text{Ru/Pd}}^{-1} \text{h}^{-1}$) and turnover frequencies (TOF_0 , h^{-1}), defined as the number of NDMA molecules reduced per surface Ru/Pd atom per hour. Initial observed pseudo-first-order rate constants ($k_{\text{obs},0}$, h^{-1}) were determined by fitting the natural log of substrate concentration versus time data for the first reaction half-life, and the corresponding mass-normalized rate constants were determined by:

$$k_0 = \frac{k_{\text{obs},0}}{C_{\text{catalyst}} W_{\text{metal}}} \quad (4.1)$$

where C_{catalyst} is the catalyst mass loading in the aqueous suspension (g L^{-1}), and W_{metal} is the metal wt fraction of the catalyst. The corresponding TOF_0 value was then calculated by dividing the initial NDMA reduction rate (R_0 , $\text{mol L}^{-1} \text{h}^{-1}$) by the concentration of surface Ru or Pd atoms ($C_{\text{metal surface}}$, mol L^{-1}):

$$\text{TOF}_0 = \frac{R_0}{C_{\text{metal surface}}} = \frac{k_{\text{obs},0} C_0}{(\text{Dispersion} \times C_{\text{catalyst}} W_{\text{metal}}) / M} \quad (4.2)$$

where R_0 is the product of $k_{\text{obs},0}$ and the initial NDMA concentration (C_0 , mol L^{-1}), and $C_{\text{metal surface}}$ is estimated from dispersion coupled with information on C_{catalyst} , W_{metal} and the atomic weight of Ru or Pd (M , g mol^{-1}). Experiments with other reducible substrates, e.g., 4-nitrophenol, 4-chlorophenol, and diatrizoate, followed the same protocol as that for NDMA.

Endproduct distributions and carbon/nitrogen balances were quantified using closed-system batch experiments. The reactor setup was the same as that described above, except that the reactor was sealed immediately after introducing NDMA stock solution (to prevent

volatilization of selected products during continuous H₂ sparging). Aliquots were collected at predetermined times for analysis of NDMA plus its daughter products.

4.3.4 Catalytic reduction of *N*-nitrosamines under environmentally relevant conditions

An experiment was conducted to validate that the reactions observed with NDMA described apply to a range of *N*-nitrosamines and to conditions relevant to water treatment operations (i.e., natural water matrix with trace initial concentrations of *N*-nitrosamines). Tap water was initially heated to approximately 80 °C to volatilize free chlorine. Composition of the tap water, including alkalinity, total dissolved solids (TDS), common anions and metals, total organic carbon (TOC), ammonium and pH are provided in Table C.1 in Appendix C. Several replicate reactors were then prepared by adding 400 mL of the tap water and 40 mg of catalyst to a 500 mL amber graduated media bottle equipped with an Omnifit T Series Bottle Cap and Teflon-coated stir bar, and the catalyst suspension was mixed and sparged with H₂ for 3 h before introducing an aqueous stock mixture of NDMA, NDEA, NDPA, NPIP, and NMOR (1 µg L⁻¹ of each *N*-nitrosamine) to initiate the reaction. The procedure was repeated several times, with the entire contents of the bottle being sacrificed for extraction and analysis of *N*-nitrosamines after different reaction times. The bottle contents were vacuum filtered through a 0.45 µm mixed cellulose esters membrane to remove catalyst particles before solid phase extraction. The same protocol was followed in a separate experiment using deionized water for comparison. To test *N*-nitrosamine adsorption to the catalyst, the same amount of catalyst, tap water, and aqueous *N*-nitrosamine mixture stock solution was mixed in the absence of H₂ sparging.

A control test for *N*-nitrosamine adsorption to the catalyst was conducted by mixing the same amount of catalyst, tap water, and aqueous *N*-nitrosamine mixture stock solution in the absence of H₂ sparging.

4.3.5 Analytical methods

NDMA, 4-chlorophenol, 4-nitrophenol, and diatrizoate were directly analyzed by HPLC with UV/vis photodiode array detector (Shimazu SPD-M20A) and a Waters Spherisorb ODS2 Column (4.6 mm × 150 m, 5 μm packing material). DMA and UDMH were analyzed by the same equipment after pre-column derivatization. Composition and flow rate of mobile phase, detection wavelength, and derivatization protocols followed published methods.^{19, 26, 31-34} Ammonia was quantified using the Hach salicylate method (low range, 0.02 to 2.50 mg L⁻¹ NH₃-N, method 10023). Dissolved Ru was measured by ICP-AES (PerkinElmer 5300DV).

For tests with *N*-nitrosamine mixture at environmentally relevant concentrations, water samples were fortified with the surrogate NDMA-*d*₆ at the final concentration of 0.5 μg L⁻¹ and extracted by passing filtered reaction solution through a solid phase extraction (SPE) cartridge filled with 2 g of coconut charcoal (Restek). The cartridge was conditioned with dichloromethane, methanol, and Nanopure water according to EPA Method 521.³⁵ The extract was passed through a drying column packed with 6 g of anhydrous sodium sulfate and concentrated by N₂ blow down. After addition of internal standard NDPA-*d*₁₄ at the final concentration of 100 μg L⁻¹, the volume was adjusted to 2 mL with dichloromethane, and the sample was analyzed by a TSQ 8000 Evo Triple Quadrupole GC-MS/MS (ThermoFisher) with electron impact ionization. A Rxi-5Sil MS column (30 m × 0.32 mm I.D. × 0.25 μm film thickness) was operated under the following oven temperature program: initial temperature 35 °C was held for 4 min, raised first to 60 °C at 5 °C min⁻¹ and then to 80 °C at 4 °C min⁻¹. The injector was heated at 250 °C, and the injection volume was 1 μL in the splitless mode. Transfer line and ion source temperatures were held at 250 °C and 220 °C, respectively. A calibration

curve covering the range 10-300 $\mu\text{g L}^{-1}$ was corrected for the surrogate recovery. Each sample was analyzed in triplicate.

4.4 Results and Discussion

4.4.1 Catalytic NDMA reduction activity

Control experiments confirmed that aqueous NDMA cannot be reduced by H_2 in the absence of catalysts, and loss of NDMA by adsorption to the catalyst support is insignificant (Figure C.1 in Appendix C). Commercial $\text{Ru}/\text{Al}_2\text{O}_3$ shows significantly higher activities than either $\text{Pd}/\text{Al}_2\text{O}_3$ or $\text{Pd-In}/\text{Al}_2\text{O}_3$ catalysts under the same conditions (Figure 4.1). The estimated Weisz-Prater parameter (C_{WP}) was found to be $\ll 1$ (see Section C.1 in Appendix C), indicating that the internal mass transfer within the catalyst support particles is not rate limiting. This is an interesting finding given that Pd-based materials are considered the state-of-the-art catalysts for NDMA and related contaminants.

The initial reaction rate increases with initial NDMA concentration and plateaus at higher NDMA concentrations (Figure C.2a in Appendix C), which has been observed for NDMA reduction on Pd-based³⁶ and Ni catalysts,²⁶ and is described by the Langmuir- Hinshelwood model³⁷ for surface-mediated reactions. Assuming that NDMA and hydrogen adsorb non-competitively to Ru surface sites and that the surface reaction is rate-limiting, the Langmuir-Hinshelwood model can be expressed as

$$r_0 = k_{\text{rxn}} \frac{K_{\text{ads}}[\text{NDMA}]_0}{1 + K_{\text{ads}}[\text{NDMA}]_0} \quad (4.3)$$

where r_0 is the metal weight-normalized initial NDMA reduction rate ($\text{mol g}_{\text{Ru}}^{-1} \text{h}^{-1}$), k_{rxn} is the rate constant ($\text{mol g}_{\text{Ru}}^{-1} \text{h}^{-1}$) for adsorbed NDMA reacting with adsorbed atomic hydrogen, K_{ads} is

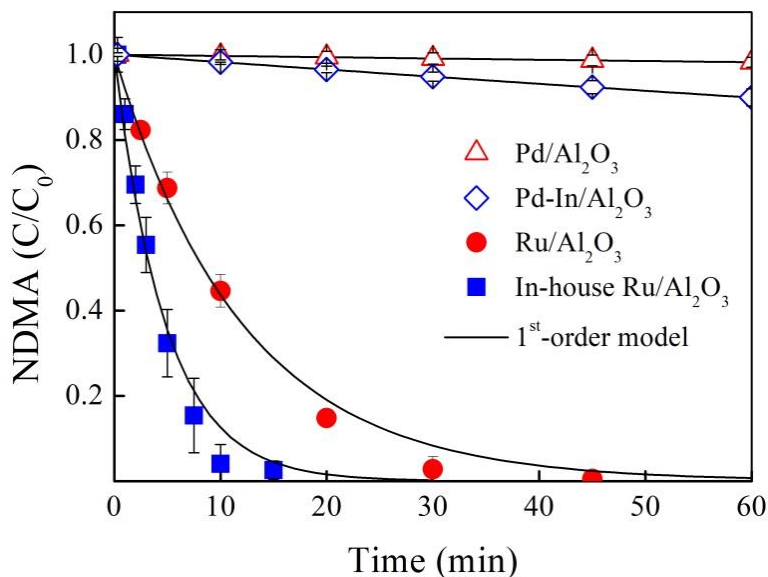


Figure 4.1 Timecourse of NDMA reduction with different catalysts in the semi-batch reactor system ($[\text{NDMA}]_0 = 100 \mu\text{M}$, 0.1 g L^{-1} catalyst, pH 6.0 buffered by 10 mM MES buffer, continuous sparging of 1 atm H_2 , $22 \pm 0.5 \text{ }^\circ\text{C}$). Error bars represent standard deviations of triplicate reactions. Catalyst formulation details provided in Table 4.1.

the equilibrium adsorption constant ($\text{mol}^{-1} \text{ L}$) for NDMA on the catalyst surface, and $[\text{NDMA}]_0$ is the initial aqueous concentration (mol L^{-1}). A plot of reaction rate versus NDMA concentration according to Eq. 4.3 features a linear region at low NDMA concentrations where reaction rate increases proportionally with initial NDMA concentration. At higher initial NDMA concentrations, further increases in reaction rate are less than proportional and eventually plateau as surface reaction sites become saturated. This trend is consistent with the Langmuir-Hinshelwood kinetic model for surface reaction processes (Eq. 4.3). It is observed from Figure S2 that the initial NDMA concentration used in most experiments ($100 \mu\text{M}$) was not within the linear region of the Langmuir-Hinshelwood model. To estimate the pseudo-first-order rate constant in the linear region, which is constant and characteristic of reaction kinetics at more environmentally relevant concentrations of NDMA (e.g., $< 1 \mu\text{g L}^{-1}$), Eq. 4.3 was fit to experimental data by nonlinear least squares regression, and two model parameters, k_{rxn} and K_{ads} , were determined to be $0.15 \pm 0.01 \text{ mol g}_{\text{Ru}}^{-1} \text{ h}^{-1}$ and $33,500 \pm 5,900 \text{ mol}^{-1} \text{ L}$ (uncertainty

represents 95% confidence limits), respectively. Therefore, the metal weight-normalized pseudo-first-order rate constant in the linear region was calculated to be $5,030 \text{ L g}_{\text{Ru}}^{-1} \text{ h}^{-1}$. Compared with other catalysts reported to date (Table C.2 in Appendix C), the commercial Ru/Al₂O₃ shows extremely high activity for catalyzing NDMA reduction (e.g., Pd/Al₂O₃ and Pd-In/Al₂O₃ catalysts all reported $< 100 \text{ L g}_{\text{Pd}}^{-1} \text{ h}^{-1}$). Density functional theory (DFT) study of NDMA decomposition over Ni and Pd surfaces showed that NDMA has stronger binding on the Ni surface than on Pd.³⁸ It follows that the high activity of Ru catalysts is potentially related to stronger binding of NDMA on Ru surface. However, further computational studies of NDMA and intermediate adsorption energies and the activation energies of rate-determining steps on metal surfaces are needed to evaluate this rationale.

A second Ru/Al₂O₃ was synthesized in lab and compared with the commercial Ru/Al₂O₃. Physical properties of catalysts are summarized in Table 4.1. At comparable catalyst mass loadings, the in-house prepared Ru/Al₂O₃ shows 150% increase in NDMA reduction activity compared with the commercial Ru/Al₂O₃ (Figure 4.1, Table C.2 in Appendix C). The greater activity is attributed to higher Ru dispersion or smaller Ru nanoparticle size. Commercial Ru/Al₂O₃ has a wide distribution of Ru particle sizes with an average value of 4.5 nm (Figure 4.2a). In comparison, in-house prepared Ru/Al₂O₃ has more evenly distributed fine nanoparticles, with average particle size of 1.9 nm (Figure 4.2b). Note that the average particle size and distribution may vary slightly when increasing the number of particles counted. However, when reaction rates are normalized to Ru surface sites, the estimated TOF₀ of NDMA on in-house prepared Ru/Al₂O₃ is lower than that estimated for commercial Ru/Al₂O₃ (Table 4.1), indicating that the reaction is sensitive to the surface structure of the supported Ru nanoparticles.³⁹ Comparing the TOF₀ values to Pd catalysts shows that the intrinsic reactivity of Ru surfaces with

NDMA is approximately two orders-of-magnitude higher than that of Pd surface and In-promoted Pd surfaces (Table 4.1). Previously, the most active catalyst reported was a 2.4%Pd0.6%Ni/ γ -Al₂O₃ catalyst that exhibited a TOF of 1.0 h⁻¹ at an initial NDMA concentration of 2 μ M.³⁶ Due to the dependence of TOF₀ on initial NDMA concentration, it is not rigorous to directly compare values in Table 4.1 with reports from the literature. To overcome this challenge, TOF₀ on commercial Ru/Al₂O₃ at an initial NDMA concentration of 2 μ M was estimated by combining Eqs. 4.2 and 4.3, where all the variables are known. The resulting TOF₀ was estimated to be ~6.0 h⁻¹, six times greater than that reported for the optimized Pd-Ni/ γ -Al₂O₃ catalyst.

Table 4.1 Properties of catalysts used for NDMA reduction activity test.

Catalyst	BET surface area (m ² g ⁻¹)	Total pore volume ^a (cm ³ g ⁻¹)	Average pore diameter ^b (nm)	Metal loading (wt%) ^c	Metal dispersion (%)	Particle size (nm)	TOF ₀ (h ⁻¹)
Commercial Ru/Al ₂ O ₃	86.3	0.23	10.8	4.51	19	4.5 ± 2.8	58.0 ± 7.0
In-house Ru/Al ₂ O ₃	122.0	0.21	7.0	4.58	81	1.9 ± 0.7	34.1 ± 4.0
Commercial Pd/Al ₂ O ₃	94.7	0.22	9.4	4.59	31	ND ^d	0.14 ± 0.05
Pd-In/Al ₂ O ₃	94.4	0.22	9.3	4.43 (Pd) 0.87 (In)	45 ^e	ND	0.56 ± 0.12

^aAdsorption total pore volume at P/P₀ = 0.98. ^bCalculated from total pore volume and BET surface area. ^cMeasured by ICP-AES analysis. ^dNot determined. ^eCO was assumed to be chemisorbed only on Pd surface.

The stability of Ru/Al₂O₃ for NDMA reduction was evaluated by repeatedly spiking NDMA into a semi-batch reactor and comparing rates of NDMA disappearance over repeated reaction cycles. Activities of the Ru/Al₂O₃ showed slight variation over 7 consecutive reaction cycles (Figure C.3 in Appendix C). Analysis of dissolved Ru in the reaction solution collected at the end of the last reaction cycle was below the detection limit of the ICP-AES method ($\leq 0.14 \mu\text{g L}^{-1}$). Ultimately, on-stream continuous treatment studies are needed to assess catalyst stability,

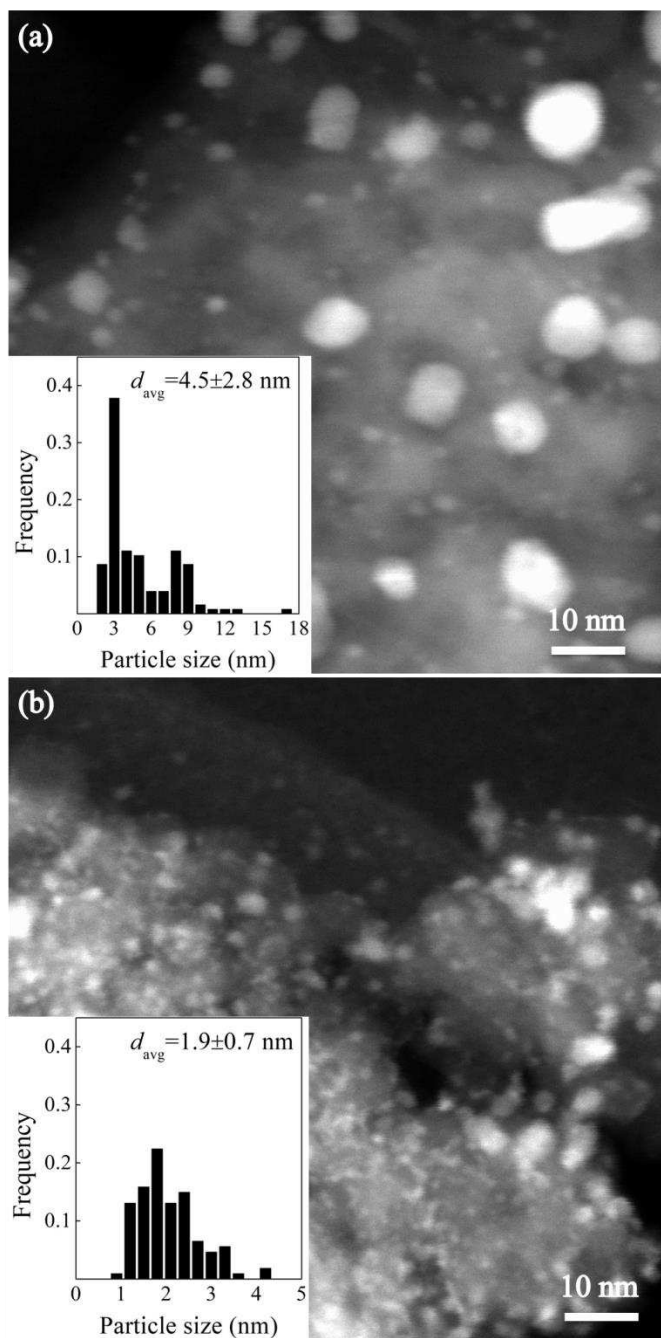


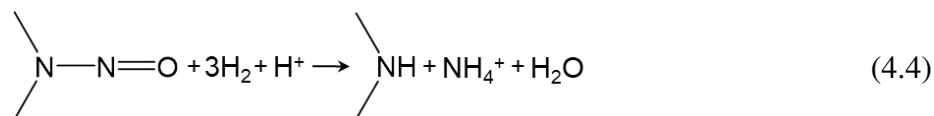
Figure 4.2 HAADF-STEM images of (a) commercial Ru/Al₂O₃ and (b) in-house prepared Ru/Al₂O₃. The insets show Ru particle size distributions.

but results from these initial tests are suggestive of a stable catalytic process with minimal potential for Ru leaching. It is also worth noting that for this study we chose to use Al₂O₃-supported Ru catalysts to avoid potential artifacts from *N*-nitrosamine adsorption to

carbonaceous supports and facilitate comparison with other Al₂O₃-supported catalysts reported in the literature (Table C.21 in Appendix C), but previous work examining nitrate reduction found greater activity for carbon-supported Ru catalysts than Al₂O₃-supported Ru catalysts.²⁷ Future research is suggested to examine the influence of catalyst supports in order to optimize practical treatment applications.

4.4.2 NDMA reduction products

Figure 4.3 shows the disappearance of NDMA and formation of intermediates and endproducts on Ru/Al₂O₃. A carbon mass balance (Figure 4.3a) was mostly closed by using NDMA and endproduct DMA, but a small amount (<2%) of UDMH was also detected as a transient intermediate during the reaction. The largest deviation in the carbon mass balance (<4%) occurred at an early stage of the reaction, and is likely a result of summing species measured using different methods. The nitrogen mass balance (Figure 4.3b) also showed stoichiometric generation of ammonia in addition to DMA. Although reactor headspace was not analyzed, the good nitrogen mass balance strongly suggests a high, and possibly complete, selectivity to ammonia. The high selectivity to ammonia was consistent across a wide range of solution pH conditions (Figure C.4 in Appendix C). Therefore, reduction of NDMA yielded quantitative amounts of DMA and ammonia according to the following stoichiometry, consistent with oxidation of 3 equivalents of H₂.



The quantitative formation of DMA as an endproduct is widely reported in reductive transformation of NDMA, such as with granular iron and Fe enhanced iron,¹⁹ Ni,^{21, 26} Pd and bimetallic Pd catalysts.^{21, 36} Recent studies on zerovalent Fe and Zn observed a loss of nitrogen

mass during reduction of NDMA and UDMH, and attributed this to ammonia and other unmeasured products.^{7, 20} Considering the high metal dose (10 g L^{-1}) employed in these earlier studies, the loss of nitrogen may result of adsorption to metal surfaces, as observed with granular iron.¹⁹ Organic amines (either DMA or MA) are a product of most reported treatment processes for NDMA,^{10, 15, 19, 22} so their complete elimination and complete mineralization of NDMA remains a general challenge if that is ultimate treatment objective. In comparison, the fate of nitrosyl group in NDMA during reduction depends on catalyst (Table C.2 In Appendix C).

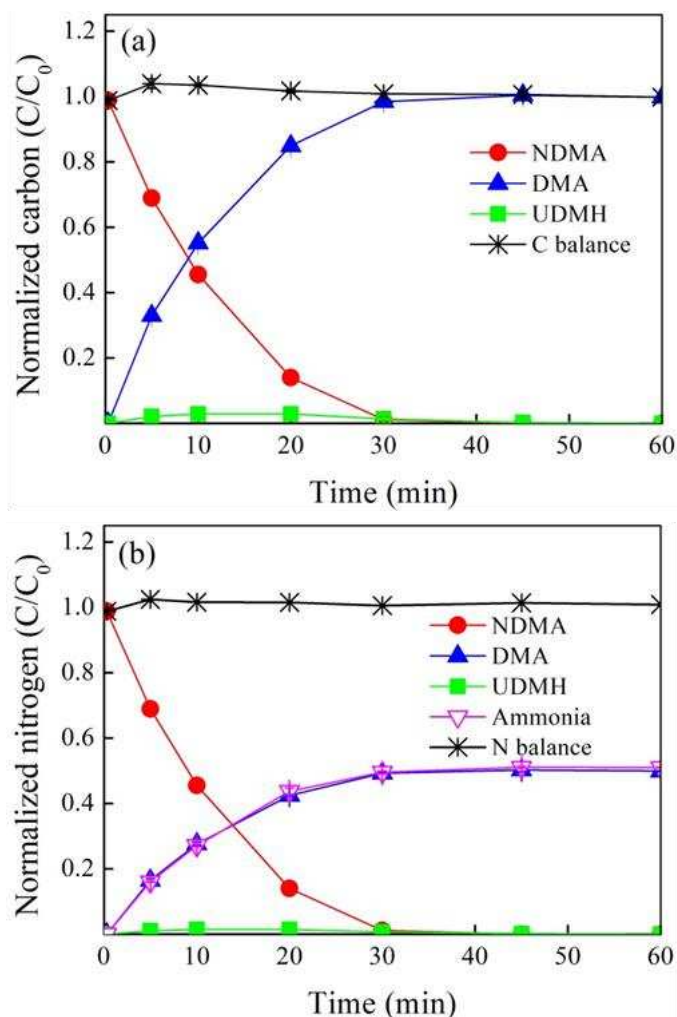


Figure 4.3 (a) Carbon and (b) nitrogen balance of NDMA reduction on commercial $\text{Ru}/\text{Al}_2\text{O}_3$ in the batch system ($[\text{NDMA}]_0 = 100 \mu\text{M}$, 0.1 g L^{-1} catalyst, pH 6.0 buffered by 10 mM MES buffer, 1 atm H_2 , $22 \pm 0.5 \text{ }^\circ\text{C}$). Error bars represent range of results from duplicate reactions (smaller than symbol if not visible).

Similar to granular Fe¹⁹ and Pd-based catalysts,²² Ru reduces the nitrosyl group ultimately to ammonia. In contrast, this group was found to be reduced to N₂ by porous Ni catalysts.²⁶ Modification of Ni catalyst with boron changes product selectivity from N₂ to ammonia.⁴⁰ It is also worth noting that the endproducts, DMA and ammonia, are both much less hazardous than NDMA.¹⁹ Furthermore, the concentrations of these endproducts that would form from typically detected concentrations of NDMA ($\leq 1 \mu\text{g L}^{-1}$) are much lower than typical concentrations of ammonia and DMA in natural water matrices.^{41, 42} Still, if necessary, these products can be oxidized chemically or biologically by introduction of a separate unit process.

4.4.3 Mechanistic considerations

As a member of Pt-group metals, Ru has low activation energy for dissociative adsorption of H₂ on its surface at ambient temperature.^{43, 44} Thus, like Pd-based catalysts, Ru-catalyzed reduction of NDMA is expected to proceed by NDMA reaction with Ru-adsorbed atomic hydrogen. A question with less obvious answer is whether there also exists a direct electron transfer reaction between reduced Ru surface atoms and NDMA. Thermodynamic considerations indicate that redox reaction is not likely. Previous study of NDMA reduction with granular iron concluded that adsorbed atomic hydrogen resulting from iron corrosion in water was responsible for NDMA reduction rather than direct electron transfer from Fe(0). This was concluded because the measured reduction potential of the Fe grains ($\geq -0.52 \text{ V}$) are higher than the required potential for reducing NDMA (approximately -1.3 V at NDMA concentrations of a few millimolar and more negative at NDMA concentrations below 1 mM).⁴⁵ Ru(0) is an even weaker reducing agent than Fe(0). For example, the formal standard reduction potential of Ru²⁺/Ru(0) is $+0.455 \text{ V}$, much higher than that of Fe²⁺/Fe(0) (-0.447 V).⁴⁶ Mediated electron transfer through the redox couple Ru³⁺/Ru²⁺ ($+0.2487 \text{ V}$) is also not close to the value required

for NDMA reduction. Figure C.1 in Appendix C confirms that without addition of H₂, no NDMA reduction occurs in Ru catalyst suspensions (catalyst suspension was pre-sparged with H₂ to ensure reduction of Ru surface atoms, but then sparged with Ar to remove dissolved H₂ from the suspension before adding NDMA). Thus, NDMA reduction most likely proceeds via hydrogenation by surface-adsorbed atomic hydrogen.

Postulated pathways of aqueous NDMA reduction with various metals mainly differ in the sequence of cleaving two bonds, i.e., N=O bond and N-N bond. Initial hydrogenation/cleavage of N=O bond features the formation of UDMH, which was only experimentally observed in systems where metal acts as sacrificing electron donor, including aluminum-nickel alloy in alkaline solution,^{47, 48} Zn powder,^{20, 49} and Cu(II) promoted Fe powder.⁷ Therefore, it is an interesting observation that small quantities of UDMH are detected from NDMA reduction on Ru surface with H₂ as an electron donor (Figure 4.3a). Experiments initiated with UDMH show slower overall reduction kinetics than observed for NDMA reduction across a range of initial substrate concentrations (Figure C.5a in Appendix C), justifying the observed UDMH generation during NDMA reduction.

Based on experimental observations in this study and insights from previous studies, a hypothesized NDMA reduction mechanism on Ru is presented in Figure 4.4. According to the Langmuir-Hinshelwood reaction mechanism, NDMA and H₂ adsorb onto Ru surface and get activated. The N=O bond of NDMA is initially hydrogenated and subsequently cleaved to form UDMH. Subsequently, scission of N-N bond in adsorbed UDMH results in unstable surface-bound DMA and amine fragments that are rapidly reduced by surface hydrogen atoms to produce the observed DMA and ammonia endproducts, consistent with the selective production of ammonia from UDMH reduction (Figure C.5b in Appendix C).

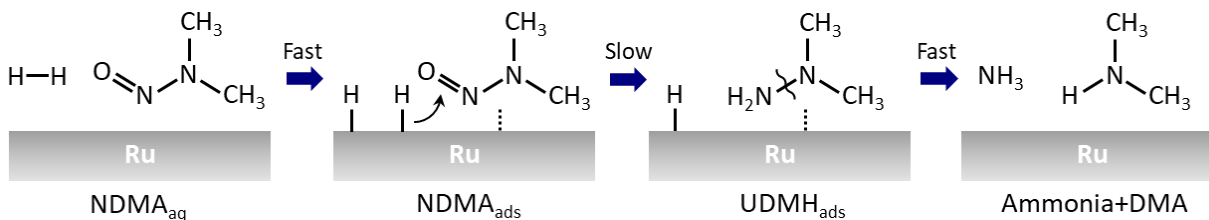


Figure 4.4 Proposed mechanism of NDMA reduction on Ru catalyst surfaces.

4.4.4 Catalytic reduction of *N*-nitrosamines under environmentally relevant conditions

Although high concentrations of NDMA (tens to hundreds of parts per billion) have been detected in groundwater at a rocket engine testing facility in Sacramento County, CA,⁴ more often the concentrations concerning wastewater and drinking water treatment facilities are $\leq 1 \mu\text{g L}^{-1}$.⁹ There is very limited study assessing catalytic technologies for NDMA or other *N*-nitrosamines at these environmentally relevant concentrations. To further demonstrate the applicability of Ru catalysts, five *N*-nitrosamines ($1 \mu\text{g L}^{-1}$ each) were simultaneously reduced with Ru/Al₂O₃ in tap water. Control experiments show little loss of *N*-nitrosamines due to adsorption in the absence of H₂ (data not shown). When H₂ sparging is present, concentrations of all five *N*-nitrosamines rapidly decreased (Figure 4.5). Data from two replicates were fitted with a pseudo-first order rate law by nonlinear least squares, and the optimal rate constants were obtained with uncertainty representing 95% confidence limits. All five *N*-nitrosamines tested are reduced at rates on the same order of magnitude, similar to the observation of four dialkyl *N*-nitrosamines and one diphenyl *N*-nitrosamine reduction catalyzed by porous nickel catalyst.²⁶ The metal weight-normalized pseudo-first-order rate constant for NDMA, NDEA, NDPA, NMOR, and NPIP are $5,700 \pm 490$, $3,530 \pm 430$, $2,950 \pm 510$, $10,400 \pm 300$, $7,510 \pm 690 \text{ L g}_{\text{Ru}}^{-1} \text{ h}^{-1}$, respectively. The observed rate constant for NDMA is comparable to that derived from extrapolation of the Langmuir-Hinshelwood model down to the initial concentration of $1 \mu\text{g L}^{-1}$

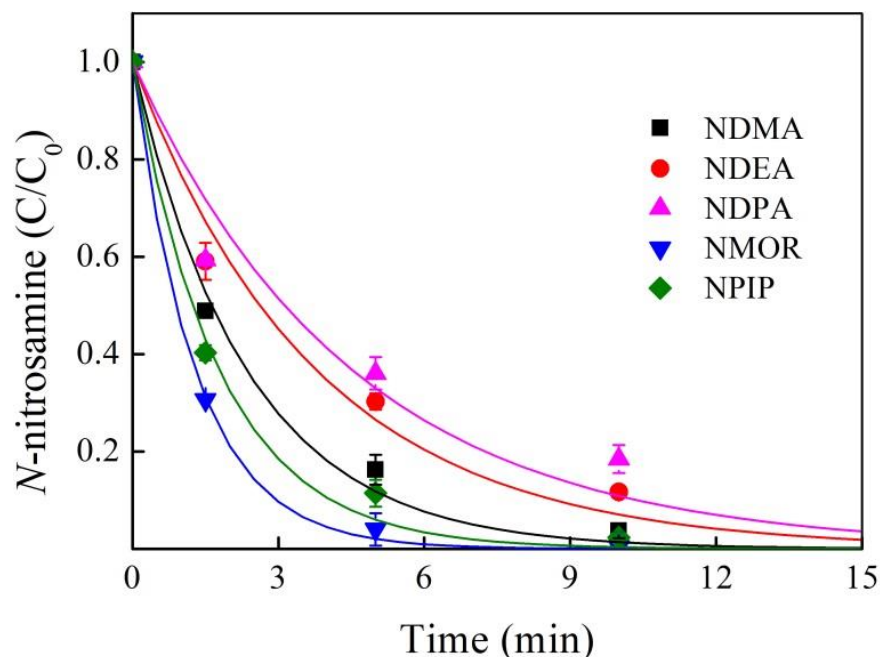


Figure 4.5 Catalytic reduction of a mixture of *N*-nitrosamines added to tap water (1 $\mu\text{g L}^{-1}$ of each *N*-nitrosamine, 0.1 g L^{-1} commercial $\text{Ru}/\text{Al}_2\text{O}_3$ catalyst, initial solution pH 9.0, continuous sparging of 1 atm H_2 , 22 ± 0.5 $^\circ\text{C}$). Lines show pseudo-first-order model fits for disappearance of each *N*-nitrosamine. Error bars represent the range of measured values in duplicate reactions (smaller than symbol if not visible).

($5,030 \text{ L g}_{\text{Ru}}^{-1} \text{ h}^{-1}$). While differences in the observed rates for the five *N*-nitrosamines were small, comparison of fit-derived rate constants reveals a relationship between molecular structure (Figure C.6 in Appendix C) and reactivity. For dialkyl *N*-nitrosamines, increasing length of alkyl group reduces reactivity, and *N*-heterocycle *N*-nitrosamines show higher reactivity than dialkyl *N*-nitrosamines. The reduction of *N*-nitrosamines observed in deionized water at these same *N*-nitrosamine concentrations is faster than in tap water (Figure C.7 in Appendix C), indicating that water matrix constituents in the tap water negatively affect catalyst activity. Future research is needed to examine in detail water matrix effects on Ru catalyzed water treatment processes, which will complement findings reported for Pd-based catalysts and advance the practical development of catalytic processes for treating contaminated sourcewaters of varying

composition. Nonetheless, the findings presented here verify effective catalytic treatment of *N*-nitrosamines at realistic micropollutant concentrations in a relevant water matrix.

4.4.5 Role of Ru catalysts in water purification and remediation toolbox

Traditional strategies to reductively transform water contaminants employ materials containing zerovalent Fe.^{50, 51} Despite their competitiveness in price, the inefficiency for removing certain contaminants,^{21, 52} stringent requirement of solution pH,⁵³ sacrificial nature and generation of iron oxides waste³⁶ prompted research for more effective and sustainable materials. Hydrogenation metal-based materials have emerged as a promising alternative. Particularly, Pd-based catalysts have demonstrated their superior performance and stability in reducing a number of drinking water contaminants.^{24, 54, 55} The fact that Pd exhibits poor activity for reduction of selected contaminants, together with the scarcity and the high cost of this metal, necessitates an expansion of the catalyst toolbox and improved mechanistic understanding of metal-catalyzed hydrogenation reactions. We have explored other Pt group metals in addition to Pd for catalytic reduction of oxyanions, and gained new understanding of reaction mechanisms of oxyanions with different metals.²⁵ Motivated by promising results for nitrate reduction with Ru, a contribution focusing on a renewed evaluation of the kinetics and mechanisms of nitrate and nitrite reduction by supported Ru catalysts followed.²⁷ The strong adsorption of nitrite and postulated reduction intermediate, nitrous oxide, and the rapid conversion of these species at low concentrations prompted the hypothesis that Ru is potentially effective for catalyzing the reduction of other water contaminants containing nitro and nitroso functional groups. This contribution reveals the extremely high activity of Ru for catalyzing the reduction of *N*-nitrosamines, including the ubiquitous contaminant NDMA, supporting the abovementioned hypothesis. To further explore the strength of Ru catalysts in water purification and remediation,

we screened Ru/Al₂O₃ and Pd/Al₂O₃ catalysts for reduction of a suit of contaminants featuring different reducible functional groups (Figure C.8 in Appendix C). Contrary to expectations, Ru is nearly one order-of-magnitude less active than Pd for 4-nitrophenol reduction. Without further in-depth investigation, an initial examination of the molecule structure suggests that the phenol group in 4-nitrophenol can affect activity in at least two ways. The presence of benzene ring and the hydroxyl group alter the adsorption geometry of nitro group, and the benzene ring donates electron to the nitro group, modifying its electron density and subsequently the adsorption energy. Despite the influence of phenol group, the TOF₀ measured for 4-nitrophenol on Ru is similar to those measured for nitrate and NDMA. We also tested Ru/Al₂O₃ activity with halogenated arenes (4-chlorophenol and diatrizoate). The activities are in the same order of magnitude as nitrate, NDMA and 4-nitrophenol. In comparison, Pd/Al₂O₃ showed much higher activity for substituted arene reduction than nitrate and NDMA reduction. Activities of Pd/Al₂O₃ for reducing 4-nitrophenol, 4-chlorophenol and diatrizoate are 6.1, 3.3, and 1.1 times higher than those of Ru/Al₂O₃, respectively. Considering the price of Ru is roughly one order-of-magnitude lower than that of Pd,²⁵ Ru can still be a viable alternative to Pd for treating these contaminants. It is also worth mentioning that Ru is also an exceptional catalyst for oxidation of water contaminants with permanganate,^{56, 57} ozone,⁵⁸ and peroxymonosulfate,⁵⁹ making it a versatile heterogeneous catalyst for water purification and remediation. Still, further research is needed to assess Ru catalyst activity and stability during continuous treatment (e.g., in packed bed reactors) of relevant water matrices. Such studies will be critical to demonstrating the feasibility this and related technology pathways.

4.5 References

1. Richardson, S. D.; Plewa, M. J.; Wagner, E. D.; Schoeny, R.; DeMarini, D. M. Occurrence, genotoxicity, and carcinogenicity of regulated and emerging disinfection by-products in drinking water: A review and roadmap for research. *Mutat. Res.-Rev. Mut. Res.* **2007**, *636* (1–3), 178-242.
2. Krasner, S. W.; Mitch, W. A.; McCurry, D. L.; Hanigan, D.; Westerhoff, P. Formation, precursors, control, and occurrence of nitrosamines in drinking water: A review. *Water Res.* **2013**, *47* (13), 4433-4450.
3. Sen, N. P.; Baddoo, P. A.; Weber, D.; Boyle, M. A sensitive and specific method for the determination of *N*-nitrosodimethylamine in drinking water and fruit drinks. *Int. J. Environ. Anal. Chem.* **1994**, *56* (2), 149-163.
4. Mitch, W. A.; Sharp, J. O.; Trussell, R. R.; Valentine, R. L.; Alvarez-Cohen, L.; Sedlak, D. L. *N*-nitrosodimethylamine (NDMA) as a drinking water contaminant: A review. *Environ. Eng. Sci.* **2003**, *20* (5), 389-404.
5. World Health Organization. *Guidelines for Drinking-Water Quality*; WHO: Geneva, Switzerland, 2011; Vol. 216, pp 303-4.
6. U.S. Environmental Protection Agency. *Chemical Contaminants - CCL 4*. <https://www.epa.gov/ccl/chemical-contaminants-ccl-4> (accessed Nov 1, 2017).
7. Han, Y.; Chen, Z.; Shen, J.; Wang, J.; Li, W.; Li, J.; Wang, B.; Tong, L. The role of Cu(II) in the reduction of *N*-nitrosodimethylamine with iron and zinc. *Chemosphere* **2017**, *167*, 171-177.
8. Li, Y.; Kemper, J. M.; Datuin, G.; Akey, A.; Mitch, W. A.; Luthy, R. G. Reductive dehalogenation of disinfection byproducts by an activated carbon-based electrode system. *Water Res.* **2016**, *98*, 354-362.
9. Plumlee, M. H.; López-Mesas, M.; Heidlberger, A.; Ishida, K. P.; Reinhard, M. *N*-nitrosodimethylamine (NDMA) removal by reverse osmosis and UV treatment and analysis via LC-MS/MS. *Water Res.* **2008**, *42* (1), 347-355.
10. Lee, C.; Choi, W.; Kim, Y. G.; Yoon, J. UV photolytic mechanism of *N*-nitrosodimethylamine in water: Dual pathways to methylamine versus dimethylamine. *Environ. Sci. Technol.* **2005**, *39* (7), 2101-2106.
11. Sedlak, D. L.; Deeb, R. A.; Hawley, E. L.; Mitch, W. A.; Durbin, T. D.; Mowbray, S.; Carr, S. Sources and fate of nitrosodimethylamine and its precursors in municipal wastewater treatment plants. *Water Environ. Res.* **2005**, *77* (1), 32-39.
12. Beita-Sandí, W.; Ersan, M. S.; Uzun, H.; Karanfil, T. Removal of *N*-nitrosodimethylamine precursors with powdered activated carbon adsorption. *Water Res.* **2016**, *88*, 711-718.

13. Miyashita, Y.; Park, S.-H.; Hyung, H.; Huang, C.-H.; Kim, J.-H. Removal of *N*-nitrosamines and their precursors by nanofiltration and reverse osmosis membranes. *J. Environ. Eng.* **2009**, *135* (9), 788-795.
14. Gunnison, D.; Zappi, M. E.; Teeter, C.; Pennington, J. C.; Bajpai, R. Attenuation mechanisms of *N*-nitrosodimethylamine at an operating intercept and treat groundwater remediation system. *J. Hazard. Mater.* **2000**, *73* (2), 179-197.
15. Lee, C.; Yoon, J.; Von Gunten, U. Oxidative degradation of *N*-nitrosodimethylamine by conventional ozonation and the advanced oxidation process ozone/hydrogen peroxide. *Water Res.* **2007**, *41* (3), 581-590.
16. Buxton, G. V.; Greenstock, C. L.; Helman, W. P.; Ross, A. B. Critical review of rate constants for reactions of hydrated electrons, hydrogen atoms and hydroxyl radicals ($\cdot\text{OH}/\cdot\text{O}^-$) in aqueous solution. *J. Phys. Chem. Ref. Data* **1988**, *17* (2), 513-886.
17. Mezyk, S. P.; Cooper, W. J.; Madden, K. P.; Bartels, D. M. Free radical destruction of *N*-nitrosodimethylamine in water. *Environ. Sci. Technol.* **2004**, *38* (11), 3161-3167.
18. Sun, Z.; Zhang, C.; Zhao, X.; Chen, J.; Zhou, Q. Efficient photoreductive decomposition of *N*-nitrosodimethylamine by UV/iodide process. *J. Hazard. Mater.* **2017**, *329*, 185-192.
19. Gui, L.; Gillham, R. W.; Odziemkowski, M. S. Reduction of *N*-nitrosodimethylamine with granular iron and nickel-enhanced iron. 1. Pathways and kinetics. *Environ. Sci. Technol.* **2000**, *34* (16), 3489-3494.
20. Han, Y.; Chen, Z.; Tong, L.; Yang, L.; Shen, J.; Wang, B.; Liu, Y.; Liu, Y.; Chen, Q. Reduction of *N*-nitrosodimethylamine with zero-valent zinc. *Water Res.* **2013**, *47* (1), 216-224.
21. Davie, M. G.; Reinhard, M.; Shapley, J. R. Metal-catalyzed reduction of *N*-nitrosodimethylamine with hydrogen in water. *Environ. Sci. Technol.* **2006**, *40* (23), 7329-7335.
22. Davie, M. G.; Shih, K.; Pacheco, F. A.; Leckie, J. O.; Reinhard, M. Palladium-indium catalyzed reduction of *N*-nitrosodimethylamine: Indium as a promoter metal. *Environ. Sci. Technol.* **2008**, *42* (8), 3040-3046.
23. Shuai, D.; McCalman, D. C.; Choe, J. K.; Shapley, J. R.; Schneider, W. F.; Werth, C. J. Structure sensitivity study of waterborne contaminant hydrogenation using shape- and size-controlled Pd nanoparticles. *ACS Catal.* **2013**, *3* (3), 453-463.
24. Chen, H.; Xu, Z.; Wan, H.; Zheng, J.; Yin, D.; Zheng, S. Aqueous bromate reduction by catalytic hydrogenation over Pd/Al₂O₃ catalysts. *Appl. Catal., B* **2010**, *96* (3-4), 307-313.
25. Chen, X.; Huo, X.; Liu, J.; Wang, Y.; Werth, C. J.; Strathmann, T. J. Exploring beyond palladium: Catalytic reduction of aqueous oxyanion pollutants with alternative platinum group metals and new mechanistic implications. *Chem. Eng. J.* **2017**, *313*, 745-752.

26. Frierdich, A. J.; Shapley, J. R.; Strathmann, T. J. Rapid reduction of *N*-nitrosamine disinfection byproducts in water with hydrogen and porous nickel catalysts. *Environ. Sci. Technol.* **2008**, *42* (1), 262-269.
27. Huo, X.; Van Hoomissen, D. J.; Liu, J.; Vyas, S.; Strathmann, T. J. Hydrogenation of aqueous nitrate and nitrite with ruthenium catalysts. *Appl. Catal., B* **2017**, *211*, 188-198.
28. Karim, A. M.; Prasad, V.; Mpourmpakis, G.; Lonergan, W. W.; Frenkel, A. I.; Chen, J. G.; Vlachos, D. G. Correlating particle size and shape of supported Ru/ γ -Al₂O₃ catalysts with NH₃ decomposition activity. *J. Am. Chem. Soc.* **2009**, *131* (34), 12230-12239.
29. Yin, S.-F.; Zhang, Q.-H.; Xu, B.-Q.; Zhu, W.-X.; Ng, C.-F.; Au, C.-T. Investigation on the catalysis of CO_x-free hydrogen generation from ammonia. *J. Catal.* **2004**, *224* (2), 384-396.
30. García-García, F. R.; Guerrero-Ruiz, A.; Rodríguez-Ramos, I. Role of B5-type sites in Ru catalysts used for the NH₃ decomposition reaction. *Top. Catal.* **2009**, *52* (6), 758-764.
31. Denisov, A. A.; Smolenkov, A. D.; Shpigun, O. A. Determination of 1,1-dimethylhydrazine by reversed-phase high-performance liquid chromatography with spectrophotometric detection as a derivative with 4-nitrobenzaldehyde. *J. Anal. Chem.* **2004**, *59* (5), 452-456.
32. Jadbabaei, N.; Ye, T.; Shuai, D.; Zhang, H. Development of palladium-resin composites for catalytic hydrodechlorination of 4-chlorophenol. *Appl. Catal., B* **2017**, *205*, 576-586.
33. Daneshvar, N.; Behnajady, M. A.; Zorriyeh Asghar, Y. Photooxidative degradation of 4-nitrophenol (4-NP) in UV/H₂O₂ process: Influence of operational parameters and reaction mechanism. *J. Hazard. Mater.* **2007**, *139* (2), 275-279.
34. Knitt, L. E.; Shapley, J. R.; Strathmann, T. J. Rapid metal-catalyzed hydrodehalogenation of iodinated X-ray contrast media. *Environ. Sci. Technol.* **2008**, *42* (2), 577-583.
35. Munch, J.; Basset, M. Method 521. *Determination of nitrosamines in drinking water by solid-phase extraction and capillary column gas chromatography with large volume injection and chemical ionization tandem mass spectrometry (MS/MS)*; U.S. Environmental Protection Agency: Cincinnati, OH, 2004.
36. Chen, H.; Li, T.; Jiang, F.; Wang, Z. Enhanced catalytic reduction of *N*-nitrosodimethylamine over bimetallic Pd-Ni catalysts. *J. Mol. Catal. A: Chem.* **2016**, *421*, 167-177.
37. Pintar, A.; Batista, J.; Levec, J.; Kajiuchi, T. Kinetics of the catalytic liquid-phase hydrogenation of aqueous nitrate solutions. *Appl. Catal., B* **1996**, *11* (1), 81-98.
38. Ranea, V. A.; Strathmann, T. J.; Shapley, J. R.; Schneider, W. F. DFT Comparison of *N*-nitrosodimethylamine decomposition pathways over Ni and Pd. *ChemCatChem* **2011**, *3* (5), 898-903.

39. Gómez-Quero, S.; Cárdenas-Lizana, F.; Keane, M. A. Effect of metal dispersion on the liquid-phase hydrodechlorination of 2,4-dichlorophenol over Pd/Al₂O₃. *Ind. Eng. Chem. Res.* **2008**, *47* (18), 6841-6853.
40. Frierdich, A. J.; Joseph, C. E.; Strathmann, T. J. Catalytic reduction of *N*-nitrosodimethylamine with nanophase nickel-boron. *Appl. Catal. B-Environ.* **2009**, *90* (1-2), 175-183.
41. Turan, M.; Celik, M. S. Regenerability of Turkish clinoptilolite for use in ammonia removal from drinking water. *J. Water Supply Res. T.* **2003**, *52* (1), 59-66.
42. Gerecke, A. C.; Sedlak, D. L. Precursors of *N*-nitrosodimethylamine in natural waters. *Environ. Sci. Technol.* **2003**, *37* (7), 1331-1336.
43. Bond, G. C. Chemisorption and reactions of hydrogen. In *Metal-Catalysed Reactions of Hydrocarbons*; Springer US: Boston, MA, 2005; pp 93-152.
44. Norskov, J. K.; Bligaard, T.; Rossmeisl, J.; Christensen, C. H. Towards the computational design of solid catalysts. *Nat. Chem.* **2009**, *1* (1), 37-46.
45. Odziemkowski, M. S.; Gui, L.; Gillham, R. W. Reduction of *N*-nitrosodimethylamine with granular iron and nickel-enhanced iron. 2. Mechanistic studies. *Environ. Sci. Technol.* **2000**, *34* (16), 3495-3500.
46. Vanýsek, P. Electrochemical series. In *CRC Handbook of Chemistry and Physics*; 91st ed.; Haynes, W. M., Ed. Taylor & Francis: Boca Raton, FL, 2010-2011; pp 8-21/23.
47. Lunn, G.; Sansone, E. B.; Keefer, L. K. Safe disposal of carcinogenic nitrosamines. *Carcinogenesis* **1983**, *4* (3), 315-319.
48. Lunn, G.; Sansone, E. B.; Keefer, L. K. General cleavage of N-N and N-O bonds using nickel/aluminum alloy. *Synthesis* **1985**, *1985* (12), 1104-1108.
49. Hayes, B. T.; Stevens, T. S. Reduction of nitrosamines to hydrazines. *J. Chem. Soc. C* **1970**, *0*, 1088-1089.
50. Sayles, G. D.; You, G.; Wang, M.; Kupferle, M. J. DDT, DDD, and DDE dechlorination by zero-valent iron. *Environ. Sci. Technol.* **1997**, *31* (12), 3448-3454.
51. Wilkin, R. T.; Su, C.; Ford, R. G.; Paul, C. J. Chromium-removal processes during groundwater remediation by a zerovalent iron permeable reactive barrier. *Environ. Sci. Technol.* **2005**, *39* (12), 4599-4605.
52. Choe, J. K.; Shapley, J. R.; Strathmann, T. J.; Werth, C. J. Influence of rhenium speciation on the stability and activity of Re/Pd bimetal catalysts used for perchlorate reduction. *Environ. Sci. Technol.* **2010**, *44* (12), 4716-4721.

53. Huang, C.-P.; Wang, H.-W.; Chiu, P.-C. Nitrate reduction by metallic iron. *Water Res.* **1998**, *32* (8), 2257-2264.
54. McNab, W. W.; Ruiz, R.; Reinhard, M. In-situ destruction of chlorinated hydrocarbons in groundwater using catalytic reductive dehalogenation in a reactive well: Testing and operational experiences. *Environ. Sci. Technol.* **2000**, *34* (1), 149-153.
55. Chaplin, B. P.; Reinhard, M.; Schneider, W. F.; Schuth, C.; Shapley, J. R.; Strathmann, T. J.; Werth, C. J. Critical review of Pd-based catalytic treatment of priority contaminants in water. *Environ. Sci. Technol.* **2012**, *46* (7), 3655-3670.
56. Zhang, J.; Sun, B.; Guan, X.; Wang, H.; Bao, H.; Huang, Y.; Qiao, J.; Zhou, G. Ruthenium Nanoparticles Supported on CeO₂ for Catalytic Permanganate Oxidation of Butylparaben. *Environ. Sci. Technol.* **2013**, *47* (22), 13011-13019.
57. Zhang, J.; Sun, B.; Xiong, X.; Gao, N.; Song, W.; Du, E.; Guan, X.; Zhou, G. Removal of emerging pollutants by Ru/TiO₂-catalyzed permanganate oxidation. *Water Res.* **2014**, *63*, 262-270.
58. Delanoë, F.; Acedo, B.; Karpel Vel Leitner, N.; Legube, B. Relationship between the structure of Ru/CeO₂ catalysts and their activity in the catalytic ozonation of succinic acid aqueous solutions. *Appl. Catal., B* **2001**, *29* (4), 315-325.
59. Muhammad, S.; Shukla, P. R.; Tadé, M. O.; Wang, S. Heterogeneous activation of peroxymonosulphate by supported ruthenium catalysts for phenol degradation in water. *J. Hazard. Mater.* **2012**, *215*, 183-190.

CHAPTER 5

A HYBRID CATALYTIC HYDROGENATION/MEMBRANE DISTILLATION PROCESS FOR NITROGEN RESOURCE RECOVERY FROM NITRATE-CONTAMINATED WASTE ION EXCHANGE BRINES

This chapter is in preparation

Xiangchen Huo, Johan Vanneste, Tzahi Y. Cath, and Timothy J. Strathmann

5.1 Abstract

Ion exchange is a common approach to treating nitrate-contaminated ground water. To reduce salt usage and waste brine disposal following from resin regeneration, catalyst treatment systems have been evaluated and show promise for reducing both life cycle costs and environmental impacts. Past efforts focused on improving nitrate removal kinetics and selectivity to the N_2 reduction product versus NH_3 , but the potential value of nitrogen resources has been overlooked in this approach. This work evaluated a hybrid catalytic hydrogenation/membrane distillation process for nitrogen resource recovery from nitrate-contaminated waste ion exchange brines. A commercial Ru/C catalyst with high selectivity for ammonia production was tested for nitrate hydrogenation and showed capability to reduce a wide concentration range of nitrate under typical waste brine conditions, including conditions representative of expected salt buildup upon brine reuse. The apparent rate constant for nitrate reduction was influenced by both solution chemistry and reaction temperature. In the second stage of the hybrid process, membrane distillation efficiently recovered ammonia from the brine matrix, capturing nitrogen

X.H. performed most of the experiments and analyzed data; J.V. and Z.Y.C. assisted membrane distillation experiments and provided helpful advice; X.H. and T.J.S. wrote the manuscript with input from all authors. All authors are affiliated with Colorado School of Mines.

as ammonium sulfate, a commercial fertilizer product. At low temperatures (<35 °C), solution pH significantly influenced the ammonia mass transfer coefficient through the membrane by controlling the fraction of free ammonia species present. Ammonia recovery efficiency was not affected by salt levels, indicating the feasibility of membrane distillation for recovering ammonia from reused brine as well. Application of the hybrid catalytic hydrogenation/membrane distillation process to a real ion exchange waste brine showed both high rates of nitrate hydrogenation and ammonia recovery. These findings provide alternative lower-cost catalyst for treatment of ion exchange waste brine to allow for both waste brine reuse and nitrogen resource recovery.

5.2 Introduction

Industrial nitrogen fixation through energy-intensive Haber-Bosch process has been playing a critical role in sustainable food supply. However, a significant portion of this nitrogen resource exits agricultural and industrial activities as waste and enters surface and ground waters, endangering aquatic environments and ecosystems.¹ Particularly, nitrate in drinking water has been recognized as a human health hazard, for which health guidelines and regulations have been established to protect populations from its adverse effects. Therefore, there has been a considerable interest in developing technologies for nitrate removal from impacted drinking water sources.²⁻⁵

Ion exchange is a common approach to treating nitrate-contaminated ground water and has been proven effective at multiple drinking water treatment plants.⁶ Due to their finite exchange capacities, anion exchange resins (AER) require periodic regeneration using a concentrated salt solution (commonly sodium chloride or sodium bicarbonate). This regeneration process results in nitrate-contaminated waste brine, incurring operation and maintenance (O&M)

costs associated with brine makeup and disposal.^{7, 8} Disposal of waste brine containing regenerant salt residue also reduces salt use efficiency and increases fresh salt demand, which significantly increases O&M costs.⁹ Thus, strategies to increase salt use efficiency and minimize brine waste are critical to improving the economics and environmental sustainability on ion exchange processes for drinking water treatment.

Transforming nitrate to gaseous species or aqueous species that have much lower affinity to the AER can potentially enable brine recycling and minimize salt inputs. The highly oxidized state of nitrogen in nitrate allows it to be reductively transformed, either biologically, chemically or catalytically.¹⁰⁻¹⁴ Efforts have typically focused on selectively converting nitrate to gaseous N₂ and minimizing byproduct formation including nitrite, N₂O_(g), and ammonia.^{2, 15, 16}

Catalytic hydrogenation is among the emerging nitrate transformation technologies and considered to have potential for industrial applications.^{17, 18} Advantages of this technology include short start-up times, fast reactions, use of a clean reducing agent that can be produced renewably (H₂), low possibility of bacterial contamination, and minimal production of contaminated disposals.^{5, 19-22} The most common reactor configurations for catalytic hydrogenation are three-phase reactors (e.g., semi-batch, fixed bed) where a metal surface catalyzes aqueous nitrate reduction by H_{2(g)}, a reductant with lower life cycle environmental impacts than organic donors used for biological reduction.²³ Supported bimetallic Pd catalysts (e.g., Pd-Cu, Pd-In, Pd-Sn) have been most extensively studied due to their high activity and tunable selectivity towards N₂.^{16, 19, 24-26} Studies with these catalysts have shown that some natural water constituents can significantly influence catalyst reactions with nitrate through competitive adsorption or modification of catalyst surface.²⁷⁻²⁹ These results are particularly important as they predict inhibitory effects of high salt levels ion exchange waste brines, which

were confirmed for Pd-In catalysts in recent studies performed in brine matrices.^{8, 21, 22} Despite these reports, brine reuse enabled by catalytic hydrogenation of nitrate is a promising strategy to significantly bring down salt costs and reduce environmental impacts associated with conventional ion exchange treatment processes.^{21, 22}

Reductive transformation of concentrated nitrate in ion exchange brine, including catalytic hydrogenation, often results in ammonia formation.^{15, 22, 30} Although selectivity to ammonia has typically been deemed undesirable when directly treating drinking water, ammonia species have potential value as fertilizer products. Therefore, conversion to ammonia can be advantageous if a suitable process for recovering the endproduct is available, and opportunities for recovering ammonia are most practical in matrices where nitrate concentrations are elevated like waste brines (where nitrogen concentrations can reach g/L levels).^{15, 31, 32} In this work, we describe efforts aimed at evaluating a hybrid catalytic hydrogenation/membrane distillation process for ion exchange waste brine nitrate treatment and nitrogen recovery (Figure 5.1). Specifically, we assessed treatment of nitrate-contaminated ion exchange waste brines using a commercial Ru/C catalyst, an alternative to much more costly Pd-based catalysts, which was recently reported to exhibit complete selectivity to ammonia when treating nitrate-contaminated freshwater matrices.⁴ The catalytic hydrogenation process was studied in a stirred semi-batch reactor, a reactor design suitable for treating highly concentrated nitrate solutions.²¹ Membrane distillation was then applied to recover the ammonia product from the waste brine as ammonium sulfate (NH_4)₂SO₄, a potentially valuable fertilizer product.³³⁻³⁵ Experiments using synthetic waste solutions were conducted to identify critical operating parameters of both the hydrogenation and membrane distillation processes, and a demonstration of the integrated process with real ion exchange waste brine obtained from a drinking water utility is presented.

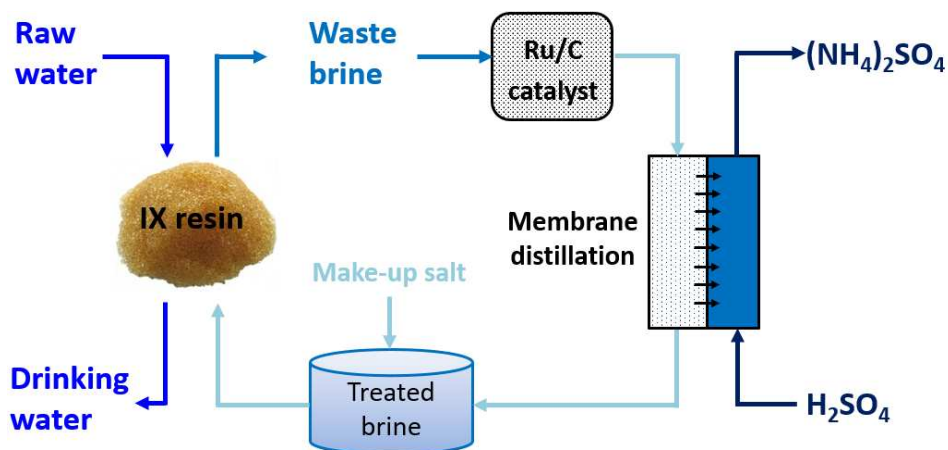


Figure 5.1 Flow diagram of the hybrid catalytic hydrogenation/membrane distillation process to enable ion exchange regenerant brine reuse and nitrogen resource recovery.

5.3 Materials and Methods

5.3.1 Materials

Ru/C catalyst powder with a nominal Ru loading of 5 wt% was purchased from Sigma Aldrich and used as received. Detailed characterization of this material was described previously.⁴ This catalyst exhibited high surface area and Ru metal dispersion. Sodium nitrate and ammonium chloride were also obtained from Sigma Aldrich. Sodium sulfate, sodium bicarbonate, ammonium hydroxide solution, sodium hydroxide, and hydrochloric acid were acquired from Fisher Scientific. Concentrated sulfuric acid was purchased from EMD Millipore. Ultra-high purity H₂ gas was supplied by General Air. Ion exchange waste brine was collected from a drinking water treatment plant in California. Composition of the waste brine is summarized in Table 5.1.

5.3.2 Catalytic hydrogenation experiments

To determine the influence of operating parameters on nitrate hydrogenation efficiency, kinetic studies were conducted with synthetic brine solutions using a procedure adapted from a previous study.⁴ Predetermined mass of Ru/C and a test solution (120 mL) of designed salt

concentrations (NaCl, NaHCO₃, and/or Na₂SO₄) were added to a 250 mL three-neck flask equipped with rubber stoppers and a Teflon-coated magnetic stir bar. The loading of Ru/C was chosen to achieve a condition where external mass transfer limitations are absent. Prior to the reaction, Ru/C was reduced overnight in the suspension (constant stirring, 1100 rpm) at room temperature under 1 atm H₂ headspace by flowing H₂ gas through the reactor (300 mL min⁻¹). Reaction was initiated by adding a concentrated NaNO₃ stock solution (5 M) to achieve the designed initial nitrate concentration (50-200 mM). Reaction temperature was maintained with a water bath calibrated by an external thermometer. The change of solution pH over the course of reaction was monitored by using a pH probe (Orion™ double junction combination pH electrode, calibrated by standard NIST buffers, apparent pH values were reported). In the case where the effect of pH on reactions was evaluated, solution pH was maintained by adding HCl solution from an automatic pH-stat (Metrohm). Aliquots of the catalyst suspension (1.5 mL) were periodically collected by a syringe and immediately filtered (0.45 μm cellulose acetate) to quench the reaction. The filtrate was diluted with deionized water and analyzed for nitrate, nitrite, and/or ammonia concentrations. All experiments were performed in duplicate.

The procedure for catalytic hydrogenation of real waste brine was modified to avoid the complication of parallel *in situ* catalyst reduction and nitrate reduction. Prior to the reaction, a Ru/C slurry (0.6 g Ru/C in 10 mL deionized water) was reduced overnight under H₂ flow (300 mL min⁻¹) at room temperature. Reaction was then initiated by introducing 100 mL waste brine to the flask containing the pre-reduced catalyst. As a control, experiments were also conducted in a synthetic brine prepared to mimic the major ion composition of the real waste brine. For tests with CO_{2(g)} as a pH buffer, CO₂ was introduced to the reactor at 65 mL min⁻¹. The rest of the procedure follows that as previously described. A catalyst recycle experiment was also carried

Table 5.1 Ion exchange waste brine composition.

Component	Concentration (mg/L)
pH	8.5
Inorganic C	3,057
DOC	8.8
Alkalinity	13,100 mg/L as CaCO ₃ (232 mM as NaHCO ₃)
Major anions	
Cl ⁻	13,685 (2.3 wt% as NaCl)
NO ₂ ⁻	<15 (detection limit)
NO ₃ ⁻	9,262 (149 mM)
SO ₄ ²⁻	4,346 (45 mM)
PO ₄ ³⁻	<15 (detection limit)
Major cation	
Na ⁺	16,860
Other metals	
K	35.7
Mg	15.8
Ca	5.8
Cr	2.9
V	1.2
Li	0.6
Mo	0.5
Sr	0.2

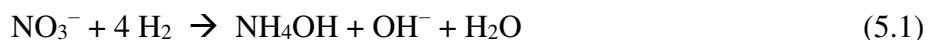
out to evaluate the reusability of Ru/C for waste brine treatment. At the end of the reaction, the catalyst was collected by filtering the suspension with a membrane filter (0.45 μm cellulose acetate), washed with deionized water several times, and dried in air at 70 °C before reusing.

5.3.3 Membrane distillation experiments

A bench-scale membrane distillation assembly was operated in batch mode to recover ammonia from synthetic solutions or catalytically hydrogenated real waste brine (Figure 5.2). The membrane cell was custom-made acrylic plastic cell, and spacers were used in both the feed and the acid adsorbent channels of the cell. A hydrophobic, microporous membrane acquired from Clarcor Industrial Air (QL822) was tested in this study. The membrane is a polypropylene backed PTFE membrane having a nominal pore size of 0.45 μm with the functional layer in contact with the feed. Three cells were used in sequence, and each cell had a membrane surface area of 195 cm². The experiments were performed using co-current flow to minimize the local

pressure differential across the membrane. The feed stream was pumped continuously during operation using a positive-displacement gear pump (Micropump Integral Series, IDEX Corp. Vancouver, WA). The acid adsorbent stream was pumped continuously using a peristaltic pump (Masterflex L/S Series, Cole-Parmer, USA). Flow rates of the feed and the acid adsorbent were kept equal. A heat exchanger was used to control the temperature of the feed stream. Membrane integrity was tested prior to experiments to validate integrity and ensure that the membranes are not wetted.

Four liters of feed solution was used for each batch experiment. Sulfuric acid solution (0.25 M, 1-2 L) was prepared from concentrated sulfuric acid and used as acid adsorbent. Kinetic studies were conducted with synthetic solutions to examine the impact of operating parameters on ammonia recovery efficiency. The synthetic solutions were prepared by dissolving predetermined amount of salts (NaCl, NaHCO₃, and/or Na₂SO₄), NH₄OH aqueous solution, and base (NaOH) in deionized water. The amount of NH₄OH and NaOH was determined through the following reaction stoichiometry assuming complete hydrogenation of nitrate:



Time zero was recorded once the feed reached the designed temperature (heat-up time 1-2 min), and the test duration was 60 min. The initial pH of the feed and pH at the end of a test were recorded. Feed solution was sampled periodically (8-10 mL) to track the change of total ammonia concentration. For selected tests, acid adsorbent solution was also sampled (1 mL) to evaluate the mass balance on ammonia in the system. Batch experiments were performed in duplicate. The procedure for catalytically treated real waste brine was the same as for synthetic solutions.

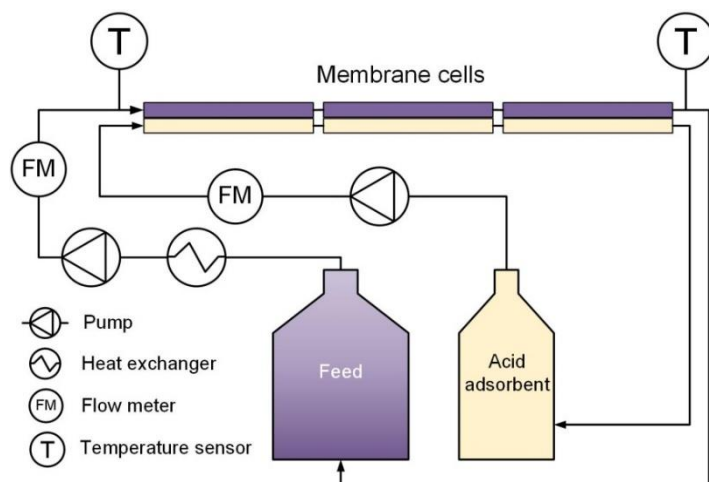


Figure 5.2 Schematic diagram of the bench scale membrane distillation system.

5.3.4 Aqueous analysis

Anions, including Cl^- , NO_3^- , SO_4^{2-} , NO_2^- , and PO_4^{3-} , were quantified by ion chromatography with conductivity detection (ICS-90, Dionex, Sunnyvale, CA). Metals were quantified by inductively coupled plasma–atomic emission spectroscopy (ICP-AES; Optima 5300, Perkin-Elmer, Fremont, CA). ICP samples were acidified with nitric acid to a pH <2 before analysis. Total ammonia ($\text{NH}_3/\text{NH}_4^+$) was analyzed by colorimetric analysis (Hach salicylate method). Alkalinity was measured by titration with 1 N H_2SO_4 . Dissolved organic carbon (DOC) and inorganic carbon were determined using a total organic carbon analyzer (Shimadzu TOC-L, Columbia, MD).

5.4 Results and Discussion

5.4.1 Catalytic hydrogenation of nitrate

Catalytic hydrogenation tests with Ru/C were initially conducted in synthetic brine solutions to assess the influence of major anions and operating conditions on nitrate hydrogenation rates. A baseline testing condition was chosen to facilitate the evaluation process, where an initial NaNO_3 concentration of 100 mM was reduced in a brine matrix (5 wt% NaCl,

100 mM NaHCO₃, 100 mM Na₂SO₄) at 30°C without controlling solution pH. The elevated initial concentration was selected to mimic conditions observed previously in waste ion exchange regenerant brines.^{15, 22} To verify that reaction rates were not subject to external mass transfer limitations, the initial nitrate hydrogenation rate was measured for catalyst loadings ranging from 1 to 7.5 g L⁻¹. It was observed that the initial reaction rate linearly increased with the catalyst loading (Figure D.1 in Appendix D), consistent with no external mass transfer limitation. However, the possibility of internal mass transfer limitation cannot be ruled out. A catalyst loading of 5 g L⁻¹ was then selected to use in subsequent experiments.

The kinetics of nitrate hydrogenation with Ru/C under baseline testing condition can be characterized by the zero-order rate law to at least the first half-life (Figure 5.3). Similarly, zero-order kinetics has been observed for hydrogenation of concentrated nitrate (81 mM) with Pd-In/C catalyst in both freshwater and synthetic brine solutions, and was attributed to saturation of active catalyst surface sites by the elevated concentrations of nitrate and other anions.²¹ To obtain a quantitative description of apparent catalyst activity for comparison with other operating conditions and literature values, the experimental data were fit with a zero-order kinetic model (Eq. 5.2) to the first half-life:

$$C_{\text{nitrate}, t} = C_{\text{nitrate}, 0} - k_0 t \quad (5.2)$$

where $C_{\text{nitrate}, 0}$ is the initial nitrate concentration (mM), $C_{\text{nitrate}, t}$ is the nitrate concentration at reaction time t (min), k_0 is the apparent zero-order rate constant (mM min⁻¹). To compare catalyst activity with existing literature, k_0 was normalized to Ru mass (mM min⁻¹ g_{Ru}⁻¹) by using loading of Ru metal in the reactor suspension (g_{Ru} L⁻¹). Under the baseline testing condition, k_0 was found to be 0.30 ± 0.03 mM min⁻¹ g_{Ru}⁻¹. This value falls within the same order-of-magnitude as values reported for Pd-In/C catalysts using a similar semi-batch reactor (11-50 mgNO₃⁻ min⁻¹ g_{Pd}⁻¹

¹),²¹ suggesting that applying Ru/C for nitrate hydrogenation in ion exchange waste brine is technically feasible. This is also notable because Ru is significantly less expensive than Pd.^{4, 36-59}

The influence of critical operating parameters, including solution pH, salt levels, initial nitrate concentration, and temperature, were then evaluated. Because the reaction produces hydroxide (or consumes proton) as shown in Eq. 5.1, the solution pH increases as nitrate hydrogenation proceeds in the absence of a buffer. Under the baseline condition, solution pH increased from an initial value of 9.5 to 12.6 by the end of the reaction (Figure 5.3). To evaluate the potential influence of solution pH, apparent zero-order rate constants were determined for reactions where pH was maintained by automatic pH-stat (with HCl addition). Two solution pH conditions were tested, circum-neutral (pH 7.5) and basic (pH 11). The difference in catalyst activity between these two conditions was within 20% (entries no. 2 and 3 in Table 5.2), with the apparent rate constant slightly higher under basic conditions. At first glance, the limited effect of solution pH appears to conflict with findings reported previously for the same catalyst reacting with lower initial nitrate concentrations (1.6 mM), where the first-order reaction constant decreased at high pH conditions.⁴ The inhibitory effects of increasing hydroxide ion concentrations has been reported for hydrogenation of nitrite and bromate with Pd catalysts and attributed to the inhibition of oxyanion adsorption as surfaces become more negatively charged at high pH conditions.³⁷⁻³⁹ However, the hydroxide concentrations under the two solution pH conditions (0.32 μ M for pH 7.5 and 1.0 mM for pH 11) are considerably lower than nitrate concentration in the brine matrix, explaining the much smaller difference between the apparent zero-order rate constants observed here. In the absence of pH control (entry no. 4 in Table 5.2), the apparent zero-order rate constant increased 46%, despite the rapid increase in solution pH. This observation suggests that the chloride introduced during pH control (from use of HCl in the

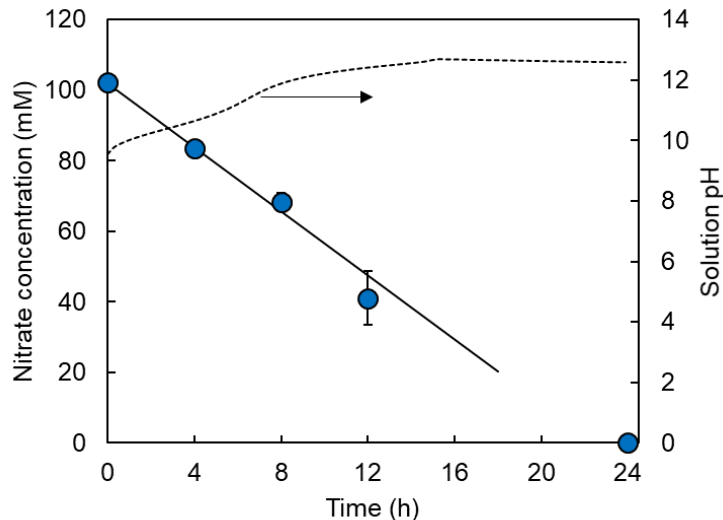


Figure 5.3 Catalytic nitrate hydrogenation under baseline testing condition and evolution of solution pH. Conditions: 5 g L⁻¹ Ru/C, initial [NO₃⁻] = 100 mM, brine matrix (5 wt% NaCl, 100 mM NaHCO₃, 100 mM Na₂SO₄), 30°C, no solution pH control, 1 atm H₂ headspace maintained by flowing H₂ at ca. 300 mL min⁻¹. Error bars indicate standard deviation from duplicate measurements (smaller than symbol if not visible). Solid line indicates zero-order rate law fit. Dashed line indicates change in measured pH during the reaction.

pH stat) may have inhibitory effects on nitrate hydrogenation activity.

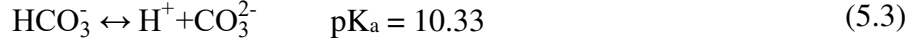
Three major non-target anions in waste brines and reused brines (i.e., chloride, bicarbonate, and sulfate) were then examined for their influence on nitrate hydrogenation activity. These anions have been reported to exert negligible or negative effects on nitrate reduction with Pd-based catalysts.^{21, 22, 29} Therefore, it was surprising to find that the apparent rate constant observed in the absence of all these anions was 40% lower than that observed under the baseline condition. Unlike chloride and sulfate, bicarbonate is acid-base reactive. Tests were then performed to evaluate bicarbonate and the two other anions separately. With a solution containing only bicarbonate and nitrate (entry no. 5 in Table 5.2), the observed rate constant increased significantly to 0.58 ± 0.01 mM min⁻¹ g_{Ru}⁻¹, more than twice the rate observed under the baseline condition, suggesting an inhibitive effect of chloride and sulfate anions. This conclusion was confirmed by results at higher salt levels (entry no. 6 in Table 5.2), where a two-

Table 5.2 Summary of nitrate hydrogenation zero-order rate constants under different reaction conditions (1 atm H₂, Ru/C dose 5 g L⁻¹)

Test no.	NaCl %	NaHCO ₃ ^a mM	Na ₂ SO ₄ mM	NaNO ₃ ^a mM	Temp °C	pH	k ₀ mM min ⁻¹ g _{Ru} ⁻¹
Baseline condition							
1	5	100	100	100	30	No control	0.30 ± 0.03
Effect of solution pH							
2	0	0	0	100	30	7.5	0.09 ± 0.01
3	0	0	0	100	30	11	0.11 ± 0.01
Effect of salts							
4	0	0	0	100	30	No control	0.15 ± 0.01
5	0	100	0	100	30	No control	0.58 ± 0.01
6	10	100	200	100	30	No control	0.10 ± 0.01
7	5	0	100	100	30	No control	0.16 ± 0.03
Effect of initial nitrate concentration							
8	5	100	100	50	30	No control	0.70 ± 0.07
9	5	100	100	200	30	No control	0.08 ± 0.01
Effect of temperature							
10	5	100	100	100	25	No control	0.18 ± 0.01
11	5	100	100	100	35	No control	0.32 ± 0.04

^aAmounts initially added.

fold increase in the concentrations of these two anions lowered the apparent rate constant by 37% compared with the baseline condition. These results are consistent with observations with Pd-based catalysts. More interestingly, addition of bicarbonate showed a positive effect on nitrate hydrogenation with Ru/C. For example, the apparent rate constant observed in solution containing both bicarbonate and nitrate was nearly four times higher than that observed in the absence of bicarbonate (entries no. 4 and 5 in Table 5.2). Also, when bicarbonate was eliminated from the baseline testing condition the apparent rate constant decreased by 62% (entry no.7 in Table 5.2). Positive effects of bicarbonate on nitrate reduction activity have only been reported when co-feeding CO₂ to maintain the solution acidity.^{40, 41} Under conditions where the solution pH was maintained by adding HCl, higher concentration of bicarbonate led to reduced activity, similar to two other anions.²¹ Therefore, the promoting effect of bicarbonate may be associated with its ability to donate proton:



For example, under the baseline testing condition, the solution pH rose past the bicarbonate pK_a value in less than 2 h, suggesting significant dissociation of bicarbonate and consumption of protons. However, the impact of bicarbonate on reaction kinetics may cease to be positive with increasing bicarbonate concentration, because high concentration of negatively charged bicarbonate and carbonate ions can compete with nitrate for available catalyst surface sites.

Nitrate concentration was found to be an important factor for the reaction rate. Compared with the baseline condition, the nitrate reduction apparent zero-order rate constant increased with decreasing initial nitrate concentration (entries no. 8 and 9 in Table 5.2). Although the possibility of internal mass transfer limitation cannot be ruled out at this time, these observations are consistent with Langmuir-Hinshelwood model, a surface reaction model widely adopted for catalytic hydrogenation of oxyanions.^{4, 37, 38, 42} The higher apparent rate constant at lower initial nitrate concentrations may result from inhibition of hydrogen adsorption at the higher concentrations of nitrate and its conversion intermediates.^{4, 43} The surface reaction kinetic model considering reactants competition can be written as follows:

$$\text{Rate} = \frac{kK_{\text{nitrate}}C_{\text{nitrate}}K_{\text{hydrogen}}C_{\text{hydrogen}}}{(1+K_{\text{nitrate}}C_{\text{nitrate}}+K_{\text{hydrogen}}C_{\text{hydrogen}})^2} \quad (5.4)$$

Where k is the rate constant for the surface reaction, K_{nitrate} and K_{hydrogen} are the adsorption equilibrium constants for nitrate and hydrogen, respectively, C_{nitrate} is the aqueous concentration of nitrate, and C_{hydrogen} is the aqueous concentration of hydrogen, which is proportional to hydrogen partial pressure in the gas phase according to Henry's law. Under the current testing

conditions, nitrate concentration is much higher than hydrogen ($K_{\text{nitrate}}C_{\text{nitrate}} \gg 1 \gg K_{\text{hydrogen}}C_{\text{hydrogen}}$), and Eq. 5.4 can be reduced to

$$\text{Rate} = \frac{kK_{\text{hydrogen}}C_{\text{hydrogen}}}{K_{\text{nitrate}}C_{\text{nitrate}}} \quad (5.5)$$

Since k , K_{nitrate} , K_{hydrogen} , and C_{hydrogen} are all constant, the reaction rate is expected to be inversely dependent on C_{nitrate} . The initial reaction rate, coincident with the apparent zero-order rate constant k_0 , was roughly proportional to the inverse of the initial nitrate concentration (Figure D.2 in Appendix D), further confirming that surface hydrogen is at very low concentrations and limiting the reaction kinetics.

Temperature showed a positive effect on reaction rate (entries no. 10 and 11 in Table 5.2), and similar observations have been reported for nitrate reduction with Pd-based catalysts.^{44, 45} Arrhenius plot of the apparent zero-order rate constant between 25-35 °C yielded an apparent activation energy of $45 \pm 6 \text{ kJ mol}^{-1}$. This value is comparable with the apparent activity energy for nitrate hydrogenation with a Pd-Cu/Al₂O₃ catalyst.⁴⁶

5.4.2 Ammonia recovery by membrane distillation

The membranes employed in membrane distillation process are hydrophobic, allowing vapor phase species to permeate while rejecting ionic constituents in the aqueous phase. Due to the relatively low temperature studied (no higher than 35 °C for all tests), water evaporation through the membranes was not expected to be significant during ammonia recovery. The concentration of H₂SO₄ in the acid adsorbent was designed to be excessive to ensure complete capture of ammonia as (NH₄)₂SO₄.

To study the reaction kinetics and identify important operating factors for membrane distillation, a similar research approach was employed to that used for catalytic hydrogenation

studies. Under the baseline testing condition, the feed was a synthetic solution whose composition was based on the baseline testing solution in catalytic hydrogenation assuming complete nitrate reduction to ammonia according to Eq. 5.1 without pH control. Feed temperature was 30 °C, same as the baseline testing condition in catalytic hydrogenation. Different flow rates were varied, and 1.5 L min⁻¹ was chosen to achieve a high flux while maintaining the system at low pressure (7.5 psig) to minimize the risk of wetting the membranes.

Under the baseline condition, the kinetics of ammonia removal from the feed can be well described by a first-order rate law over the entire reaction time course (Figure 5.4a). The driving force for ammonia mass transfer is the difference between free ammonia concentration in the feed and that in the acid adsorbent. Under the baseline testing condition, the solution pH decreased from 11.2 to 10.8 due to the removal of a base (NH₃) from the solution.⁴⁷ In all but one test (entry no. 5 in Table 5.3), solution pH remained higher than 10.7, where free ammonia is the dominant species (>96%). It can also be assumed that free ammonia reacted immediately with sulfuric acid on the other side of the membrane to form ammonium sulfate, so the concentration of free ammonia in the acid adsorbent was practically zero. Therefore, the flux of ammonia transfer from the feed to the acid adsorbent can be represented by the following equation:

$$J_{\text{NH}_3} = K C_{\text{NH}_3, f} \quad (5.6)$$

Where J_{NH_3} is the mass flux of ammonia (gNH₃-N m⁻² h⁻¹), K is the overall mass transfer coefficient (m h⁻¹), and $C_{\text{NH}_3, f}$ is the concentration of ammonia in the feed (mgNH₃-N L⁻¹). The overall mass transfer coefficient comprises three resistances (i.e., feed liquid side boundary resistance, membrane resistance, and acid adsorbent side boundary resistance) and depends on the membrane and operating conditions.⁴⁸ Practically, the value of K can be determined by the following equation:⁴⁸⁻⁵⁰

$$K = \frac{V}{At} \ln \left(\frac{C_{\text{NH}_3,0}}{C_{\text{NH}_3,t}} \right) \quad (5.7)$$

Where V is the volume of the feed (m^3), A is the membrane area (m^2), $C_{\text{NH}_3,0}$ is the initial concentration of ammonia in the feed (mM), and $C_{\text{NH}_3,t}$ is the ammonia concentration in the feed at time t (h). By plotting $\ln(C_{\text{NH}_3,0}/C_{\text{NH}_3,t})$ over t , a straight line with the slope of KA/V can be obtained, and subsequently K was found. The initial J_{NH_3} was then calculated from Eq. 5.6. Under the baseline condition, the initial J_{NH_3} was $268 \pm 3 \text{ gNH}_3\text{-N m}^{-2} \text{ h}^{-1}$ with the corresponding K of $0.19 \pm 0.01 \text{ m h}^{-1}$. Nitrogen balance of the membrane distillation system was closed by measuring the total ammonia in the feed and the acid adsorbent (Figure 5.4b), suggesting that the system was well sealed, and loss of ammonia in the void space in the system was negligible.

Since the efficiency of ammonia transfer strongly depends on system configuration and membrane properties, it is challenging to directly compare the kinetic parameters observed in this study with those reported in the literature. However, within the same system, the effects of feed solution chemistry and operating conditions can be studied. The influence of operating

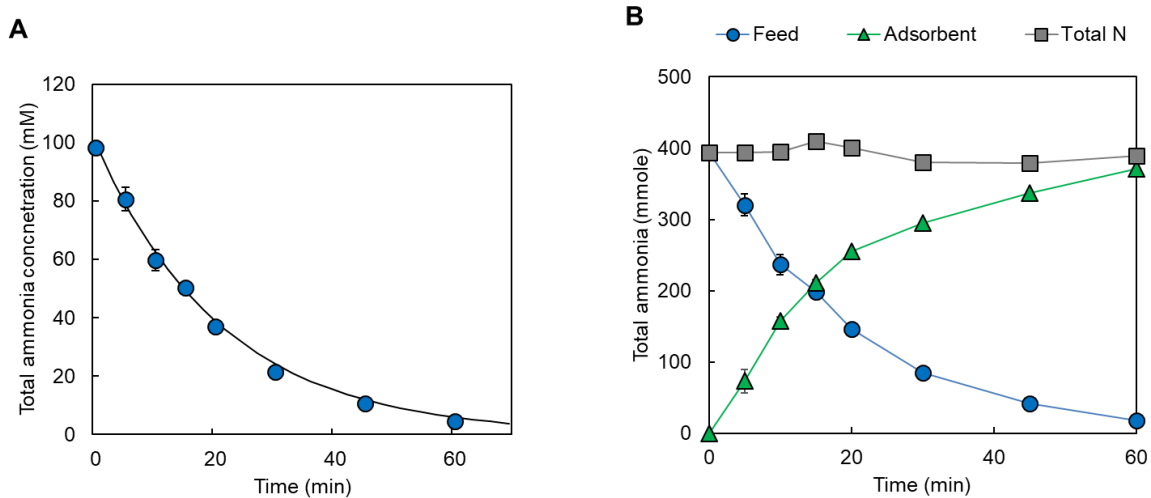


Figure 5.4 (A) Ammonia removal from brine by membrane distillation under baseline testing conditions. (B) Ammonia mass balance in feed and H_2SO_4 adsorbent solution. Solid line in (A) refers to the first-order rate law fit.

temperature was studied at three feed temperatures, i.e., 25 °C, 30 °C, and 35 °C. It was observed that ammonia removal kinetics (both K and initial J_{NH_3}) increased 17% when increasing temperature from 25 °C to 30 °C (entries no. 1 and 2 in Table 5.3). Further increasing the temperature to 35 °C improved the kinetics by 22% (entry no. 3 in Table 5.3). This positive influence of temperature on ammonia removal efficiency is consistent with literature findings with various membrane distillation configurations such as vacuum and sweep gas membrane distillation.⁵¹⁻⁵³ On the other hand, using temperature to tune ammonia removal efficiency will be increasingly limited at higher temperature, because the mass transfer of water vapor is intensified due to higher water vapor pressure and diffusivity, resulting in reduced ammonia selectivity.⁵²

Table 5.3 Summary of ammonia mass transfer coefficient (K) and initial mass flux (J_{NH_3}) with different feed characteristics and operating conditions

Test no.	NaCl %	NaHCO ₃ ^a mM	Na ₂ SO ₄ mM	Ammonia ^{ab} mM	Temp °C	Initial pH	Final pH ^c	K ^b m h ⁻¹	Initial J_{NH_3} ^b gNH ₃ -N m ⁻² h ⁻¹
Baseline condition									
1	5	100	100	100	30	11.2	10.8	0.19 ± 0.01	268 ± 3
Effect of temperature									
2	5	100	100	100	25	11.2	10.9	0.16 ± 0.01	229 ± 3
3	5	100	100	100	35	11.2	10.7	0.23 ± 0.03	326 ± 37
Effect of salt									
4	0	100	0	100	30	11.6	11.3	0.19 ± 0.02	258 ± 21
5	10	100	200	100	30	11.1	10.7	0.18 ± 0.02	258 ± 26
Effect of solution pH and ammonia concentration									
6	5	50	100	50	30	11.1	10.7	0.20 ± 0.03	141 ± 21
7	5	200	100	50	30	9.2	9.1	0.10 ± 0.01	71 ± 1
8	5	50	100	200	30	12.7	12.6	0.16 ± 0.02	457 ± 49
9	5	200	100	200	30	11.5	11.0	0.17 ± 0.01	482 ± 39

^aAmounts initially added.

^bCalculated by using total ammonia concentration.

^cOperation time 1h.

The impact of salts was studied by controlling the concentrations of NaCl and Na₂SO₄ in the feed solutions. Tests demonstrated that large variations in concentrations of these salts (0-10 wt% for NaCl, 0-200 mM for Na₂SO₄) had little influence on rates of ammonia removal from the

brine (entries no. 4 and 5 in Table 5.3). It has been reported that the solution ionic strength has slightly negative effect on the fraction of free ammonia species by increasing ammonium dissociation constant at higher ionic strength.⁵⁴ However, at the relatively high pH (>10.7) used in these tests, the fraction of free ammonia species remained high, rendering the effect of ionic strength negligible.

Two factors, solution pH and initial ammonia concentration, were inherently coupled due to the hydroxide generated when simulating nitrate reduction to ammonia Eq. 5.1 In addition, the solution pH was also influenced by the buffering capacity of the solution during catalytic hydrogenation. Therefore, four tests were designed, combining two factors relevant to solution pH, i.e., initial nitrate concentration and bicarbonate concentration, each at two levels. Because we have assumed complete nitrate hydrogenation according to Eq. 5.1 and no loss of ammonia to the gas phase, the initial nitrate concentration in the feed to catalytic hydrogenation equals the initial ammonia concentration in the feed to membrane distillation. At low initial nitrate concentration (50 mM), the feed pH varied dramatically depending on the concentration of bicarbonate (entries no. 6 and 7 in Table 5.3). A low bicarbonate concentration (50 mM) led to a higher solution pH and K similar to values measured under the baseline testing condition. At higher bicarbonate concentration (200 mM), on the other hand, the brine was buffered more strongly during nitrate hydrogenation, resulting in an apparent solution pH of 9.2 in the membrane distillation feed, a condition wherein only ~50% of the ammonia is present as the free ammonia species. The mass transfer coefficient K (calculated by using total ammonia concentration) decreased 51% compared to that at low bicarbonate concentration. When the initial nitrate concentration was equal to or greater than the initial bicarbonate concentrations (entries no. 8 and 9 in Table 5.3), the solution pH of the ammonia product solution used as

membrane distillation feed was high (>11), leading to K values comparable with that measured at the baseline testing condition. Therefore, solution pH is a critical factor for ammonia recovery by membrane distillation. The initial J_{NH_3} also increased with the initial ammonia concentration as expected from Eq. 5.6.

5.4.3 Ion exchange waste brine nitrate removal and nitrogen recovery

Based on findings with synthetic brine solutions, we then demonstrated nitrate removal and nitrogen recovery from a real ion exchange waste brine (Table 5.1 and Table 5.4) obtained from a California water utility. Kinetics of nitrate hydrogenation with Ru/C in the waste brine can be characterized by the zero-order rate law (Figure 5.5), and the apparent zero-order rate constant normalized to Ru mass was found to be significantly higher ($1.80 \pm 0.04 \text{ mM min}^{-1} \text{ g}_{\text{Ru}}^{-1}$) than those measured in synthetic brines (Table 5.2). As a control, a synthetic waste brine was prepared with the same concentrations of major anions (chloride, nitrate and sulfate), alkalinity (by adding sodium bicarbonate), and initial solution pH (adjusted with NaOH) as the real waste brine. Experiments revealed a lower rate of nitrate hydrogenation in the synthetic waste brine than in the real waste brine (Figure 5.5), with the apparent zero-order rate constant ~30% lower ($1.24 \pm 0.02 \text{ mM min}^{-1} \text{ g}_{\text{Ru}}^{-1}$). The origin of the higher activity observed in the real waste brine is unclear at this time, but the results support the technical feasibility of applying Ru/C for nitrate hydrogenation in ion exchange waste brine. Further research is needed to identify the cause of faster kinetics in the real waste brine, but it is noteworthy that the real waste brine contains several cations in addition to Na^+ (Table 1), the sole cation used in preparation of the synthetic waste brine. Divalent and trivalent cations (e.g., Ca^{2+} , Mg^{2+}) have been shown previously to enhance rates of nitrate hydrogenation.²⁹ In addition, the real waste brine contains a number of

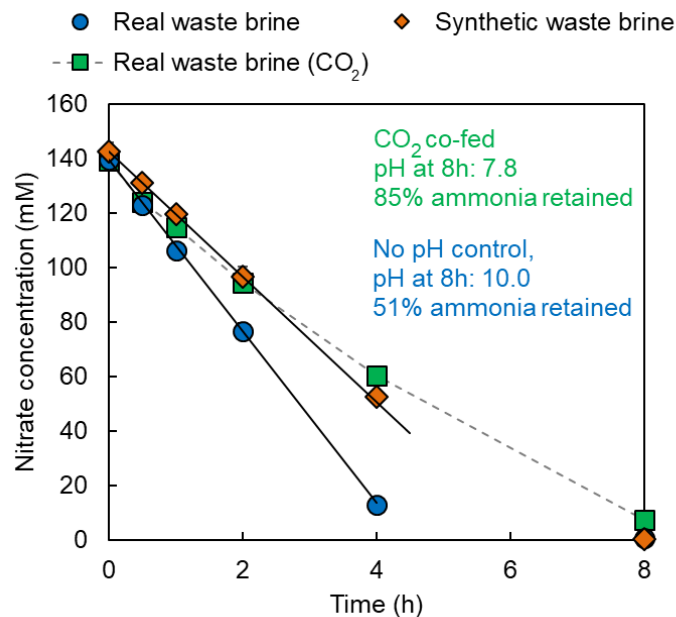


Figure 5.5 Catalytic nitrate hydrogenation in real waste brine and synthetic waste brine prepared with similar anionic composition. Conditions: 6 g L⁻¹ Ru/C, 30 °C, no solution pH control, 1 atm H₂ headspace maintained by flowing H₂ at ca. 300 mL min⁻¹. The effect of pH control by flowing CO₂ (at ca. 65 mL min⁻¹) was also examined. Error bars indicate standard deviation from duplicate measurements (smaller than symbol if not visible). Solid line refers to the zero-order rate law fit.

minor constituents, including organics and trace metals (Table 5.1), which may interact with catalyst surfaces to promote nitrate enhanced reactivity.⁵⁵⁻⁵⁷

Considering that bicarbonate has shown positive influence on nitrate hydrogenation kinetics (Table 5.2), tests were conducted to co-feed CO₂ with H₂, which is a common practice for solution pH control when treating nitrate with Pd-based catalysts.^{21, 22} The nitrate hydrogenation rate was comparable with that in the absence of CO₂ in the initial 0.5 h, but the rate gradually decreased with reaction time (Figure 5.5). This observation could be a result of lower hydrogen partial pressure and the accumulation of bicarbonate over time. For example, the inorganic carbon concentration increased from 238 mM to 466 mM after 12 h of treatment. On the other hand, co-feeding CO₂ maintained solution pH between 7.6-7.9 and significantly improved retention of ammonia in the open reactor system. After 8 h of reaction, 85% of the

Table 5.4 Water quality comparison of initial real waste brine, brine solution after treatment with Ru/C, and solution after membrane distillation.

Solution chemistry	Real waste brine	After hydrogenation	After membrane distillation
pH	8.5	8.6	9.9 ^a
Cl ⁻	13,685 mg L ⁻¹ (2.3 wt% as NaCl)	14,198 mg L ⁻¹ (2.3 wt% as NaCl)	14,204 mg L ⁻¹ (2.3 wt% as NaCl)
HCO ₃ ⁻ and CO ₃ ²⁻	232 mM	485 mM	484 mM
NO ₃ ⁻	9,262 mg L ⁻¹ (149 mM)	79 mg L ⁻¹ (1.2 mM)	75 mg L ⁻¹ (1.2 mM)
SO ₄ ²⁻	4,346 mg L ⁻¹ (45 mM)	4,515 mg L ⁻¹ (47 mM)	4,283 mg L ⁻¹ (45 mM)
Total ammonia	<3.2 mM (detection limit)	136 mM	9 mM

^aSolution pH was adjusted to 10.0 by adding NaOH prior to membrane distillation

ammonia was retained in the liquid phase when co-feeding CO₂ compared to only 51% in the absence of CO₂ buffer.

Catalytic hydrogenation of real waste brine was scaled up in 1 L graduated glass bottle to provide feed solution for membrane distillation. Reactor design likely affects reaction kinetics, but its optimization is beyond the scope of this study, and the reaction was conducted up to 24 h while co-feeding CO₂ to enhance ammonia retention in the liquid phase. These conditions resulted in near complete nitrate hydrogenation, and the liquid phase retained 91% of the ammonia reaction product (Table 5.4). Prior to membrane distillation, the solution pH was adjusted to ~10.0 with NaOH to reflect the pH conditions observed when pH was allowed to drift without CO₂ buffer.

Kinetics of ammonia removal from the catalytically treated real waste brine can be characterized by a first-order rate law (Figure 5.6a), with K and initial J_{NH_3} being 0.11 m h⁻¹ and 199 gNH₃-N m⁻² h⁻¹, respectively (uncertainty not reported due to lack of duplicate experiment of limited real waste brine supply). These observations are qualitatively consistent with results obtained with synthetic solutions prepared to mimic the major waste brine components. Nitrogen

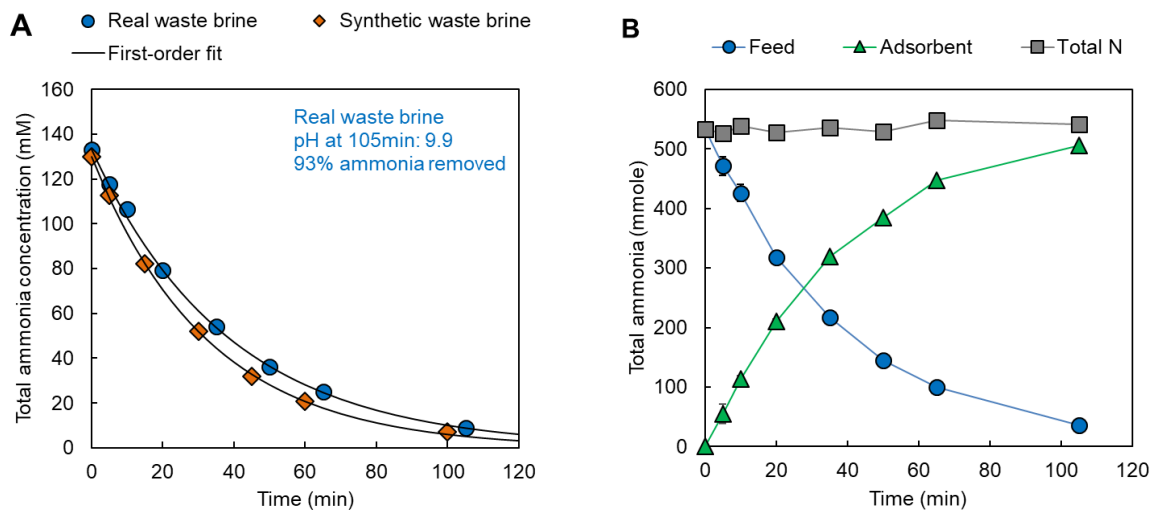


Figure 5.6 (A) Ammonia removal from real waste brine and synthetic solution by membrane distillation. Conditions: 4 L feed at 1.5 L min^{-1} , 1.15 L $0.25 \text{ M H}_2\text{SO}_4$ adsorbent solution at 1.5 L min^{-1} , $30 \text{ }^\circ\text{C}$. (B) Ammonia mass balance in real waste brine feed and H_2SO_4 adsorbent solution. Solid line in (A) refers to the first-order rate law fit.

balance was also well closed by measuring the total ammonia in the feed and the acid adsorbent solution (Figure 5.6b). Salt composition and concentrations after membrane distillation were almost invariant (Table 5.4), verifying the membrane integrity during the experiment and high selectivity to ammonia for mass transfer. Similar to the study of catalytic hydrogenation, a synthetic waste brine was prepared with the same concentrations of major anions (chloride, bicarbonate, and sulfate), total ammonia concentration, and initial solution pH (adjusted with NaOH) as the real waste brine. Ammonia removal K ($0.12 \pm 0.01 \text{ m h}^{-1}$) and initial J_{NH_3} ($225 \pm 4 \text{ gNH}_3\text{-N m}^{-2} \text{ h}^{-1}$) for in the synthetic waste brine were similar to values measured in the real waste brine. These results suggest membrane distillation is effective at recovering ammonia from real waste brine. Potential membrane fouling from continuous treatment of real waste brine and its impact on ammonia recovery efficiency need to be future evaluated at longer operation timescale.

The overall nitrogen recovery from the real waste brine through the hybrid catalytic hydrogenation/membrane distillation process is 79%, validating the use of this process for efficient nitrogen resource recovery from waste ion exchange brines.

5.4.4 Application considerations of the hybrid process

Conceptual evaluation of the economic and environmental viability of the hybrid catalytic hydrogenation/membrane distillation process may be achieved by comparing with a more developed brine treatment system using Pd-based catalysts.^{21, 22} Previous work showed that both the O&M costs and environmental impacts of recycling ion exchange brines by treating nitrate with Pd-In/C catalysts can be lower than those of conventional ion exchange processes.²¹ A critical factor to delivering these benefits is reducing the catalyst cost, particularly the use of Pd.⁵⁸ Catalyst cost is directly associated with the cost of the active metal (dominated by Pd for Pd-In/C catalysts) and catalyst activity. Less catalyst material is required for catalysts that exhibit higher activity. Along this line of consideration, Ru catalysts have an advantage over Pd-based catalysts due to the historically lower cost of Ru.^{4, 36, 59} In addition, Ru catalysts have been reported to have high activity for nitrate reduction, similar to Pd-Cu/C catalysts.³ This study further confirmed that Ru/C is active for nitrate hydrogenation in various brine conditions. Although activity comparison between Ru/C determined in this study and literature reported values for Pd-In/C catalysts is not straightforward due to difference in reaction conditions, their metal mass-normalized apparent zero-order rate constants are of similar magnitude when treating synthetic waste brines, and the rate constant with Ru/C for treating a real waste brine is approximately two-fold higher than the highest value reported for Pd-In/C catalysts,^{21, 22} all suggesting that Ru catalysts have a potential to improve the economic and environmental sustainability of the catalytic treatment step of the hybrid process.

A less often studied, but critically important consideration, for catalytic processes is catalyst stability and longevity. Catalyst longevity is ultimately required to fulfill the assumptions of catalyst lifetime (usually years) during techno-economic analysis and/or life cycle assessment.^{21, 23, 59} Catalyst stability also affects catalyst loading design for a fixed volume of water brine and vice versa, brine regeneration cycle design with a fixed loading of catalyst. Generally, the higher the total volume of waste brine that can be treated with the same catalyst, the more savings that can be gained from brine reuse.²² Ru/C stability for waste brine hydrogenation was initially assessed using a batch recycle test. After the first use, catalyst activity increased in the following cycles (Figure 5.7). This increase in activity is likely related to catalyst activation. As shown in a previous study, elevated temperature in either inert or reducing gas environment improved the activity of the commercial Ru/C by desorbing synthesis residue and exposing redox-labile Ru species.⁴ ICP analysis of the filtrate from catalyst collection detected trace amounts of Ru (<0.2% of the total amount of Ru). However, it is unclear whether the detected Ru resulted from metal dissolution or the release of loosely bound Ru nanoparticles from attrition. These results demonstrated that Ru/C can be recycled in a semi-batch reactor, and catalyst deactivation through leaching or fouling is insignificant within four use cycles. Further study, ideally in continuous flow reactors, is required to evaluate the longer-term stability of Ru/C during waste brine treatment applications.

Compared with previous brine treatment systems, the hybrid catalytic hydrogenation/membrane distillation process enables nitrogen recovery, providing potential economic and environmental benefits in addition to reduced salt consumption. When considering the entire process for source water treatment (Figure 5.1), nitrogen in the form of dilute nitrate was transformed to a much more concentrated $(\text{NH}_4)_2\text{SO}_4$ aqueous solution, which can be used

as a liquid fertilizer or a precursor for solid fertilizer.³³⁻³⁵ This process likely has higher energy efficiency compared to the traditional Haber–Bosch ammonia synthesis process that demands high temperature and pressure, because it requires minimal thermal energy; instead, it leverages chemical potential difference as the driving force (e.g., nitrate adsorption to ion exchange resin, nitrate hydrogenation on Ru surface, and ammonia mass transfer across membrane). A detailed techno-economic analysis is required to estimate the minimum selling price of the brine-derived $(\text{NH}_4)_2\text{SO}_4$ product.

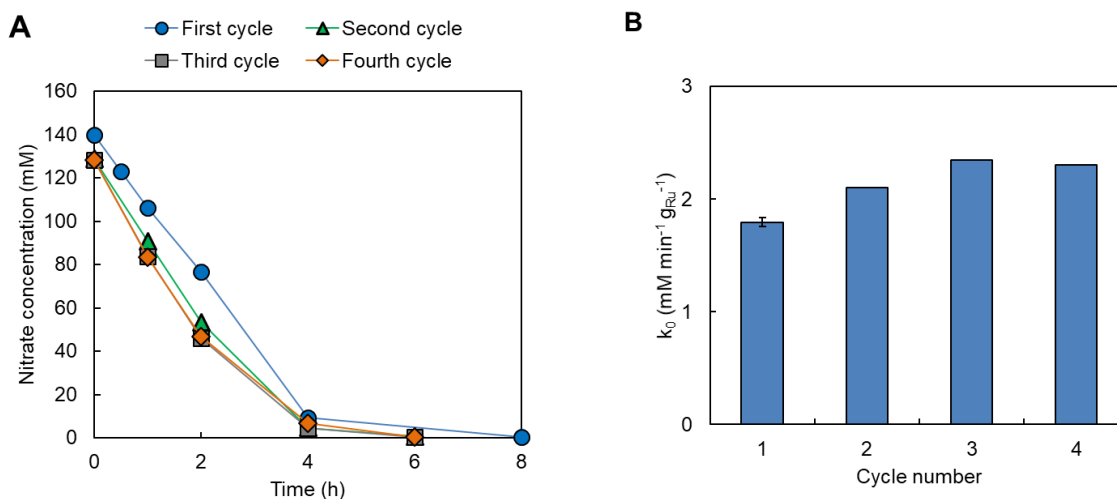


Figure 5.7 Ru/C reused for three reaction cycles in real waste brine: (a) nitrate hydrogenation time courses, and (b) apparent zero-order rate constants. Conditions: 6 g L⁻¹ Ru/C, 30 °C, no solution pH control, 1 atm H₂ headspace maintained by flowing H₂ at ca. 300 mL min⁻¹, catalyst dried at 70°C in between reuse cycles.

To meet the increasing demand for fertilizer,³⁴ the yield of the ammonium sulfate should be maximized, which depends on the nitrogen recovery efficiency of the catalytic hydrogenation/membrane distillation process. As shown in Figure 5.7, in the absence of pH control, solution pH rose beyond the pK_a of NH₄⁺ and accelerated ammonia loss to the flowing H₂. To better understand the dynamics of ammonia formation and volatilization, the total ammonia concentration was monitored during waste brine hydrogenation (Figure 5.8a). Initially,

total ammonia concentration increased with nitrate hydrogenation. When nitrate conversion was near complete, total ammonia concentration began to decrease. Gas-liquid partition of NH_3 led to a decreasing total nitrogen concentration with time. Therefore, liquid phase ammonia retainment can be improved by controlling the reaction time. For example, at 4 h the ammonia retainment retention was 70%, 39% higher than that observed at 8 h. However, it came with the trade-off of incomplete nitrate conversion. With flowing CO_2 as a pH buffer, ammonia retainment can be improved by maintaining the solution pH below the pK_a of NH_4^+ . Even at this low pH (7.8), the slow and steady loss of ammonia was still observed (Figure 5.8b). Instead of semi-batch reactor, a completely enclosed batch reactor may be used to curb the loss of ammonia to the flowing H_2 and/or CO_2 . The key to the batch reactor design is minimizing the reactor size while ensuring sufficient hydrogen supply, which may require a pressurized system. Increasing the hydrogen pressure can also enhance nitrate hydrogenation kinetics as discussed before and potentially improve hydrogen and Ru utilization efficiency, leading to reduced cost and environmental impact.^{21, 22}

Membrane distillation (or membrane contactor) has been considered a cost effective, energy efficient technology for removing ammonia from industrial and agricultural wastewater.^{52,}
⁶⁰ This study demonstrated its successful application to recovering ammonia from ion exchange waste brine at high efficiency under ambient temperatures. The high ammonia removal efficiency is attributed to several factors including the large membrane surface area and high feed solution pH. As nitrate hydrogenation produces hydroxide to raise solution pH, the membrane distillation process can benefit from an upstream catalytic reactor operated without pH control, which also saves the cost on alkali for adjusting pH for membrane distillation. In addition to the aforementioned pressurized batch reactor, optimization of the existing system,

such as directing the H₂ flow to the acid adsorbent, can be explored to maximize ammonia recovery. Alternative membrane distillation should be assessed to further improve unit efficiency and reduce membrane cost.⁶¹ A major concern during membrane distillation implementation is membrane fouling, such as by particulate and organics.^{48, 62, 63} The risk of particulate fouling caused by catalyst particle can be reduced by filtration, which is also an effective method for removing scalants precipitated at high solution pH (e.g., calcium carbonate). Organic fouling is less of a concern for the ion exchange waste brine due to its low organic carbon content (Table 5.1), but the accumulation of organic carbon over several brine regenerant cycles may lead to fouling over long-term operation and needs to be evaluated.

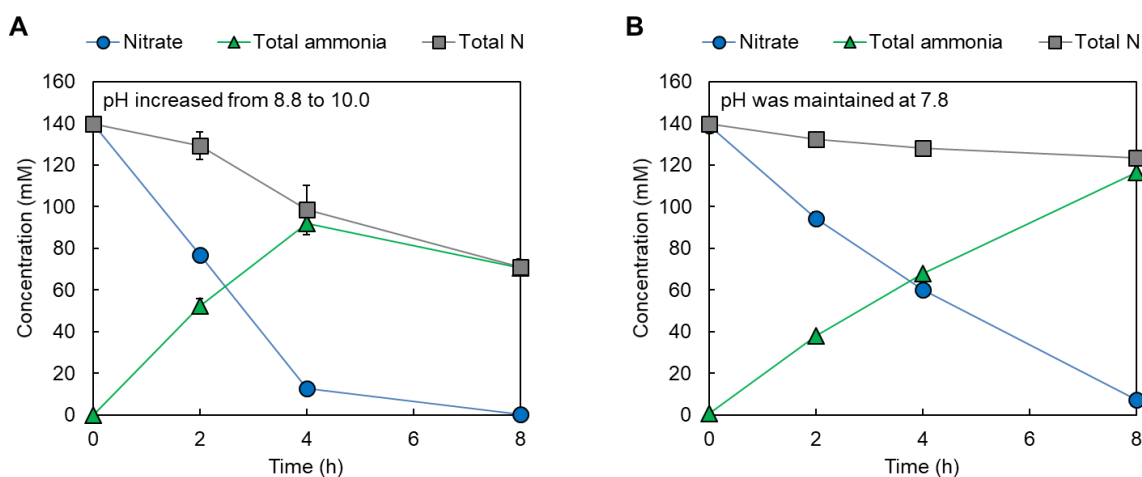


Figure 5.8 Aqueous concentration of nitrate and total ammonia during real waste brine catalytic hydrogenation: (a) no pH control (b) pH maintained by flowing CO₂. Conditions: 6 g L⁻¹ Ru/C, 30 °C, 1 atm H₂ headspace maintained by flowing H₂ at ca. 300 mL min⁻¹, in (b) CO₂ flow at ca. 65 mL min⁻¹. Error bars indicate standard deviation from duplicate measurements (smaller than symbol if not visible).

5.5 Conclusions

This work demonstrated a hybrid catalytic hydrogenation/membrane distillation process that potentially enables ion exchange waste brine reuse and captures nitrogen in the form of potential fertilizer product. A commercial Ru/C catalyst, much lower in cost than widely studied

Pd-based catalysts, was found to be active for nitrate reduction to ammonia in real and synthetic waste brine matrices. In a well-mixed semi-batch reactor, nitrate hydrogenation with Ru/C exhibited zero-order kinetics, and nitrate was hydrogenated to ammonia at high selectivity. Further, the resulting ammonia product could be efficiently recovered as (NH₄)₂SO₄ by membrane distillation. The mass transfer efficiency was favored by high solution pH and temperature and not affected by salt composition or concentration in the waste brine solution. The hybrid process was finally applied to a real ion exchange waste brine and demonstrated high nitrate hydrogenation and ammonia recovery efficiency. Further studies are needed to evaluate alternative reactor designs for improving nitrate hydrogenation kinetics and overall ammonia recovery and to evaluate the reuse of treated brines for regeneration ion exchange resins.

5.6 References

1. Camargo, J. A.; Alonso, Á. Ecological and toxicological effects of inorganic nitrogen pollution in aquatic ecosystems: A global assessment. *Environment International* **2006**, *32* (6), 831-849.
2. Garcia-Segura, S.; Lanzarini-Lopes, M.; Hristovski, K.; Westerhoff, P. Electrocatalytic reduction of nitrate: Fundamentals to full-scale water treatment applications. *Applied Catalysis B: Environmental* **2018**, *236*, 546-568.
3. Chen, G.; Hanukovich, S.; Chebeir, M.; Christopher, P.; Liu, H. Nitrate Removal via a Formate Radical-Induced Photochemical Process. *Environmental Science & Technology* **2019**, *53* (1), 316-324.
4. Huo, X.; Van Hoomissen, D. J.; Liu, J.; Vyas, S.; Strathmann, T. J. Hydrogenation of aqueous nitrate and nitrite with ruthenium catalysts. *Applied Catalysis B: Environmental* **2017**, *211*, 188-198.
5. Martínez, J.; Ortiz, A.; Ortiz, I. State-of-the-art and perspectives of the catalytic and electrocatalytic reduction of aqueous nitrates. *Appl. Catal., B* **2017**, *207* (Supplement C), 42-59.
6. Kapoor, A.; Viraraghavan, T. Nitrate removal from drinking water - Review. *J. Environ. Eng.-ASCE* **1997**, *123* (4), 371-380.
7. Jensen, V. B.; Darby, J. L. Brine Disposal Options for Small Systems in California's Central Valley. *Journal - American Water Works Association* **2016**, *108* (5), E276-E289.

8. Bergquist, A. M.; Bertoch, M.; Gildert, G.; Strathmann, T. J.; Werth, C. J. Catalytic denitrification in a trickle bed reactor: Ion exchange waste brine treatment. *Journal - American Water Works Association* **2017**, *109* (5), E129-E151.
9. Wang, L.; Chen, A. S.; Wang, A.; Condit, W. E.; Battelle, C.; Sorg, T. J.; Supply, W. Arsenic and nitrate removal from drinking water by ion exchange: US EPA demonstration project at Vale, OR. Final performance evaluation report. National Risk Management Research Laboratory, Cincinnati, Ohio, 2011.
10. Mellor, R. B.; Ronnenberg, J.; Campbell, W. H.; Diekmann, S. Reduction of nitrate and nitrite in water by immobilized enzymes. *Nature* **1992**, *355* (6362), 717-719.
11. Yang, G. C. C.; Lee, H.-L. Chemical reduction of nitrate by nanosized iron: kinetics and pathways. *Water Res.* **2005**, *39* (5), 884-894.
12. Wang, Y.; Qu, J.; Wu, R.; Lei, P. The electrocatalytic reduction of nitrate in water on Pd/Sn-modified activated carbon fiber electrode. *Water Res.* **2006**, *40* (6), 1224-1232.
13. Doudrick, K.; Yang, T.; Hristovski, K.; Westerhoff, P. Photocatalytic nitrate reduction in water: Managing the hole scavenger and reaction by-product selectivity. *Appl. Catal. B-Environ.* **2013**, *136*, 40-47.
14. Ye, T.; Durkin, D. P.; Banek, N. A.; Wagner, M. J.; Shuai, D. Graphitic carbon nitride supported ultrafine Pd and Pd-Cu catalysts: Enhanced reactivity, selectivity, and longevity for nitrite and nitrate hydrogenation. *ACS Applied Materials & Interfaces* **2017**, *9* (33), 27421-27426.
15. Yang, T.; Doudrick, K.; Westerhoff, P. Photocatalytic reduction of nitrate using titanium dioxide for regeneration of ion exchange brine. *Water Research* **2013**, *47* (3), 1299-1307.
16. Jung, S.; Bae, S.; Lee, W. Development of Pd-Cu/hematite catalyst for selective nitrate reduction. *Environ. Sci. Technol.* **2014**, *48* (16), 9651-9658.
17. Corma, A.; Palomares, A. E.; Rey, F.; Prato, J. G. Catalytic reduction of nitrates in natural water: is this a realistic objective? *J. Catal.* **2004**, *227* (2), 561-562.
18. WellToDo, <http://welltodo.co.il/>.
19. Chen, Y.-X.; Zhang, Y.; Chen, G.-H. Appropriate conditions for maximizing catalytic reduction efficiency of nitrate into nitrogen gas in groundwater. *Water Res.* **2003**, *37* (10), 2489-2495.
20. Papa, F.; Balint, I.; Negrila, C.; Olaru, E. A.; Zgura, I.; Bradu, C. Supported Pd-Cu nanoparticles for water phase reduction of nitrates. Influence of the support and of the pH conditions. *Ind. Eng. Chem. Res.* **2014**, *53* (49), 19094-19103.

21. Choe, J. K.; Bergquist, A. M.; Jeong, S.; Guest, J. S.; Werth, C. J.; Strathmann, T. J. Performance and life cycle environmental benefits of recycling spent ion exchange brines by catalytic treatment of nitrate. *Water Research* **2015**, *80* (0), 267-280.
22. Bergquist, A. M.; Choe, J. K.; Strathmann, T. J.; Werth, C. J. Evaluation of a hybrid ion exchange-catalyst treatment technology for nitrate removal from drinking water. *Water Research* **2016**, *96*, 177-187.
23. Choe, J. K.; Mehnert, M. H.; Guest, J. S.; Strathmann, T. J.; Werth, C. J. Comparative assessment of the environmental sustainability of existing and emerging perchlorate treatment technologies for drinking water. *Environmental Science & Technology* **2013**, *47* (9), 4644-4652.
24. Sá, J.; Vinek, H. Catalytic hydrogenation of nitrates in water over a bimetallic catalyst. *Appl. Catal., B* **2005**, *57* (4), 247-256.
25. Constantinou, C. L.; Costa, C. N.; Efstathiou, A. M. The remarkable effect of oxygen on the N₂ selectivity of water catalytic denitrification by hydrogen. *Environ. Sci. Technol.* **2006**, *41* (3), 950-956.
26. Xie, Y.; Cao, H.; Li, Y.; Zhang, Y.; Crittenden, J. C. Highly selective PdCu/amorphous silica–alumina (ASA) catalysts for groundwater denitration. *Environ. Sci. Technol.* **2011**, *45* (9), 4066-4072.
27. Chaplin, B. P.; Roundy, E.; Guy, K. A.; Shapley, J. R.; Werth, C. J. Effects of natural water ions and humic acid on catalytic nitrate reduction kinetics using an alumina supported Pd–Cu catalyst. *Environ. Sci. Technol.* **2006**, *40* (9), 3075-3081.
28. Wang, Y.; Sakamoto, Y.; Kamiya, Y. Remediation of actual groundwater polluted with nitrate by the catalytic reduction over copper–palladium supported on active carbon. *Appl. Catal., A* **2009**, *361* (1–2), 123-129.
29. Pintar, A.; vetinc, M.; Levec, J. Hardness and salt effects on catalytic hydrogenation of aqueous nitrate solutions. *J. Catal.* **1998**, *174* (1), 72-87.
30. Dortsiou, M.; Katsounaros, I.; Polatides, C.; Kyriacou, G. Electrochemical removal of nitrate from the spent regenerant solution of the ion exchange. *Desalination* **2009**, *248* (1-3), 923-930.
31. McAdam, E. J.; Judd, S. J. Biological treatment of ion-exchange brine regenerant for re-use: A review. *Separation and Purification Technology* **2008**, *62* (2), 264-272.
32. Bae, B.-U.; Jung, Y.-H.; Han, W.-W.; Shin, H.-S. Improved brine recycling during nitrate removal using ion exchange. *Water Res.* **2002**, *36* (13), 3330-3340.
33. Amaral, M. C. S.; Magalhães, N. C.; Moravia, W. G.; Ferreira, C. D. Ammonia recovery from landfill leachate using hydrophobic membrane contactors. *Water Science and Technology* **2016**, *74* (9), 2177-2184.

34. Garcia-González, M. C.; Vanotti, M. B. Recovery of ammonia from swine manure using gas-permeable membranes: Effect of waste strength and pH. *Waste Management* **2015**, *38*, 455-461.
35. Li, Y.; Tarpeh, W. A.; Nelson, K. L.; Strathmann, T. J. Quantitative evaluation of an integrated system for valorization of wastewater algae as bio-oil, fuel gas, and fertilizer products. *Environ. Sci. Technol.* **2018**, *52* (21), 12717-12727.
36. Chen, X.; Huo, X.; Liu, J.; Wang, Y.; Werth, C. J.; Strathmann, T. J. Exploring beyond palladium: Catalytic reduction of aqueous oxyanion pollutants with alternative platinum group metals and new mechanistic implications. *Chem. Eng. J.* **2017**, *313*, 745-752.
37. Chen, H.; Xu, Z.; Wan, H.; Zheng, J.; Yin, D.; Zheng, S. Aqueous bromate reduction by catalytic hydrogenation over Pd/Al₂O₃ catalysts. *Applied Catalysis B: Environmental* **2010**, *96* (3-4), 307-313.
38. Wang, Y.; Liu, J.; Wang, P.; Werth, C. J.; Strathmann, T. J. Palladium nanoparticles encapsulated in core-shell silica: A structured hydrogenation catalyst with enhanced activity for reduction of oxyanion water pollutants. *ACS Catal.* **2014**, *4* (10), 3551-3559.
39. Epron, F.; Gauthard, F.; Barbier, J. Reduction of Nitrate in Water on a Monometallic Pd/CeO₂ Catalyst. *J. Catal.* **2002**, *206* (2), 363-367.
40. Chaplin, B.; Shapley, J.; Werth, C. The selectivity and sustainability of a Pd-In/ γ -Al₂O₃ catalyst in a packed-bed reactor: The effect of solution composition. *Catal. Lett.* **2009**, *130* (1-2), 56-62.
41. Deganello, F.; Liotta, L. F.; Macaluso, A.; Venezia, A. M.; Deganello, G. Catalytic reduction of nitrates and nitrites in water solution on pumice-supported Pd-Cu catalysts. *Appl. Catal., B* **2000**, *24* (3-4), 265-273.
42. Chinthaginjala, J. K.; Lefferts, L. Support effect on selectivity of nitrite reduction in water. *Appl. Catal., B* **2010**, *101* (1-2), 144-149.
43. Knitt, L. E.; Shapley, J. R.; Strathmann, T. J. Rapid metal-catalyzed hydrodehalogenation of iodinated X-ray contrast media. *Environ. Sci. Technol.* **2008**, *42* (2), 577-583.
44. Kim, Y.-N.; Kim, M. Y.; Choi, M. Synergistic integration of catalysis and ion-exchange for highly selective reduction of nitrate into N₂. *Chem. Eng. J.* **2016**, *289*, 423-432.
45. Soares, O. S. G. P.; Fan, X.; Órfão, J. J. M.; Lapkin, A. A.; Pereira, M. F. R. Kinetic Modeling of Nitrate Reduction Catalyzed by Pd-Cu Supported on Carbon Nanotubes. *Ind. Eng. Chem. Res.* **2012**, *51* (13), 4854-4860.
46. Pintar, A.; Batista, J.; Levec, J.; Kajiuchi, T. Kinetics of the catalytic liquid-phase hydrogenation of aqueous nitrate solutions. *Appl. Catal., B* **1996**, *11* (1), 81-98.

47. Tao, W.; Ukwuani, A. T. Coupling thermal stripping and acid absorption for ammonia recovery from dairy manure: Ammonia volatilization kinetics and effects of temperature, pH and dissolved solids content. *Chemical Engineering Journal* **2015**, *280* (Supplement C), 188-196.
48. Zarebska, A.; Nieto, D. R.; Christensen, K. V.; Norddahl, B. Ammonia recovery from agricultural wastes by membrane distillation: Fouling characterization and mechanism. *Water Research* **2014**, *56*, 1-10.
49. El-Bourawi, M. S.; Khayet, M.; Ma, R.; Ding, Z.; Li, Z.; Zhang, X. Application of vacuum membrane distillation for ammonia removal. *Journal of Membrane Science* **2007**, *301* (1-2), 200-209.
50. du Preez, J.; Norddahl, B.; Christensen, K. The BIOREK® concept: a hybrid membrane bioreactor concept for very strong wastewater. *Desalination* **2005**, *183* (1-3), 407-415.
51. Ding, Z.; Liu, L.; Li, Z.; Ma, R.; Yang, Z. Experimental study of ammonia removal from water by membrane distillation (MD): The comparison of three configurations. *Journal of Membrane Science* **2006**, *286* (1-2), 93-103.
52. Xie, Z.; Duong, T.; Hoang, M.; Nguyen, C.; Bolto, B. Ammonia removal by sweep gas membrane distillation. *Water Research* **2009**, *43* (6), 1693-1699.
53. Wu, C.; Yan, H.; Li, Z.; Lu, X. Ammonia recovery from high concentration wastewater of soda ash industry with membrane distillation process. *Desalination and Water Treatment* **2016**, *57* (15), 6792-6800.
54. Bower, C. E.; Bidwell, J. P. Ionization of ammonia in seawater: Effects of temperature, pH, and salinity. *Journal of the Fisheries Research Board of Canada* **1978**, *35* (7), 1012-1016.
55. Moyer, B. A.; Meyer, T. J. Reduction of nitrate ion by (bpy)₂pyRu(OH₂)²⁺. *J. Am. Chem. Soc.* **1979**, *101* (5), 1326-1328.
56. Liu, J.; Choe, J. K.; Wang, Y.; Shapley, J. R.; Werth, C. J.; Strathmann, T. J. Bioinspired complex-nanoparticle hybrid catalyst system for aqueous perchlorate reduction: Rhenium speciation and its influence on catalyst activity. *ACS Catal.* **2014**, 511-522.
57. Hörold, S.; Tacke, T.; Vorlop, K. D. Catalytical removal of nitrate and nitrite from drinking water: 1. Screening for hydrogenation catalysts and influence of reaction conditions on activity and selectivity. *Environ. Technol.* **1993**, *14* (10), 931-939.
58. Chiueh, P. T.; Lee, Y. H.; Su, C. Y.; Lo, S. L. Assessing the environmental impact of five Pd-based catalytic technologies in removing of nitrates. *J. Hazard. Mater.* **2011**, *192* (2), 837-845.
59. Hutchison, J. M.; Guest, J. S.; Zilles, J. L. Evaluating the development of biocatalytic technology for the targeted removal of perchlorate from drinking water. *Environ. Sci. Technol.* **2017**.

60. Darestani, M.; Haigh, V.; Couperthwaite, S. J.; Millar, G. J.; Nghiem, L. D. Hollow fibre membrane contactors for ammonia recovery: Current status and future developments. *Journal of Environmental Chemical Engineering* **2017**, *5* (2), 1349-1359.
61. Qu, D.; Sun, D.; Wang, H.; Yun, Y. Experimental study of ammonia removal from water by modified direct contact membrane distillation. *Desalination* **2013**, *326*, 135-140.
62. Warsinger, D. M.; Swaminathan, J.; Guillen-Burrieza, E.; Arafat, H. A.; Lienhard V, J. H. Scaling and fouling in membrane distillation for desalination applications: A review. *Desalination* **2015**, *356*, 294-313.
63. Tijing, L. D.; Woo, Y. C.; Choi, J.-S.; Lee, S.; Kim, S.-H.; Shon, H. K. Fouling and its control in membrane distillation—A review. *Journal of Membrane Science* **2015**, *475*, 215-244.

CHAPTER 6

TAILORING DIESEL BIOBLENDSTOCK FROM INTEGRATED CATALYTIC UPGRADING OF CARBOXYLIC ACIDS: A “FUEL PROPERTY FIRST” APPROACH

A modified version of this chapter was submitted to *Energy & Environmental Science*

Xiangchen Huo, Nabila A. Huq, Jim Stunkel, Nicholas S. Cleveland, Anne K. Starace, Amy E. Settle, Allyson M. York, Robert S. Nelson, David G. Brandner, Lisa Fouts, Peter C. St. John, Earl D. Christensen, Jon Luecke, J. Hunter Mack, Charles S. McEnally, Patrick A. Cherry, Lisa D. Pfefferle, Timothy J. Strathmann, Davinia Salvachúa, Seonah Kim, Robert L. McCormick, Gregg T. Beckham, and Derek R. Vardon*

6.1 Abstract

Lignocellulosic biomass offers the potential to produce renewable fuels at a scale commensurate with petroleum consumption. Hybrid approaches that combine biological and chemocatalytic processes have garnered increasing attention due to their flexibility for feedstock utilization and diversity of potential products. Of note, lignocellulosic sugars can be converted biologically to short-chain carboxylic acids, while subsequent chemocatalytic upgrading can elongate the carbon backbone and remove oxygen from the structure to produce drop-in hydrocarbon fuels. However, hybrid conversion processes are typically not designed with the

X.H., N.A.H, J.S., N.S.C., A.K.S., A.E.S., A.M.Y., R.S.N., D.G.B., L.F., P.C.S.J., E.D.C., J.L., J.H.M., C.S.M., and P.A.C. performed research and analyzed data; L.D.P., T.J.S., D.S., S.K., R.L.M., G.T.B., and D.R.V. provided supervision; and X.H. and D.R.V. wrote the paper with input from all authors. X. H., A.M.Y., and T.J.S. are affiliated with Colorado School of Mines; X. H., N.A.H, J.S., N.S.C., A.K.S., A.E.S., A.M.Y., R.S.N., D.G.B., L.F., P.C.S.J., E.D.C., J.L., D.S., S.K., R.L.M., G.T.B., and D.R.V. are affiliated with National Renewable Energy Laboratory; J.H.M. is affiliated with University of Massachusetts Lowell. C.S.M., P.A.C, and L.D.P. are affiliated with Yale University.

fuel properties in mind *a priori*. In this work, we apply a “fuel property first” design approach to a tailored hydrocarbon diesel bioblendstock. Initially, model predictions for six fuel properties critical to diesel applications were used to screen an array of hydrocarbons accessible from upgrading individual and mixed C₂/C₄ acids. This screening step allowed for down-selection to a non-cyclic branched C₁₄ hydrocarbon (5-ethyl-4-propylnonane) that can be synthesized from butyric acid through sequential catalytic reactions of acid ketonization, ketone condensation, and hydrodeoxygenation. Following evaluation of each conversion step with model compounds, butyric acid was then converted through an integrated catalytic process scheme to achieve >80% overall carbon yield to a hydrocarbon mixture product containing >60% of the target C₁₄ hydrocarbon. The potential of this conversion strategy to produce a hydrocarbon diesel bioblendstock from lignocellulosic biomass was then demonstrated using corn stover-derived butyric acid produced from *Clostridium butyricum* fermentation. Experimental fuel property testing of the purified C₁₄ blendstock validated the majority of the fuel property model predictions. Meanwhile, the crude conversion product met fuel property target metrics, validating conversion process development. When the C₁₄ bioblendstock was blended into a petroleum diesel at 20 vol.%, the blend maintained low cloud point, high energy density, and cetane number. Notably, the blend reduced sooting tendency by more than 10%, highlighting the potential of the tailored bioblendstock to reduce particulate emissions.

6.2 Introduction

Biofuels have the potential to offset environmental impacts of the transportation sector, which accounts for 55% of oil consumption and 23% of energy-related CO₂ emissions globally.¹

² Passenger vehicles rank number one in consumption of oil, closely followed by road freight vehicles. Due to technology advances such as electrification, oil demand for passenger vehicles

has begun to plateau, but the demand of oil (primarily diesel) for road freight vehicles is projected to continue rising over the next few decades.³ Therefore, identifying routes to sustainable diesel fuel production is particularly important to both meeting future demand and curbing climate change. Lignocellulosic biomass is a relatively low-cost feedstock that allows renewable fuels to be produced at a meaningful scale.⁴ A wide array of molecules can be accessed from lignocellulosic biomass through diverse conversion pathways (e.g., biochemical, thermochemical, hybrid),⁵⁻⁷ creating ample opportunities to produce biofuels. A rational fuel design approach can have a major impact on enhancing the value proposition of biofuels.

Computational tools have seen growing application in multiple product development fields to reduce time, manpower, and cost.⁸⁻¹⁰ For example, computer-aided molecular design leverages quantitative structure–property relationships (QSPRs) and numerical optimization algorithms to search for optimal molecular structures across massive design space that includes completely novel structures.¹¹ In the context of biofuel design, computational fuel property prediction can be employed to screen potential fuel molecules and select a subset of the most promising candidates for further experimental study.^{12, 13} This process is enabled by fuel property predictive models, which provide estimates of fuel characteristics relevant to its handling and application, such as physical and chemical properties (e.g., density, boiling point, and C/H/O composition). Models specifically related to fuel performance have received increasing attention and can provide valuable information for designing performance-advantaged fuel molecules. These include octane number (ON), cetane number (CN), and yield sooting index (YSI), which describe fuel antiknock quality, autoignition ability, and sooting tendency, respectively.^{14, 15}

Hybrid conversion routes integrating biochemical and chemocatalytic processes provide numerous routes to access promising fuel molecules from biomass. Of note, short-chain

carboxylic acids can be produced from the low-cost anaerobic fermentation of lignocellulosic sugars and waste streams in high yield.¹⁶⁻²⁰ Although acids cannot be used directly as fuel due to their low energy density and corrosive nature, the functionality of the carboxylic acid group allows for diverse chemocatalytic chemistries to extend the carbon chain length and reduce oxygen content. For example, recent efforts have identified catalysts and reaction parameters for converting carboxylic acids to ketones, alcohols, and hydrocarbons of higher carbon number and diverse connectivity (e.g., linear, branched, cyclic) through a combination of C-C coupling, dehydration, and hydrogenation chemistries.²¹⁻²⁴ However, the viability of the conversion products as biofuel has not been evaluated. Efficient evaluation of these fuel candidates can be facilitated by computational tools, which remain underutilized.

To address these gaps, we demonstrate a “fuel property first” design approach to identify, synthesize, and experimentally confirm the fuel properties of promising hydrocarbon molecules derived from short-chain carboxylic acids to serve as drop-in diesel bioblendstocks (Figure 6.1). Initially, we mapped the potential array of long-chain hydrocarbon molecules accessible from the catalytic upgrading of acetic and butyric acid. The hydrocarbon functionality was targeted to take advantage of its compatibility with existing fuel infrastructure that would allow it to be deployed in the near term as a drop-in blendstock.^{25, 26} Fuel property prediction tools were then used to screen and down-select target molecules for further conversion pathway development. The catalytic conversion efficiency and product yield were evaluated for both single-step conversion and integrated catalytic process scheme using butyric acid, and this integrated scheme was then demonstrated using butyric acid derived from the anaerobic fermentation of corn stover hydrolysate. Lastly, fuel property testing evaluated both the neat blendstock and 20 vol.% blend

fuel properties. Results from this work provide justification for future process scale-up and fuel performance evaluation.

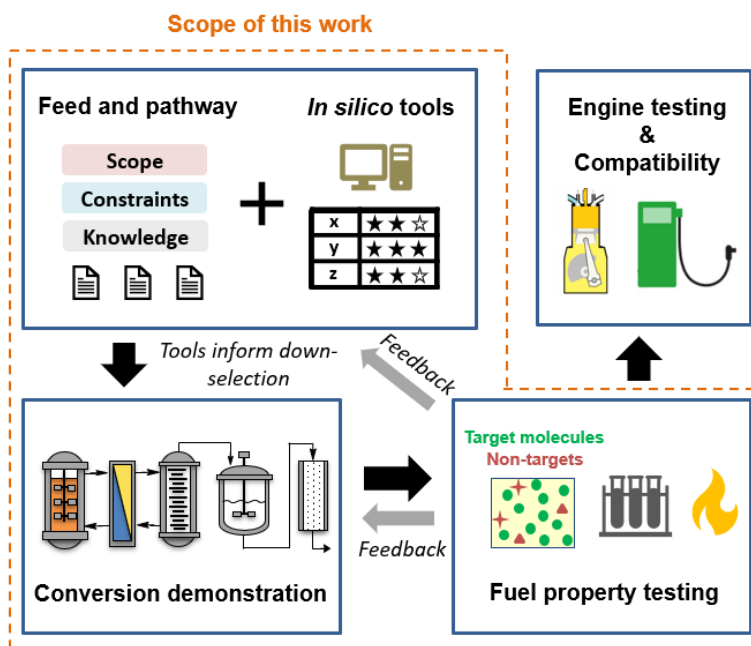


Figure 6.1 “Fuel property first” design approach to leverage fuel property predictive models for the design of performance-advantaged diesel bioblendstock.

6.3 Results

6.3.1 Fuel property prediction

6.3.1.1 Mapping hydrocarbons derived from C2/C4 acids

Fermentation-derived acetic acid and butyric acid were selected for combinatorial screening since they can be anaerobically produced from mixed lignocellulosic sugars in high yields.^{17, 27} Hydrocarbons with potential to be generated from upgrading individual and mixed C₂/C₄ carboxylic acids were then mapped using a multi-step catalytic conversion route consisting of ketonization, condensation, and hydrodeoxygenation (HDO) (Figure 6.2). Ketonization reacts two carboxylic acids to extend their carbon chain-length by forming a ketone with the release of CO₂ and H₂O.^{28, 29} Self-ketonization of acetic acid and butyric acid generates acetone and 4-

heptanone, respectively, while cross-ketonization between these two acids generates 2-pentanone. The ketone carbon backbone can be further elongated by condensation reactions that form non-cyclic branched dimers and cyclic trimers, while fully retaining all carbon and releasing oxygen in the form of water.³⁰ Lastly, HDO converts condensation products to hydrocarbons, with dimers resulting in non-cyclic branched hydrocarbons and trimers resulting in cyclic hydrocarbons.^{21, 24, 30} Overall, the reaction mapping process resulted in 30 hydrocarbons spanning from C₆ to C₂₁ (Table E.1 in Appendix E). While most of these hydrocarbons displayed carbon numbers within the range of diesel fuel (C₁₀ to C₂₅),³¹ their fuel properties were evaluated computationally to determine their dependence on molecular structure.

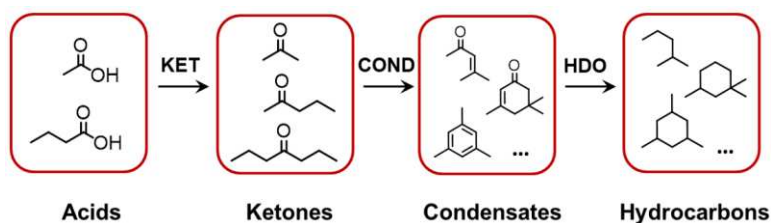


Figure 6.2 Upgrading scheme for converting C₂/C₄ carboxylic acids to hydrocarbon molecules via ketonization (KET), condensation (COND), and hydrodeoxygenation (HDO).

Fuel properties of the hydrocarbons were estimated using predictive models and compared against target metrics to identify desirable molecules and structures. These properties concern multiple aspects of fuel deployment, including physicochemical requirements, energy content, safety considerations, and emission potential. Starting with low-temperature handling ability, a fuel with an adequate regional and seasonal applicability requires a low melting point (or low cloud point for mixtures). A maximum value of 0 °C was used for initial screening.³² Using predictive models based on group contribution and correlation,^{33, 34} the non-cyclic branched hydrocarbons were all anticipated to exhibit low melting points (<-30 °C) suitable for cold environments, while cyclic hydrocarbons of C₁₅ or larger risk failing to meet the

requirement. Similarly, efficient fuel utilization must also satisfy a boiling point requirement, because non-volatile compounds resist evaporation/burning and remain in-cylinder, causing long-term operation issues. This fuel criterion was defined to be $<338\text{ }^{\circ}\text{C}$, consistent with the maximum allowable T90 specified for petroleum diesel by ASTM D975.³⁵ Except for C₂₁ molecules, group contribution methods^{33, 34, 36} predicted that all of the hydrocarbons evaluated herein meet this requirement. Meanwhile, low boiling point compounds cause safety concerns because they may form a flammable fuel-air mixture above the liquid. To ensure the safe handling and storage of a fuel, a minimum flash point of $52\text{ }^{\circ}\text{C}$ is specified for general purpose diesel by ASTM D975 and employed as a screening criterion in current study.³⁵ Molecules of C₁₁ and above in both non-cyclic branched and cyclic hydrocarbon groups were predicted to meet this requirement using correlations built from fuel and hydrocarbon databases,^{37, 38} Generally, a positive trend with carbon number was observed for these three fuel properties (Figure E.1a-c in Appendix E), as expected for paraffinic hydrocarbons.³⁹⁻⁴¹

Energy density, which is essential to fuel economy, was quantified by the lower heating value (LHV) of each compound. This is a measure of the heat released by combusting a quantity of fuel, minus the heat of vaporization of the combustion-generated water. LHV varies between 32-44 MJ kg⁻¹ for petroleum diesel, and a value of 40 MJ kg⁻¹ was selected as the minimum requirement to ensure a competitive energy density. Utilizing models correlating heats of combustion with elemental analysis,⁴²⁻⁴⁴ all mapped hydrocarbon molecule predictions fell well above the LHV requirement and were nearly uniform (Figure E.1d in Appendix E) due to similarities in elemental composition (e.g., 84-86 wt% carbon).

The autoignition and sooting behavior of the hydrocarbons were informed by predicting CN and YSI using machine learning methods.⁴⁵⁻⁴⁷ For CN, a higher value indicates faster

autoignition, which in turn can improve heat release rates and engine cold-start capabilities. The minimum requirement of 40, in line with ASTM D975 requirements, was selected to ensure adequate fuel reactivity,³⁵ although CN requirements can vary depending on the region (e.g., a minimum CN of 51 required by DIN EN 590 in Europe⁴⁸). Nine non-cyclic branched hydrocarbon molecules and two cyclic hydrocarbon molecules were predicted to meet the minimum requirement of 40 (Table E.1 in Appendix E). Previous studies have shown that CN increases with the secondary C-H:primary C-H ratio due to a lower-energy alkylperoxy radical isomerization pathway enabled by secondary C-H bonds.⁴⁹⁻⁵¹ However, the absence of a strong correlation in this study (Figure E.1e in Appendix E) suggested significant influence from tertiary C-H and/or quaternary carbon as well.⁵²

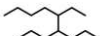
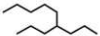
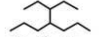
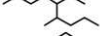
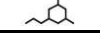
In contrast to autoignition ability, soot emission from diesel combustion currently does not have a known verified predictive fuel property metric. Diesel combustion is largely mixing-controlled, and soot formation is likely to depend on intrinsic sooting tendency, ignition delay, and physical properties relative to spray penetration and breakup. For this initial screening, YSI was chosen to assess the sooting potential of fuel candidates, with the higher value denoting stronger chemical sooting tendency.⁴⁷ Predicted YSI of the mapped hydrocarbons was shown to generally increase with carbon number in (Figure E.1f in Appendix E). YSI normalized by carbon number characterizes the average contribution of each carbon atom in the molecule to soot formation and was roughly constant for each category of hydrocarbons (see last column of Table E.1 in Appendix E). For the non-cyclic branched hydrocarbons, normalized YSI values varied between 5.9–6.8 and were lower than those of the cyclic hydrocarbons (7.3–9.0). The stronger sooting tendency of the cyclic structure agrees with experimental observations in the

literature,¹⁵ as small cyclic hydrocarbons tend to have lower energy barrier pathways towards forming resonantly-stabilized soot precursors.⁵³

6.3.1.2 Down-selection of targets for diesel blendstock

Based on these predicted fuel properties, a subset of C₁₂–C₁₄ molecules was identified to contain promising diesel candidates, including four non-cyclic branched hydrocarbon molecules and one cyclic hydrocarbon molecule (Table 6.1). These molecules are accessed from either single C₄ acid or mixed C₂/C₄ acids. With butyric acid, the C₁₄ hydrocarbon in Table 6.1 can be synthesized from self-condensation of 4-heptanone that is generated from butyric acid ketonization. When mixed C₂/C₄ acids are used, acetone and 2-pentanone are formed in addition to 4-heptanone, which provides a pathway to all five of the down-selected molecule candidates. However, the presence of acetone and 2-pentanone negatively impacts the ability to selectively produce the target hydrocarbon molecules due to their facile condensation into cyclic trimers that react to form cyclic hydrocarbons after HDO.^{21, 24, 30} As noted, the resulting cyclic hydrocarbons display less desirable diesel fuel properties, such as low CN and high YSI. Therefore, we chose to focus on the conversion pathway that starts solely with butyric acid targeting the non-cyclic

Table 6.1 Model predictions of melting point, boiling point, flash point, lower heating value (LHV), cetane number (CN), and yield sooting index (YSI, normalized to carbon number in parentheses) for down-selected hydrocarbon molecules. Average values reported when multiple predictions are available. Full list of molecule candidates and model predictions provided in Table E.1 in Appendix E.

Hydrocarbons	C No.	Melting point (°C)	Boiling point (°C)	Flash point (°C)	LHV (MJ kg ⁻¹)	CN	YSI
Screening criteria	None	<0	<338	>52	>40	>40	None
	14	-38	241	82	45	48	91 (6.5)
	12	-48	204	62	45	45	71 (5.9)
	12	-61	199	61	45	44	75 (6.2)
	12	-61	199	61	45	43	75 (6.2)
	13	-24	231	84	45	44	99 (7.6)

branched C₁₄ hydrocarbon, 5-ethyl-4-propylnonane, shown in the first entry of Table 6.1. Previous studies have shown proof-of-concept for the individual catalytic conversion steps comprising this pathway.^{24, 30} As such, this work looked to evaluate the integrated catalytic conversion scheme and validate diesel blendstock properties for both the target C₁₄ hydrocarbon and crude conversion product.

6.3.2 Catalytic upgrading of butyric acid

6.3.2.1 Single step conversion of model compounds

Initially, each catalytic conversion step in the butyric acid upgrading scheme was evaluated individually for conversion efficiency and carbon yield with the aim of moving towards process relevant conditions. The ketonization reaction was first performed using commercial butyric acid ($\geq 99\%$ purity, Sigma Aldrich) in a continuous flow reactor to remove the corrosive acid functional group and increase the C₄ carbon chain length to C₇, producing CO₂ and water in the process. The reactor was packed with a commercial ZrO₂ catalyst, which is an amphoteric redox metal oxide known to provide high activity and selectivity for this chemistry.⁵⁴ The catalyst displayed a surface area of 65 m² g⁻¹ and total acidity of 163 $\mu\text{mol g}^{-1}$ (Table E.2 in Appendix E). At 435 °C and a weight hourly space velocity (WHSV) of 3.8 h⁻¹, butyric acid was completely converted for over 11 hours of time-on-stream with an overall mass recovery >92% (Figure 6.3). The gas phase product was primarily CO₂, and the condensable liquid product was biphasic due to the low water solubility of 4-heptanone (approx. 3 g L⁻¹ at room temperature). The purity of 4-heptanone in the organic liquid phase was 90%. Although the non-target products were not fully identified, work was conducted to determine the impact of these compounds on the integrated catalytic upgrading steps and final fuel properties, as discussed below.

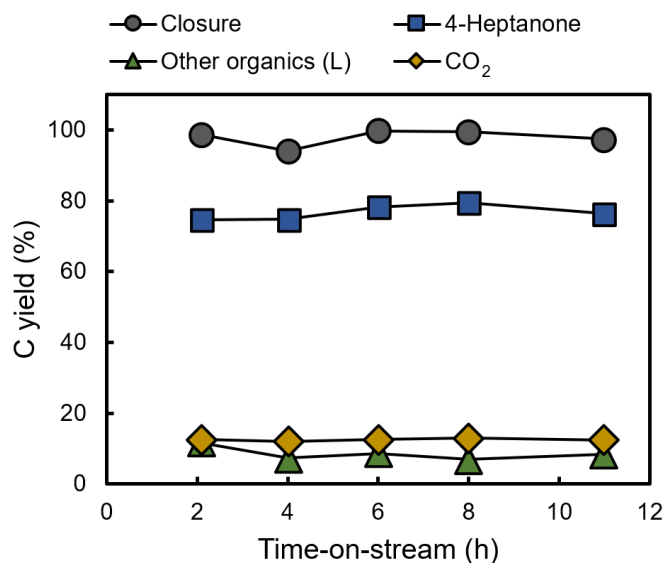


Figure 6.3 On-stream performance and product distribution of commercial butyric acid ketonization over 3 g ZrO₂ in flowing Ar [1 atm, 100 mL (STP) min⁻¹] at 435 °C and WHSV = 3.8 h⁻¹. WHSV was calculated using the mass flow rate of butyric acid and the mass of the catalyst.

Aldol-type condensation was then performed on the 4-heptanone product stream to further elongate the carbon chain to C₁₄ and reduce the oxygen content. While significant work has been performed to date with terminal ketones,^{21, 55, 56} condensation of internal ketones, such as 4-heptanone, is far less studied. Recently, Nb₂O₅ was identified as a highly selective catalyst (>80% carbon selectivity) to the dimer (mixture of positional and stereoisomers) for 4-heptanone condensation, but the chemistry has only been demonstrated for single-pass batch reactions with 8 wt% of 4-heptanone in toluene.^{16, 21} When considering process design impacts, the relatively low ketone loading will require large equipment and high energy consumption for solvent separation. Therefore, we evaluated conversion efficiency at elevated ketone loadings with catalyst regeneration and recycle (Figure 6.4).

4-Heptanone condensation was performed in a bench-scale batch reactor. A commercial Nb₂O₅ catalyst acquired from CBMM was calcined at 350 °C prior to use, resulting in a surface area of 137 m² g⁻¹ and total acidity of 255 μmol g⁻¹ (Table E.2 in Appendix E). Initial

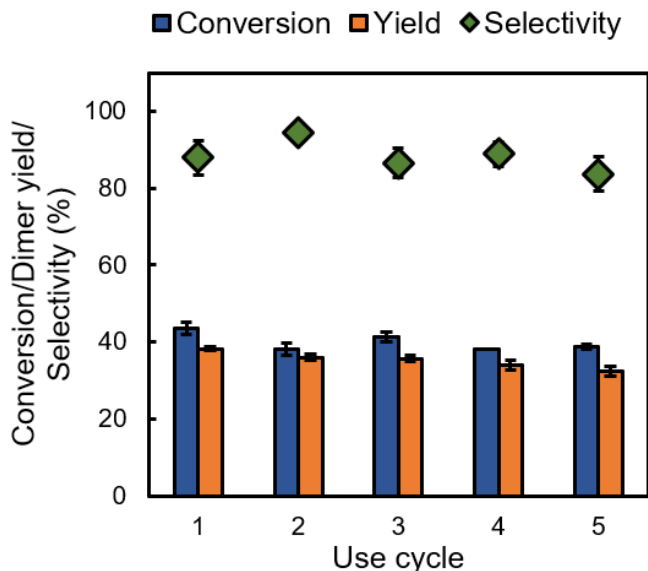


Figure 6.4 Nb₂O₅ reused for 4-heptanone condensation four times in a batch reactor by regeneration at 350 °C in between cycles. Reaction conditions: 15 g feed, 20 wt% 4-heptanone in toluene, 0.75 g catalyst, catalyst-to-ketone mass ratio = 1:4, initial He headspace at atmospheric pressure, 180 °C, 10 h.

experiments were performed using commercial 4-heptanone (98% purity, Sigma Aldrich) with a ketone loading of 20 wt% in toluene, ketone-to-catalyst mass ratio of 4:1, reaction temperature of 180 °C, and an initial atmospheric pressure He headspace. Under these conditions, conversion progressed rapidly in the first 3 h to 27% and then gradually to 58% after 24 h (Figure E.2a in Appendix E). At 24 h, selectivity to the desired dimer was 81%, similar to previous studies.^{16, 21} The overall mass recovery was >98% with negligible mass loss to the gas phase, and the carbon mass recovery was >96%. The reactivity of 4-heptanone is significantly lower compared to that of the terminal ketone, as demonstrated for example by conversion of 2-heptanone reaching 90% in the first 3 h under similar conditions (data not shown). The lower reactivity is likely due to steric hinderance, making internal ketones inherently more difficult to process. The average reaction rate for 4-heptanone condensation plotted over time (Figure E.2b in Appendix E)

revealed rapid degradation in activity. A carbon content of 2.3 wt% was measured for spent Nb₂O₅ after 24 h reaction, suggesting fouling as a mode of deactivation.

To assess catalyst recyclability, spent Nb₂O₅ was washed with solvent, dried, and tested under the same reaction conditions as the fresh catalyst. Continuous decline in activity was still observed in subsequent reuses (Figure E.2c in Appendix E), likely due to incomplete removal of adsorbed species. Calcination of the spent catalyst in air at 350 °C for 12 h was then employed to regenerate the catalyst. Over four cycles of reuse, a 15% decrease in dimer carbon yield was observed (Figure 6.4). Surface area and total acidity of the regenerated catalysts showed insignificant change compared to those of the fresh catalyst, while small quantities of carbon residue were measured on the regenerated catalysts (Table E.3 in Appendix E). These observations suggest that the most active sites are vulnerable to deactivation and like not fully regenerated under mild conditions. Although carbon residue can be removed at higher calcination temperatures, further evaluation of catalyst activity will be needed as increasing temperature can lead to loss of water content and phase transition, accompanied by reduced surface area and acidity for this catalyst.⁵⁷

Additional reaction conditions were then evaluated to further reduce solvent use and improve single-pass conversion by increasing the ketone loading (20 wt% to 100 wt.%), catalyst loading (catalyst-to-ketone mass ratio from 1:20 to 1:5), and operating temperature (180 °C to 220 °C). When the ketone loading increased from 20 wt.% to 100 wt.% (i.e., neat solvent-free) for a given catalyst loading, 10 h conversion decreased (Figure E.3a in Appendix E), while the average ketone reaction rate was nearly constant (Figure E.3b in Appendix E), indicating a high coverage of surface intermediates at these ketone loadings.⁵⁸ Increasing the catalyst loading under neat conditions increased dimer concentration in the liquid product (Figure E.3c in

Appendix E) but also enhanced carbon loss to catalyst surface. For example, 0.04 g carbon was measured for the spent catalyst at a catalyst-to-ketone mass ratio of 1:20, and this value increased more than three-fold to 0.13 g when the mass ratio increased to 1:5. With respect to operating temperature, raising the temperature from 180 °C to 220 °C at 20 wt.% ketone loading increased conversion by 30% after 10 hours of reaction but reduced dimer selectivity by 20% (Figure E.4a in Appendix E). Estimating the activation energy from Arrhenius plots was hindered (Figure E.4b in Appendix E), potentially due to rapid carbon laydown from the reaction. Although beyond the scope of this study, high temperature processing of neat internal ketones requires further analysis to evaluate the tradeoff between increased conversion at the expense of selectivity and final fuel properties.

The final HDO step was then examined to convert the purified dimer into the target C₁₄ hydrocarbon. The dimer feed was derived from commercial 4-heptanone and prepared by removing the reaction solvent and unreacted ketone through distillation, resulting in a mixture of 81% dimer and 19% non-target compounds. The latter may include higher boiling point trimer and larger oligomers that we were unable to identify by GC (Figure E.5 in Appendix E). HDO was performed in a packed bed flow reactor using a 3.3 wt% Pt/Al₂O₃ catalyst due to its metal-acid bifunctionality.^{59,60} The catalyst displayed a surface area of 198 m² g⁻¹, metal dispersion of 9.4%, and total acidity of 329 μmol g⁻¹, with the latter dominated by Lewis acidity (Table E.2 in Appendix E). At 334 °C and a WHSV of 4.4 h⁻¹, the dimer was completely converted with >97% overall mass recovery and >90% selectivity to a C₁₄ hydrocarbon based on incoming dimer purity (Figure 6.5). Deoxygenation of the feed was also complete, resulting in a biphasic product comprising an organic phase (85 wt% C and 15 wt% H) and an aqueous phase. The C₁₄ hydrocarbon was confirmed to exhibit the target structure by a combination of high-resolution

mass spectrometry (Figure E.6 in Appendix E) and nuclear magnetic resonance spectroscopy (Figure E.7 in Appendix E). A 10% decrease in C₁₄ hydrocarbon yield was observed over 12 hours of time-on-stream due to an increasing degree of isomerization and cracking of the C₁₄ hydrocarbon. The spent Pt/Al₂O₃ catalyst contained 5.5 wt% carbon, relatively small (<0.2%) compared with the total carbon mass processed. Regeneration by calcination completely restored the catalyst physicochemical properties (Table E.6 in Appendix E), indicating catalyst fouling as the likely cause for the decrease in C₁₄ hydrocarbon yield. Future work is needed to identify the cause of catalyst fouling and understand its impact on reaction network and consequent change of product distribution.

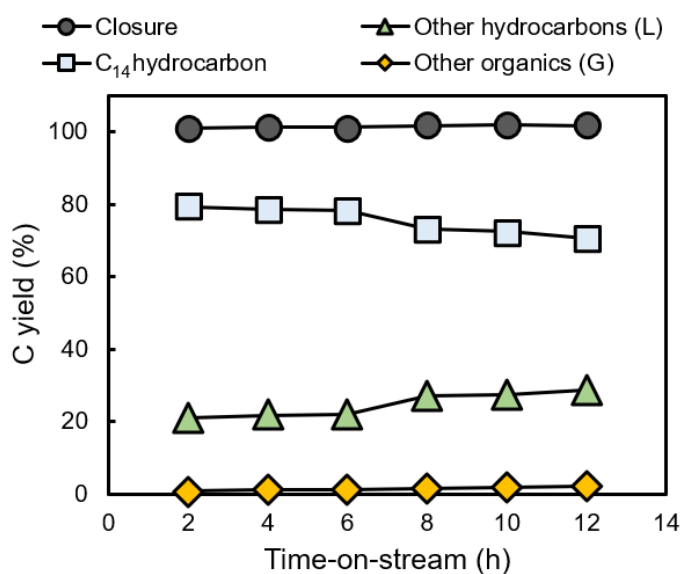


Figure 6.5 On-stream performance and product distribution of dimer HDO over 1 g Pt/Al₂O₃ in flowing H₂ [500 psi, 165 mL (STP) min⁻¹] at 334 °C and WHSV = 4.4 h⁻¹. The dimer feed (81% dimer purity) was derived from commercial 4-heptanone. WHSV was calculated using the mass flow rate of the dimer feed and the mass of the catalyst.

6.3.2.2 Integrated conversion of model and bio-butyric acid

Although the individual catalytic conversion steps above were demonstrated to have high selectivity (>85%) towards target products, the formation of non-target compounds poses additional challenges when using a fuel design approach based on evaluation of individual

compounds. To this end, butyric acid was upgraded through the integrated catalytic conversion scheme shown in Figure 6.6. Starting with a model butyric acid feed, the ketonization resulted in complete butyric acid conversion with 13% carbon converted to CO₂ and 78% carbon converted to 4-heptanone (Figure 6.7). While the formation of CO₂ was stoichiometric and consistent with complete acid conversion, carbon yield to 4-heptanone was 88% of the theoretical yield. The remaining 9% of the carbon was retained in non-target byproducts primarily in the same phase as 4-heptanone. The organic phase of the liquid product was then decanted for separation from water. Note that carryover of water to the next conversion step may not affect process efficiency as the Nb₂O₅ catalyst used for ketone condensation is water tolerant.^{24, 61}

The ketonization organic phase was then mixed with toluene at 20 wt% for the condensation reaction under the conditions shown in Figure E.2a in Appendix E. After 24 h, conversion of 4-heptanone reached 55% with an 82% selectivity to the dimer, nearly identical to the results obtained with commercial 4-heptanone (58% conversion and 81% selectivity). Due to byproduct formation during condensation, the fraction of carbon in the non-target compounds increased from 10% to 15% after the reaction (Figure 6.7). The reaction product was distilled to separate the dimer and heavier byproducts from solvent and ketone residue. Three fractions were obtained from distillation (Figure E.8 in Appendix E): solvent and unreacted ketone were primarily recovered in fractions 1 and 2, while fraction 3 comprised dimer (68% purity), heavier byproducts and minor lighter components (e.g., 2% 4-heptanone). Fraction 1 and 2 were recycled for condensation, and fraction 3 was used as the feed for the HDO reaction. Under the same operating conditions previously described (Figure 6.5), complete deoxygenation was achieved with selective conversion of dimer to the target C₁₄ hydrocarbon at 65% purity in the organic phase (Figure 6.7). Organic phase non-target compounds included C₁₄ hydrocarbon isomers,

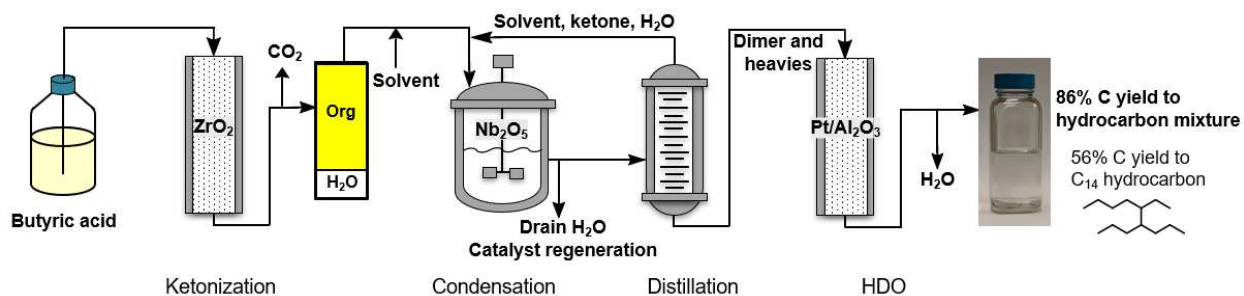


Figure 6.6 Integrated process scheme for upgrading butyric acid to hydrocarbon diesel blendstock.

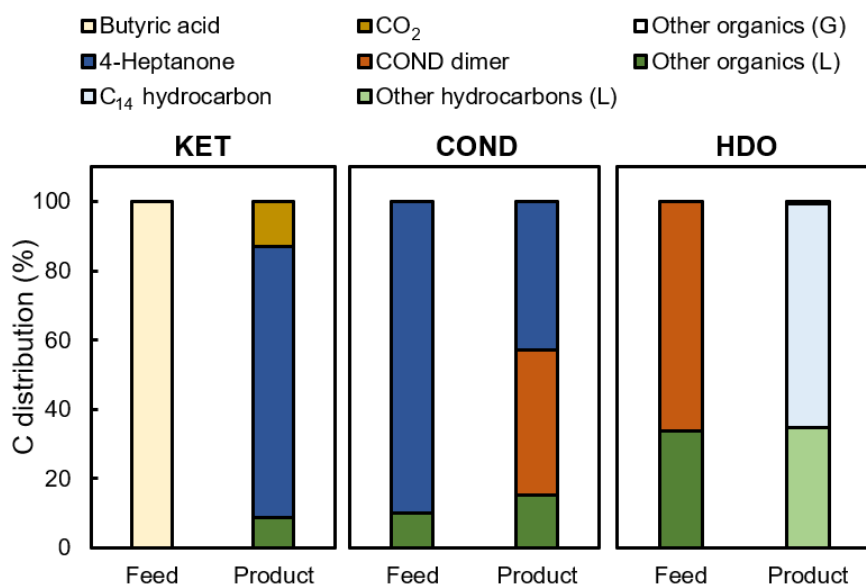


Figure 6.7 Carbon yield analysis of ketonization, condensation, and HDO when upgrading commercial butyric acid to hydrocarbon diesel blendstock through the integrated process scheme as shown in Figure 6.6. Conditions: ketonization same as in Figure 6.3; condensation same as in Figure E.2a in Appendix E, 24 h reaction, C distribution not accounting for solvent; HDO same as in Figure 6.5, 2 hours of time-on-stream. Analysis assumed ideal mass recovery.

other non-cyclic alkanes, cyclic alkanes, and a minor fraction of unsaturated structures (Figure E.9-E.11 in Appendix E). Assuming ideal separation and complete mass recovery during transfer,²⁵ the overall carbon yield of butyric acid to HDO organic phase was as high as 86%, while the overall carbon yield to the target C₁₄ hydrocarbon was 56%. It is clear from these results that utilization of non-target hydrocarbons in the final diesel blendstock is critical to high carbon efficiency of the integrated process.

Finally, biologically-derived butyric acid was upgraded through the same integrated conversion scheme to demonstrate bioblendstock production from lignocellulosic biomass. Batch fermentation was performed with *Clostridium butyricum* on corn stover hydrolysate, the major components of which are glucose and xylose (Table E.5 in Appendix E).⁶² Utilization of sugars in the hydrolysate was nearly complete after 56 h (Figure E.12a in Appendix E), and butyric acid was produced at a final titer of 20.4 g L⁻¹ and yield of 0.32 g g_{sugar}⁻¹ (Figure E.12b in Appendix E). A multi-step purification process recovered butyric acid from the fermentation broth at purity >99%, with separation optimization beyond the scope of this study.

Catalytic upgrading of the biologically-derived butyric acid achieved initial conversion efficiency and target product yield comparable to those from upgrading commercial butyric acid (Table 6.2). Under the same ketonization and condensation conditions, conversion of the target reactants and carbon yield to the desired products deviated by <2% from model compound experiments. After condensation, solvent and unreacted ketone were removed through distillation as previously described. Due to limited volume of the biologically-derived substrate, the feed for HDO was diluted with cyclohexane to facilitate sample handling. This modification did not change conversion efficiency, resulting in complete conversion of the dimer and production of an oxygen-free organic phase. The concentrations of non-metallic and metallic impurities in the biologically-derived feed and organic phase products were consistently low (Table E.6 in Appendix E, variation of Si may be due to the wear of reactor coating), suggesting an insignificant impact on catalyst performance or product purity for the time scale studied. However, the variety and level of impurities can vary greatly depending on biological conversion and separation conditions,⁶³⁻⁶⁵ and a systematic evaluation of their impact on downstream catalytic processes is needed to provide valuable information for further process

integration with upstream processes. The target C₁₄ hydrocarbon was produced at 61% purity in the final hydrocarbon mixture product after solvent (cyclohexane) removal, comparable with the results from upgrading commercial butyric acid. Carbon mass balance analysis was not performed due to limited volume of biologically-derived materials. However, both similar conversion performance (Table 6.2) and product gas chromatography profile (Figure 6.8) suggest that the carbon efficiency of upgrading biologically-derived butyric acid can be represented by those with commercial butyric acid, where the overall carbon yield to the final hydrocarbon mixture product was 86%.

Table 6.2 Conversion of target reactants (butyric acid, 4-heptanone, and dimer) and carbon yield to the desired products (4-heptanone, dimer, and C₁₄ hydrocarbon, respectively) from upgrading biologically-derived and commercial butyric acid through the integrated process scheme.

Conversion step	Bio-acid		Commercial acid	
	Conversion	Yield	Conversion	Yield
KET	100%	76%	100%	77%
COND	54%	42%	55%	45%
HDO	100% ^a	88% ^a	100%	87-97%

^aFeed prepared by diluting distillation fraction 3 in cyclohexane at 20 wt.%, total feed WHSV = 8.2 h⁻¹.

6.3.3 Blendstock and blend fuel properties verification

Fuel properties were experimentally determined for both purified and crude C₁₄ hydrocarbon blendstocks to verify model predictions and evaluate fuel quality of the crude conversion product mixture. Measured boiling point, LHV, flash point, and YSI of the purified blendstock (94% purity, Table 6.3) were well within 10% of the predicted values summarized in Table 6.1. Measured CN of an 81% C₁₄ blendstock also matched the model prediction very well. In contrast, the measured melting point was notably more than 40°C lower than the predicted value. A melting point or cloud point below -80 °C indicates that this blendstock is likely suitable for use in even the coldest environments. Predicted values for melting point deviated substantially from experimental measurements. However, melting point prediction is inherently

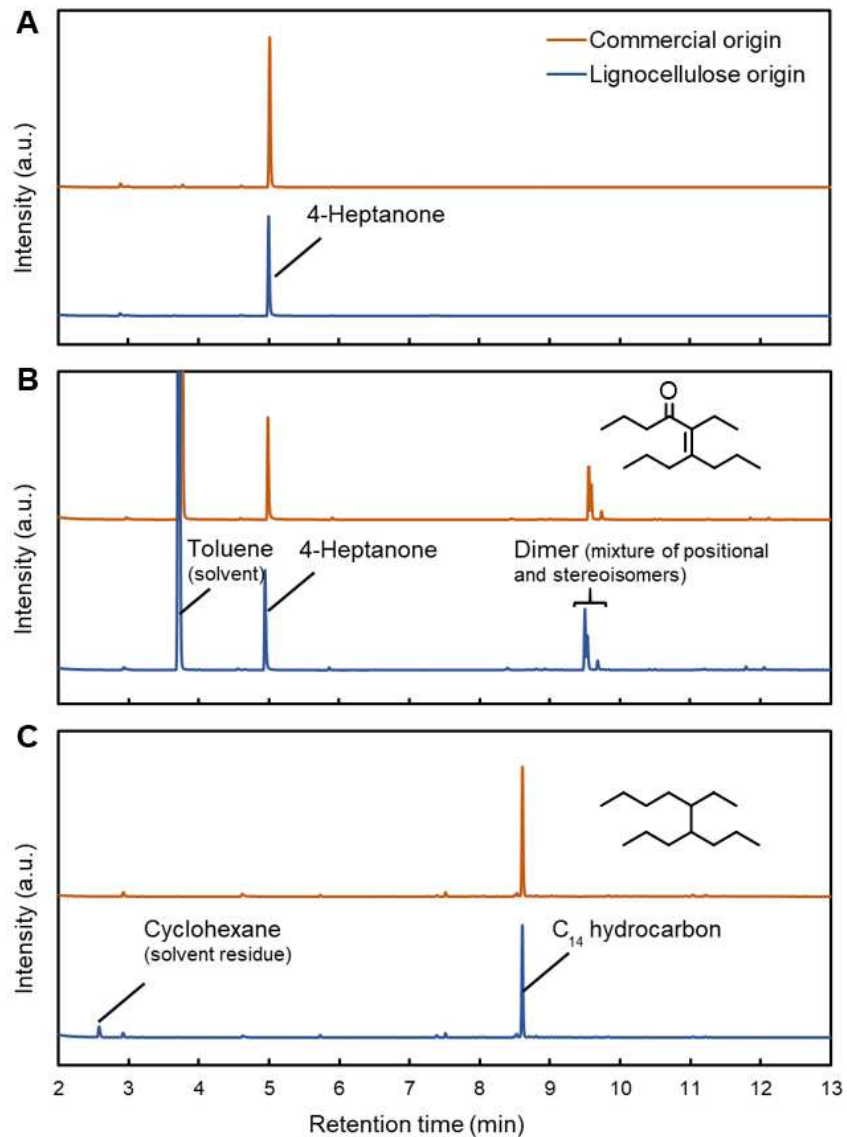


Figure 6.8 GC-Polyarc/FID chromatograms of organic phase products from (A) ketonization, (B) condensation, and (C) HDO (solvent was removed from biologically derived product by distillation) when upgrading butyric acid through the integrated process scheme.

difficult, with mean prediction errors often exceeding 40 °C.⁶⁶

After verifying the target C₁₄ molecule fuel properties, the crude blendstock was characterized to a similar extent to assess the impact of non-target compounds on fuel properties. Due to limited quantity of the biologically-derived materials, crude blendstock was prepared from commercial reagents. Compared with the purified blendstock, crude blendstock displayed

similar bulk properties, such as LHV and density (Table 6.3), which was expected given the target C₁₄ hydrocarbon being the major component. In contrast to bulk properties, the crude blendstock exhibited a flash point 12 °C lower than that of the purified blendstock (Table 6.3). As previously shown, hydrocarbons with lower boiling point tend to have lower flash point (Figure E.1c in Appendix E). Therefore, the decrease in flash point was likely due to the short-chain hydrocarbons in the crude blendstock (<15 vol.% based on simulated distillation analysis), which resulted from HDO of 4-heptanone residue and undesired cracking reactions on acid catalysts. These low boiling point byproducts need to be monitored to ensure compliance with safety requirement. Nevertheless, the crude blendstock was well above the minimum flash point requirement for diesel fuels. To evaluate the sooting tendency of the crude blendstock on a volumetric basis that is consistent with volumetric blending, normalized soot concentration (NSC) was used. NSC is defined as the concentration of soot measured for a blendstock or a blend normalized to that of the base diesel (by definition having an NSC of 1). Both the purified and crude blendstocks exhibited NSC more than 50% lower than that of the base diesel, with the purified blendstock showing 21% lower NSC than the crude blendstock due to fewer non-target compounds (Table 6.3). Overall, these results validated the fuel properties of the crude blendstock and confirmed the successful conversion process development.

The promising fuel characteristics of the crude blendstock strongly indicate its suitability for use as drop-in diesel blendstock. This was further verified by measuring the fuel properties of a diesel blend containing a base diesel and 20 vol% crude blendstock derived from bio-butyric acid. The base diesel is a petroleum diesel (commercial additives were removed) that has excellent properties including low cloud point, high energy density, and cetane number. When comparing the measured fuel properties between the blend and the base diesel, it was evident that

Table 6.3 Measured fuel properties of C₁₄ blendstocks, base diesel, and a 20 vol% blend.

Properties	C ₁₄ blendstock		Diesel and blend	
	Purified	Crude ^a	Base diesel ^b	Blend ^c
Melting point (°C)	<-80	<-80	-9.7	-12
Cloud point (°C)	<-80	<-80	-7.6	-8.7
Boiling point (°C)	230	266 ^d	333 ^d	327 ^d
Flash point (°C)	74	62 ^e	55	54 ^e
LHV (MJ kg ⁻¹)	44	44	45	43
LHV (MJ L ⁻¹)	34	34	39	37
CN ^f	ND	48 ^e	47	46 ^e
YSI	98	NA	NA	NA
NSC	0.37	0.47	1	0.89
Viscosity (cSt)	ND	1.49 ^e	2.66	2.08 ^e
Density (g mL ⁻¹)	0.78	0.78	0.86	0.85

ND = Not determined. NA = Not applicable. ^aDerived from commercial butyric acid (65% C₁₄ purity). ^bCommercial additives were removed by clay treatment. ^c20 vol% bio-butyric acid derived blendstock (61% C₁₄ purity) in base diesel. ^dT90 from simulated distillation profile. ^e20 vol% 4-heptanone derived blendstock (81% C₁₄ purity). ^fMeasured as indicated cetane number using ASTM method D8183.

the bioblendstock was able to maintain the base diesel quality (Table 6.3). For example, the bioblendstock slightly lowered the cloud point, demonstrating excellent solubility in the diesel fuel. The T90 was slightly reduced due to the lower boiling-range of the bioblendstock compared to the base diesel (Figure E.13 in Appendix E). Because the base diesel has a lower flash point than the blendstock, the flash point of the blend was dominated by that of the base diesel. The bioblendstock exhibited good ability to maintain diesel energy density compared with biodiesel and alcoholic diesel blendstocks,^{67, 68} with only 5% reduction in blend LHV on either mass or volume basis. The measured CN of the blend was nearly unchanged and remained sufficiently beyond the minimum requirement of 40, which was expected considering the similar CN values between the base diesel and the blendstock (Figure E.14a in Appendix E). It is notable that the bioblendstock demonstrated the potential to reduce diesel soot formation, with the blend reducing NSC by 11% compared with the base diesel (Table 6.3). In addition, NSC appeared to linearly decrease with the blending volume of the bioblendstock (Figure E.14b in Appendix E), suggesting the potential to further reduce diesel sooting by increasing the blend ratio.

6.4 Discussion

To rationally target bioblendstocks that lead to advantageous properties, we leveraged fuel property prediction tools to inform the conversion pathway and molecule selection based on a “fuel property first” approach. This approach prioritizes fuel quality by estimating the fuel properties of potential products from an array of conversion pathways. We demonstrated this approach by employing a variety of empirical, predictive models derived from functional group contributions, molecular descriptors, and physical property correlations to screen 30 diesel-range hydrocarbon molecules accessible from short-chain C₂ and C₄ carboxylic acids derived from biological processes. This screening step allowed us to down-select butyric acid as the primary feedstock of interest for further catalytic upgrading to a non-cyclic branched C₁₄ hydrocarbon as a potentially high combustion efficiency, low soot formation diesel blendstock. Tailoring hydrocarbon diesel blendstock from biological-chemocatalytic conversion routes is only one example of the “fuel property first” approach. This approach can be applied to diverse conversion routes and molecules accessible from lignocellulosic biomass⁶⁹⁻⁷³ to accelerate biofuel development, and the growing availability of fuel property prediction tools and metrics^{12, 52, 74-76} can also guide design for a variety of fuel applications and combustion modes.

Fuel property predictive models enable low-cost rapid fuel property evaluation by removing the sample quantity constraints associated with experimental synthesis and testing. This allowed us to evaluate six fuel properties related to handling and storage, fuel economy, and combustion performance, all of which are critical to successful fuel deployment. Notably, the YSI predictive model made it possible to screen fuel molecules for their sooting tendency, which is an emerging fuel property metric to evaluate particulate emissions.^{47, 77, 78} Comparing fuel property predictions across an array of molecule candidates narrowed the candidate pool from 30

down to 5 molecules; more importantly, it also provided quantitative information to facilitate further conversion pathway down-selection. Non-cyclic structures were identified as preferred targets for diesel applications, when compared to cyclic structures, due to the higher autoignition ability and lower sooting tendency of the former (Figure E.1e-f in Appendix E). Fuel property measurements of the target C₁₄ hydrocarbon validated five out of six fuel property predictions, highlighting the value of the predictive models in rational fuel design.

Upgrading butyric acid through an integrated process scheme validated the conversion pathway and the advantageous fuel properties of the C₁₄ hydrocarbon. Furthermore, conversion product analysis identified catalytic reaction byproducts as a key consideration for the “fuel property first” approach, which has rarely been addressed in fuel design. When producing the C₁₄ hydrocarbon from butyric acid through sequential reactions, multiple non-target hydrocarbons were accumulated in the crude conversion product (Figures 6.7, Figure E.10 and E.11 in Appendix E) and entailed experimental evaluation of their influence on fuel properties. Although these non-target compounds did not significantly affect the bulk properties for the C₁₄ blendstock, minor components have the potential to dramatically impact fuel properties at low levels, such as depressing flash point by >10°C with <15 vol.% low boiling point byproducts (Table 6.3). These observations encourage future consideration of conversion byproducts in the early phase of fuel design, which may be achieved by estimating the properties of mixtures for selected fuel parameters. A critical consideration for designing blendstocks is their blending behavior, and linear mixing rules have often been assumed to simplify prediction methodology in fuel blend design studies.^{13, 79, 80} This simple blending behavior has been experimentally observed for bulk properties such as CN and viscosity with hydrocarbon mixture,^{81, 82} whereas non-ideal behaviors are frequently reported for other properties and oxygenate-hydrocarbon mixtures.^{68, 83-85} For our

bioblendstock blend, further testing is needed to determine the blend dependency since only single point blends measurements were performed. The ability to accurately predict mixture properties and blending relationships remains a grand challenge for computation and underscores the need to couple experimental validation of product fuel quality with the specific conversion routes and feedstocks of interest.

To further develop the butyric acid upgrading process we investigated, specific improvements can be made to each catalytic step. The initial acid ketonization reaction will likely not be a limiting step, as this work demonstrated complete butyric acid conversion and high molar selectivity (88%) to the target ketone under solvent-free and continuous production conditions and similarly high yields have been shown in other studies for acetic acid.^{86, 87} Further improvement of selectivity may be attained by adjusting operating conditions and introducing metal sites to improve the reducibility of metal oxide catalysts.^{88, 89} For 4-heptanone condensation, although we have demonstrated promising single-pass productivity at process-relevant ketone loadings, it will be important to understand the catalyst requirements and reaction mechanism for internal ketone condensation. Knowledge of both will be critical to developing effective strategies for increasing yields and stability,⁹⁰⁻⁹³ as rapid catalyst deactivation has been reported with acid, base, and amphoteric catalysts for a broad class of aldol-type condensation reactions.⁹⁴⁻⁹⁷ Introducing hydrogenation functionality to catalysts has shown promise to improve dimer selectivity or catalyst stability for C₃-C₆ methyl ketone or aldehydes,^{55, 58, 97} but its potential to improve longer-chain internal ketone condensation still needs to be assessed. Lastly, continuous HDO was demonstrated with very high initial selectivity (98%) to the target hydrocarbon, but reversible catalyst deactivation by fouling resulted in gradual decrease in selectivity. To prevent catalyst fouling, further work is needed to identify if

carbon deposition is caused by heavy compounds in the feed or *in situ* formation. Depending on the cause of deactivation, countermeasures can be taken such as pretreating the feed, tuning catalysts and process conditions, and controlling reaction rate regimes.^{98, 99} When considering process integration, work is ongoing to improve the biological and separation efficiency of microbial acids, as well as understand the impact of biogenic impurities on catalyst performance.^{62, 65, 100}

Lastly, based on promising fuel property validation results, the C₁₄ blendstock warrants further engine testing to fully de-risk the bioblendstock from a fuel standpoint. Engine testing can assess fuel performance and quantify air pollutant emissions over a range of operating conditions reflective of use (e.g., compression ratio, air-fuel ratio, fuel injection pressure, cold starting).¹⁰¹⁻¹⁰³ Testing results can inform the “fuel property first” approach by improving our understanding of priority fuel property metrics that reflect desired engine and emission performance in actual use scenarios. Because traditional engine testing requires gallons of fuel, *in silico* and bench scale tools will be valuable to facilitating fuel performance evaluation. Bench scale evaluation of combustion kinetics can be performed with samples on the order of several hundred milliliters of bioblendstock,^{104, 105} and these data can serve as the basis for kinetic simulations that could ultimately be used – in reduced form – as part of an engine simulation to predict efficiency and approximate emissions effects.^{106, 107} Bench scale studies of fuel sprays and measurement of related properties can also inform these simulations.¹⁰⁸ Together with fuel property predictive models, these strategies can further accelerate the development of performance-advantaged bioblendstocks for diesel engines.

6.5 Conclusions

Advancement of renewable biofuels requires high quality bioblendstocks accessible from low-cost feedstocks with efficient conversion pathways. Here, we demonstrated a “fuel property first” design approach to access low-sooting, drop-in hydrocarbon diesel bioblendstock from lignocellulose derived short-chain carboxylic acids. By leveraging predictive models, critical fuel properties were rapidly screened for an array of hydrocarbons accessible from C₂/C₄ acids, leading to a down-selected conversion pathway targeting a non-cyclic branched C₁₄ hydrocarbon molecule, 5-ethyl-4-propylnonane. Catalytic upgrading of butyric acid through an integrated process scheme showed high selectivity (>85%) for individual conversion steps and achieved >80% overall carbon yield to a hydrocarbon mixture product containing >60% of the target C₁₄ hydrocarbon. The majority of fuel property predictions were verified using a purified C₁₄ blendstock, while the crude conversion product exhibited similar bulk properties. Furthermore, blending of the C₁₄ bioblendstock into a base diesel at 20 vol.% validated its suitability for use as a drop-in diesel blendstock, reducing soot formation of the base diesel by 10%. Overall, this work demonstrates the potential of a “fuel property first” design approach to inform conversion pathway development and produce advantageous bioblendstock from biomass.

6.6 Materials and Methods

6.6.1 Predictive models

Two models were used to estimate melting point. The first was sourced from commercial software, ChemDraw Professional 15.1 (PerkinElmer) which exploits both Joback’s fragmentation method as well as Stein’s modification to Joback’s method.³³ The second prediction was obtained from the estimation program MPBPWIN™ in EPI Suite™ (US EPA, Syracuse Research Corp.).³⁴ This program estimates melting point by giving a weighted average

of the results of two methods, the Joback Method (a group contribution method) and the Gold and Ogle method (a correlation between melting point and boiling point). Boiling point predictions also utilized the ChemDraw and EPI Suite tools, with the addition of a third available predictive model developed by Satou et al.³⁶ Flashpoint was estimated via two predictive models, both requiring a reliable boiling point. One of the earliest was developed by Butler *et al.*,³⁷ which was built on correlation for petroleum boiling in the range of about 90 to 370 °C. The second correlation was later developed by Prugh and based on a larger database of hydrocarbons and fuel mixtures.³⁸ Numerous predictive models for the higher heating value for a variety of samples have been developed, primarily based around species mass contributions. The first model applied in this work is the Dulong equation, which was used to determine higher heating value estimates for coal and fossil fuels.⁴² This work also includes two predictive estimates which are from modifications to Dulong's formula. Lloyd and Davenport⁴³ included ethers and other oxygenates in their modification, and Boie⁴⁴ adapted the formula for a larger dataset. Lower heating values reported here are determined by the following equation, which is a function of the estimated mass% hydrogen (H) in a sample (ASTM D240, Section 10.5.1).¹⁰⁹

$$\text{LHV} = \text{HHV} - (0.2122 * \text{H}) \quad (6.1)$$

Cetane number predictions were produced using a back-propagating artificial neural network (ANN) with inputs including experimental CN values and quantitative structure-property relationships (QSPR) for individual molecules. The model uses an iterative regression analysis technique to reduce the number of input parameters; in the case of CN, from >1500 to 15. The ANN randomly assigns an individual molecule from the known data set to one of three conditions: learning, validation, and testing, with proportions of 65%, 25%, and 10% respectively. The trained model is subsequently applied to the new molecule of interest's QSPR

parameters in order to produce a predicted CN. The method has been shown to provide high accuracy and repeatability across a broad range of hydrocarbons when predicting CN.^{45, 46} Yield sooting index predictions were generated using a group contribution model that sums contributions from each carbon atom.⁴⁷

6.6.2 Catalytic upgrading

Commercial butyric acid, 4-heptanone, toluene and cyclohexane were purchased from standard chemical suppliers such as Sigma-Aldrich or Acros. Biologically derived butyric acid was obtained from lignocellulosic sugars fermentation as detailed in Appendix E.

Fresh catalysts and selected post-reaction catalysts were characterized by N₂ physisorption, ammonia TPD, pyridine DRIFTS, chemisorption, and TGA-IR. Details on catalyst synthesis and characterization methods are provided in Appendix E.

Packed-bed reactor experiments were performed in a stainless-steel tubular reactor system. The reactor tube was coated with a silica Dursan coating provided by SilcoTek Coating Co. Batch reactor experiments were performed in a Parr multi-batch reactor system (Parr Instrument Co.), and the reactors were also coated with the silica Dursan coating. Liquid products were analyzed by gas chromatography with a flame ionization detector and a mass spectrometer (GC-FID/MS). Carbon, hydrocarbon, nitrogen, sulfur, and metals analyses were performed by Huffman Hazen Laboratories. Selected samples were analyzed by high resolution mass spectrometry, nuclear magnetic resonance spectroscopy, and two-dimensional gas chromatography with time-of-flight mass spectrometry (GC×GC-TOFMS). Further details on catalytic testing systems, data analysis, and analytical methods were provided in Appendix E.

6.6.3 Fuel property testing

Cetane number was measured as indicated cetane number using 40 mL of sample in an AFIDA instrument (ASTM D8183). Boiling point was estimated using simulated distillation (D2887). Higher heating value was measured by combusting samples in a bomb calorimeter (D240), with hydrogen content used to calculate lower heating value being measured for each sample using a LECO TruSpec CHN determinator. Samples were combusted at 950 °C under a flow of excess oxygen and the gas produced was analyzed with infrared spectroscopy to quantify the amount of CO₂ and H₂O produced. Ethylenediaminetetraacetic acid (EDTA) was used as the calibration standard. Density was found using a Mettler-Toledo DM40 density meter (D4052). Viscosity was measured at 40 °C using D445 or a TA Instrument AR1500 equipped with a recessed rotor at a shear rate of 1-100 s⁻¹. Melting point and cloud point was measured using a Phase Technology Series 70X (a modified version of D5773). Flash point was measured using D7094. Two different types of sooting tendency measurements were performed. Measurement of YSI followed published procedures.¹¹⁰ Briefly, samples of the test substance, n-heptane, and toluene were doped into the fuel of a methane/air nonpremixed flame at a mole fraction of 1000 ppm. Soot concentrations in the resulting flames were quantified with line-of-sight spectral radiance (LSSR). The maximum LSSR in each flame was then converted to a YSI by a linear rescaling with the specified endpoints of n-heptane = 36.0 YSI units and toluene = 170.9 YSI units. To obtain normalized soot concentration (NSC), the same procedures were followed except that all of the dopants were added at a fixed volumetric flowrate of 100 μL h⁻¹. The results were not indexed to toluene and heptane; instead the soot concentration from the undoped flame was subtracted off and then the concentration attributable to the dopant was normalized to the value for the reference base diesel fuel.

6.7 References

1. World Energy Look; International Energy Agency: London, UK, 2017.
2. Tracking Clean Energy Progress; International Energy Agency: 2017.
3. The Future of Trucks Implications for Energy and the Environment; International Energy Agency: 2017.
4. Langholtz, M. H.; Stokes, B. J.; Eaton, L. M. 2016 Billion-Ton Report: Advancing Domestic Resources for a Thriving Bioeconomy, Volume 1: Economic Availability of Feedstocks; U.S. Department of Energy Oak Ridge National Laboratory: 2016.
5. Serrano-Ruiz, J. C.; Dumesic, J. A. Catalytic routes for the conversion of biomass into liquid hydrocarbon transportation fuels. *Energy & Environmental Science* **2011**, *4* (1), 83-99.
6. Shylesh, S.; Gokhale, A. A.; Ho, C. R.; Bell, A. T. Novel Strategies for the Production of Fuels, Lubricants, and Chemicals from Biomass. *Accounts of Chemical Research* **2017**, *50* (10), 2589-2597.
7. Shen, Y.; Jarboe, L.; Brown, R.; Wen, Z. A thermochemical–biochemical hybrid processing of lignocellulosic biomass for producing fuels and chemicals. *Biotechnology Advances* **2015**, *33* (8), 1799-1813.
8. Gani, R.; Jiménez-González, C.; Constable, D. J. C. Method for selection of solvents for promotion of organic reactions. *Computers & Chemical Engineering* **2005**, *29* (7), 1661-1676.
9. Ng, L. Y.; Chong, F. K.; Chemmangattuvalappil, N. G. Challenges and opportunities in computer-aided molecular design. *Computers & Chemical Engineering* **2015**, *81*, 115-129.
10. Macalino, S. J. Y.; Gosu, V.; Hong, S.; Choi, S. Role of computer-aided drug design in modern drug discovery. *Archives of Pharmacal Research* **2015**, *38* (9), 1686-1701.
11. Austin, N. D.; Sahinidis, N. V.; Trahan, D. W. Computer-aided molecular design: An introduction and review of tools, applications, and solution techniques. *Chemical Engineering Research and Design* **2016**, *116*, 2-26.
12. Dahmen, M.; Marquardt, W. Model-Based Design of Tailor-Made Biofuels. *Energy & Fuels* **2016**, *30* (2), 1109-1134.
13. Dahmen, M.; Marquardt, W. Model-Based Formulation of Biofuel Blends by Simultaneous Product and Pathway Design. *Energy & Fuels* **2017**, *31* (4), 4096-4121.
14. Kubic, W. L.; Jenkins, R. W.; Moore, C. M.; Semelsberger, T. A.; Sutton, A. D. Artificial Neural Network Based Group Contribution Method for Estimating Cetane and Octane Numbers of Hydrocarbons and Oxygenated Organic Compounds. *Industrial & Engineering Chemistry Research* **2017**, *56* (42), 12236-12245.

15. McEnally, C. S.; Pfefferle, L. D. Sooting Tendencies of Oxygenated Hydrocarbons in Laboratory-Scale Flames. *Environmental Science & Technology* **2011**, *45* (6), 2498-2503.
16. Straathof, A. J. J. Transformation of Biomass into Commodity Chemicals Using Enzymes or Cells. *Chemical Reviews* **2014**, *114* (3), 1871-1908.
17. Sjöblom, M.; Matsakas, L.; Christakopoulos, P.; Rova, U. Catalytic upgrading of butyric acid towards fine chemicals and biofuels. *FEMS Microbiology Letters* **2016**, *363* (8), fnw064.
18. Khan, M. A.; Ngo, H. H.; Guo, W. S.; Liu, Y.; Nghiem, L. D.; Hai, F. I.; Deng, L. J.; Wang, J.; Wu, Y. Optimization of process parameters for production of volatile fatty acid, biohydrogen and methane from anaerobic digestion. *Bioresource Technology* **2016**, *219*, 738-748.
19. Agler, M. T.; Wrenn, B. A.; Zinder, S. H.; Angenent, L. T. Waste to bioproduct conversion with undefined mixed cultures: the carboxylate platform. *Trends in Biotechnology* **2011**, *29* (2), 70-78.
20. Vassilev, I.; Hernandez, P. A.; Batlle-Vilanova, P.; Freguia, S.; Krömer, J. O.; Keller, J.; Ledezma, P.; Virdis, B. Microbial Electrosynthesis of Isobutyric, Butyric, Caproic Acids, and Corresponding Alcohols from Carbon Dioxide. *ACS Sustainable Chemistry & Engineering* **2018**, *6* (7), 8485-8493.
21. Sacia, E. R.; Balakrishnan, M.; Deaner, M. H.; Goulas, K. A.; Toste, F. D.; Bell, A. T. Highly Selective Condensation of Biomass-Derived Methyl Ketones as a Source of Aviation Fuel. *ChemSusChem* **2015**, *8* (10), 1726-1736.
22. Climent, M. J.; Corma, A.; Iborra, S. Conversion of biomass platform molecules into fuel additives and liquid hydrocarbon fuels. *Green Chemistry* **2014**, *16* (2), 516-547.
23. Alonso, D. M.; Bond, J. Q.; Dumesic, J. A. Catalytic conversion of biomass to biofuels. *Green Chemistry* **2010**, *12* (9), 1493-1513.
24. Shylesh, S.; Gokhale, A. A.; Sun, K.; Grippo, A.; Jadhav, D.; Yeh, A.; Ho, C. R.; Bell, A. T. Integrated catalytic sequences for catalytic upgrading of bio-derived carboxylic acids to fuels, lubricants and chemical feedstocks. *Sustainable Energy & Fuels* **2017**, *1* (8), 1805-1809.
25. Olcay, H.; Subrahmanyam, A. V.; Xing, R.; Lajoie, J.; Dumesic, J. A.; Huber, G. W. Production of renewable petroleum refinery diesel and jet fuel feedstocks from hemicellulose sugar streams. *Energy & Environmental Science* **2013**, *6* (1), 205-216.
26. Deneyer, A.; Peeters, E.; Renders, T.; Van den Bosch, S.; Van Oeckel, N.; Ennaert, T.; Szarvas, T.; Korányi, T. I.; Dusselier, M.; Sels, B. F. Direct upstream integration of biogasoline production into current light straight run naphtha petrorefinery processes. *Nature Energy* **2018**, *3*, 969-977.

27. Jang, Y.-S.; Im, J. A.; Choi, S. Y.; Lee, J. I.; Lee, S. Y. Metabolic engineering of *Clostridium acetobutylicum* for butyric acid production with high butyric acid selectivity. *Metabolic Engineering* **2014**, *23*, 165-174.
28. Nagashima, O.; Sato, S.; Takahashi, R.; Sodesawa, T. Ketonization of carboxylic acids over CeO₂-based composite oxides. *Journal of Molecular Catalysis A: Chemical* **2005**, *227* (1), 231-239.
29. Gaertner, C. A.; Serrano-Ruiz, J. C.; Braden, D. J.; Dumesic, J. A. Catalytic coupling of carboxylic acids by ketonization as a processing step in biomass conversion. *Journal of Catalysis* **2009**, *266* (1), 71-78.
30. Balakrishnan, M.; Sacia, E. R.; Sreekumar, S.; Gunbas, G.; Gokhale, A. A.; Scown, C. D.; Toste, F. D.; Bell, A. T. Novel pathways for fuels and lubricants from biomass optimized using life-cycle greenhouse gas assessment. *Proceedings of the National Academy of Sciences* **2015**, *112* (25), 7645-7649.
31. Jenkins, R. W.; Moore, C. M.; Semelsberger, T. A.; Chuck, C. J.; Gordon, J. C.; Sutton, A. D. The Effect of Functional Groups in Bio-Derived Fuel Candidates. *ChemSusChem* **2016**, *9* (9), 922-931.
32. Gaspar, D. J.; McCormick, R. L.; Polikarpov, E.; Fioroni, G.; George, A.; Albrecht, K. O. *Functional Group Analysis for Diesel-like Mixing-Controlled Compression Ignition Combustion Blendstocks*; Pacific Northwest National Lab.(PNNL), Richland, WA (United States): 2016.
33. Goncalves, A. G.; Orfao, J. J. M.; Pereira, M. F. R. Catalytic ozonation of sulphamethoxazole in the presence of carbon materials: Catalytic performance and reaction pathways. *J. Hazard. Mater.* **2012**, *239*, 167-174.
34. Estimation Programs Interface Suite™ for Microsoft® Windows, v 4.11; United States Environmental Protection Agency: Washington, DC, USA, 2018.
35. ASTM International, "Standard Specification for Diesel Fuel Oils" 2018.
36. Satou, M.; Yokoyama, S.; Sanada, Y. Structural analysis and estimation of boiling point of hydrocarbons in a coal-derived liquid by a group contribution method. *Fuel* **1992**, *71* (5), 565-574.
37. Butler, R. M.; Cooke, G. M.; Lukk, G. G.; Jameson, B. G. Prediction of Flash Points of Middle Distillates. *Industrial & Engineering Chemistry* **1956**, *48* (4), 808-812.
38. Prugh, R. W. Estimation of flash point temperature. *Journal of Chemical Education* **1973**, *50* (2), A85.
39. Hoekman, S. K.; Broch, A.; Robbins, C.; Cenicerros, E.; Natarajan, M. Review of biodiesel composition, properties, and specifications. *Renewable and Sustainable Energy Reviews* **2012**, *16* (1), 143-169.

40. Diesel Fuels Technical Review; Chevron Global Marketing: 2007.
41. Saldana, D. A.; Starck, L.; Mougin, P.; Rousseau, B.; Pidol, L.; Jeuland, N.; Creton, B. Flash Point and Cetane Number Predictions for Fuel Compounds Using Quantitative Structure Property Relationship (QSPR) Methods. *Energy & Fuels* **2011**, *25* (9), 3900-3908.
42. Mott, R.; Spooner, C. The calorific value of carbon in coal: the Dulong relationship. *Fuel* **1940**, *19* (226), 242.
43. Lloyd, W. G.; Davenport, D. A. Applying thermodynamics to fossil fuels: Heats of combustion from elemental compositions. *Journal of Chemical Education* **1980**, *57* (1), 56.
44. Boie, W. Fuel technology calculations. *Energietechnik* **1953**, *3*, 309-316.
45. Kessler, T.; Mack, J. H. ECNet: Large scale machine learning projects for fuel property prediction. *The Journal of Open Source Software* **2017**, *2*, 401.
46. Kessler, T.; Sacia, E. R.; Bell, A. T.; Mack, J. H. Artificial neural network based predictions of cetane number for furanic biofuel additives. *Fuel* **2017**, *206*, 171-179.
47. Das, D. D.; St. John, P. C.; McEnally, C. S.; Kim, S.; Pfefferle, L. D. Measuring and predicting sooting tendencies of oxygenates, alkanes, alkenes, cycloalkanes, and aromatics on a unified scale. *Combustion and Flame* **2018**, *190*, 349-364.
48. *DIN EN 590 Automotive fuels - Diesel - Requirements and test methods (includes Amendment: 2017)*; Deutsches Institut für Normung E.V. (DIN): 2017.
49. O'Connor, C. T.; Forrester, R. D.; Scurrill, M. S. Cetane number determination of synthetic diesel fuels. *Fuel* **1992**, *71* (11), 1323-1327.
50. M. Heck, S.; O. Pritchard, H.; F. Griffiths, J. Cetane number vs. structure in paraffin hydrocarbons. *Journal of the Chemical Society, Faraday Transactions* **1998**, *94* (12), 1725-1727.
51. Westbrook, C. K. Chemical kinetics of hydrocarbon ignition in practical combustion systems. *Proceedings of the Combustion Institute* **2000**, *28* (2), 1563-1577.
52. Dahmen, M.; Marquardt, W. A Novel Group Contribution Method for the Prediction of the Derived Cetane Number of Oxygenated Hydrocarbons. *Energy & Fuels* **2015**, *29* (9), 5781-5801.
53. Johansson, K. O.; Head-Gordon, M. P.; Schrader, P. E.; Wilson, K. R.; Michelsen, H. A. Resonance-stabilized hydrocarbon-radical chain reactions may explain soot inception and growth. *Science* **2018**, *361* (6406), 997-1000.
54. Pham, T. N.; Sooknoi, T.; Crossley, S. P.; Resasco, D. E. Ketonization of Carboxylic Acids: Mechanisms, Catalysts, and Implications for Biomass Conversion. *ACS Catal.* **2013**, *3* (11), 2456-2473.

55. Kunkes, E. L.; Gürbüz, E. I.; Dumesic, J. A. Vapour-phase C–C coupling reactions of biomass-derived oxygenates over Pd/CeZrOx catalysts. *Journal of Catalysis* **2009**, *266* (2), 236-249.
56. Shylesh, S.; Kim, D.; Gokhale, A. A.; Canlas, C. G.; Struppe, J. O.; Ho, C. R.; Jadhav, D.; Yeh, A.; Bell, A. T. Effects of Composition and Structure of Mg/Al Oxides on Their Activity and Selectivity for the Condensation of Methyl Ketones. *Industrial & Engineering Chemistry Research* **2016**, *55* (40), 10635-10644.
57. Foo, G. S.; Wei, D.; Sholl, D. S.; Sievers, C. Role of Lewis and Brønsted Acid Sites in the Dehydration of Glycerol over Niobia. *ACS Catalysis* **2014**, *4* (9), 3180-3192.
58. Ho, C. R.; Zheng, S.; Shylesh, S.; Bell, A. T. The mechanism and kinetics of methyl isobutyl ketone synthesis from acetone over ion-exchanged hydroxyapatite. *Journal of Catalysis* **2018**, *365*, 174-183.
59. Ashish, B.; Basudeb, S.; M., A.-O. M. Catalytic Upgrading of 5-Hydroxymethylfurfural to Drop-in Biofuels by Solid Base and Bifunctional Metal–Acid Catalysts. *ChemSusChem* **2015**, *8* (23), 4022-4029.
60. Li, H.; Riisager, A.; Saravanamurugan, S.; Pandey, A.; Sangwan, R. S.; Yang, S.; Luque, R. Carbon-Increasing Catalytic Strategies for Upgrading Biomass into Energy-Intensive Fuels and Chemicals. *ACS Catalysis* **2018**, *8* (1), 148-187.
61. Okuhara, T. Water-Tolerant Solid Acid Catalysts. *Chemical Reviews* **2002**, *102* (10), 3641-3666.
62. Nelson, R.; Peterson, D.; Karp, E.; Beckham, G.; Salvachúa, D. Mixed Carboxylic Acid Production by *Megasphaera elsdenii* from Glucose and Lignocellulosic Hydrolysate. *Fermentation* **2017**, *3* (1), 10.
63. Vassilev, S. V.; Baxter, D.; Andersen, L. K.; Vassileva, C. G.; Morgan, T. J. An overview of the organic and inorganic phase composition of biomass. *Fuel* **2012**, *94*, 1-33.
64. Vardon, D. R.; Rorrer, N. A.; Salvachua, D.; Settle, A. E.; Johnson, C. W.; Menart, M. J.; Cleveland, N. S.; Ciesielski, P. N.; Steirer, K. X.; Dorgan, J. R.; Beckham, G. T. cis,cis-Muconic acid: separation and catalysis to bio-adipic acid for nylon-6,6 polymerization. *Green Chemistry* **2016**, *18* (11), 3397-3413.
65. Karp, E. M.; Cywar, R. M.; Manker, L. P.; Saboe, P. O.; Nimlos, C. T.; Salvachúa, D.; Wang, X.; Black, B. A.; Reed, M. L.; Michener, W. E.; Rorrer, N. A.; Beckham, G. T. Post-Fermentation Recovery of Biobased Carboxylic Acids. *ACS Sustainable Chemistry & Engineering* **2018**, *6* (11), 15273-15283.
66. Hughes, L. D.; Palmer, D. S.; Nigsch, F.; Mitchell, J. B. O. Why Are Some Properties More Difficult To Predict than Others? A Study of QSPR Models of Solubility, Melting Point, and Log P. *Journal of Chemical Information and Modeling* **2008**, *48* (1), 220-232.

67. Murugesan, A.; Umarani, C.; Subramanian, R.; Nedunchezian, N. Bio-diesel as an alternative fuel for diesel engines—A review. *Renewable and Sustainable Energy Reviews* **2009**, *13* (3), 653-662.
68. Lapuerta, M.; García-Contreras, R.; Campos-Fernández, J.; Dorado, M. P. Stability, Lubricity, Viscosity, and Cold-Flow Properties of Alcohol–Diesel Blends. *Energy & Fuels* **2010**, *24* (8), 4497-4502.
69. Linger, J. G.; Vardon, D. R.; Guarnieri, M. T.; Karp, E. M.; Hunsinger, G. B.; Franden, M. A.; Johnson, C. W.; Chupka, G.; Strathmann, T. J.; Pienkos, P. T.; Beckham, G. T. Lignin valorization through integrated biological funneling and chemical catalysis. *Proceedings of the National Academy of Sciences* **2014**, *111* (33), 12013-12018.
70. Schwartz, T. J.; O'Neill, B. J.; Shanks, B. H.; Dumesic, J. A. Bridging the Chemical and Biological Catalysis Gap: Challenges and Outlooks for Producing Sustainable Chemicals. *ACS Catalysis* **2014**, *4* (6), 2060-2069.
71. Xing, R.; Subrahmanyam, A. V.; Olcay, H.; Qi, W.; van Walsum, G. P.; Pendse, H.; Huber, G. W. Production of jet and diesel fuel range alkanes from waste hemicellulose-derived aqueous solutions. *Green Chemistry* **2010**, *12* (11), 1933-1946.
72. Deneyer, A.; Renders, T.; Van Aelst, J.; Van den Bosch, S.; Gabriëls, D.; Sels, B. F. Alkane production from biomass: chemo-, bio- and integrated catalytic approaches. *Current Opinion in Chemical Biology* **2015**, *29*, 40-48.
73. Op de Beeck, B.; Dusselier, M.; Geboers, J.; Holsbeek, J.; Morré, E.; Oswald, S.; Giebel, L.; Sels, B. F. Direct catalytic conversion of cellulose to liquid straight-chain alkanes. *Energy & Environmental Science* **2015**, *8* (1), 230-240.
74. Whitmore, L. S.; Davis, R. W.; McCormick, R. L.; Gladden, J. M.; Simmons, B. A.; George, A.; Hudson, C. M. BioCompoundML: A General Biofuel Property Screening Tool for Biological Molecules Using Random Forest Classifiers. *Energy & Fuels* **2016**, *30* (10), 8410-8418.
75. McCormick, R.; Fioroni, G.; Fouts, L.; Christensen, E.; Yanowitz, J.; Polikarpov, E.; Albrecht, K.; Gaspar, D.; Gladden, J.; George, A. Selection Criteria and Screening of Potential Biomass-Derived Streams as Fuel Blendstocks for Advanced Spark-Ignition Engines. *SAE Int. J. Fuels Lubr.* **2017**, *10* (2), 442-460.
76. Fioroni, G.; Fouts, L.; Luecke, J.; Vardon, D. R.; Huq, N. A.; Christensen, E.; Huo, X.; Alleman, T.; McCormick, R. Screening of Potential Biomass-Derived Streams as Fuel Blendstocks for Mixing Controlled Compression Ignition Combustion. *Submitted*.
77. Das, D. D.; McEnally, C. S.; Kwan, T. A.; Zimmerman, J. B.; Cannella, W. J.; Mueller, C. J.; Pfefferle, L. D. Sooting tendencies of diesel fuels, jet fuels, and their surrogates in diffusion flames. *Fuel* **2017**, *197*, 445-458.

78. St. John, P. C.; Kairys, P.; Das, D. D.; McEnally, C. S.; Pfefferle, L. D.; Robichaud, D. J.; Nimlos, M. R.; Zigler, B. T.; McCormick, R. L.; Foust, T. D.; Bomble, Y. J.; Kim, S. A Quantitative Model for the Prediction of Sooting Tendency from Molecular Structure. *Energy & Fuels* **2017**, *31* (9), 9983-9990.
79. Yunus, N. A.; Gernaey, K. V.; Woodley, J. M.; Gani, R. A systematic methodology for design of tailor-made blended products. *Computers & Chemical Engineering* **2014**, *66*, 201-213.
80. Kalakul, S.; Zhang, L.; Fang, Z.; Choudhury, H. A.; Intikhab, S.; Elbashir, N.; Eden, M. R.; Gani, R. Computer aided chemical product design – ProCAPD and tailor-made blended products. *Computers & Chemical Engineering* **2018**.
81. Ghosh, P.; Jaffe, S. B. Detailed Composition-Based Model for Predicting the Cetane Number of Diesel Fuels. *Industrial & Engineering Chemistry Research* **2006**, *45* (1), 346-351.
82. Lapuerta, M.; Villajos, M.; Agudelo, J. R.; Boehman, A. L. Key properties and blending strategies of hydrotreated vegetable oil as biofuel for diesel engines. *Fuel Processing Technology* **2011**, *92* (12), 2406-2411.
83. Canoira, L.; García Galeán, J.; Alcántara, R.; Lapuerta, M.; García-Contreras, R. Fatty acid methyl esters (FAMEs) from castor oil: Production process assessment and synergistic effects in its properties. *Renewable Energy* **2010**, *35* (1), 208-217.
84. Botero, M. L.; Huang, Y.; Zhu, D. L.; Molina, A.; Law, C. K. Synergistic combustion of droplets of ethanol, diesel and biodiesel mixtures. *Fuel* **2012**, *94*, 342-347.
85. Phoon, L. Y.; Mustafa, A. A.; Hashim, H.; Mat, R. A Review of Flash Point Prediction Models for Flammable Liquid Mixtures. *Industrial & Engineering Chemistry Research* **2014**, *53* (32), 12553-12565.
86. Martinez, R.; Huff, M. C.; Barteau, M. A. Ketonization of acetic acid on titania-functionalized silica monoliths. *Journal of Catalysis* **2004**, *222* (2), 404-409.
87. Gliński, M.; Kijeński, J.; Jakubowski, A. Ketones from monocarboxylic acids: Catalytic ketonization over oxide systems. *Applied Catalysis A: General* **1995**, *128* (2), 209-217.
88. Dooley, K. M.; Bhat, A. K.; Plaisance, C. P.; Roy, A. D. Ketones from acid condensation using supported CeO₂ catalysts: Effect of additives. *Applied Catalysis A: General* **2007**, *320*, 122-133.
89. Pham, T. N.; Shi, D.; Resasco, D. E. Reaction kinetics and mechanism of ketonization of aliphatic carboxylic acids with different carbon chain lengths over Ru/TiO₂ catalyst. *Journal of Catalysis* **2014**, *314*, 149-158.
90. Singh, M.; Zhou, N.; Paul, D. K.; Klabunde, K. J. IR spectral evidence of aldol condensation: Acetaldehyde adsorption over TiO₂ surface. *Journal of Catalysis* **2008**, *260* (2), 371-379.

91. Shylesh, S.; Hanna, D.; Gomes, J.; Krishna, S.; Canlas, C. G.; Head-Gordon, M.; Bell, A. T. Tailoring the Cooperative Acid–Base Effects in Silica-Supported Amine Catalysts: Applications in the Continuous Gas-Phase Self-Condensation of n-Butanal. *ChemCatChem* **2014**, *6* (5), 1283-1290.
92. Zhao, L.; An, H.; Zhao, X.; Wang, Y. TiO₂-Catalyzed n-Valeraldehyde Self-Condensation Reaction Mechanism and Kinetics. *ACS Catalysis* **2017**, *7* (7), 4451-4461.
93. Wang, S.; Goulas, K.; Iglesia, E. Condensation and esterification reactions of alkanals, alkanones, and alkanols on TiO₂: Elementary steps, site requirements, and synergistic effects of bifunctional strategies. *Journal of Catalysis* **2016**, *340*, 302-320.
94. Rekoske, J. E.; Barteau, M. A. Kinetics, Selectivity, and Deactivation in the Aldol Condensation of Acetaldehyde on Anatase Titanium Dioxide. *Industrial & Engineering Chemistry Research* **2011**, *50* (1), 41-51.
95. Kikhtyanin, O.; Kelbichová, V.; Vitvarová, D.; Kubů, M.; Kubička, D. Aldol condensation of furfural and acetone on zeolites. *Catalysis Today* **2014**, *227*, 154-162.
96. Young, Z. D.; Hanspal, S.; Davis, R. J. Aldol Condensation of Acetaldehyde over Titania, Hydroxyapatite, and Magnesia. *ACS Catalysis* **2016**, *6* (5), 3193-3202.
97. Sun, D.; Moriya, S.; Yamada, Y.; Sato, S. Vapor-phase self-aldol condensation of butanal over Ag-modified TiO₂. *Applied Catalysis A: General* **2016**, *524*, 8-16.
98. Argyle, M.; Bartholomew, C. Heterogeneous Catalyst Deactivation and Regeneration: A Review. *Catalysts* **2015**, *5* (1), 145.
99. Lange, J.-P. Renewable Feedstocks: The Problem of Catalyst Deactivation and its Mitigation. *Angewandte Chemie International Edition* **2015**, *54* (45), 13186-13197.
100. Saboe, P. O.; Manker, L. P.; Michener, W. E.; Peterson, D. J.; Brandner, D. G.; Deutch, S. P.; Kumar, M.; Cywar, R. M.; Beckham, G. T.; Karp, E. M. In situ recovery of bio-based carboxylic acids. *Green Chemistry* **2018**, *20* (8), 1791-1804.
101. Happonen, M.; Heikkilä, J.; Murtonen, T.; Lehto, K.; Sarjovaara, T.; Larmi, M.; Keskinen, J.; Virtanen, A. Reductions in Particulate and NO_x Emissions by Diesel Engine Parameter Adjustments with HVO Fuel. *Environmental Science & Technology* **2012**, *46* (11), 6198-6204.
102. Prokopowicz, A.; Zaciera, M.; Sobczak, A.; Bielaczyc, P.; Woodburn, J. The Effects of Neat Biodiesel and Biodiesel and HVO Blends in Diesel Fuel on Exhaust Emissions from a Light Duty Vehicle with a Diesel Engine. *Environmental Science & Technology* **2015**, *49* (12), 7473-7482.
103. Ashraful, A. M.; Masjuki, H. H.; Kalam, M. A.; Rizwanul Fattah, I. M.; Imtenan, S.; Shahir, S. A.; Mobarak, H. M. Production and comparison of fuel properties, engine performance, and

emission characteristics of biodiesel from various non-edible vegetable oils: A review. *Energy Conversion and Management* **2014**, *80*, 202-228.

104. Barraza-Botet, C. L.; Luecke, J.; Zigler, B. T.; Wooldridge, M. S. The impact of physicochemical property interactions of iso-octane/ethanol blends on ignition timescales. *Fuel* **2018**, *224*, 401-411.

105. Goldsborough, S. S.; Santner, J.; Kang, D.; Fridlyand, A.; Rockstroh, T.; Jespersen, M. C. Heat release analysis for rapid compression machines: Challenges and opportunities. *Proceedings of the Combustion Institute* **2018**.

106. Kukkadapu, G.; Kang, D.; Wagnon, S. W.; Zhang, K.; Mehl, M.; Monge-Palacios, M.; Wang, H.; Goldsborough, S. S.; Westbrook, C. K.; Pitz, W. J. Kinetic modeling study of surrogate components for gasoline, jet and diesel fuels: C7-C11 methylated aromatics. *Proceedings of the Combustion Institute* **2018**.

107. Westbrook, C. K.; Mehl, M.; Pitz, W. J.; Kukkadapu, G.; Wagnon, S.; Zhang, K. Multi-fuel surrogate chemical kinetic mechanisms for real world applications. *Physical Chemistry Chemical Physics* **2018**, *20* (16), 10588-10606.

108. Daly, S.; Cenker, E.; Pickett, L.; Skeen, S. The Effects of Injector Temperature on Spray Characteristics in Heavy-Duty Diesel Sprays. *SAE International* **2018**.

109. *ASTM D240-17, Standard Test Method for Heat of Combustion of Liquid Hydrocarbon Fuels by Bomb Calorimeter*; ASTM International: West Conshohocken, PA, 2017.

110. McEnally, C. S.; Xuan, Y.; St. John, P. C.; Das, D. D.; Jain, A.; Kim, S.; Kwan, T. A.; Tan, L. K.; Zhu, J.; Pfefferle, L. D. Sooting tendencies of co-optima test gasolines and their surrogates. *Proceedings of the Combustion Institute* **2018**.

CHAPTER 7

SUMMARY, CONCLUSIONS, AND FUTURE WORK

7.7 Conclusions

This work identified alternatives to Pd-based catalysts for catalytic reduction of water pollutants and integrated catalysts with other processes to advance the application of catalytic reduction for drinking water treatment. The major findings are summarized as below.

Supported catalysts of four platinum group metals (Ru, Rh, Ir, and Pt) were shown to exhibit favorable reactivity with aqueous bromate, chlorate, nitrate and perchlorate at ambient conditions. Specifically, Rh and Ru showed significant advantages over Pd in terms of catalytic turnover frequency, pH dependence, oxyanion substrate scope, or cost. Cross comparison of multiple metals and tri-oxyanion substrates suggested that some previous interpretations of the pH influence on catalyst reactivity should be revisited. The chemical nature of each metal element is a key factor determining the catalyst activity and adaptability to different water treatment conditions.

It was then demonstrated that supported Ru catalysts, which are much lower in cost than Pd-based catalysts, have a high intrinsic activity in nitrate activation. The key features for supported Ru catalysts that need to be controlled to achieve high activity are that reduced Ru surface can be obtained by H₂ reduction at reaction temperature and that the surface is not blocked by residues from the synthesis process or other surface-active substrates. Ru reduced nitrate selectively to ammonia, while nitrite was reduced to a mixture of N₂ and ammonia, with selectivity shifting towards N₂ at increasing nitrite:hydrogen ratio. The reaction mechanism was proposed that sequential hydrogenation of nitrate to nitrite and NO is followed by parallel

pathways involving the adsorbed NO: (1) sequential hydrogenation to ammonia, and (2) N-N coupling with aqueous nitrite followed by hydrogenation to the detected N₂O intermediate and N₂ endproduct.

Supported Ru catalysts were further shown to rapidly reduce *N*-nitrosodimethylamine (NDMA), a highly toxic nitrogenous disinfection byproduct that poses significant challenges to potable water reuse systems. The high activity was demonstrated with both commercial and in-house prepared Ru/Al₂O₃ catalysts, with the commercial material yielding an initial metal weight-normalized pseudo-first-order rate constant (k_0) of $1103 \pm 133 \text{ L} \cdot \text{g}_{\text{Ru}}^{-1} \cdot \text{h}^{-1}$ and an initial turnover frequency (TOF₀) of $58.0 \pm 7.0 \text{ h}^{-1}$. NDMA was reduced to dimethylamine (DMA) and ammonia end-products, and a small amount of 1,1-dimethylhydrazine (UDMH) was detected as a transient intermediate. Experiment with a mixture of five *N*-nitrosamines spiked into tap water ($1 \mu\text{g L}^{-1}$ each) demonstrated that Ru catalysts are very effective in reducing a range of *N*-nitrosamine structures at environmentally relevant concentrations.

Based on these promising results with Ru catalysts, this work demonstrated a hybrid catalytic hydrogenation/membrane distillation process to enable nitrate-contaminated ion exchange brine reuse and capture nitrogen as potential fertilizer product. A commercial Ru/C catalyst was able to hydrogenate nitrate in typical waste brine conditions including conditions representative of expected considering salt buildup upon brine reuse without requiring solution pH control. In a real ion exchange waste brine, nitrate was hydrogenated to ammonia at high selectivity. The resulting ammonia product was efficiently recovered using membrane distillation. The ammonia mass transfer efficiency was favored by high solution pH and temperature and not affected by salt concentration.

Overall, this work revealed the importance and feasibility of applying metal catalysts alternative to Pd-based materials for catalytic water treatment. Particularly, supported Ru catalysts demonstrated cost competitiveness and high catalytic activities with a range of contaminants, encouraging further catalyst development and process integration to advance the development of practical water catalysis technologies.

In the last part of this dissertation, a “fuel property first” design approach was demonstrated to access low-sooting, drop-in hydrocarbon diesel bioblendstock from lignocellulose derived short-chain carboxylic acids. By leveraging predictive models, critical fuel properties were rapidly screened for an array of hydrocarbons accessible from C₂/C₄ acids, leading to a down-selected conversion pathway targeting a non-cyclic branched C₁₄ hydrocarbon molecule, 5-ethyl-4-propylnonane. Catalytic upgrading of butyric acid through an integrated process scheme showed high selectivity (>85%) for individual conversion steps and achieved >80% overall carbon yield to a hydrocarbon mixture product containing >60% of the target C₁₄ hydrocarbon. The majority of fuel property predictions were verified using a purified C₁₄ blendstock, while the crude conversion product exhibited similar bulk properties. Furthermore, blending of the C₁₄ bioblendstock into a base diesel at 20 vol% validated its suitability for use as a drop-in diesel blendstock, reducing soot formation of the base diesel by 10%. Overall, the potential of the “fuel property first” design approach to inform conversion pathway development and produce advantageous bioblendstock from biomass was demonstrated.

7.7 Future Work

Results in chapter 2 identified that catalytic activity of supported metal catalysts for hydrogenating individual substrate primarily depends on the chemical nature of the metal. Further work is needed to provide greater mechanistic insights into these relationships, which is

important to rational catalyst design and informs catalytic water treatment process design. A common approach to investigating activity trend is to plot the measured activity over chemical descriptors such as the adsorption energy of reactants (e.g., hydrogen) or reaction intermediates (e.g., NO during nitrate and nitrite reduction) on metal surface. This type of plot often leads to unambiguous identification of the optimal binding energy and the type of metal imparting such properties. Even though it does not require detailed reaction pathway study to perform such analysis, the most relevant chemical descriptors are likely those involved in the rate-limiting step. Identification of the rate-limiting step can be achieved by experimental approach (e.g., kinetic analysis, isotope exchange test), Density Functional Theory calculation, or a combination of both.

Chapter 3 provided a more in-depth investigation of nitrate and nitrite hydrogenation with supported Ru catalysts, including reaction kinetics, pathway, and the influence of catalyst pretreatment on activities. This work identified factors that have significant impact on catalyst activity and product selectivity, which suggest a target for future Ru catalyst design. For example, surface alloying may be used to improve catalyst activity at higher nitrate concentrations by reducing the binding strength of nitrite, or to open up alternative N–N coupling pathway by altering the surface species diffusion rates.

Both chapter 3 and chapter 4 showed that catalyst performance depends on the size and morphology of the metal nanoparticles for supported metal catalysts. The catalyst structure-activity relationship was not explored in detail in this work, but this is an important area to study in future work to inform catalyst development. To study the influence of catalyst structure or surface properties on catalyst activity, a series of supported metal catalysts can be synthesized with various metal loading or using different synthetic techniques, followed by extensive characterization of structural and chemical properties. By comparing catalytic activity among

these catalysts, the critical structural or chemical properties may be identified. Alternatively, synthetic control strategies can be leveraged to obtain catalysts with uniform nanoparticle size and shape, facilitating the elucidation of surface site distribution (e.g., different facets, terrace versus edge sites) to catalyst activity. The potential interaction between catalyst support and metal nanoparticle needs to be considered during experimental design as well.

The ability of Ru/C for efficient nitrate hydrogenation was demonstrated in a semi-batch reactor under both freshwater conditions (chapter 3) and ion exchange waste brine conditions (chapter 5). Moving towards practical application, efforts are required to develop and evaluate other reactor configurations. Particularly, packed-bed reactors have the advantage of easy liquid-catalyst separation and low catalyst attrition rate, resulting in their wide adoption in petroleum processing and chemical production. Supported Ru catalysts in pellet or extrude form need to be synthesized using scalable synthesis method and evaluated for catalyst activity under various packed-bed reactor operating conditions. Catalyst performance will likely depend on H₂ mass transfer rate, solution chemistry and temperature. When treating concentrated nitrate in ion exchange waste brine, H₂ mass transfer can become a major limitation. Increasing H₂ pressure warrants further study as it is expected to improve H₂ gas-liquid transfer rate and enhance surface kinetics for nitrate hydrogenation. Alternative H₂ source (e.g., formic acid) and delivery mechanism (e.g., electrochemical system) are worth exploring with Ru catalysts as well. Continuous treatment of realistic matrices needs to be demonstrated at more industrially-relevant timescale to assess catalyst stability and identify the potential deactivation mechanism. Subsequently, catalyst regeneration and source water pretreatment strategies need to be studied to extend catalyst lifetime. Finally, there are tremendous opportunities for further techno-economic analysis and life cycle assessment of Ru catalyst systems to identify performance and

lifetime benchmarks and evaluate their potential advantage over Pd catalysts and existing technologies.

APPENDIX A

SUPPLEMENTARY DATA FOR CHAPTER 2

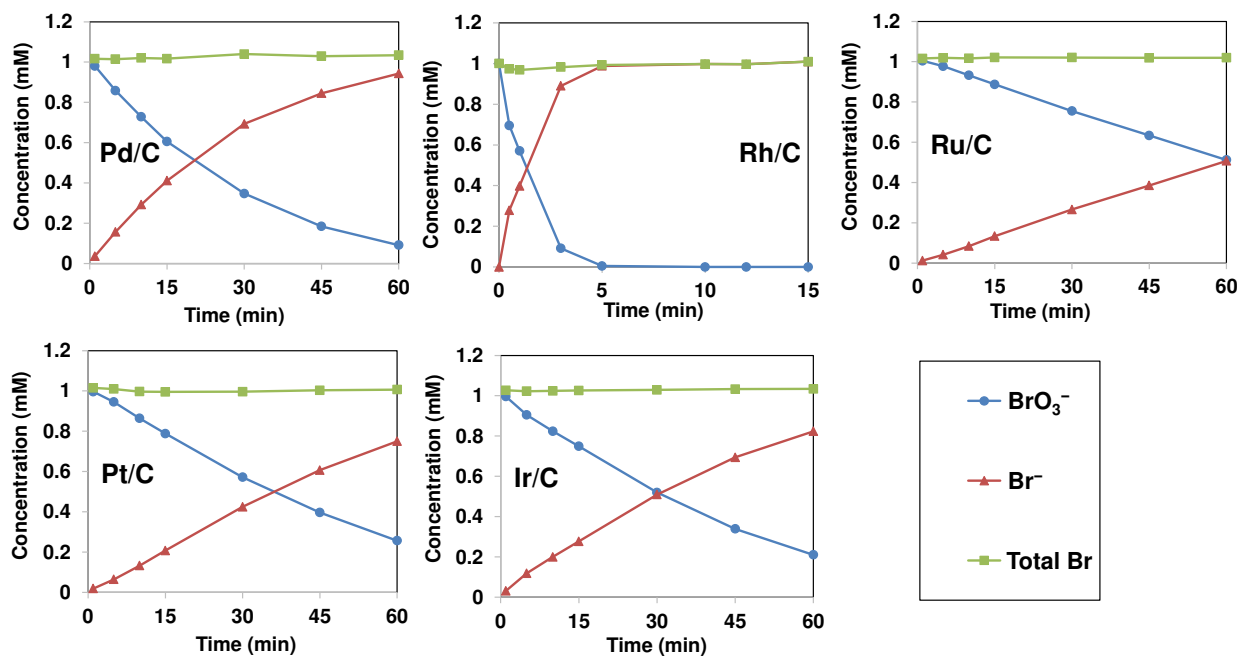


Figure A.1 Timecourse profiles with Br mass balance for reduction of 1 mM BrO₃⁻ and Br⁻ product formation using 0.1 g L⁻¹ M/C (nominal 5 wt% metal for Pd, Rh, Ru, and Pt; 1 wt% metal for Ir) and 1 atm H₂ (100 mL min⁻¹ sparging rate) at pH 7.2, 22 °C.

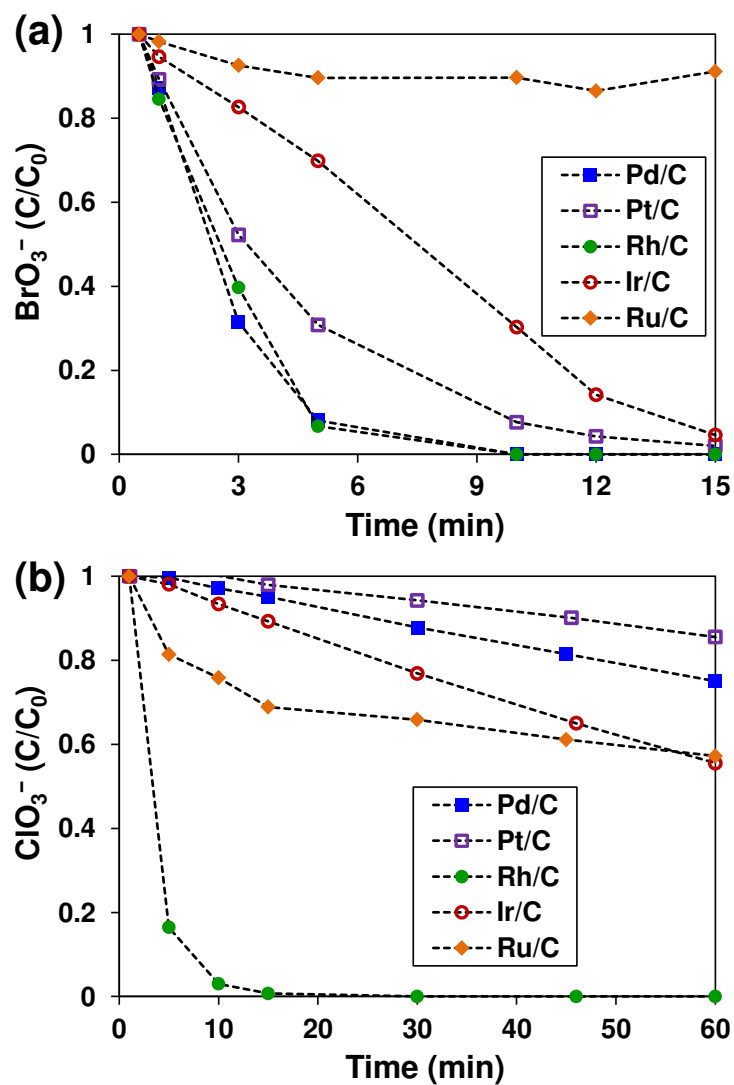


Figure A.2 Timecourse profiles observed at acidic pH conditions (pH 3.0) for reduction of (a) 1 mM BrO_3^- by 0.1 g L^{-1} M/C catalysts and (b) 1 mM ClO_3^- by 0.5 g L^{-1} M/C catalysts. All experiments were carried out in continuously mixed aqueous suspensions and sparged with 1 atm H_2 at 22 °C.

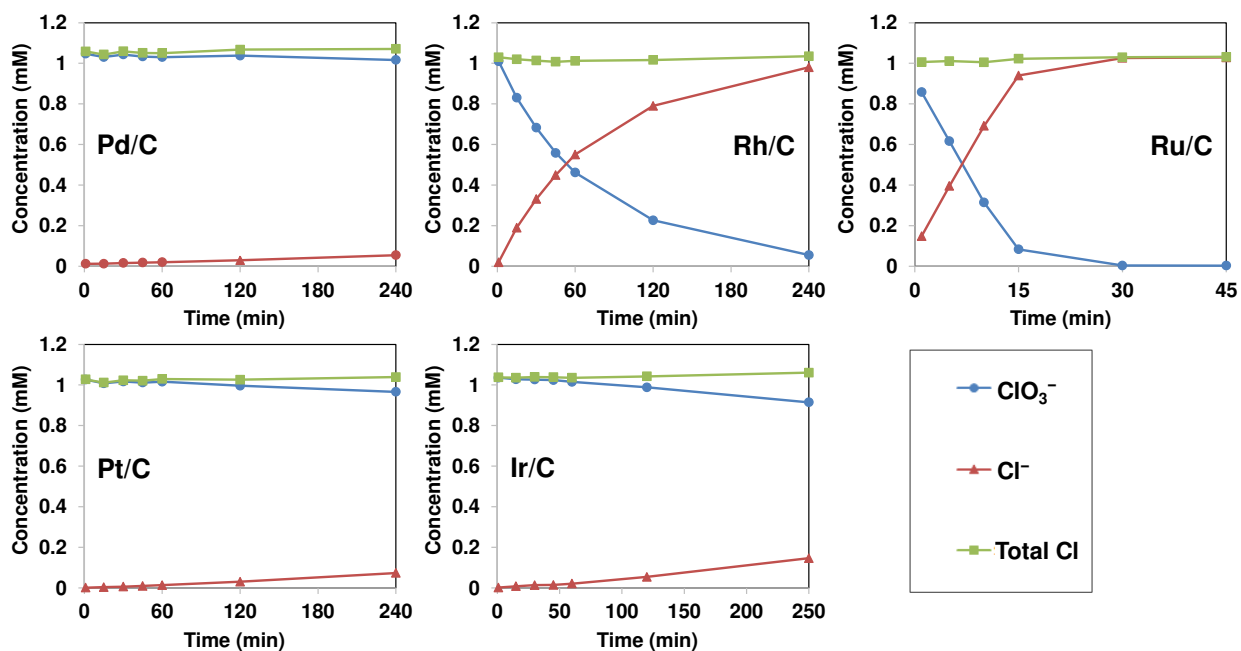


Figure A.3 Timecourse profiles with Cl mass balance for reduction of 1 mM ClO_3^- and Cl^- product formation using 0.5 g L^{-1} M/C (nominal 5 wt% metal for Pd, Rh, Ru, and Pt; 1 wt% metal for Ir) and 1 atm H_2 (20 mL min^{-1} sparging rate) at pH 7.2, 22 °C.

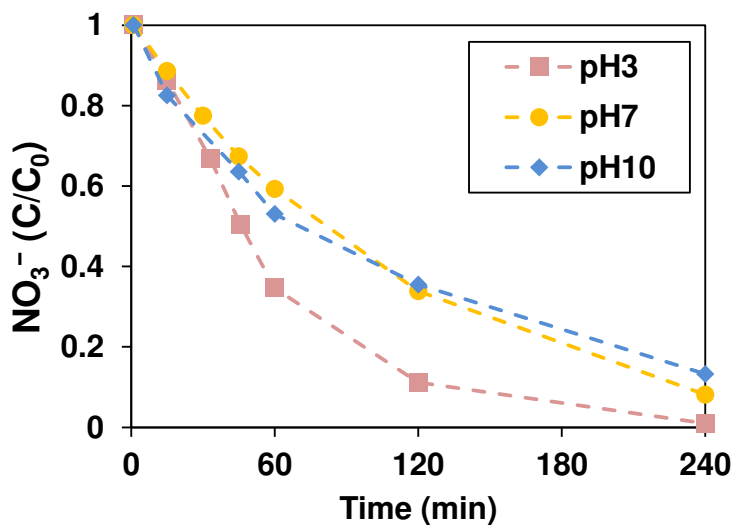


Figure A.4 Reduction profiles for 1 mM NO_3^- by 0.5 g L^{-1} Ru/C catalyst at different pH.

Table A.1 Market price range of the five hydrogenation metals.^a

	6-month price range (US \$ per gram)	5-year price range (US \$ per gram)
Pd	17~23	16~29
Rh	20~24	20~80
Ru	1.35	1.3~5.8
Pt	30~38	27~61
Ir	17~21	13~35

^aData collected from <http://www.infomine.com> as of September 2016.

Table A.2 Perchlorate reduction results by M/C catalysts (without Re).^a

	Reaction time	pH	C/C ₀
Pd/C	8 h	3.0	1.02
Rh/C	8 h	3.0	0.99
Ru/C	25 h	3.0	1.01
Ru/C	25 h	7.2	1.03
Pt/C	8 h	3.0	0.99
Ir/C	8 h	3.0	1.01

^aReaction conditions: ClO₄⁻ C₀ = 1 mM, 2.0 g L⁻¹ catalyst, 1 atm H₂, 22 °C.

APPENDIX B

SUPPLEMENTARY DATA FOR CHAPTER 3

B.1 Experimental Methods

B.1.1 Chemical reagents

Ru on carbon (Ru/C, catalog # 206180), Ru on alumina (Ru/Al₂O₃, catalog # 381152), Pd on carbon (Pd/C, catalog # 330116, dried in the air) and Pd on alumina (Pd/Al₂O₃ catalog # 205710), all in the form of a nominal 5 wt% noble metal, were purchased from Sigma-Aldrich. NaNO₃ (≥99.0%), Na¹⁵NO₃ (98 atom % ¹⁵N), ¹⁵N₂(g) (98 atom % ¹⁵N), Cu(NO₃)₂·3H₂O (puriss. p.a., 99-104%), In(NO₃)₃·3H₂O (99.999%) and MES hydrate pH buffer (≥99.5%) were also obtained from Sigma-Aldrich. Reagent-grade HCl and NaOH were purchased from Fisher Scientific. Na¹⁵NO₂ (≥98%) was obtained from Cambridge Isotope Laboratories. Cylinders of ultrahigh purity H₂(g) (99.999%) and N₂(g) (99.999%) were supplied by Matheson Tri-Gas. Deionized water (≥18 MΩ cm⁻¹; Barnstead Nanopure system) was used for all experiments.

B.1.2 Catalyst characterization

Metal contents were determined by inductively coupled plasma-optical emission spectrometry (ICP-OES) (PerkinElmer Optima 2000DV) after digestion in HNO₃-H₂O₂ (for Pd catalysts) or KOH-KNO₃ (for Ru catalysts). Specific surface area, total pore volume, and average pore diameter of the support materials were determined by N₂ physisorption after degassing at 350 °C for 2 h (Micromeritics ASAP 2020 analyzer); the BET method was used to calculate specific surface area.

Metal dispersion, defined as the percentage of Ru or Pd atoms present on the clean surface of the immobilized metal nanoparticles, was estimated by CO chemisorption using a Micromeritics AutoChem II analyzer equipped with a thermal conductivity detector (TCD). Clean metallic surface was obtained by reducing the as-received catalysts at 350 °C in flowing H₂ (10 mL min⁻¹) for 2 h followed by cooling the material to 25 °C in flowing He. The CO chemisorption was conducted in a pulse manner. The temperature of the sample was maintained at 25 °C. A small dose of CO was repeatedly supplied to the catalyst. CO chemically reacts with metal active sites until all active sites have reacted. The quantity of CO molecules chemisorbed is the difference between the total amount of CO gas supplied and the sum amount that did not react with the catalyst as measured by the detector. Metal dispersion was calculated following the equation below.

$$\text{Metal dispersion (\%)} = \frac{\text{CO uptake}}{\text{CO:Metal ratio}} \times \frac{M}{W_{\text{metal}}} \times 10^{-6} \left(\frac{\text{mol}}{\mu\text{mol}} \right) \times 100 \quad (\text{B.1})$$

where CO uptake is the quantity of CO molecules chemisorbed on the catalyst ($\mu\text{mol g}_{\text{cat}}^{-1}$), M is the active metal's atomic weight (g mol^{-1}), and W_{metal} is the metal wt fraction of the catalyst. A CO:Metal (Ru or Pd) stoichiometric ratio of 1:1 was assumed.^{1,2}

Active surface, defined as the percentage of Ru or Pd atoms accessible to reactants under simulated *in situ* conditions, was measured by using a CO chemisorption protocol adapted to simulate the *in situ* reduction of catalyst surfaces that occur in the semi-batch reactor where oxyanion reaction kinetics were determined. Prior to CO pulse delivery, catalysts were reduced at 25 °C in flowing H₂ (10 mL min⁻¹) for 30 min, followed by purging with He to remove weakly physisorbed H₂. Active surface was calculated using the same equation as metal dispersion except that the value of CO uptake was obtained from a different protocol.

Morphology of the supported metal nanoparticles was characterized by high angle annular dark field (HAADF) imaging with scanning transmission electron microscopy (FEI Titan S/TEM operated at 200 kV) or bright field imaging with transmission electron microscopy (TEM; Philips/FEI CM200 microscope operated at 200 kV). Samples were dispersed in methanol and mounted onto holey carbon Cu grids prior to analysis. To obtain the particle size distribution, at least 150 particles were counted for each image. Long-range structural order was determined by powder X-ray powder diffraction (XRD; Siemens, Kristalloflex 810, Cu K α radiation). The X-ray source was set 30 kV and 25 mA, with a sampling step of 0.02° and dwell time of 1 s. Spectra were compared to reference card files from the International Center for Diffraction Data (ICDD) database. Ru reducibility was determined by H₂ temperature-programmed reduction (TPR) using the same instrument used for CO chemisorption analysis. Samples were first treated with flowing Ar at 20 °C for 60 min to remove any air trapped in the catalysts prior to being heated to 800 °C at 10 °C min⁻¹ in a gas stream of 10% H₂/Ar.

B.1.3 Calculation of kinetic parameters

Catalyst activity was assessed by measuring initial mass-normalized pseudo-first-order rate constants (k_0 , L g_{Ru/Pd}⁻¹ min⁻¹) and turnover frequencies (TOF₀, min⁻¹), defined as the number of nitrate or nitrite ions reduced per active catalyst surface site per minute. Initial observed pseudo-first-order rate constants ($k_{\text{obs},0}$, min⁻¹) were determined by fitting the natural log of NO₃⁻ or NO₂⁻ concentration versus time data for the first reaction half-life, and the corresponding mass-normalized rate constants were determined by:

$$k_0 = \frac{k_{\text{obs},0}}{C_{\text{catalyst}} W_{\text{metal}}} \quad (\text{B.2})$$

where C_{catalyst} is the catalyst mass loading in the aqueous suspension (g L^{-1}). The corresponding TOF_0 value was then calculated by dividing the product of the $k_{\text{obs},0}$ and the initial oxyanion concentration (C_0 , mol L^{-1}) by the concentration of active surface Ru or Pd atoms ($C_{\text{metal surface}}$, mol L^{-1})³:

$$\text{TOF}_0 = \frac{k_{\text{obs},0} C_0}{C_{\text{metal surface}}} = \frac{k_{\text{obs},0} C_0 M}{\text{Active surface} \times C_{\text{catalyst}} W_{\text{metal}}} \quad (\text{B.3})$$

where $C_{\text{metal surface}}$ is estimated from active surface coupled with information on C_{catalyst} , W_{metal} and M .

B.1.4 Analytical methods

Aqueous nitrate and nitrite concentrations were analyzed by ion chromatography with conductivity detection (Dionex ICS-2100 system; Dionex IonPac AS19 column; 20 mM KOH as eluent; 1 mL min^{-1} eluent flow rate). Total ammonia ($\text{NH}_3/\text{NH}_4^+$) was analyzed by colorimetric analysis (Hach salicylate method). Headspace samples in closed batch reactor experiments were analyzed for ^{15}N -labeled products by gas chromatography with mass spectrometry (GC-MS; Agilent Technologies; 6850 Network GC System; 5975C VL MSD with Triple-Axis Detector; Column, Varian Plot CP-Molsieve 5Å, 25 m \times 0.25 mm; oven temperature 165 °C; He carrier gas, 1.0 mL min^{-1}). $^{15}\text{N}_2$ calibration standards were prepared by adding known masses of $^{15}\text{N}_2$ to 160 mL serum bottles containing 75 mL DI water and 85 mL headspace filled with H_2 (the same water and headspace volumes as the catalyst-containing closed reactors). Six standards, ranging from 2.05 μmol to 40.9 μmol $^{15}\text{N}_2\text{-N}$, were prepared. After equilibrating the labeled standard in the reactor, 0.1 mL of headspace was collected by gas tight syringe and injected onto the GC-MS. As the total amount of $^{15}\text{N}_2$ in the reactor (including headspace and aqueous phase) is linearly proportional to $^{15}\text{N}_2$ concentration in the headspace, the calibration curve for total $^{15}\text{N}_2$

was developed by plotting the peak area of the selected species ($m/z = 30$ for $^{15}\text{N}_2$) against the total moles of N as $^{15}\text{N}_2$ added to the reference standard reactor (Figure B.1 in Appendix B).

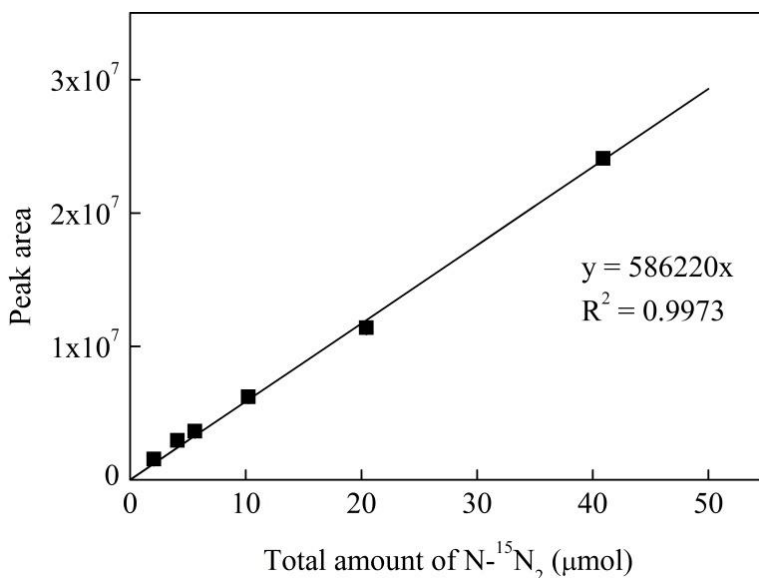


Figure B.1 Example calibration curve of total N- $^{15}\text{N}_2$ in the reactor.

In the absence of a $^{15}\text{N}_2\text{O}$ standard, a relative response factor (RRF) between N_2 and N_2O determined in a previous study that used the same instrument and analytical method⁴ was used to estimate $^{15}\text{N}_2\text{O}$ quantities in this study assuming that the RRF between N_2 and N_2O is the same as the RRF between $^{15}\text{N}_2$ and $^{15}\text{N}_2\text{O}$:

$$\text{RRF} = \text{RF}_{\text{N}_2\text{O}} / \text{RF}_{\text{N}_2} = \text{RF}_{^{15}\text{N}_2\text{O}} / \text{RF}_{^{15}\text{N}_2} \quad (\text{B.4})$$

where RF refers to a response factor, which is the ratio between the concentration of a compound and the response of the mass spec detector to the compound. The RFs for the gas species were calculated by dividing the peak area integrated from the chromatogram of selected species by the concentration of the species in the headspace gas sample:

$$\text{RF}_{\text{N}_2} = \frac{\text{Peak area}}{C_{\text{N}_2, \text{g}}} \quad (\text{B.5})$$

$$\text{RF}_{\text{N}_2\text{O}} = \frac{\text{Peak area}}{C_{\text{N}_2\text{O}, \text{g}}} \quad (\text{B.6})$$

The calibration curve for $^{15}\text{N}_2\text{O}$, which is the relationship between the integrated peak area of $^{15}\text{N}_2\text{O}$ and the total amount of $^{15}\text{N}_2\text{O}$ in the reactor, can be obtained from the following equation:

$$\begin{aligned} \text{Total } ^{15}\text{N}_2\text{O} &= (K_{\text{H},\text{N}_2\text{O}}RTV_{\text{a}} + V_{\text{g}}) \times C_{^{15}\text{N}_2\text{O}, \text{g}} \\ &= (K_{\text{H},\text{N}_2\text{O}}RTV_{\text{a}} + V_{\text{g}}) \times \frac{\text{Peak area}_{^{15}\text{N}_2\text{O}}}{\text{RRF} \times \text{RF}_{^{15}\text{N}_2}} \\ &= \frac{(K_{\text{H},\text{N}_2\text{O}}RTV_{\text{a}} + V_{\text{g}}) \times \text{Peak area}_{^{15}\text{N}_2\text{O}} \times \text{Total } ^{15}\text{N}_2}{\text{RRF} \times (K_{\text{H},\text{N}_2}RTV_{\text{a}} + V_{\text{g}}) \times \text{Peak area}_{^{15}\text{N}_2}} \end{aligned} \quad (\text{B.7})$$

The Henry's constant values for N_2O and N_2 , $K_{\text{H},\text{N}_2\text{O}}$ and K_{H,N_2} , are $2.4 \times 10^{-2} \text{ M atm}^{-1}$ and $6.5 \times 10^{-4} \text{ M atm}^{-1}$, respectively,⁵ V_{a} is the volume of the aqueous phase (75 mL), V_{g} is the volume of the headspace (85 mL), R is the gas constant ($0.082 \text{ L atm K}^{-1} \text{ mol}^{-1}$), T is absolute temperature (294.15 K), RRF is calculated to be 3.16 based on the slopes of the calibration curves of N_2 and N_2O ,⁴ and the ratio between the peak area of $^{15}\text{N}_2$ and total amount of $^{15}\text{N}_2$ can be obtained from Figure B.1 in Appendix B.

B.2 Experimental Results

B.2.1 Evaluation of mass transfer limitation

Data presented in Figure B.2 in Appendix B support the conclusion that reaction is not limited by external mass transfer processes at the conditions used in experiments. The Weisz-Prater parameter (C_{WP})⁶ provides a measure of the characteristic time scale of an observed reaction in comparison to the estimated characteristic time for internal diffusion of a reactant within the porous catalyst support. Values of $C_{\text{WP}} \ll 1$ indicate that the observed reaction is much slower than the rate of internal mass transfer, so the latter can be assumed to not be

limiting, whereas values of C_{WP} approaching unity or > 1 indicate that mass transfer may be limiting the observed reaction rate. For this study, C_{WP} is defined as:

$$C_{WP} = \frac{R^2 k_{obs,0} \tau}{D \theta} \quad (B.8)$$

where R is the radius of the catalyst support particle, τ is the tortuosity factor of the catalyst (typically varies from 2 to 10),⁷ D is the diffusion coefficient of nitrate in bulk solution ($1.7 \times 10^{-9} \text{ m}^2 \text{ s}^{-1}$),⁸ and θ is the porosity of the catalyst particle (typically varies from 0.2 to 0.7).⁹ The projected area of the particles was determined by optical microscope, and the radius R was estimated by treating the particles as spheres. A conservative estimate of the maximum value of C_{WP} was obtained by choosing the smallest θ (0.2), largest τ (10), and maximum R (66 μm). The resulting C_{WP} estimate of 0.18 is $\ll 1$ when nitrate is reacted with the highest Ru/C loading tested (0.5 g L^{-1}), indicating that internal mass transfer is not limiting.^{6,10} It is inferred that mass transfer limitation is not significant for Al_2O_3 supported catalysts for the reason that Al_2O_3 supports have much larger pore size than C supports and smaller $k_{obs,0}$ values (Table B.1).

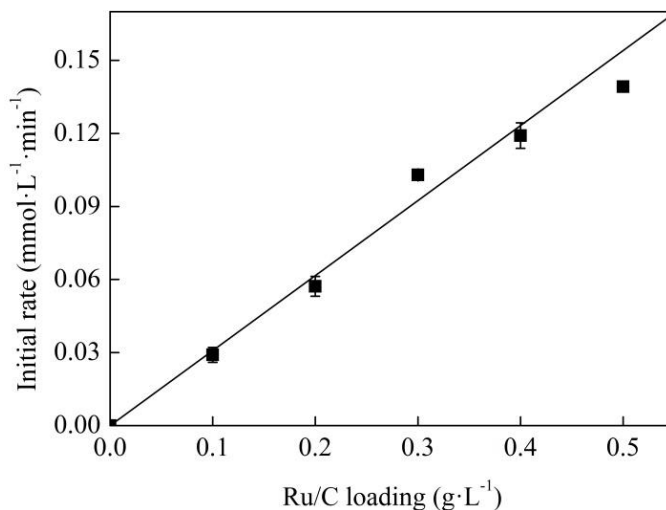


Figure B.2 Influence of 5 wt% Ru/C catalyst loading in the aqueous suspension on the initial rate of nitrate reduction (1 atm H_2 continuous sparging, pH 5.0 maintained by automatic pH stat, 25 ± 0.5 °C, $[\text{NO}_3^-]_0 = 1.6 \text{ mM}$). Error bars represent standard deviations of triplicate reactions.

B.2.2 Experimental results

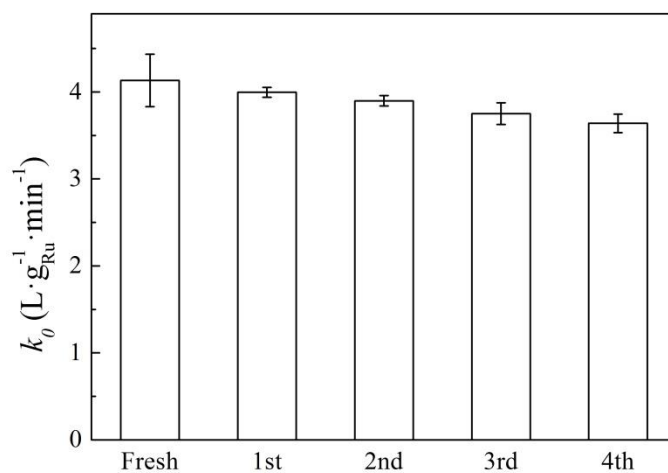


Figure B.3 Re-use of Ru/C in semi-batch system. Error bar for fresh catalyst represents standard deviations of triplicate reactions. For reuse experiments, error bars represent the min/max values measured in duplicate reactions.

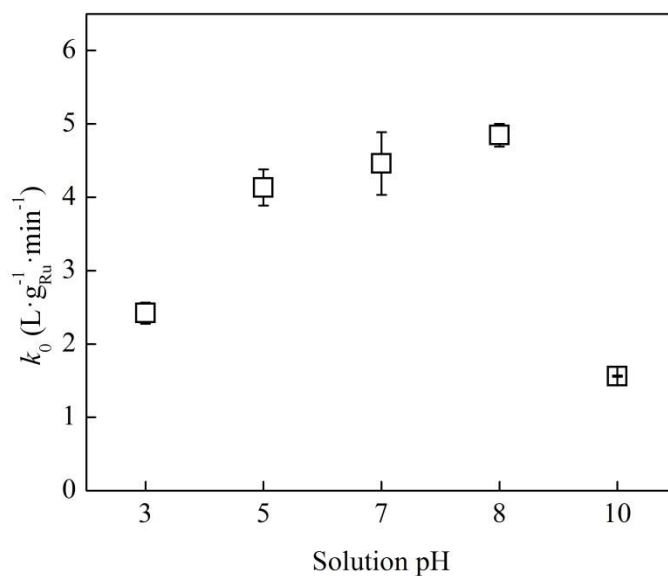


Figure B.4 Influence of pH on the Ru-mass-normalized pseudo-first-order rate constants for nitrate reduction on Ru/C (1 atm H_2 continuous sparging, 25 ± 0.5 °C, 0.2 g L^{-1} Ru/C, $[\text{NO}_3^-]_0 = 1.6 \text{ mM}$). Error bars represent standard deviations of triplicate reactions.

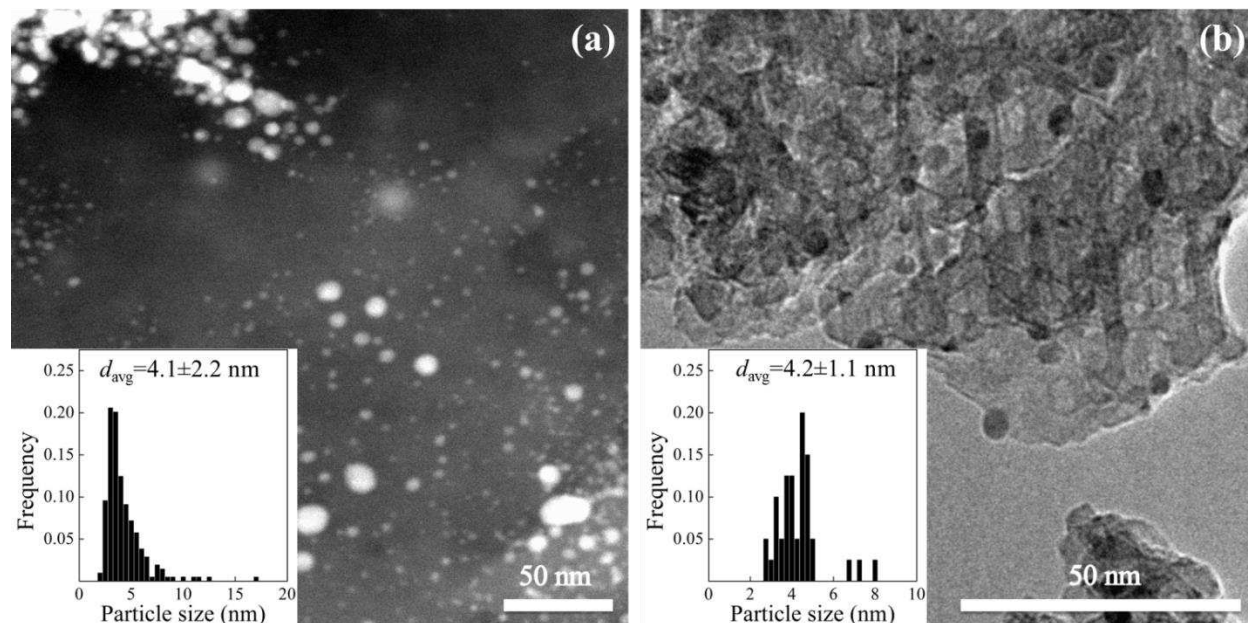


Figure B.5 (a) HAADF-STEM image of *ex situ* H₂ pretreated Pd/C and (b) TEM image of *ex situ* H₂ pretreated Pd/Al₂O₃. The insets show Pd particle size distributions.

Table B.1 Nitrate reduction activity of Pd-Cu and Ru catalysts in batch reactor and using H₂ as a reductant.

Catalyst	T (°C)	[NO ₃ ⁻] ₀ (mM)	Initial rate (mmol g _{Pd/Ru} ⁻¹ min ⁻¹) ^a	Ref.
4.7 wt% Pd-1.4 wt% Cu/γ-Al ₂ O ₃	20	1.6	5.2	11
5 wt% Pd-1.25 wt% Cu/C	25	1.5	9.9	12
5 wt % Pd-1.5 wt % Cu/γ-Al ₂ O ₃	21	2.1	10.8	13
5 wt% Pd-1 wt% Cu/C	25	1.6	0.6	14
2.8 wt % Pd-1.6 wt % Cu/α-Fe ₂ O ₃	25	2.1	2.0	15
5 wt% Pd-1 wt% Cu/C	25	1.6	6.7	This study
5 wt% Ru/C	25	1.6	6.7	This study
5 wt% Ru/Al ₂ O ₃	25	1.6	1.5	This study

^aIn the case that rate constant instead of reaction rate was reported, the initial reaction rate was calculated by multiplying the first-order rate constant by the initial nitrate concentration.

Table B.2 Surface and bulk properties of Ru catalysts from chemisorption analyses.

Catalyst	Active surface (%)	H ₂ consumption (μmol _{H2} μmol _{Ru} ⁻¹) ^a
Ru/C	As-received	11
	N ₂ pretreated	33
	H ₂ pretreated	32
Ru/Al ₂ O ₃	As-received	0
	N ₂ pretreated	0
	H ₂ pretreated	9

^aCalculated from the major peak below 400 °C of the TPR profile.

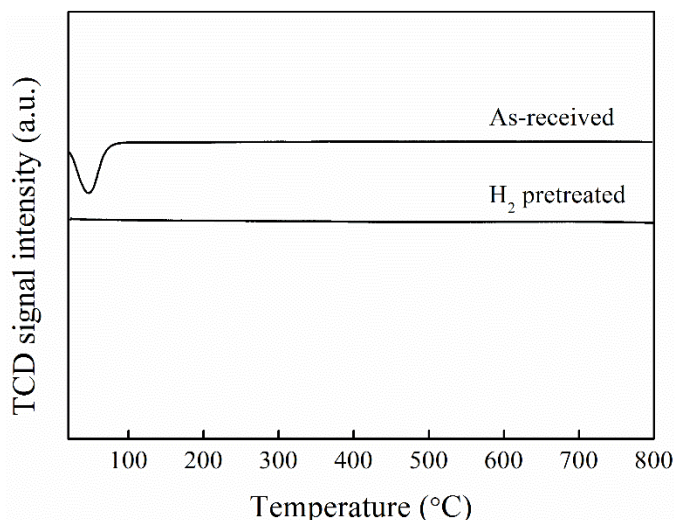


Figure B.6 Temperature-programmed desorption profile of Ru/C.

Table B.3 TOF₀ of nitrate reduction and nitrite reduction measured in mixture of nitrate and nitrite added to Ru/C reactors with varying initial concentration ratio.

[NO ₃ ⁻] ₀ (mM)	[NO ₂ ⁻] ₀ (mM)	TOF ₀ -NO ₃ ⁻ (min ⁻¹)	TOF ₀ -NO ₂ ⁻ (min ⁻¹)
1.6	1.6	0.026 ± 0.003	0.26 ± 0.04
1.6	0.26	0.36 ± 0.03	0.95 ± 0.05
0.26	0.26	0.21 ± 0.01	1.3 ± 0.2
0.26	0	1.1 ± 0.1	
1.6	0	2.1 ± 0.2	
0	0.26		3.4 ± 0.2
0	1.6		0.73 ± 0.06

B.2.2 DFT calculation notes and results

DFT calculations were carried out to describe the thermodynamic favorability of the reactions taking place in the experimental systems. A Ru₁₈ cluster was kept rigid during the optimization of various small molecular adsorbed species. As a result, some small imaginary frequencies were observed, which were ignored. The Ru₁₈ structure was optimized to a true minimum (no imaginary frequencies). To limit the effect of imaginary frequencies on the results, only the bottom of the well (HF energies) were utilized to calculate adsorption energies and compute the thermodynamic favorability of proposed reactions pathways. Additionally, surface

conformations showing imaginary frequencies larger than 150 cm^{-1} or showing multiple (4 or greater) imaginary frequencies were immediately disqualified from the mechanism. Furthermore, multiple conformations were optimized for a variety of individual molecular species, including edge bond moieties. To maintain consistency, edge bound species were omitted from the analysis.

Given the computational methods and assumptions within this study, we want to emphasize the qualitative or semi-quantitative nature of the results. Additionally, all Ru_{18} clusters were optimized as restricted ground state singlets, with all electrons paired. For additional consistency, reactions involving reductions by a hydrogen atom assumed to proceed via surface absorbed hydrogen atoms. The same strategy was used when H_2O is produced in a reaction. However, acidic protons were modeled by a bulk solvated H_3O^+ molecule unbound to the surface. No significant difference was observed when a free implicitly solvated H-atom was used to calculate reaction energetics. Similar strategy was used when H_2O was evolved in certain reactions; H_2O was treated as an unbound, implicitly solvated water molecule. Finally, hydrogen ions (H^+) were approximated by the difference between H_2O and H_3O^+ complexes.

Spin contamination was present in the optimization of many complexes containing unpaired electrons. As a result, ROPBE0 HF energies were computed with single point calculations using geometries obtained at the spin contaminated UPBE0 level.

Table B.4 Adsorption energies (eV) of nitrogen species (major reactants, hypothesized intermediates, and products) on Ru_{18} clusters.^a

Species	ΔE_{ads} (eV)
$\text{Ru}_{18}\text{-NO}_3^-$	-1.2
$\text{Ru}_{18}\text{-NO}_2^-$	-1.3
$\text{Ru}_{18}\text{-NO}_2$	-3.3
$\text{Ru}_{18}\text{-NO}$	-2.0
$\text{Ru}_{18}\text{-N}_2\text{O}$	-1.7
$\text{Ru}_{18}\text{-NH}_3$	-0.97
$\text{Ru}_{18}\text{-N}_2$	-1.4
$\text{Ru}_{18}\text{-H}_2\text{O}$	-1.1
$\text{Ru}_{18}\text{-H}$	-1.9

Table B.5 Energetics of the most thermodynamically favorable reaction pathways for aqueous nitrate reduction on Ru₁₈ clusters.

Reaction steps	ΔE (eV)
Sequential reduction of NO ₃ ⁻ to NO	
NO ₃ ⁻ _{ads} + 2H _{ads} → NO ₂ ⁻ _{ads} + H ₂ O _{ads}	-3.5
NO ₂ ⁻ _{ads} + H _{ads} + H ⁺ → NO _{ads} + H ₂ O _{ads}	-5.6
Sequential reduction of NO to NH ₃	
NO _{ads} + H _{ads} → HNO _{ads}	-1.1
HNO _{ads} + H _{ads} → H ₂ NO _{ads}	-0.8
H ₂ NO _{ads} + H _{ads} → H ₂ NOH _{ads}	-0.9
H ₂ NOH _{ads} + H _{ads} → NH ₂ _{ads} + H ₂ O _{ads}	-2.8
NH ₂ _{ads} + H _{ads} → NH ₃ _{ads}	-1.4
N-N coupling and N ₂ production	
NO _{ads} + NO ₂ ⁻ _{aq} → N ₂ O ₃ ⁻ _{ads} + H ₂ O _{ads}	-1.3
N ₂ O ₃ ⁻ _{ads} + 2H _{ads} → N ₂ O ₂ ⁻ _{ads} + H ₂ O _{ads}	-3.1
N ₂ O ₂ ⁻ _{ads} + H _{ads} H ⁺ → N ₂ O _{ads} + H ₂ O _{ads}	-6.3
N ₂ O _{ads} + 2H _{ads} → N ₂ _{ads} + H ₂ O _{ads}	-4.9

B.2.3 References

1. Yin, S.-F.; Zhang, Q.-H.; Xu, B.-Q.; Zhu, W.-X.; Ng, C.-F.; Au, C.-T. Investigation on the catalysis of CO_x-free hydrogen generation from ammonia. *J. Catal.* **2004**, *224* (2), 384-396.
2. García-García, F. R.; Guerrero-Ruiz, A.; Rodríguez-Ramos, I. Role of B5-Type Sites in Ru Catalysts used for the NH₃ Decomposition Reaction. *Topics in Catalysis* **2009**, *52* (6), 758-764.
3. Shuai, D.; McCalman, D. C.; Choe, J. K.; Shapley, J. R.; Schneider, W. F.; Werth, C. J. Structure Sensitivity Study of Waterborne Contaminant Hydrogenation Using Shape- and Size-Controlled Pd Nanoparticles. *ACS Catal.* **2013**, *3* (3), 453-463.
4. Kelley, K. H. Catalytic reduction of NO and N₂O with hydrogen in water by polymer-protected palladium nanoparticles. University of Illinois at Urbana-Champaign, 2010.
5. Sander, R. Compilation of Henry's law constants for inorganic and organic species of potential importance in environmental chemistry. In Max-Planck Institute of Chemistry, Air Chemistry Department Mainz, Germany: 1999.
6. Weisz, P.; Prater, C. Interpretation of measurements in experimental catalysis. *Adv. Catal* **1954**, *6*, 143-196.

7. Satterfield, C. N. Mass transfer in heterogeneous catalysis. In The MIT Press: 1970.
8. Picioreanu, C.; van Loosdrecht, M. C. M.; Heijnen, J. J. Modelling the effect of oxygen concentration on nitrite accumulation in a biofilm airlift suspension reactor. *Water Sci. Technol.* **1997**, *36* (1), 147-156.
9. Davie, M. G.; Reinhard, M.; Shapley, J. R. Metal-Catalyzed Reduction of N-Nitrosodimethylamine with Hydrogen in Water†. *Environ. Sci. Technol.* **2006**, *40* (23), 7329-7335.
10. Shuai, D.; Choe, J. K.; Shapley, J. R.; Werth, C. J. Enhanced Activity and Selectivity of Carbon Nanofiber Supported Pd Catalysts for Nitrite Reduction. *Environ. Sci. Technol.* **2012**, *46* (5), 2847-2855.
11. Pintar, A.; Batista, J.; Levec, J.; Kajiuchi, T. Kinetics of the catalytic liquid-phase hydrogenation of aqueous nitrate solutions. *Appl. Catal., B* **1996**, *11* (1), 81-98.
12. Lemaignen, L.; Tong, C.; Begon, V.; Burch, R.; Chadwick, D. Catalytic denitrification of water with palladium-based catalysts supported on activated carbons. *Catal. Today* **2002**, *75* (1-4), 43-48.
13. Chaplin, B. P.; Roundy, E.; Guy, K. A.; Shapley, J. R.; Werth, C. J. Effects of natural water ions and humic acid on catalytic nitrate reduction kinetics using an alumina supported Pd-Cu catalyst. *Environ. Sci. Technol.* **2006**, *40* (9), 3075-3081.
14. Trawczyński, J.; Gheek, P.; Okal, J.; Zawadzki, M.; Gomez, M. J. I. Reduction of nitrate on active carbon supported Pd-Cu catalysts. *Appl. Catal., A* **2011**, *409-410* (0), 39-47.
15. Jung, S.; Bae, S.; Lee, W. Development of Pd-Cu/Hematite Catalyst for Selective Nitrate Reduction. *Environ. Sci. Technol.* **2014**, *48* (16), 9651-9658.

APPENDIX C

SUPPLEMENTARY DATA FOR CHAPTER 4

C.1 Evaluation of Internal Mass Transfer Limitation

The Weisz-Prater parameter (C_{WP}) was estimated to evaluate internal mass transfer limitations.¹ It provides a measure of the characteristic time scale of an observed reaction in comparison to the estimated characteristic time for internal diffusion of a reactant within the porous catalyst support. Values of $C_{WP} \ll 1$ indicate that the observed reaction is much slower than the expected rate of internal mass transfer, so the latter can be assumed to not be limiting, whereas values of C_{WP} approaching unity or >1 indicate that internal mass transfer may be limiting the observed reaction rate. For this study, C_{WP} is defined as:

$$C_{WP} = \frac{R^2 k_{obs,0} \tau}{D\theta} \quad (C.1)$$

Where R is the radius of the catalyst support particle, τ is the tortuosity factor of the catalyst (typically varies from 2 to 10),² D is the diffusion coefficient of NDMA in bulk solution ($9.64 \times 10^{-10} \text{ m}^2 \text{ s}^{-1}$)³ and θ is the porosity of the catalyst particle (typically varies from 0.2 to 0.7).⁴ The projected area of the particles was determined by optical microscope, and the radius R was estimated by treating the particles as spheres. A conservative estimate of the maximum value of C_{WP} was obtained by choosing the smallest θ (0.2), largest τ (10), and maximum R (101 μm). The resulting C_{WP} estimate of 0.16 is $\ll 1$ under standard testing conditions ($[\text{NDMA}]_0 = 100 \mu\text{M}$, $0.1 \text{ g L}^{-1} \text{ Ru/Al}_2\text{O}_3$), indicating that internal mass transfer is not rate limiting.^{1,5}

C.2 Experimental Results

Table C.1 Composition of dechlorinated tap water.

Component	Concentration
Alkalinity	35.6 mg L ⁻¹ as CaCO ₃
TDS	202 mg L ⁻¹
Chloride	27.7 mg L ⁻¹ as Cl ⁻
Nitrate	1.2 mg L ⁻¹ as NO ₃ ⁻
Nitrite	ND ^a
Sulfate	90.8 mg L ⁻¹ as SO ₄ ²⁻
Phosphate	ND ^a
Ca	29.8 mg L ⁻¹
Mg	7.0 mg L ⁻¹
Fe	ND ^a
Mn	ND ^a
TOC	1.3 mg L ⁻¹
Ammonia	<0.02 mg L ⁻¹ NH ₃ -N
pH	7.6

^aNot detected

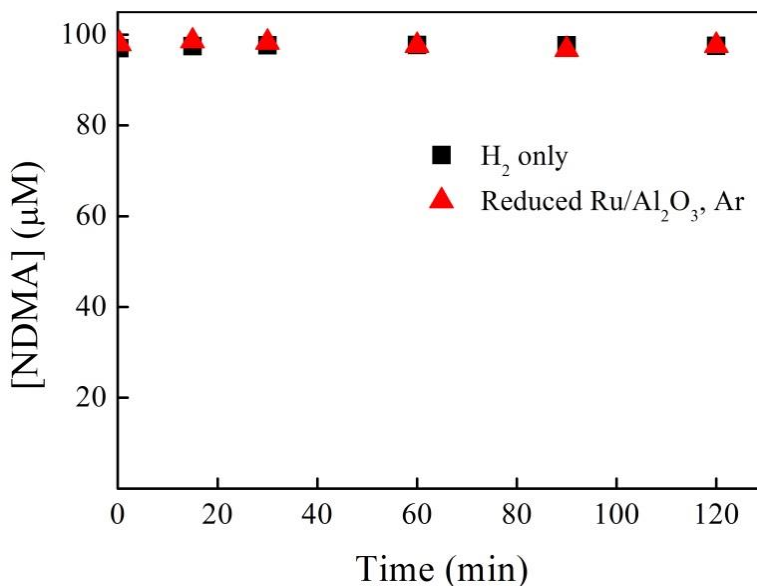


Figure C.1 Control experiments for NDMA reaction in H₂-sparged solution (no catalyst) and suspensions of commercial Ru/Al₂O₃ catalyst sparged with Ar (inert gas) in place of H₂. Error bars representing the range of values measured in duplicate reactions are all smaller than symbols shown.

Table C.2 NDMA reduction activity and products over different catalysts.

Catalyst	Catalyst dose	[NDMA] ₀ (μ M)	Metal weight normalized pseudo-first-order rate constant	Organic product	Inorganic product	Ref.
1%Pd/ γ -Al ₂ O ₃	10 mg _{Pd} L ⁻¹	1.4	11.5±0.9 L g _{Pd} ⁻¹ h ⁻¹	DMA	- ^a	4
1%Pd0.3%Cu/ γ -Al ₂ O ₃	10 mg _{me} L ⁻¹ ^b , 3 mg _{Cu} L ⁻¹	1.4	66.5±7.4 L g _{me} ⁻¹ h ⁻¹ ^b	DMA	- ^a	4
5%Pd1%In/ γ -Al ₂ O ₃	5.5 mg _{Pd} L ⁻¹ , 1.0 mg _{In} L ⁻¹	1.4	45.3±3.6 L g _{Pd} ⁻¹ h ⁻¹	DMA	Ammonia	6
2.4%Pd0.6%Ni/ γ -Al ₂ O ₃	3.6 mg _{Pd} L ⁻¹ , 0.9 mg _{Ni} L ⁻¹	2	836±21 L g _{me} ⁻¹ h ⁻¹ ^b	DMA	- ^a	7
Low surface area Ni	10 mg _{Ni} L ⁻¹	1.4	8.3±2.9 L g _{Ni} ⁻¹ h ⁻¹	DMA	- ^a	4
Raney Ni	435 mg _{Ni} L ⁻¹ , 40 mg _{Al} L ⁻¹	100	77.9±13.1 L g _{Ni} ⁻¹ h ⁻¹	DMA	N ₂	3
NiB	425 mg _{Ni} L ⁻¹ , 35 mg _B L ⁻¹	100	29.5±2.4 L g _{Ni} ⁻¹ h ⁻¹	DMA	Ammonia	8
5%Pd/Al ₂ O ₃	4.6 mg _{Pd} L ⁻¹	100	3.9±1.3 L g _{Pd} ⁻¹ h ⁻¹	Not analyzed	Not analyzed	This study
5%Pd1%In/Al ₂ O ₃	4.6 mg _{Pd} L ⁻¹ , 0.87 mg _{In} L ⁻¹	100	23.9±5.1 L g _{Pd} ⁻¹ h ⁻¹	Not analyzed	Not analyzed	This study
Commercial 5%Ru/Al ₂ O ₃	4.5 mg _{Ru} L ⁻¹	100 Low ^c 0.014 ^d	1103±133 L g _{Ru} ⁻¹ h ⁻¹ 5030 L g _{Ru} ⁻¹ h ⁻¹ ^c 5700±490 L g _{Ru} ⁻¹ h ⁻¹ ^d	DMA	Ammonia	This study
In-house 5%Ru/Al ₂ O ₃	4.6 mg _{Ru} L ⁻¹	100	2718±321 L g _{Ru} ⁻¹ h ⁻¹	Not analyzed	Not analyzed	This study

^aAmmonia was not detected potentially due to the limitation of detection method, and N₂ was not measured.

^bMetal is not specified.

^cExtrapolation from Langmuir-Hinshelwood model to linear region.

^dFrom test of five *N*-nitrosamines mixed in tap water.

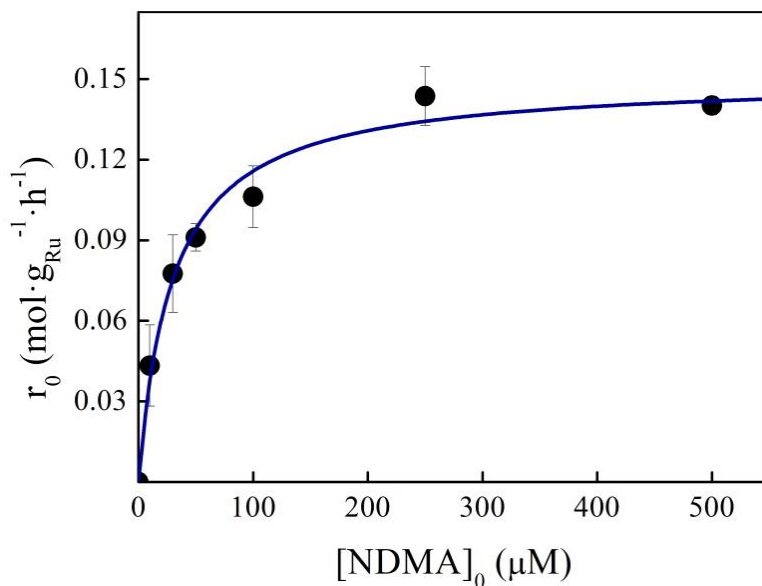


Figure C.2 Initial reaction rate as a function of initial NDMA concentration. Lines represent least-squares fit of Langmuir-Hinshelwood model to the data shown. Error bars represent standard deviations of triplicate experiments.

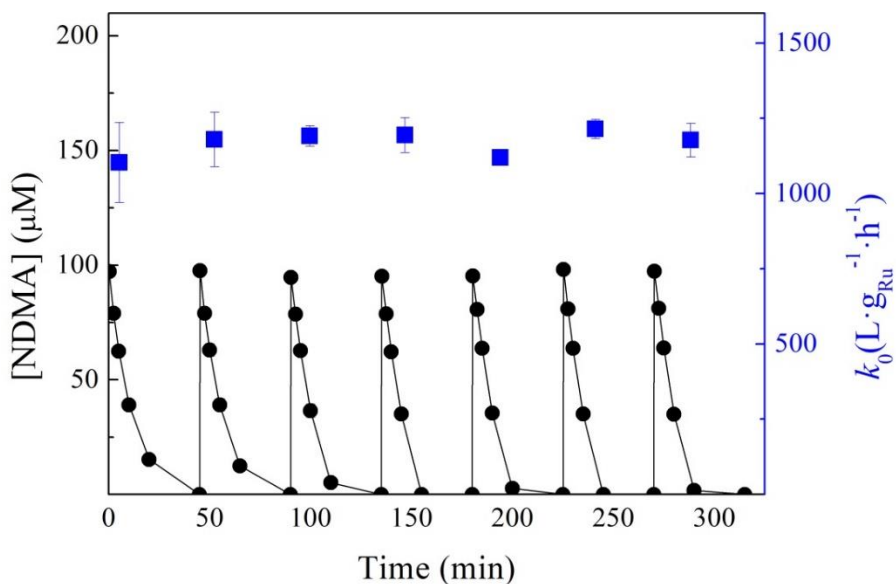


Figure C.3 NDMA reduction activity of commercial Ru/Al₂O₃ in repetitive NDMA spiking experiments (0.1 g L⁻¹ catalyst, pH 6.0 buffered by 10 mM MES buffer, continuous sparging of 1 atm H₂, 22 ± 0.5 °C). Error bars represent range of results from duplicate reactions (smaller than symbol if not visible).

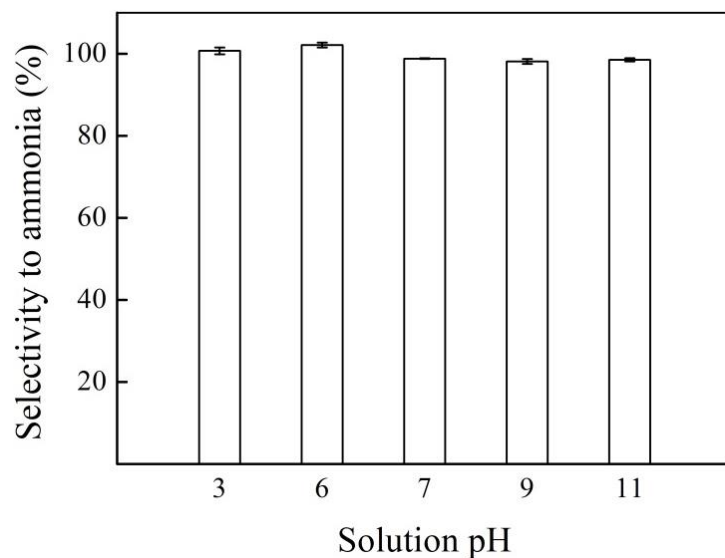


Figure C.4 NDMA reduction product selectivity to ammonia as a function of solution pH. Error bars represent the range of observed values in duplicate experiments.

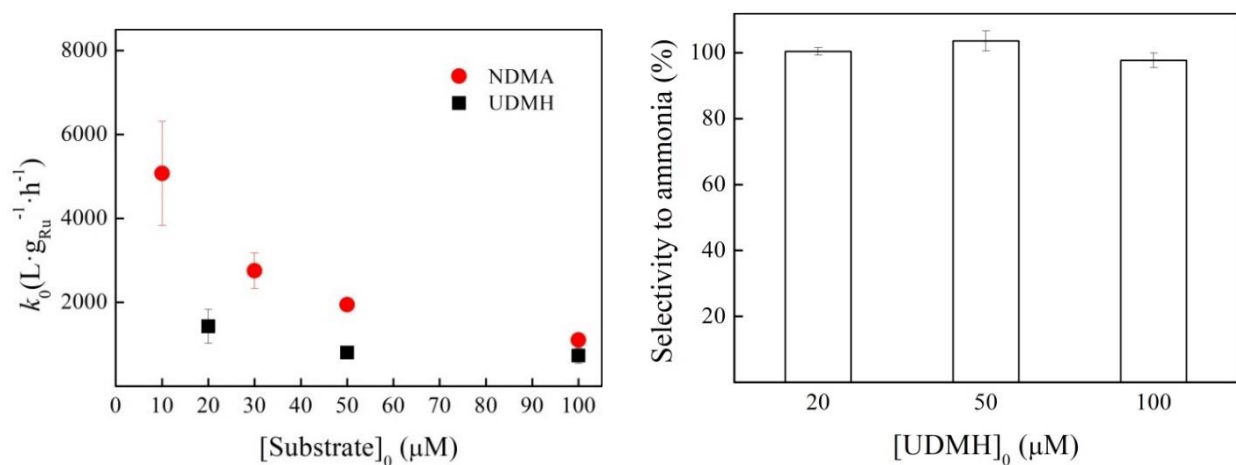


Figure C.5 (A) Comparison of metal weight-normalized pseudo-first-order rate constants for reduction of NDMA and UDMH, and (B) UDMH reduction product selectivity as a function of initial UDMH concentration in the semi-batch reactor system (0.1 g L⁻¹ catalyst, pH 6.0 buffered by 10 mM MES buffer, continuous sparging of 1 atm H₂, 22 ± 0.5 °C). Error bars represent standard deviations obtained from triplicate experiments.

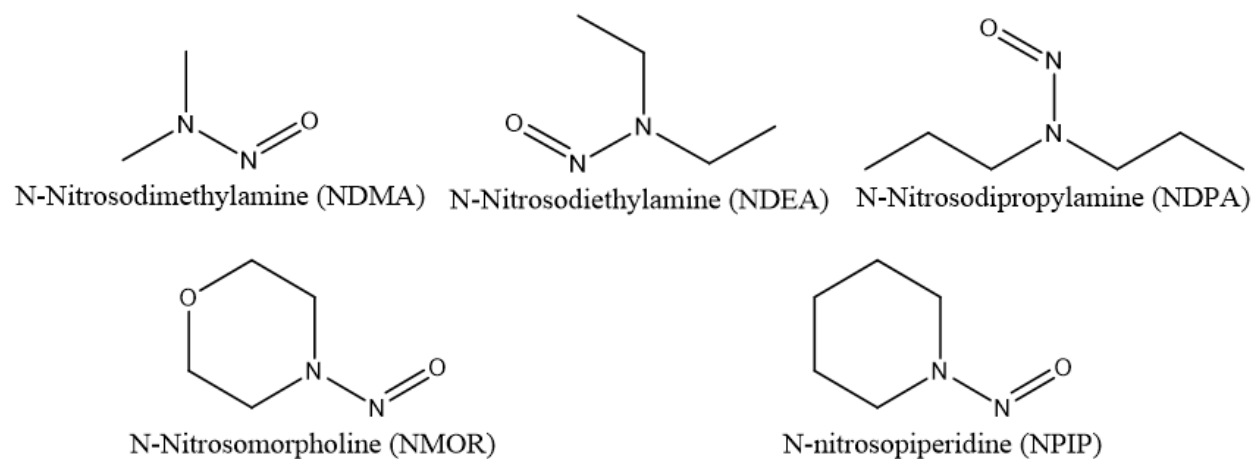


Figure C.6 Structures of *N*-nitrosamines examined in treatment experiments conducted in tap water.

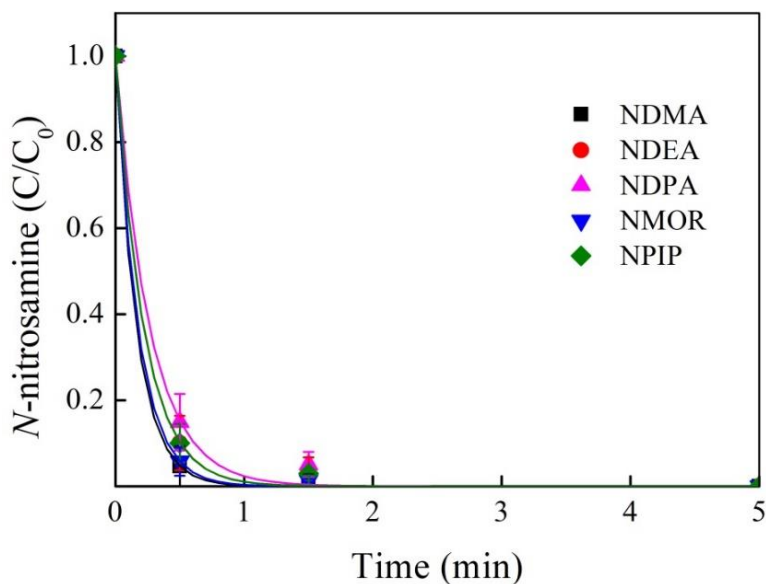


Figure C.7 Catalytic reduction of a mixture of *N*-nitrosamines added to deionized water ($1 \mu\text{g L}^{-1}$ of each *N*-nitrosamine, 0.1 g L^{-1} commercial $\text{Ru/Al}_2\text{O}_3$ catalyst, initial solution pH 9.0, continuous sparging of 1 atm H_2 , $22 \pm 0.5 \text{ }^\circ\text{C}$). Error bars represent the range of measured values in duplicate reactions (smaller than symbol if not visible).

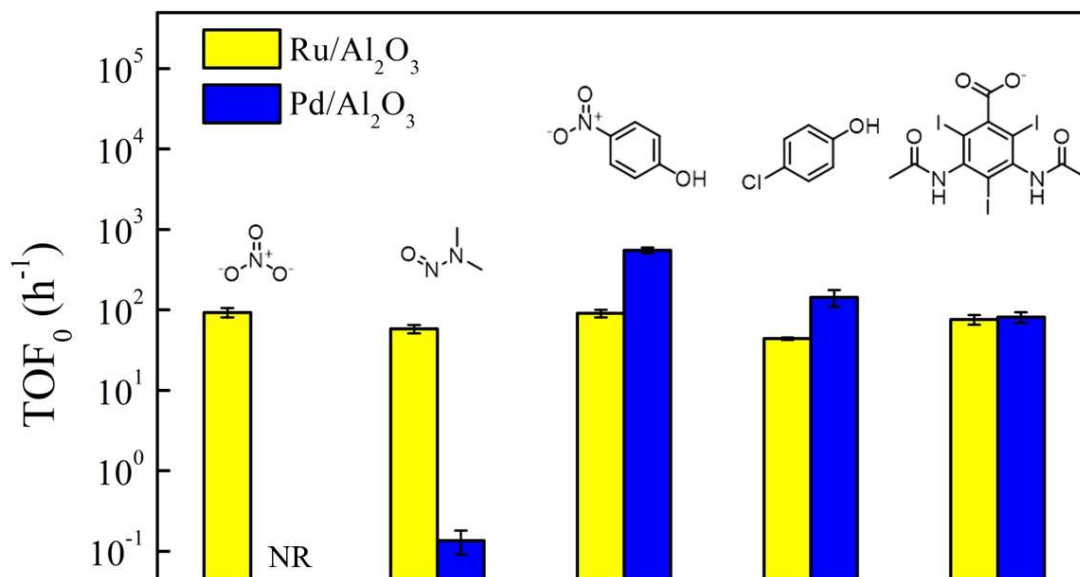


Figure C.8 Comparison between Ru/Al₂O₃ and Pd/Al₂O₃ catalyst activities for reduction of different N-containing contaminants and halogenated aromatic contaminants. Error bars represent standard deviations of triplicate reactions. Data for NO₃⁻ from previous study.⁹

C.3 References

1. Weisz, P.; Prater, C. Interpretation of measurements in experimental catalysis. *Adv. Catal* **1954**, *6*, 143-196.
2. Satterfield, C. N. Mass transfer in heterogeneous catalysis. In The MIT Press: 1970.
3. Frierdich, A. J.; Shapley, J. R.; Strathmann, T. J. Rapid reduction of N-nitrosamine disinfection byproducts in water with hydrogen and porous nickel catalysts. *Environ. Sci. Technol.* **2008**, *42* (1), 262-269.
4. Davie, M. G.; Reinhard, M.; Shapley, J. R. Metal-catalyzed reduction of N-nitrosodimethylamine with hydrogen in water. *Environ. Sci. Technol.* **2006**, *40* (23), 7329-7335.
5. Shuai, D.; Choe, J. K.; Shapley, J. R.; Werth, C. J. Enhanced Activity and Selectivity of Carbon Nanofiber Supported Pd Catalysts for Nitrite Reduction. *Environ. Sci. Technol.* **2012**, *46* (5), 2847-2855.
6. Davie, M. G.; Shih, K.; Pacheco, F. A.; Leckie, J. O.; Reinhard, M. Palladium-indium catalyzed reduction of N-nitrosodimethylamine: Indium as a promoter metal. *Environ. Sci. Technol.* **2008**, *42* (8), 3040-3046.
7. Chen, H.; Li, T.; Jiang, F.; Wang, Z. Enhanced catalytic reduction of N-nitrosodimethylamine over bimetallic Pd-Ni catalysts. *J. Mol. Catal. A: Chem.* **2016**, *421*, 167-177.

8. Friedrich, A. J.; Joseph, C. E.; Strathmann, T. J. Catalytic reduction of N-nitrosodimethylamine with nanophase nickel-boron. *Appl. Catal. B-Environ.* **2009**, *90* (1-2), 175-183.
9. Huo, X.; Van Hoomissen, D. J.; Liu, J.; Vyas, S.; Strathmann, T. J. Hydrogenation of aqueous nitrate and nitrite with ruthenium catalysts. *Appl. Catal., B* **2017**, *211*, 188-198.

APPENDIX D

SUPPLEMENTARY DATA FOR CHAPTER 5

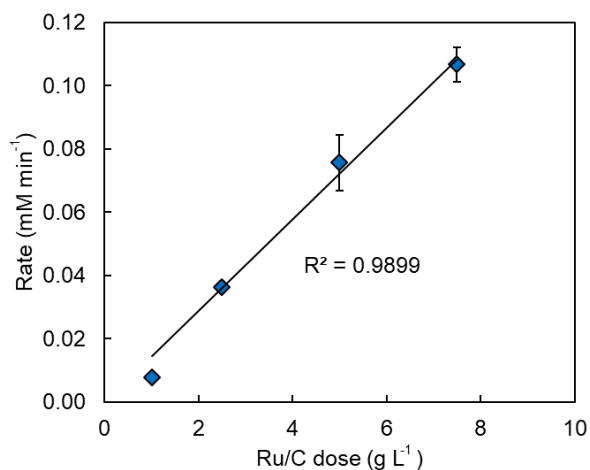


Figure D.1 Initial nitrate hydrogenation rate as a function of Ru/C loading. Conditions: Initial $[\text{NO}_3^-] = 100 \text{ mM}$, brine matrix (5 wt% NaCl, 100 mM NaHCO₃, 100 mM Na₂SO₄), 30 °C, no solution pH control, 1 atm H₂ headspace maintained by flowing H₂ at ca. 300 mL min⁻¹. Error bars indicate standard deviation from duplicate measurements (smaller than symbol if not visible).

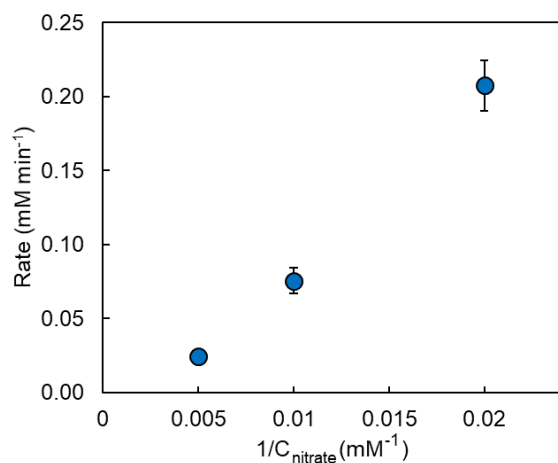


Figure D.2 Plot of initial rate versus the inverse of initial nitrate concentrations. Error bars indicate standard deviation from duplicate measurements (smaller than symbol if not visible).

APPENDIX E

SUPPLEMENTARY DATA FOR CHAPTER 6

E.1 Experimental Methods

E.1.1 Catalyst synthesis and characterization

Pt/Al₂O₃ catalyst was prepared by strong electrostatic adsorption method with chloroplatinic acid hexahydrate as Pt precursor. Al₂O₃ of 30-50 mesh and Pt precursor were added to deionized water, and solution pH was adjusted to 3 by adding HCl. After stirring overnight, the catalyst particles were recovered by filtration extensively washed with deionized water. The catalyst was dried in the air and reduced in flowing H₂ (200 mL min⁻¹) at 300 °C for 4 h.

BET surface area was determined by nitrogen physisorption using a Quadrasorb SI™ surface area analyzer from Quantachrome Instruments. Samples of ~80–120 mg were measured using a 55-point nitrogen adsorption/desorption curve at -196 °C. Prior to analysis, the samples were degassed at 300 °C for 16 h under vacuum. BET surface areas were calculated over a relative pressure range of 0.050 to 0.250 P/P₀. The surface area measurements are within 10% of deviation.

Pt dispersion on alumina was measured from CO pulse chemisorption performed using an Altamira AMI-390 micro-flow reactor system equipped with a thermal conductivity detector (TCD). Samples of ~50–100 mg were loaded in a quartz U-tube reactor and heated in 5% H₂/Ar to 250 °C at 5 °C min⁻¹ with a hold time of 2 h. After the reduction step, catalyst samples were flushed with He at 50 mL min⁻¹ for 1 h, cooled to 30 °C and dosed with sequential 500-μL pulses

of 10% CO/He mixture. A 500- μ L sample loop was used to calibrate the TCD response for CO after each experiment. Pt dispersion was calculated by assuming a Pt:CO stoichiometry of one-to-one.

The total number of acid sites was determined by NH_3 pulse chemisorption using the same Altamira Instruments AMI-390 system. Samples of ~100–150 mg were loaded in a quartz U-tube reactor. ZrO_2 samples were pretreated under flowing He at $5\text{ }^\circ\text{C min}^{-1}$ to $350\text{ }^\circ\text{C}$ and then held at this temperature for 2 h. Nb_2O_5 samples were pretreated under flowing He at $5\text{ }^\circ\text{C min}^{-1}$ to $300\text{ }^\circ\text{C}$ with a hold time of 2 h. $\text{Pt/Al}_2\text{O}_3$ samples were pretreated under flowing 5% H_2/Ar to $300\text{ }^\circ\text{C}$ at $5\text{ }^\circ\text{C min}^{-1}$ with a hold time of 2 h. The samples were cooled to $120\text{ }^\circ\text{C}$ under flowing He and dosed with sequential 2000- μ L pulses of 10% NH_3/He mixture. A 2000- μ L sample loop was used to calibrate the TCD response for NH_3 after each experiment.

The relative ratio of Brønsted to Lewis acid sites was determined by pyridine adsorption diffuse reflectance Fourier transform infrared spectroscopy (py-DRIFTS). Spectra represent the average of 64 scans collected at 4 cm^{-1} resolution using a Thermo Nicolet iS50 FT-IR spectrometer equipped with a Harrick Praying Mantis reaction chamber. Oxide samples were pretreated under flowing Ar at $5\text{ }^\circ\text{C min}^{-1}$ to $350\text{ }^\circ\text{C}$ and then held at this temperature for 2 h. $\text{Pt/Al}_2\text{O}_3$ samples were pretreated under flowing 5% H_2/Ar to $300\text{ }^\circ\text{C}$ at $5\text{ }^\circ\text{C min}^{-1}$ with a hold time of 2 h. After cooling to $150\text{ }^\circ\text{C}$ at $5\text{ }^\circ\text{C min}^{-1}$, the samples were purged with Ar for 10 min, and a background spectrum was collected. The samples were then exposed to pyridine vapor for 5 min by flowing Ar through a pyridine-filled bubbler held at room temperature. Physisorbed pyridine was subsequently desorbed in Ar by heating to $200\text{ }^\circ\text{C}$ at $5\text{ }^\circ\text{C min}^{-1}$ and holding for 30 min. After cooling to $150\text{ }^\circ\text{C}$ at $5\text{ }^\circ\text{C min}^{-1}$, a spectrum was collected and referenced to the background collected prior to pyridine exposure. The peak area of vibrational modes near 1445

cm^{-1} (Lewis) and 1540 cm^{-1} (Brønsted) were used to determine the relative ratio of Brønsted to Lewis acidic sites.

The irreversibly adsorbed carbon amount of spent catalysts was measured by a Setaram Setsys Evolution thermal gravimetric analyzer (TGA) coupled with a Nicolet 6700 Fourier Transform InfraRed (FTIR) spectrometer via a transfer line heated at $200 \text{ }^\circ\text{C}$. The FTIR spectrometer is equipped with a gas cell maintained at 225°C to prevent vapor condensation. The catalyst was heated to $800 \text{ }^\circ\text{C}$ under zero air (19-21% oxygen with a balance of nitrogen). The onset of carbon combustion was determined by the observation of carbon dioxide in the FTIR. Prior to the onset of carbon combustion, only water was observed in the FTIR spectra. Therefore, the carbon content was calculated by subtracting the mass loss due to water from the total mass loss recorded by the TGA.

E.1.2 Catalytic testing

Acid ketonization experiments were carried out in packed-bed reactor at $435 \text{ }^\circ\text{C}$ and atmospheric pressure. The liquid flow and Ar flow rates were 0.2 mL min^{-1} and $100 \text{ mL (STP) min}^{-1}$, respectively. The feed was introduced to the reactor by a HPLC pump. Both the liquid feed and Ar flew downward through a ZrO_2 catalyst (Johnson Matthey, 30-50 mesh) bed in between inert 1-mm glass beads, which were held in place with quartz wool in a $0.5''$ OD ($0.035''$ wall thickness) tubular stainless-steel reactor coated with a silica Dursan coating (SilcoTek Coating Co.). The reactor was heated by a tubular split furnace. A back-pressure regulator was used to control the reactor pressure (the regulator was fully open for ketonization experiments). Liquid products were collected in a knock-out pot and analyzed off-line. The gaseous products were monitored by an on-line gas chromatograph and a nondispersive infrared detector. Conversion and carbon yield are defined by the following equations:

$$\text{Conversion} = \frac{f_{\text{Reactant, feed}} - f_{\text{Reactant, ave}}}{f_{\text{Reactant, feed}}} \times 100\% \quad (\text{E.1})$$

$$\text{Carbon yield} = \frac{f_{\text{Product, ave}}}{f_{\text{Reactant, feed}}} \times 100\% \quad (\text{E.2})$$

where $f_{\text{Reactant, feed}}$ = molar flow rate of carbon in reactant in the feed; $f_{\text{Reactant, ave}}$ = average molar flow rate of carbon in reactant during sampling interval; $f_{\text{Product, ave}}$ = average molar flow rate of carbon in product during sampling interval.

Ketone condensation experiments were performed in a Parr multi-batch reactor system (Parr Instrument Co.). Feed solution and Nb₂O₅ catalyst (CBMM, calcined in air at 350 °C for 12 h) were added to 75-mL reactor cups, followed by purging and flushing of the system with He for three cycles. The reactors were sealed and heated to the desired temperature over a period of ~20 min. Reaction solution and catalyst were well mixed by using magnetic stir bars operating at 800 rpm. Reactors were quenched in an ice bath to terminate the reaction at predetermined time. Products were filtered through 0.2- μ m PTFE membranes to separate the liquid from the catalysts. Conversion, average rate, carbon yield and selectivity are defined by the following equations:

$$\text{Conversion} = \frac{n_{\text{Reactant, initial}} - n_{\text{Reactant, t}}}{n_{\text{Reactant, initial}}} \times 100\% \quad (\text{E.3})$$

$$\text{Average rate} = \frac{n_{\text{Reactant, initial}} - n_{\text{Reactant, t}}}{m_{\text{Catalyst}} \times t} \times M_{\text{Reactant}} \quad (\text{E.4})$$

$$\text{Yield} = \frac{n_{\text{Product, t}}}{n_{\text{Reactant, initial}}} \times 100\% \quad (\text{E.5})$$

$$\text{Selectivity} = \frac{\text{Carbon yield}}{\text{Conversion}} \times 100\% \quad (\text{E.6})$$

where $n_{\text{Reactant, initial}}$ = mole of carbon in reactant in the feed; $n_{\text{Reactant, t}}$ = mole of carbon in reactant at a given time; m_{Catalyst} = mass of catalyst; t = reaction time; M_{Reactant} = the molar mass of reactant; $n_{\text{Product, t}}$ = mole of carbon in product at a given time.

To prepare feed for HDO, the liquid product from condensation experiments were distilled by using spinning band distillation. Solvent and unreacted ketone were recycled to condensation reaction during process integration experiments. Purified condensation products were directly used as feed, with exception of biologically derived condensation products. Due to limited quantity, bioderived condensation products were mixed with cyclohexane at 20 wt%. HDO experiments were carried out at 334 °C and under a H₂ pressure of 500 psi over a Pt/Al₂O₃ catalyst (30-50 mesh) in the same flow reactor where ketonization experiments were performed. The liquid flow and H₂ flow rates were 0.1 mL min⁻¹ and 165 mL (STP) min⁻¹, respectively.

E.1.3 Chemical analysis

For GC-FID/MS, samples were analyzed using an Agilent 7890A GC operating in split mode (25:1 split ratio). The GC was outfitted with an Agilent HP-5ms column (30 m × 0.25-mm id, 0.25- μ m film), and helium was used as the carrier gas at 1.4 mL min⁻¹ column flow. The injector volume was set to 1 μ L using an Agilent auto-sampler. The GC method consisted of a front inlet temperature of 260°C and an oven temperature program that starts at 40°C, holding for 2 min and then ramping at 18°C min⁻¹ to a temperature of 280 °C before cooling down. Sample was analyzed simultaneously by a Polyarc[®] system/FID and 5975 mass spectrometer detector (Agilent Technologies). FID was set at 300°C, H₂ flow at 30 mL min⁻¹, air flow at 350 mL min⁻¹, and makeup flow at 20 mL min⁻¹. MS transfer line temperature was set at 293 °C.

High resolution mass spectra were collected using a JEOL GCmate II double-focusing mass spectrometer (JEOL, Peabody, MA) coupled with a DSC/TGA Q600 (TA Instruments, Newcastle, DE). Liquid samples were introduced to the MS via a heated transfer line and evaporated by heating in the DSC/TGA instrument to their boiling point. Calorimetric data were not collected as the aim of these experiments were to collect mass spectra of volatilized

compounds only. The ionization source was operated in electron ionization (EI) mode at 70 eV. The mass spectrometer was tuned prior to experiments to a resolving power of $\geq 6,000$ (full width at half maximum (FWHM)) based on m/z 69 using the spectrum of perfluorokerosene. The full spectrum of perfluorokerosene was used for mass calibration across the range of the spectrum collected from m/z 35 to 400.

Quantitative ^{13}C NMR spectra were acquired with ~ 400 μL sample and included a capillary tube filled with 1 mg/mL TSP- d_4 in DMSO- d_6 for referencing. Experiments were run using a Bruker AVANCE III 600 MHz spectrometer (14.7 T) equipped with a room temperature BBO (broad band optimized) 5 mm probe head. All spectra were measured at 25 $^\circ\text{C}$ using a 90 $^\circ$ pulse angle, inverse-gated decoupling, 2048 scans, and a delay of either 10 or 30 s. Integrations were performed on phased and baseline-corrected spectra, with solvent peaks excluded. Distortionless Enhancement by Polarization Transfer (DEPT) experiments were run with selection angle parameter of 135 $^\circ$ which in CH and CH $_3$ groups as positive peaks, and CH $_2$ groups as negative peaks. The coupling constant, JCH, was set to 145 Hz. All data analysis was performed in Topspin 3.6p17.

GCxGC-TOFMS was performed with LECO Pegasus $^\circledR$ 4D GCxGC-TOFMS operating in split mode (50:1 split ratio). The GC was outfitted a Restek RTX-5 column (10 m \times 0.15-mm id, 0.18- μm film) as the primary column and an Agilent DB1701 column (1 m \times 0.10-mm id, 0.10- μm film) as the secondary column. Helium was used as the carrier gas at 1.0 mL min^{-1} . The injector volume was set to 1 μL using a Gerstel MPS2 $^\circledR$ autosampler, and the inlet temperature was set at 300 $^\circ\text{C}$. The primary oven temperature was held at 35 $^\circ\text{C}$ for 7 min, ramped at 5 $^\circ\text{C}$ min^{-1} to 255 $^\circ\text{C}$ and held for 1 min. The primary oven temperature was held at 35 $^\circ\text{C}$ for 7 min, ramped at 5 $^\circ\text{C}$ min^{-1} to 255 $^\circ\text{C}$ and held for 1 min. The secondary oven temperature was set

10 °C offset from the primary oven, held for 4 min, ramped at 5 °C min⁻¹ to 275°C and held for 2 min. Modulator Temperature was set 15 °C offset from the secondary oven and tracking the secondary oven program. Modulator Time was set at 6 s modulation, 1.0 s hot pulse / 2.0 s cold pulse. The MS setting consisted of MS transfer line temperature of 250°C and scan range from 29 m/z to 350 m/z at 200 spectra s⁻¹. ChromaTOF® data acquisition software was used to collect the chromatograms.

E.1.4 Lignocellulosic sugars fermentation and acids separation

The production of corn stover hydrolysate from deacetylation and dilute-acid pretreatment was previously described.¹ The hydrolysate was concentrated via rotavapor to reach a sugar concentration of approximately 450 g L⁻¹ (see composition in Table E.5) and stored at 4 °C. Prior the fermentation, the hydrolysate was diluted with fermentation media to achieve an initial sugar (glucose, xylose, arabinose, and galactose) concentration of 65 g L⁻¹. The fermentation media consisted of yeast extract (5 g L⁻¹), peptone (10 g L⁻¹), ammonium sulfate (3 g L⁻¹), KH₂PO₄ (3.26 g L⁻¹), MgSO₄•7H₂O (0.3 g L⁻¹), CaCl₂•2H₂O (0.02 g L⁻¹), FeSO₄•7H₂O (0.03 g L⁻¹), MnSO₄•H₂O (0.02 g L⁻¹), cysteine-HCl (0.5 g L⁻¹) and resazurin (1 mg L⁻¹). The organism utilized for sugars conversion to carboxylic acids was *Clostridium butyricum* (ATCC 19398). This strict anaerobic bacterium was stored in sealed glycerol stocks at -80 °C and revived anaerobically in sealed serum bottles containing Reinforced Clostridial media supplemented with 20 g L⁻¹ glucose and 10 g L⁻¹ xylose. Cultures were incubated for ~15 h in a rotatory shaker at 37 °C and 150 rpm. Cells were then directly inoculated in two 10-L New Brunswick BioFlo®/CelliGen® 310 bioreactors (Eppendorf) at an initial optical density at 600 nm (OD₆₀₀) of 0.1. Nitrogen was sparged overnight (0.1 vvm) to ensure anaerobic conditions but the gas was turned off at ~7 h to reduce foaming issues. Fermentations were maintained at 37 °C


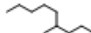
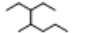
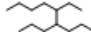




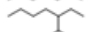

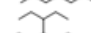
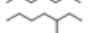

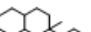
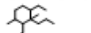
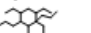

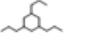

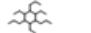
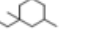
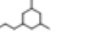
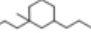
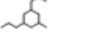
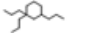
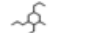
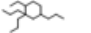
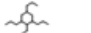
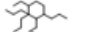
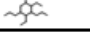
and 100 rpm. The pH was initially adjusted at pH 7 and further controlled at pH 6 by the addition of 4 N NaOH to neutralize the acids. Antifoam 204 (Sigma-Aldrich) was added when required. Samples (2 mL) were taken periodically in aseptic conditions from the bioreactors to track bacterial growth (OD_{600}), sugar utilization, and acids production. The analytical methods to quantify these metabolites were previously described.¹

To recover bio-butyric acid from the fermentation broth, cells were first removed by centrifugation at $12,000 \times g$ during 10 min. Then, the supernatants were filtered through 0.8-0.2 μm Sartopore 2 XLG cartridges (Sartorius) and further pumped through a 10 kDa hollow fiber filter (GE Model #UFP-10-C-4X2MA) maintaining a head pressure of 10 psi. After filtration, the broth, pH 6.5, was loaded with 10% w/v activated carbon and stirred for 2 hours. The activated carbon was removed using a 1L 0.45 μm PES Nalgene Rapid-Flow filter. The filtrate, pH 7.5, was further processed in 900 g batches. Each batch was concentrated to 23% of its original mass by removing water using a rotary evaporator at 30mbar and 50°C. The concentrated broth was then acidified to pH <2 using 1 g H₂SO₄ (Sigma-Aldrich ACS reagent, 95.0-98.0%) per 10 g of concentrated broth. The acidified concentrated broth was then extracted twice, 1:1 v/v with ethyl acetate (Sigma-Aldrich ACS reagent $\geq 99.5\%$) in a separatory funnel. The organic phase was collected, and the ethyl acetate was removed on the rotary evaporator at 150mbar and 50 °C. The remaining concentrated acetic and butyric acids were further purified and separated by vacuum distillation. The spinning band distillation column (BR Instruments 800 micro fractional distillation system) was operated at 100mbar. 4 fractions were collected: impurities below 112 °C, acetic acid between 112-122°C, acetic and butyric acid mixture between 122-173 °C, butyric acid between 173-175 °C. The concentration of ethyl acetate, acetic acid, and butyric acid in each fraction was determined in parallel with ¹H NMR and HPLC. Mixing several

distillation fractions to obtain the desired purity and ratio of acetic and butyric acid produced the final purified mixed acid product.

E.2 Experimental Results

Table E.1 Model predictions of melting point, boiling point, flash point, lower heating value, cetane number, and yield sooting index (normalized to carbon number in parentheses) for mapped hydrocarbons.

No.	Structure	C No.	Melting point (°C)		Boiling point (°C)			Flash point (°C)		L-heating value (MJ/kg)			CN		YSI
			M1	M2	M1	M2	M3	M4	M5	M6	M7	M8	M9	M10	
Non-cyclic branched hydrocarbons															
1		6	-131	-106	63	56	71	-29	-29	45	48	45	37	40 (6.6)	
2		10	-86	-55	155	152	173	29	34	45	47	44	46	63 (6.3)	
3		10	-101	-67	155	138	173	29	34	45	47	44	41	68 (6.8)	
4		14	-56	-20	246	221	255	76	87	44	47	44	48	91 (6.5)	
5		8	-109	-80	109	106	125	0	3	45	47	45	41	48 (6.0)	
6		8	-109	-80	109	106	125	0	3	45	47	45	44	48 (6.0)	
7		8	-124	-92	109	91	125	0	3	45	47	45	32	52 (6.5)	
8		10	-86	-55	155	152	173	29	34	45	47	44	40	59 (5.9)	
9		10	-101	-67	155	138	173	29	34	45	47	44	38	63 (6.3)	
10		12	-64	-32	201	194	216	58	65	44	47	44	45	71 (5.9)	
11		12	-79	-43	200	181	216	57	65	44	47	44	44	75 (6.2)	
12		12	-79	-43	200	181	216	57	65	44	47	44	43	75 (6.2)	
Cyclic hydrocarbons															
13		9	-55	-45	148	134	150	26	29	44	46	44	29	81 (9.0)	
14		15	8	20	280	249	272	109	119	44	46	44	35	125 (8.3)	
15		15	4	17	276	244	272	106	116	44	46	44	32	121 (8.1)	
16		21	67	74	408	331	359	188	207	44	46	44	30	161 (7.7)	
17		9	-83	-58	143	140	150	23	26	44	46	44	28	76 (8.4)	
18		15	-16	11	280	258	272	109	120	44	46	44	39	110 (7.3)	
19		15	-29	0	266	243	272	99	110	44	46	44	29	127 (8.4)	
20		21	39	50	403	334	359	185	204	44	46	44	32	161 (7.7)	
21		11	-33	-21	193	178	196	55	60	44	46	44	37	87 (7.9)	
22		11	-61	-34	188	184	196	51	57	44	46	44	38	87 (7.9)	
23		13	-10	2	239	218	236	83	92	44	46	44	37	99 (7.6)	
24		13	-38	-11	234	222	236	80	88	44	46	44	44	99 (7.6)	
25		15	12	24	285	254	272	112	123	44	46	44	35	110 (7.3)	
26		15	-20	7	275	253	272	105	116	44	46	44	38	116 (7.7)	
27		17	31	41	326	282	304	137	151	44	46	44	34	127 (7.5)	
28		17	3	28	321	286	304	134	148	44	46	44	40	127 (7.5)	
29		19	49	58	367	308	333	163	179	44	46	44	32	144 (7.6)	
30		19	21	33	362	311	333	159	176	44	46	44	34	144 (7.6)	

M1: ChemDraw.² M2: EPISuite.³ M3: Satou (1992).⁴ M4: Prugh (1973).⁵ M5: Butler (1956).⁶ M6: Lloyd (1980).⁷ M7: Mott (1940).⁸ M8: Boie (1953).⁹ M9: Kessler (2017).¹⁰ M10: Das (2018).¹¹ Note: Representative cyclic hydrocarbons were included from ketone cross-condensation reactions due to the large number of possible molecules.

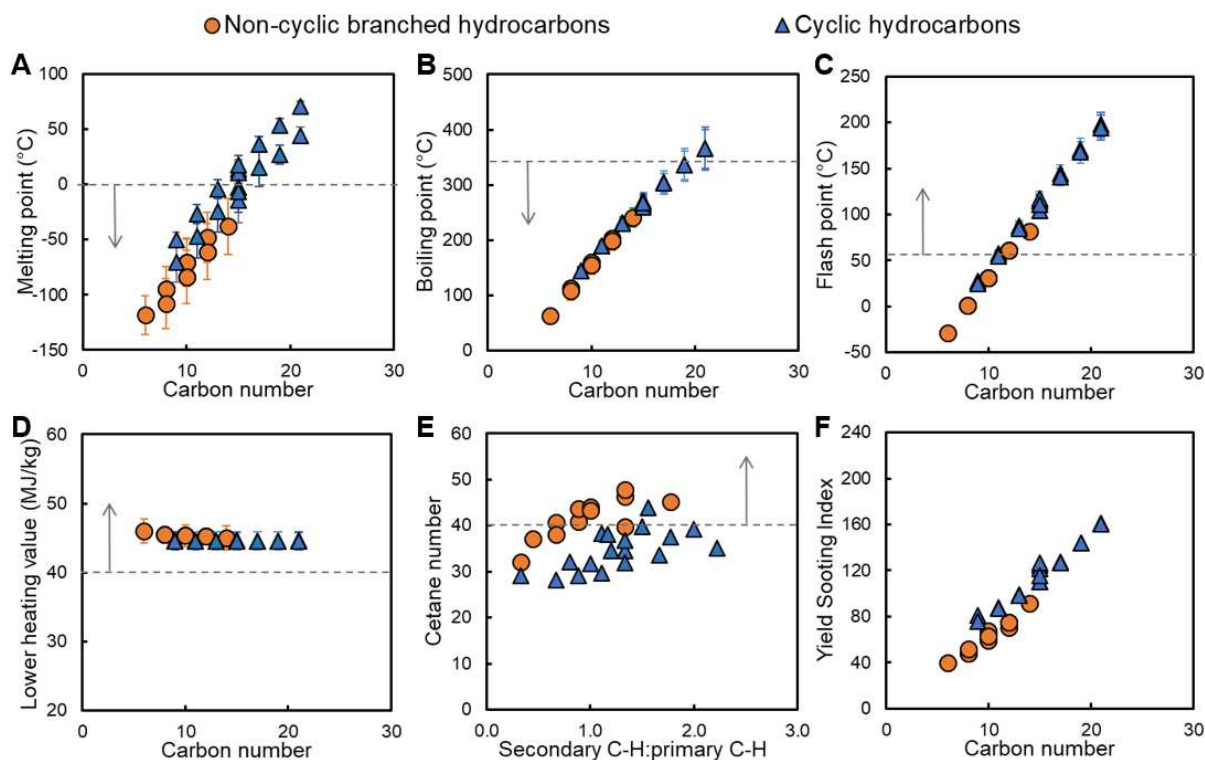


Figure E.1 Plot of model predictions of (A) melting point, (B) boiling point, (C) flash point, (D) lower heating value, (E) cetane number, and (F) yield sooting index. Error bars represent standard deviations of multiple model predictions summarized in Table E.1. Grey dash lines and arrows represent screening criteria.

Table E.2 Surface area, acidity and metal dispersion of fresh ZrO_2 , Nb_2O_5 , and $\text{Pt}/\text{Al}_2\text{O}_3$.

Catalyst	Surface area ($\text{m}^2 \text{g}^{-1}$)	Total acid sites ($\mu\text{mol g}^{-1}$)	Brønsted acid sites ($\mu\text{mol g}^{-1}$)	Lewis acid sites ($\mu\text{mol g}^{-1}$)	Metal dispersion
ZrO_2	65	163	22	141	NA
Nb_2O_5	137	255	49	206	NA
$\text{Pt}/\text{Al}_2\text{O}_3$	198	329	27	302	9.4%

NA = Not applicable

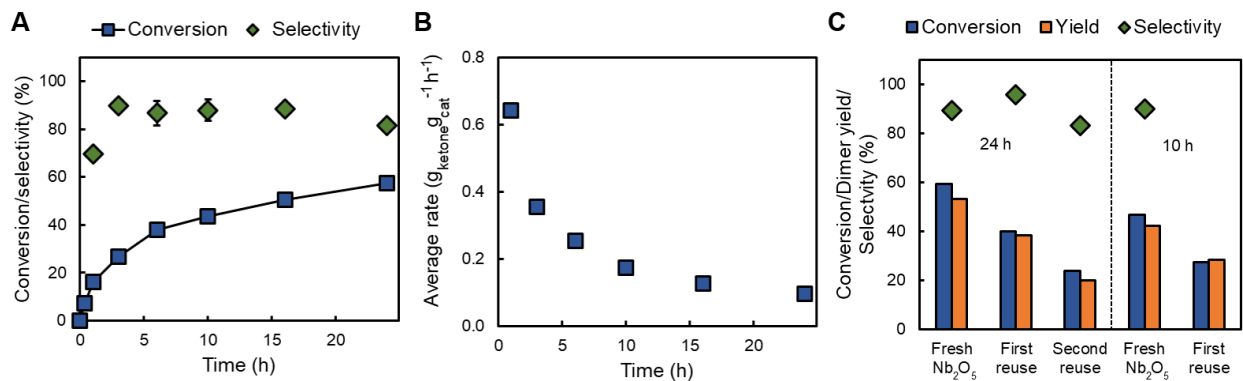


Figure E.2 (A) Conversion of commercial 4-heptanone and selectivity to dimer with reaction time (15 g feed, 20 wt.% 4-heptanone in toluene, 0.75 g fresh Nb₂O₅, catalyst-to-ketone mass ratio = 1:4, 180 °C). (B) Decreasing average rate for 4-heptanone condensation with reaction time (same reaction as figure A). (C) Performance of recycled catalyst (15 g feed, 20 wt% 4-heptanone in toluene, 0.75 g spent catalyst after washing with solvent and drying at room temperature, catalyst-to-ketone mass ratio = 1:4, 180 °C, 10 h or 24 h). All experiments were conducted in an initial He headspace at atmospheric pressure.

Table E.3 Carbon content, surface area and total acidity of fresh Nb₂O₅ and regenerated Nb₂O₅ in Figure 6.4.

Catalyst	C content (wt.%)	Surface area (m ² g ⁻¹)	Total acid sites (μmol g ⁻¹)
Fresh Nb ₂ O ₅	0	137	255
Regenerated Nb ₂ O ₅ after 1 use	<0.1	123	266
Regenerated Nb ₂ O ₅ after 4 uses	0.3	120	247

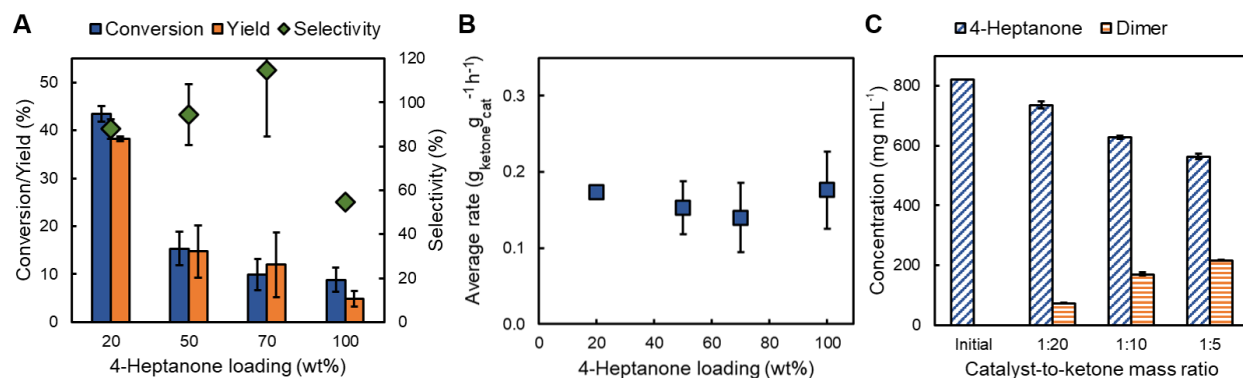


Figure E.3 (A) 4-Heptanone condensation at varying ketone loadings (15 g feed, 0.75 g fresh Nb₂O₅, 20–100 wt% 4-heptanone in toluene, corresponding catalyst-to-ketone mass ratio from 1:4 to 1:20, 180 °C, 10h). (B) Average rate for 4-heptanone condensation (same reaction as figure A). (C) 4-Heptanone and dimer concentrations in the organic phase product at varying fresh Nb₂O₅ loadings (15 g feed, neat 4-heptanone, catalyst-to-ketone mass ratio from 1:20 to 1:5,

180 °C, 24 h). All experiments were conducted in an initial He headspace at atmospheric pressure.

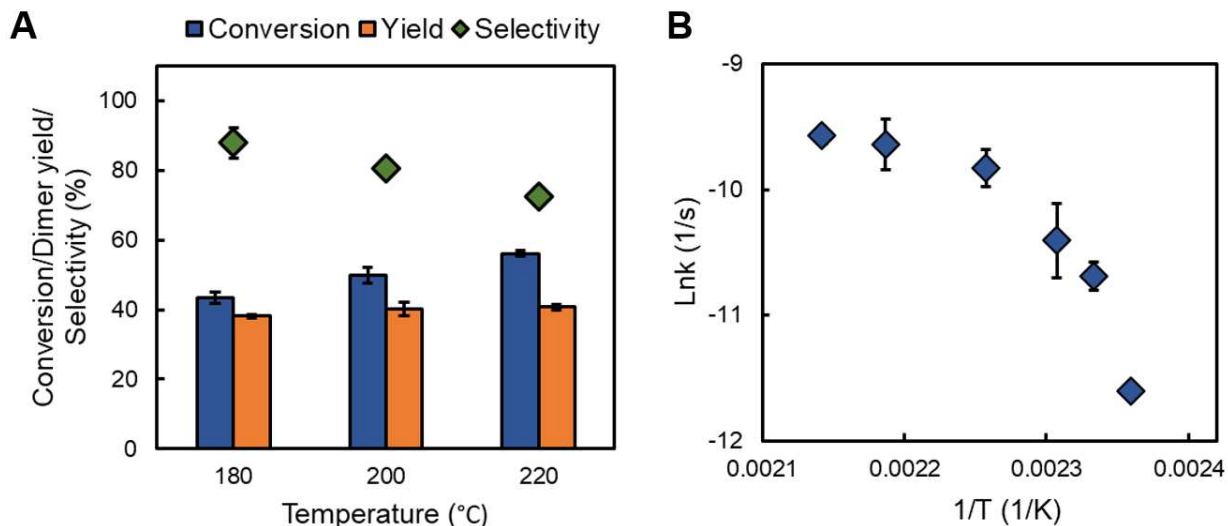


Figure E.4 (A) Conversion of 4-heptanone at varying temperatures (15 g feed, 20 wt% 4-heptanone in toluene, 0.75 g fresh Nb₂O₅, catalyst-to-ketone mass ratio = 1:4, 10 h). (B) Arrhenius plot for 4-heptanone condensation. All experiments were conducted in an initial He headspace at atmospheric pressure.

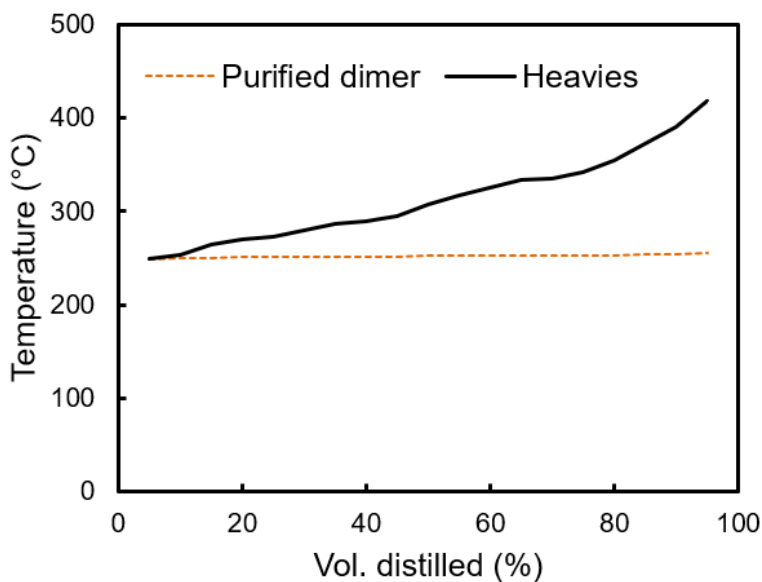


Figure E.5 Simulated distillation curves of purified dimer and heavier compounds (heavies were obtained from removing dimer by distillation).

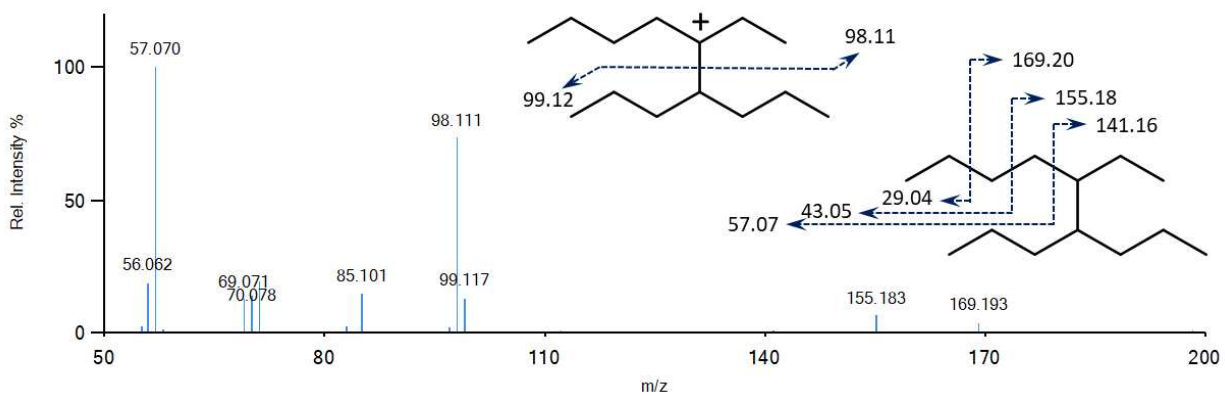


Figure E.6 High resolution mass spectra of the C₁₄ hydrocarbon.

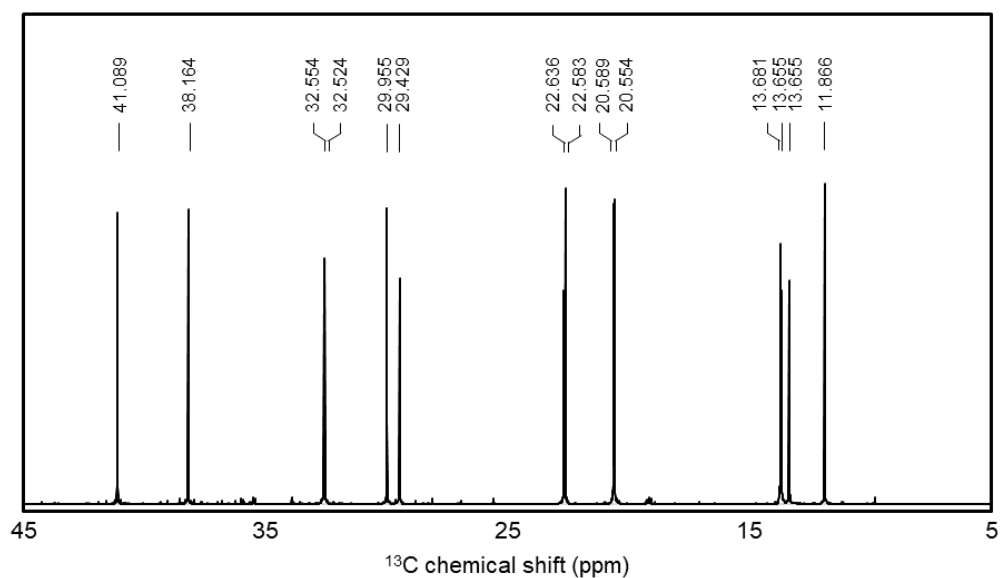


Figure E.7 ¹³C NMR spectrum of purified C₁₄ hydrocarbon.

Table E.4 Physicochemical properties of fresh and regenerated Pt/Al₂O₃.

Catalyst	Pt content (wt.%)	Metal dispersion	Surface area (m ² g ⁻¹)	Total acid sites (μmol g ⁻¹)
Fresh	3.34	9.4%	198	1054
Regenerated	3.36	9.3%	197	1044

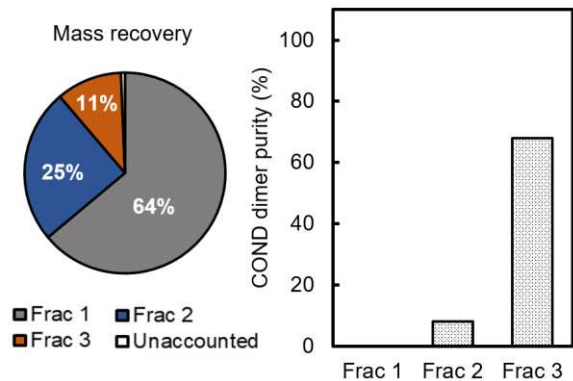


Figure E.8 Mass recovery and dimer purity in three distillation fractions when distilling condensation product.

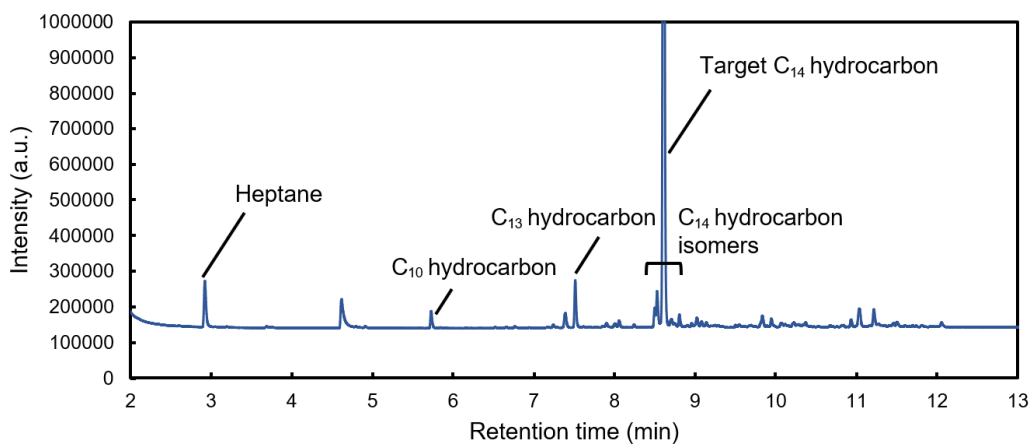


Figure E.9 GC-Polyarc/FID chromatogram of crude hydrocarbon blendstock from upgrading commercial butyric acid. The major component is the target non-cyclic branched C₁₄ hydrocarbon. Scale was adjusted to highlight minor components. Peak at 4.6 min was from solvent impurity.

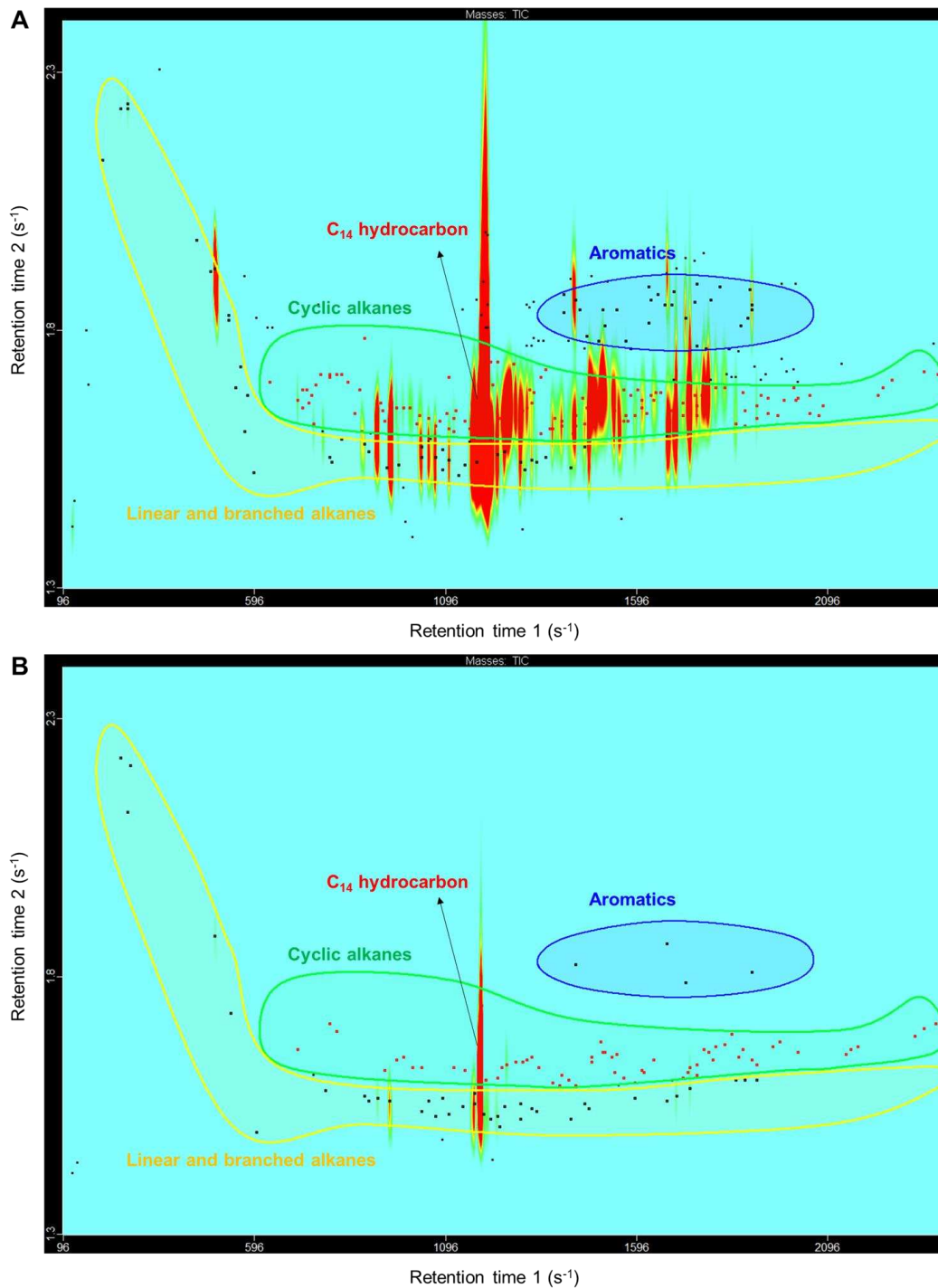


Figure E.10 GCxGC-TOFMS chromatogram of crude hydrocarbon blendstock from upgrading commercial butyric acid: (a) dilution 20:1 and (b) dilution 400:1. The major component is the target non-cyclic C₁₄ hydrocarbon. The most abundant classes present in the mixture are non-cyclic alkanes and cyclic alkanes, although there is potential overlap between these classes and ambiguous identification of linear alkanes and alkenes in these regions. Other structures identified in the plot include aromatics. Note that results are not quantitative.

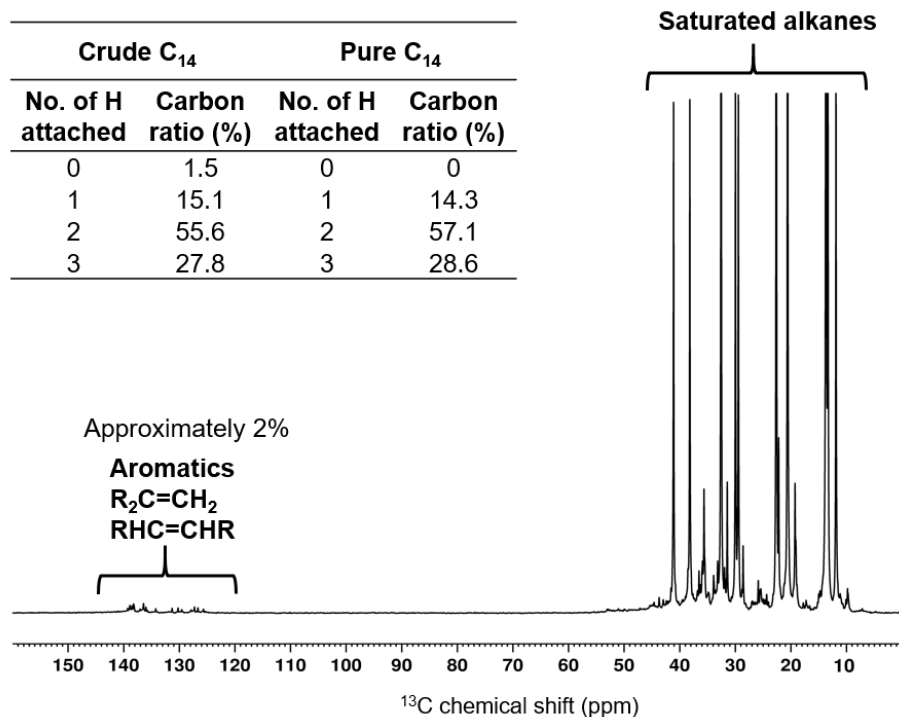


Figure E.11 ¹³C NMR analysis of crude hydrocarbon blendstock from upgrading commercial butyric acid. The crude blendstock exhibited approximately 2% carbon in double bond or aromatic bond. Compared with pure C₁₄ hydrocarbon, the crude blendstock displayed 3% decrease in the ratio of primary carbon. The ratio of carbon having two hydrogen attached (mostly secondary carbon) also decreased 3%. Accordingly, the ratio of carbon having one or no hydrogen attached (e.g., tertiary carbon, quaternary carbon, aromatic carbon) slightly increased.

Table E.5 Concentrations of monomeric and total sugars in concentrated deacetylated dilute acid enzyme hydrolysate. Total sugars account for soluble oligomeric sugars.

Concentration (g L ⁻¹)	Sucrose	Glucose	Xylose	Galactose	Arabinose	Fructose
Monomeric sugar	29.15	253.52	136.47	8.09	20.29	5.62
Total sugar	ND	292.80	149.29	8.46	19.96	1.35

ND = Not determined.

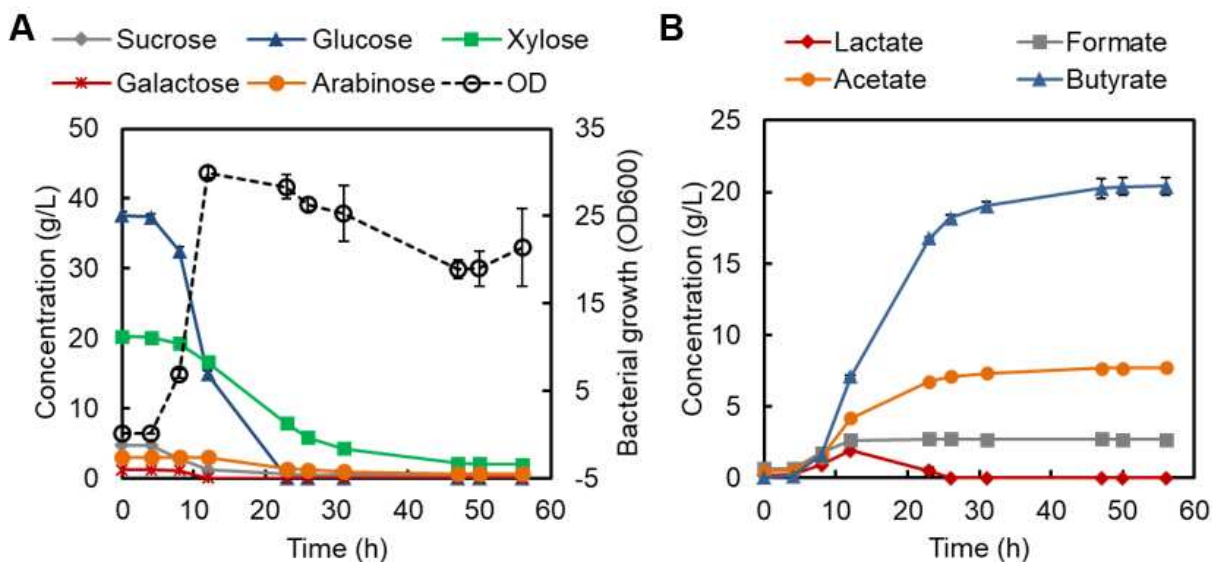


Figure E.12 Batch conversion of lignocellulosic sugars by *Clostridium butyricum* (ATCC 19398). (A) Sugar utilization and bacterial growth measured as optical density at 600 nm (OD). (B) Butyric acid and byproducts formation. Data show the average of two biological replicates. Error bars represent the absolute difference between those replicates.

Table E.6 Impurities in the acid feed and organic phase products from upgrading of biologically derived butyric acid

Element concentration ($\mu\text{g g}^{-1}$) ^a	N ^b	S	Si	Ca	Na	P	K	B	Al	Fe	Ti	Mg
Bio-butyric acid feed	<2	<5	<100	<5	24	<1	<20	<5	<1	1	<0.1	<1
Ketonization product	<2	<5	160	<5	<10	<1	<20	<5	<1	<1	<0.1	<1
Condensation product	<2	<5	340	<5	<10	<1	<20	<5	1	<1	<0.1	<1
HDO product ^c	<2	<5	<100	<5	<10	<1	<20	<5	<1	<1	<0.1	<1

^aData obtained with ICP-AES.

^bData obtained with chemiluminescence, unit is mg L^{-1} .

^cBefore removing cyclohexane solvent.

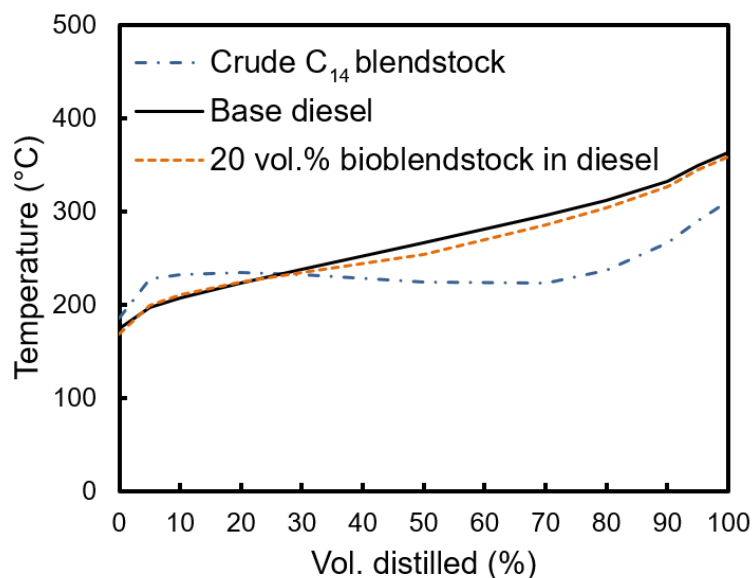


Figure E.13 Simulated distillation curves of commercial butyric acid derived crude C₁₄ blendstock, base diesel, and diesel blend with 20 vol% bioblendstock (D86 correlation was applied to all three curves).

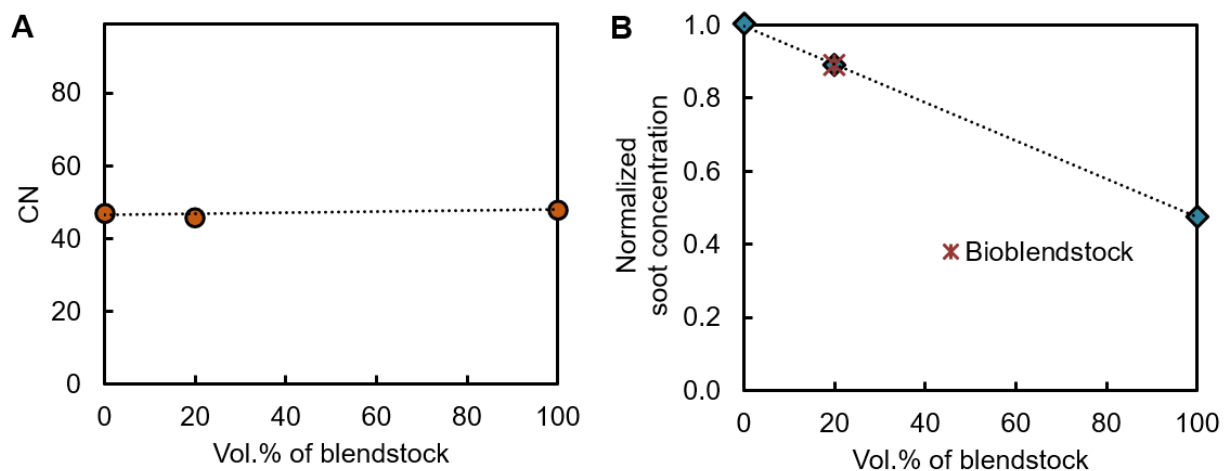


Figure E.14 Plot of (A) CN and (B) normalized soot concentration over blend ratio of commercial butyric acid derived crude C₁₄ blendstock (and bioblendstock as indicated in figure). Dotted lines are to guide the eye.

E.3 References

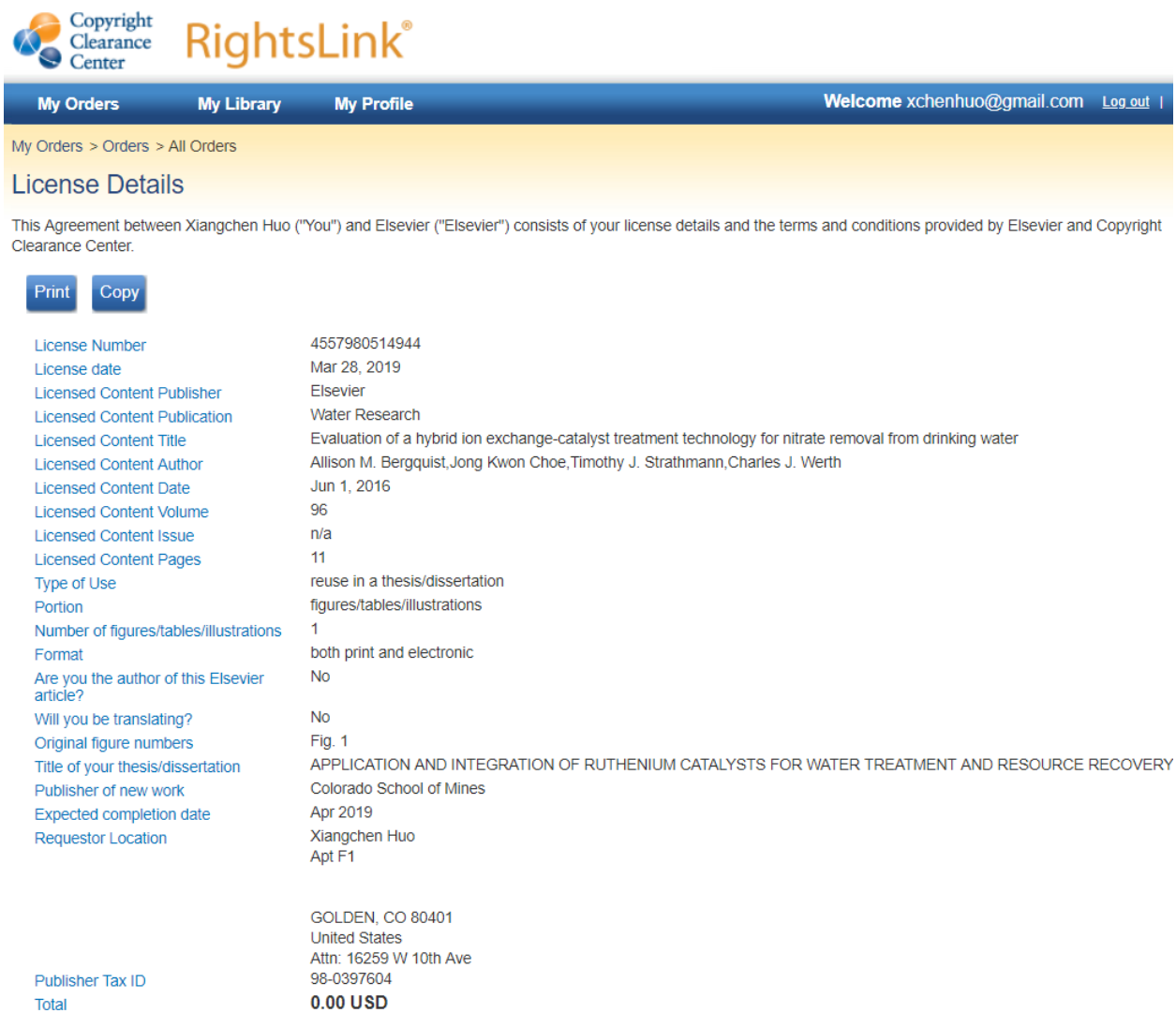
1. Nelson, R.; Peterson, D.; Karp, E.; Beckham, G.; Salvachúa, D. Mixed Carboxylic Acid Production by *Megasphaera elsdenii* from Glucose and Lignocellulosic Hydrolysate. *Fermentation* **2017**, *3* (1), 10.

2. Goncalves, A. G.; Orfao, J. J. M.; Pereira, M. F. R. Catalytic ozonation of sulphamethoxazole in the presence of carbon materials: Catalytic performance and reaction pathways. *J. Hazard. Mater.* **2012**, *239*, 167-174.
3. *Estimation Programs Interface Suite™ for Microsoft® Windows, v 4.11*; United States Environmental Protection Agency: Washington, DC, USA, 2018.
4. Satou, M.; Yokoyama, S.; Sanada, Y. Structural analysis and estimation of boiling point of hydrocarbons in a coal-derived liquid by a group contribution method. *Fuel* **1992**, *71* (5), 565-574.
5. Prugh, R. W. Estimation of flash point temperature. *Journal of Chemical Education* **1973**, *50* (2), A85.
6. Butler, R. M.; Cooke, G. M.; Lukk, G. G.; Jameson, B. G. Prediction of Flash Points of Middle Distillates. *Industrial & Engineering Chemistry* **1956**, *48* (4), 808-812.
7. Lloyd, W. G.; Davenport, D. A. Applying thermodynamics to fossil fuels: Heats of combustion from elemental compositions. *Journal of Chemical Education* **1980**, *57* (1), 56.
8. Mott, R.; Spooner, C. The calorific value of carbon in coal: the Dulong relationship. *Fuel* **1940**, *19* (226), 242.
9. Boie, W. Fuel technology calculations. *Energietechnik* **1953**, *3*, 309-316.
10. Kessler, T.; Sacia, E. R.; Bell, A. T.; Mack, J. H. Artificial neural network based predictions of cetane number for furanic biofuel additives. *Fuel* **2017**, *206*, 171-179.
11. Das, D. D.; St. John, P. C.; McEnally, C. S.; Kim, S.; Pfefferle, L. D. Measuring and predicting sooting tendencies of oxygenates, alkanes, alkenes, cycloalkanes, and aromatics on a unified scale. *Combustion and Flame* **2018**, *190*, 349-364.

APPENDIX F

PERMISSIONS

Permission for use of Figure 1.3 in Chapter 1 is given as follows:



The screenshot displays the RightsLink interface. At the top, there is a navigation bar with 'My Orders', 'My Library', and 'My Profile' links. The user is logged in as 'xchenhuo@gmail.com'. The main content area is titled 'License Details' and contains a table of license information. The table lists various fields such as License Number, License date, Licensed Content Publisher, and more. The total amount is listed as 0.00 USD.

Field	Value
License Number	4557980514944
License date	Mar 28, 2019
Licensed Content Publisher	Elsevier
Licensed Content Publication	Water Research
Licensed Content Title	Evaluation of a hybrid ion exchange-catalyst treatment technology for nitrate removal from drinking water
Licensed Content Author	Allison M. Bergquist, Jong Kwon Choe, Timothy J. Strathmann, Charles J. Werth
Licensed Content Date	Jun 1, 2016
Licensed Content Volume	96
Licensed Content Issue	n/a
Licensed Content Pages	11
Type of Use	reuse in a thesis/dissertation
Portion	figures/tables/illustrations
Number of figures/tables/illustrations	1
Format	both print and electronic
Are you the author of this Elsevier article?	No
Will you be translating?	No
Original figure numbers	Fig. 1
Title of your thesis/dissertation	APPLICATION AND INTEGRATION OF RUTHENIUM CATALYSTS FOR WATER TREATMENT AND RESOURCE RECOVERY
Publisher of new work	Colorado School of Mines
Expected completion date	Apr 2019
Requestor Location	Xiangchen Huo Apt F1 GOLDEN, CO 80401 United States Attn: 16259 W 10th Ave 98-0397604
Publisher Tax ID	98-0397604
Total	0.00 USD

Permissions from co-authors from paper reprinted in Chapter 2 are as follows:

Jinyong Liu

Sun, Mar 10, 8:28 PM ☆ ↩

to me ▾

I, Jinyong Liu, hereby authorize Xiangchen Huo to use any part or all of DOI:10.1016/j.cej.2016.12.058 within her thesis.

Werth, Charles J

Sun, Mar 10, 8:43 PM ☆

to me ▾

"I, [Charles Werth], hereby authorize Xiangchen Huo to use any part or all of DOI:10.1016/j.cej.2016.12.058 within her thesis."

Yin Wang

Sun, Mar 10, 9:32 PM ☆

to me ▾

Hello Xiangchen,

I, Yin Wang, hereby authorize Xiangchen Huo to use any part or all of DOI:10.1016/j.cej.2016.12.058 within her thesis.

Xi Chen

Mar 10, 2019, 10:56 PM ☆ ↩

to Jinyong, Charles, Timothy, me, wang292 ▾

"I, Xi Chen, hereby authorize Xiangchen Huo to use any part or all of DOI:10.1016/j.cej.2016.12.058 within her thesis."

Timothy Strathmann <strthmnn@mines.edu>

8:23 AM (12 hours ago) ☆ ↩

to me ▾

"I, Timothy Strathmann, hereby authorize Xiangchen Huo to use any part or all of DOI:10.1016/j.cej.2016.12.058 within her thesis."

Permissions from co-authors from paper reprinted in Chapter 3 are as follows:

Jinyong Liu

Sun, Mar 10, 8:29 PM ☆ ↩

to me ▾

I, Jinyong Liu, hereby authorize Xiangchen Huo to use any part or all of DOI:10.1016/j.apcatb.2017.04.045 within her thesis.

Timothy Strathmann <strthmnn@mines.edu>

Mon, Mar 11, 8:07 AM ☆ ↩ ⋮

to me ▾

"I, Timothy Strathmann, hereby authorize Xiangchen Huo to use any part or all of DOI:10.1016/j.apcatb.2017.04.045 within her thesis."

Shubham Vyas <svyas@mines.edu>

Mon, Mar 11, 9:51 AM ☆ ↩

to Daniel, Jinyong, me, Timothy ▾

I, Shubham Vyas, hereby authorize Xiangchen Huo to use any part or all of DOI:10.1016/j.apcatb.2017.04.045 within her thesis.

Daniel Van Hoomissen

Mon, Mar 11, 10:28 AM ☆ ↩

to Shubham, me, Jinyong, Timothy ▾

"I, Daniel J. Van Hoomissen, hereby authorize Xiangchen Huo to use any part or all of DOI:10.1016/j.apcatb.2017.04.045 within her thesis."

Permissions from co-authors from paper reprinted in Chapter 4 are as follows:

Jinyong Liu

Sun, Mar 10, 8:30 PM ☆ ↩

to me ▾

I, Jinyong Liu, hereby authorize Xiangchen Huo to use any part or all of DOI:10.1016/j.apcatb.2017.04.045 within her thesis.

Timothy Strathmann <strthmnn@mines.edu>

Mon, Mar 11, 8:08 AM ☆ ↩

to me ▾

"I, Timothy Strathmann, hereby authorize Xiangchen Huo to use any part or all of DOI:10.1021/acs.est.7b05834 within her thesis."

Permissions from co-authors from submitted manuscript in Chapter 6 are as follows:

From: Beckham, Gregg

Sent: Monday, March 25, 2019 6:03:04 PM (UTC-07:00) Mountain Time (US & Canada)

To: Huo, Xiangchen

Subject: Re: Request for co-author permissions to use material for dissertation

Hi Xiangchen, I, Gregg Beckham, hereby authorize Xiangchen Huo to use any part or all of "Tailoring Diesel Bioblendstock from Integrated Catalytic Upgrading of Carboxylic Acids: A 'Fuel Property First' Approach" within her dissertation.

From: Salvachua, Davinia

Sent: Monday, March 25, 2019 6:07:21 PM (UTC-07:00) Mountain Time (US & Canada)

To: Huo, Xiangchen

Subject: RE: Request for co-author permissions to use material for dissertation

I, Davinia Salvachua, hereby authorize Xiangchen Huo to use any part or all of "Tailoring Diesel Bioblendstock from Integrated Catalytic Upgrading of Carboxylic Acids: A 'Fuel Property First' Approach" within her dissertation.

From: Kim, Seonah
Sent: Monday, March 25, 2019 6:11:20 PM (UTC-07:00) Mountain Time (US & Canada)
To: Huo, Xiangchen
Subject: Re: Request for co-author permissions to use material for dissertation

Sent from my iPhone

On Mar 25, 2019, at 5:01 PM, Huo, Xiangchen <Xiangchen.Huo@nrel.gov> wrote:

Dear All,

I am writing to request permission from you. I intend to use the manuscript "Tailoring Diesel Bioblendstock from Integrated Catalytic Upgrading of Carboxylic Acids: A 'Fuel Property First' Approach" in full within my PhD dissertation. To comply with school copyright policy, I need your written consent.

Please reply with your consent in the following format:

I, Seonah Kim, hereby authorize Xiangchen Huo to use any part or all of "Tailoring Diesel Bioblendstock from Integrated Catalytic Upgrading of Carboxylic Acids: A 'Fuel Property First' Approach" within her dissertation.

Is it good enough??

Seonah.

From: Huq, Nabila
Sent: Monday, March 25, 2019 6:12:44 PM (UTC-07:00) Mountain Time (US & Canada)
To: Huo, Xiangchen
Subject: RE: Request for co-author permissions to use material for dissertation

I, Nabila Huq, hereby authorize Xiangchen Huo to use any part or all of "Tailoring Diesel Bioblendstock from Integrated Catalytic Upgrading of Carboxylic Acids: A 'Fuel Property First' Approach" within her dissertation.

From: Starace, Anne
Sent: Monday, March 25, 2019 6:13:19 PM (UTC-07:00) Mountain Time (US & Canada)
To: Huo, Xiangchen
Subject: RE: Request for co-author permissions to use material for dissertation

I, Anne Starace, hereby authorize Xiangchen Huo to use any part or all of "Tailoring Diesel Bioblendstock from Integrated Catalytic Upgrading of Carboxylic Acids: A 'Fuel Property First' Approach" within her dissertation.

From: Allyson York
Sent: Monday, March 25, 2019 6:49:26 PM (UTC-07:00) Mountain Time (US & Canada)
To: Huo, Xiangchen
Subject: Re: Request for co-author permissions to use material for dissertation

I, Allyson York, hereby authorize Xiangchen Huo to use any part or all of "Tailoring Diesel Bioblendstock from Integrated Catalytic Upgrading of Carboxylic Acids: A 'Fuel Property First' Approach" within her dissertation.

From: Christensen, Earl
Sent: Monday, March 25, 2019 6:52:55 PM (UTC-07:00) Mountain Time (US & Canada)
To: Huo, Xiangchen
Subject: Re: Request for co-author permissions to use material for dissertation

Great!

I, Earl Christensen, hereby authorize Xiangchen Huo to use any part or all of "Tailoring Diesel Bioblendstock from Integrated Catalytic Upgrading of Carboxylic Acids: A 'Fuel Property First' Approach" within her dissertation.

From: Timothy Strathmann
Sent: Monday, March 25, 2019 6:56:39 PM (UTC-07:00) Mountain Time (US & Canada)
To: Huo, Xiangchen
Subject: Re: Request for co-author permissions to use material for dissertation

I, Timothy Strathmann, hereby authorize Xiangchen Huo to use any part or all of "Tailoring Diesel Bioblendstock from Integrated Catalytic Upgrading of Carboxylic Acids: A 'Fuel Property First' Approach" within her dissertation.

From: Charles McEnally
Sent: Monday, March 25, 2019 7:05:05 PM (UTC-07:00) Mountain Time (US & Canada)
To: Huo, Xiangchen
Subject: Re: Request for co-author permissions to use material for dissertation

Hi Xiangchen,

I, Charles McEnally, hereby authorize Xiangchen Huo to use any part or all of "Tailoring Diesel Bioblendstock from Integrated Catalytic Upgrading of Carboxylic Acids: A 'Fuel Property First' Approach" within her dissertation.

From: McCormick, Robert
Sent: Monday, March 25, 2019 7:47:57 PM (UTC-07:00) Mountain Time (US & Canada)
To: Huo, Xiangchen
Subject: RE: Request for co-author permissions to use material for dissertation

Dear Xiangchen,

I, Robert McCormick, hereby authorize Xiangchen Huo to use any part or all of "Tailoring Diesel Bioblendstock from Integrated Catalytic Upgrading of Carboxylic Acids: A 'Fuel Property First' Approach" within her dissertation.

From: Vardon, Derek
Sent: Monday, March 25, 2019 9:26:22 PM (UTC-07:00) Mountain Time (US & Canada)
To: Huo, Xiangchen
Subject: Re: Request for co-author permissions to use material for dissertation

I, Derek Vardon, hereby authorize Xiangchen Huo to use any part or all of "Tailoring Diesel Bioblendstock from Integrated Catalytic Upgrading of Carboxylic Acids: A 'Fuel Property First' Approach" within her dissertation.

From: Brandner, David
Sent: Tuesday, March 26, 2019 7:32:08 AM (UTC-07:00) Mountain Time (US & Canada)
To: Huo, Xiangchen
Subject: Re: Request for co-author permissions to use material for dissertation

I, David Brandner, hereby authorize Xiangchen Huo to use any part or all of "Tailoring Diesel Bioblendstock from Integrated Catalytic Upgrading of Carboxylic Acids: A 'Fuel Property First' Approach" within her dissertation.

From: Settle, Amy
Sent: Tuesday, March 26, 2019 7:35:34 AM (UTC-07:00) Mountain Time (US & Canada)
To: Huo, Xiangchen
Subject: Re: Request for co-author permissions to use material for dissertation

I, Amy Settle, hereby authorize Xiangchen Huo to use any part or all of "Tailoring Diesel Bioblendstock from Integrated Catalytic Upgrading of Carboxylic Acids: A 'Fuel Property First' Approach" within her dissertation.

From: Stunkel, Jim
Sent: Tuesday, March 26, 2019 8:10:49 AM (UTC-07:00) Mountain Time (US & Canada)
To: Huo, Xiangchen
Subject: RE: Request for co-author permissions to use material for dissertation

I, Jim Stunkel, hereby authorize Xiangchen Huo to use any part or all of "Tailoring Diesel Bioblendstock from Integrated Catalytic Upgrading of Carboxylic Acids: A 'Fuel Property First' Approach" within her dissertation.

From: Nelson, Robert
Sent: Tuesday, March 26, 2019 8:53:34 AM (UTC-07:00) Mountain Time (US & Canada)
To: Huo, Xiangchen
Subject: RE: Request for co-author permissions to use material for dissertation

I, Robert S. Nelson, hereby authorize Xiangchen Huo to use any part or all of "Tailoring Diesel Bioblendstock from Integrated Catalytic Upgrading of Carboxylic Acids: A 'Fuel Property First' Approach" within her dissertation.

From: Fouts, Lisa
Sent: Tuesday, March 26, 2019 10:16:20 AM (UTC-07:00) Mountain Time (US & Canada)
To: Huo, Xiangchen
Subject: RE: Request for co-author permissions to use material for dissertation

Hi Xiangchen,

No problem, here you go!

I, Lisa Fouts, hereby authorize Xiangchen Huo to use any part or all of "Tailoring Diesel Bioblendstock from Integrated Catalytic Upgrading of Carboxylic Acids: A 'Fuel Property First' Approach" within her dissertation.

From: Cleveland, Nicholas
Sent: Tuesday, March 26, 2019 10:23:28 AM (UTC-07:00) Mountain Time (US & Canada)
To: Huo, Xiangchen
Subject: Re: Request for co-author permissions to use material for dissertation

I, Nicholas Cleveland, hereby authorize Xiangchen Huo to use any part or all of "Tailoring Diesel Bioblendstock from Integrated Catalytic Upgrading of Carboxylic Acids: A 'Fuel Property First' Approach" within her dissertation.

From: Hunter Mack
Sent: Tuesday, March 26, 2019 12:14:56 PM (UTC-07:00) Mountain Time (US & Canada)
To: Huo, Xiangchen
Subject: Re: Request for co-author permissions to use material for dissertation

Xiangchen,
Happy to help, statement below.
Hunter

I, John Hunter Mack, hereby authorize Xiangchen Huo to use any part or all of "Tailoring Diesel Bioblendstock from Integrated Catalytic Upgrading of Carboxylic Acids: A 'Fuel Property First' Approach" within her dissertation.

From: Patrick Cherry
Sent: Thursday, March 28, 2019 8:08:53 AM (UTC-07:00) Mountain Time (US & Canada)
To: Huo, Xiangchen
Subject: Re: Request for co-author permissions to use material for dissertation

I, Patrick Cherry, hereby authorize Xiangchen Huo to use any part or all of "Tailoring Diesel Bioblendstock from Integrated Catalytic Upgrading of Carboxylic Acids: A 'Fuel Property First' Approach" within her dissertation.

From: Lisa Pfefferle
Sent: Friday, March 29, 2019 11:18:05 AM (UTC-07:00) Mountain Time (US & Canada)
To: Huo, Xiangchen
Subject: Re: Request for co-author permissions to use material for dissertation

Is this OK by email?

I, Lisa Pfefferle, hereby authorize Xiangchen Huo to use any part or all of "Tailoring Diesel Bioblendstock from Integrated Catalytic Upgrading of Carboxylic Acids: A 'Fuel Property First' Approach" within her dissertation.

From: St. John, Peter
Sent: Friday, March 29, 2019 8:53:51 AM (UTC-07:00) Mountain Time (US & Canada)
To: Huo, Xiangchen
Subject: Re: Request for co-author permissions to use material for dissertation

Oops, meant to do this but you caught me at a conference, thanks for the reminder.
Here you go:

I, Peter St. John, hereby authorize Xiangchen Huo to use any part or all of "Tailoring Diesel Bioblendstock from Integrated Catalytic Upgrading of Carboxylic Acids: A 'Fuel Property First' Approach" within her dissertation.